

UNCLASSIFIED

AD NUMBER
AD884829
NEW LIMITATION CHANGE
TO Approved for public release, distribution unlimited
FROM Distribution authorized to U.S. Gov't. agencies only; Test and Evaluation; May 1971. Other requests shall be referred to Air Force Avionics Lab., Wright-Patterson AFB, OH 45433.
AUTHORITY
AFAL ltr, 21 Sep 1978

THIS PAGE IS UNCLASSIFIED

THIS REPORT HAS BEEN DELIMITED
AND CLEARED FOR PUBLIC RELEASE
UNDER DOD DIRECTIVE 5200.20 AND
NO RESTRICTIONS ARE IMPOSED UPON
ITS USE AND DISCLOSURE.

DISTRIBUTION STATEMENT A

APPROVED FOR PUBLIC RELEASE;
DISTRIBUTION UNLIMITED.

Best Available Copy

71-0530

AFAL-TR-71-137

PERFORMANCE SYNTHESIS
(ELECTRO-OPTICAL SENSORS)

Frederick A. Rosell
Robert H. Willson

WESTINGHOUSE DEFENSE AND SPACE CENTER
Aerospace and Electronic Systems Division
Baltimore, Maryland

TECHNICAL REPORT
AFAL-TR-71-137

May 1971



AFAL (NVA-698DF), Wright-Patterson Air Force Base,
Ohio 45433

AIR FORCE AVIONICS LABORATORY
Air Force Systems Command
Wright-Patterson Air Force Base, Ohio

Distribution limited to U.S. Gov't. agencies only.
Test and Evaluation; 3-7-71
For this document must be referred to. Other requests

293

AD No. _____
DDC FILE COPY

AD884829

UNCLASSIFIED

Security Classification

DOCUMENT CONTROL DATA - R&D		
(Security classification of title, body of abstract and indexing annotation must be entered when the overall report is classified)		
1 ORIGINATING ACTIVITY (Corporate author)		2a REPORT SECURITY CLASSIFICATION
Westinghouse Defense and Space Center Aerospace Division, Baltimore, Maryland		2b GROUP None
3 REPORT TITLE		
Performance Synthesis (Electro-Optical Sensors)		
4 DESCRIPTIVE NOTES (Type of report and inclusive dates)		
Final Report		
5 AUTHOR(S) (Last name, first name, initial)		
Rosell, Frederick A. Willson, Robert H.		
6 REPORT DATE	7a TOTAL NO. OF PAGES	7b NO. OF REFS
May 1971	292	36
8a CONTRACT OR GRANT NO.	9a ORIGINATOR'S REPORT NUMBER(S)	
F33615-70C-1461		
b. PROJECT NO.	9b OTHER REPORT NO(S) (Any other numbers that may be assigned this report)	
698DF	AFAL-TR-71-137	
10. AVAILABILITY STATEMENT (If the report is classified, it is to be made available only to those persons having a valid need for it. If the report is unclassified, it is to be made available to all persons having a valid need for it.)		
11. SUPPLEMENTARY NOTES		
12. SPONSORING MILITARY ACTIVITY		
Air Force Avionics Laboratory Wright Patterson AF Base, Ohio 45433		
13 ABSTRACT		
<p>Analytical models are developed for evaluating and predicting the performance of observers augmented by electro-optical sensors when viewing images of comparatively simple geometry. These models provide a method of associating a signal-to-noise ratio with an image as a function of the image radiance and spatial dimension. It is shown that the ability of a sensor to provide such signal-to-noise ratios can be readily determined. Through psychophysical experimentation, the probability of the observer's detecting certain images was established using images of known signal-to-noise ratio. By matching the sensor capability with the observer requirements, overall sensor system performance is predicted.</p> <p>The models are perfectly general and apply to all electro-optical sensors. Their use is illustrated by applying them to the prediction of a number of representative sensors; including image dissectors, forward-looking infrared scanners, direct view light amplifiers, and low-light-level television. While the models still require further modification and verification, good correlation between predicted and measured sensor performance has been obtained using the models as they are. It is felt that the formulation used is the most accurate representation of the fundamentals of imaging as we know them and is a good point of departure for further development.</p> <p>Using the models devised, methods of predicting the range capability of sensor-augmented observers are developed and applied to both active and passive systems. These models take into account properties of the scene, atmospherics, and level of target discrimination. Again, good correlation with measured results have been observed.</p>		

DD FORM 1 JAN 64 1473

UNCLASSIFIED

Security Classification

ABSTRACT

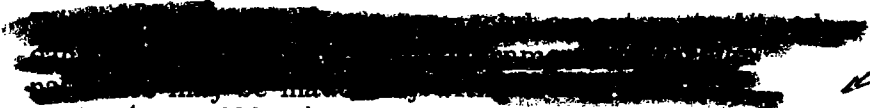
Analytical models are developed for evaluating and predicting the performance of observers augmented by electro-optical sensors when viewing images of comparatively simple geometry. These models provide a method of associating a signal-to-noise ratio with an image as a function of the image radiance and spatial dimension. It is shown that the ability of a sensor to provide such signal-to-noise ratios can be readily determined. Through psychophysical experimentation, the probability of the observer's detecting certain images was established using images of known signal-to-noise ratio. By matching the sensor capability with the observer requirements, overall sensor system performance is predicted.

The models are perfectly general and apply to all electro-optical sensors. Their use is illustrated by applying them to the prediction of a number of representative sensors; including image dissectors, forward-looking infrared scanners, direct view light amplifiers, and low-light-level television. While the models still require further modification and verification, good correlation between predicted and measured sensor performance has been obtained using the models as they are. It is felt that the formulation used is the most accurate representation of the fundamentals of imaging as we know them and is a good point of departure for further development.

Using the models devised, methods of predicting the range capability of sensor-augmented observers are developed and applied to both active and passive systems. These models take into account properties of the scene, atmospheric, and level of target discrimination. Again, good correlation with measured results have been observed.

PERFORMANCE SYNTHESIS

Frederick A. Rosell
Robert H. Willson


AFAL (NVA-698DF), Wright-Patterson Air Force Base,
Ohio 45433

Distribution limited to agencies only.
For this document must be referred to
for this document

FOREWORD

This program involved the development of mathematic models and performance of psychophysical experiments as part of the 698DF development project for a high-resolution low-light-level television system for tactical airborne application. It is felt that these studies have led to a better understanding of electro-optical sensors and their operation and could lead to improved sensors, improved methods of sensory system specification and a reduced need for costly laboratories and flight testing of systems.

The Air Force Project Director on this program was Frank A. McCann, AFAL/NVA(698DF). The Westinghouse effort was conducted principally by Frederick A. Rosell and Robert H. Willson. The program was performed by the Westinghouse Aerospace and Electronic Systems Division, Baltimore, Maryland, under Air Force Contract F33615-70C-1461.

This report was submitted by Frederick A. Rosell and Robert H. Willson.

This technical report has been reviewed and is approved.

Robert J. Doran
Deputy Director
Navigation Guidance Division
Air Force Avionics Laboratory

TABLE OF CONTENTS









<u>Section</u>	<u>Page</u>
I INTRODUCTION AND SUMMARY	1
II DETECTION OF ISOLATED RECTANGULAR IMAGES	13
III SPATIAL FREQUENCY ANALYSIS, ELEMENTARY MODEL	35
IV EFFECT OF A FINITE APERTURE	45
V PERIODIC SIGNALS AND FINITE WAVETRAINS	65
VI LEVELS OF DISCRIMINATION	99
VII DISPLAY LIMITATIONS	111
7.1 Introduction	111
7.2 The Fluctuation-Noise-Limited Eye	113
7.3 Impact on Sensory System Performance	121
7.4 Experimental Results	121
7.4.1 Influence of Monitor Brightness and Contrast With Noise in the Video Line	121
7.4.2 Influence of Monitor Brightness and Contrast - No Noise in the Video Line	122
VIII IMAGE DISSECTOR	125
IX FORWARD-LOOKING INFRARED SCANNER	135
X DIRECT VIEW IMAGE CONVERTERS AND IMAGE INTENSIFIERS	149
XI SILICON-EBIR TELEVISION CAMERAS	161
XII VIDICON CAMERA TUBES	177
12.1 Principles of Operation	177
12.2 The Silicon Vidicon	179
12.3 The Lead-Oxide Vidicon	182
12.4 The Vidicon	185

<u>Section</u>	<u>Page</u>
XIII THE SECONDARY ELECTRON CONDUCTION CAMERA TUBE	201
XIV IMAGE ORTHICONS AND IMAGE ISOCONS	211
14.1 The Image Orthicon	212
14.2 The Image Isocon	222
XV RANGE ANALYSIS	231
15.1 Analytical Model - Photoelectron-Limited Sensors	231
15.2 Analytical Model - Preamplifier-Limited and/or Photoelectron Limited	233
15.3 Atmospheric Introduction	235
15.3.1 Passive Irradiance	236
15.3.2 Active Irradiance	240
15.4 Natural Illumination	242
15.4.1 Current Methods of Analysis Using Psychometric Units	244
15.4.2 Conversion to Radiometric Analysis	248
15.5 Level of Discrimination	250
15.6 Range - Passive System, Three-Stage Intensifier	251
15.7 Range - Passive System ISEC	252
15.8 Range - Active System	254
15.9 Summary	257
XVI SYSTEM SYNTHESIS	265
REFERENCES	273

LIST OF ILLUSTRATIONS

<u>Figure</u>		<u>Page</u>
1	Display Signal-to-Noise Ratio Experiment	3
2	Measured Versus Predicted Probability of Detection	3
3	Measured Versus Predicted Probability of Detection	4
4	Probability of Recognition Versus (SNR_D) for ● Truck, ○ Tank, ■ Derrick, □ Radar Truck	7
5	Probability of Detection Versus Video Signal	8
6	Threshold Resolution Versus Input Photocurrent (Tubes with 80 or 40-mm Input Photocathode)	10
7	Electro-Optical Imaging Process	13
8	Display Signal-to-Noise Ratio Experiment	19
9	Measured Probability of Detection vs Predicted	20
10	Measured Probability of Detection vs Predicted	22
11	Measured Probability of Detection vs Predicted	23
12	Measured Probability of Detection vs Predicted	24
13	Probability of Detection vs Display S/N Ratio	25
14	Normal and Cumulative Probability	33
15	Measured Probability of Detection vs Predicted	34
16	Dirac Delta and Fourier Transform	37
17	Image $f(x, y)$ as a Weighting Function of Volume $f(\xi, \eta) d\xi d\eta$	38
18	Rectangular Image Distribution	41
19	Spatial Frequency Spectrum of Rectangular Image	43
20	Impulse Response	46
21	Signal Processor Block Diagram	48
22	Error Curve (---) Fit to Measured (—) MTF of a 3-Stage Image Intensifier and Equivalent Bandwidth, (N_{LPB}) of the Error Curve	50

<u>Figure</u>		<u>Page</u>
23	Impulse Response of Error Curve and Equivalent Pulse Duration	52
24	Modulation Transfer Function and Effective Bandwidth for Error Curve Filter in Dimensionless Coordinates	54
25	Unit Area Impulse Response and Effective Duration for Error Curve Filter in Dimensionless Units	54
26	Unit Step Response of Error Curve Filter in Dimensionless Units	56
27	Response of Error Curve Filter to Rectangular Input Pulse of Duration (x_o/a) = 1.0 and Effective Output Pulse Duration	56
28	Output-Input Pulse Amplitude vs Pulse Width Ratio (Input Rectangular with Unit Amplitude)	57
29	Effective Output vs Input Pulse Width (Input Rectangular with Unit Amplitude)	58
30	Output Pulse (-) for an Error Curve Filter as the Width of a Unit Amplitude Rectangular Input Pulse (---) Varies	59
31	Signal and S/N Ratio Reduction Factors Due to Spreading of Input Pulses by Error Curve Filter	61
32	Minimum Detectable Irradiance for Square of Width X_o	63
33	Minimum Detectable Power for Square of Width W for 3-Stage Intensifier (figure 22)	64
34	Resolution Test Chart Developed by Limansky for Calculation of Sine Wave MTF	65
35	Video S/N Ratio Required to Detect Pattern as a Function of the No. of Line Pairs Visible Through Mask	70
36	Threshold Display S/N Ratio Required to Identify Bar Patterns as a Function of Bar Length-to-Width Ratio	72
37	Fraction of Bar Patterns Identified Versus Display S/N Ratio Calculated on Basis of the Area of a Single Bar	75
38	Fraction of Bar Patterns Identified Versus Display S/N Ratio Calculated on the Basis of the Area of a Single Bar	76
39	SNR_D Required to Identify 1/2 of Bar Patterns	77
40	SNR_D Required to Identify 1/2 of Bar Patterns	78

<u>Figure</u>		<u>Page</u>
41	Display S/N Ratio as a Function of Sine Wave Pattern Frequency	80
42	Comparison of Display S/N Ratio	82
43	Periodic Sine Wave	87
44	Fourier Spectrum of a Periodic Square Wave	87
45	Equivalent Square Wave Flux Amplitude	90
46	Relationship Between Various Sensor Response Factors for an Assumed MTF	91
47	Relationship Between Various Sensor Response Factors	91
48	Portion of Wavetrain Assumed Used by the Eye to Recognize Wave Pattern	92
49	MTF, Square Wave Amplitude Response and Square Wave Energy Factor for a Typical Sensor	96
50	Geometry for Two Square Experiment	102
51	Probability of Recognition Versus $(SNR)_D$ for Square on Square $\Delta 2 \times 2$ on 16×16 , 8 Resolution Rectangles;  4×4 on 16×16 , 4RR;  2×2 on 8×8 , 4RR;  8×8 on 16×16 , 2RR;  4×4 on 8×8 , 2RR	104
52	Fractions of Patterns Identified Versus $(SNR)_D$	105
53	Fractions of Patterns Identified Versus $(SNR)_D$ for Rectangles With Nine Inscribed Bars	107
54	Probability of Recognition Versus $(SNR)_D$ for  Truck,  Tank,  Derrick,  Radar Truck	108
55	Effect of Display Controls on Output Image Brightness and Contrast	112
56	Contrast Transfer Function for an Infocus Eye	118
57	Modulation Transfer Function Estimates for the Unaided Human Eye	118
58	Threshold Contrast Versus Bar Pattern Spatial Frequency at Two Light Levels	120
59	Resolvable Temperature Difference for High- and Low-Gain CRT Contrast Control Settings	122
60	Probability of Detection of 4-Line Square Versus Total Monitor Brightness	123

<u>Figure</u>		<u>Page</u>
61	Probability of Detection Versus Video Signal	124
62	Schematic of an Image Dissector	125
63	Spectral Responsivity Versus Wavelength for Several Photoemissive Photocathodes	127
64	Modulation Transfer Function for a 40-mm Image Dissector	132
65	Threshold Resolution Versus Photocathode Irradiance for a 40-mm Dissector	133
66	FLIR Schematic	135
67	Modulation Transfer Function for Various FLIR Elements and Combined Sensory System Response	146
68	Threshold Resolution Versus Minimum Resolvable Temperature for the Assumed FLIR Parameters	147
69	Schematic of a Single-Stage Image Intensifier	150
70	Relative Spectral Radiance of a Modified P-20 Phosphor	152
71	Schematic of an Electronic Zoom Intensifier	154
72	Sine Wave Amplitude Response for a Single, Double, and Triple Intensifier (These Curves are Independent of Intensifier Size to a First Approximation)	155
73	Sine Wave Response of a Zoom Intensifier Referred to the Input Photocathode	156
74	Modular Type Cascade Image Intensifier	157
75	Threshold Resolution Versus Photocathode Irradiance	159
76	Cross Section of a Silicon EBIR Camera Tube	161
77	Schematic of Silicon-EBIR Target	163
78	Signal Current Versus Photocathode Irradiance Characteristic for the Silicon-EBIR and Intensifier-Silicon-EBIR Cameras for Various Input Photocathode Diameters	165
79	Silicon-EBIR Target Gain Versus Photoelectron Accelerating Voltage	166
80	Modulation Transfer Curves for the Silicon-EBIR Camera With Silicon Targets of Diameter 16 and 25 mm	167
81	Display Signal-to-Noise Ratio for SEBIR Camera with 16-mm Target	169

<u>Figure</u>		<u>Page</u>
82	Display Signal-to-Noise Ratio for SEBIR Camera with 25-mm Target	170
83	Limiting Resolution Versus Photocathode Current for the SEBIR Camera Tube	171
84	Modulation Transfer Function for Various Intensifier-SEBIR Tubes	172
85	Threshold Resolution Versus Input Photocathode Current for Intensifier - SEBIR Camera Tube With 16-mm Target	173
86	Threshold Resolution Versus Input Photocathode Current for Intensifier - SEBIR Camera Tubes With 25-mm Target	174
87	Threshold Resolution Versus Photocathode Irradiance for Various I-SEBIR Camera Tubes - Calculations are for Test Bars of 7:1 Length to Width Ratios of 100 Percent Contrast	176
88	Schematic of Vidicon and Associated Focus, Deflection and Alignment Coils	178
89	Spectral Response of the Silicon Vidicon	180
90	Output Signal Current Versus Photosurface Irradiance Transfer Characteristic for the Silicon Vidicon with 16-mm Photosurface Diameter	181
91	Modulation Transfer Curve for the Silicon Vidicon with Photosurface of 16-mm Diameter	182
92	Threshold Resolution Versus Photosurface Irradiance for the 16-mm Silicon Vidicon	183
93	Spectral Response of the Standard Lead Oxide Vidicon. Left Ordinate Applies to Tubes with Glass Faceplate - Right Ordinate, Fiber-Optic Faceplates	184
94	Signal Current Output for the 21.4-mm Lead Oxide Vidicon, Intensifier Lead Oxide Vidicon, and Double Intensifier Lead Oxide Vidicon as a Function of Photosurface Highlight Irradiance	186
95	Modulation Transfer Function for the 21.6-mm Lead Oxide Vidicon, Intensifier Lead Oxide Vidicon, and Double Intensifier Lead Oxide Vidicon	187
96	Threshold Resolution Versus Input Photocathode Current	188
97	Threshold Resolution Versus Photosurface Current	189

<u>Figure</u>		<u>Page</u>
98	Specific Spectral Responsivity for a Typical Porous Antimony-Trisulfide Photosurface	191
99	Signal Current Versus Photocathode Irradiance Characteristic for the 16- or 25-mm Vidicon	193
100	MTF for the 16- and 25-mm Vidicon and the 16- and 25-mm Triple Intensifier Vidicon	194
101	Threshold Resolution Versus Photosurface Irradiance for the (—) 16-mm and the (----) 25-mm Vidicon. Results Calculated for Test Bars of 7:1 Height to Width Ratio	195
102	Threshold Resolution Versus Photosurface Current for the (—) 16-mm and the (----) 25-mm Vidicon. Test Bars are of 7:1 Height to Width Ratio	195
103	Signal Current Versus Photocathode Irradiance Characteristics for the 16- and 25-mm Vidicons With Their Intensifier Variants	197
104	Prestorage Gain of the Triple Intensifier Vidicon for Intensifier and Vidicons of Equal Effective Phototransducer Area	198
105	Threshold Resolution Versus Input Photocathode Current for the (----) 25-mm and the (—) 16-mm Triple Intensifier. Results Calculated for a Test Bar of 7:1 Height to Width Ratio	199
106	Threshold Resolution Versus Input Photocathode Irradiance for the (----) 25-mm and (—) 16-mm Triple Intensifier Vidicon. Calculations for a Test Bar of 7:1 Height to Width Ratio	200
107	Cross Section of an SEC Camera Tube	201
108	Output Signal Current Versus Input Photocathode Irradiance for Various SEC and Intensifier SEC Camera Tubes	204
109	MTF of the WX31381 SEC Camera Tube Individually and in Combination With Intensifiers	206
110	Threshold Resolution Versus Photocathode Current for the 25- and 40-mm SEC Camera Tube for a Test Bar of 7:1 Height to Width Ratio	207
111	Threshold Resolution Versus Input Photocathode Current for the 80/40 and 40/40 mm Intensifier SEC Camera for a Test Bar of 7:1 Height to Width Ratio	208

<u>Figure</u>		<u>Page</u>
112	Threshold Resolution Versus Input Photocathode Current for the 25-mm Intensifier - SEC Camera - for a Test Bar of 7:1 Height to Width Ratio	209
113	Schematic of Image Orthicon	214
114	Cross Section Showing Action of Image Orthicon's Storage Target	215
115	Signal Current Versus Photocathode Irradiance Characteristic for the 3-in. Thin-Film, Metal-Oxide Targeted Image Orthicon With and Without an Intensifier	216
116	Uncompensated Horizontal Square Wave Amplitude Response for the 3-in. Thin-Film Targeted Image Orthicon	218
117	Modulation Transfer Function	218
118	Threshold Resolution Versus Photocathode Current - 7:1 Bar Length to Width Ratio	220
119	Threshold Resolution Versus Input Photocurrent - 7:1 Bar Length to Width Ratio	223
120	Schematic Arrangement of the New Image Isocon	224
121	Image Isocon Beam Separation System	225
122	Return Beam Cross Section at an Antinode	226
123	Signal Current Versus Photocathode Irradiance Characteristic for the RCA C21095 Image Isocon and Intensifier-Image Isocon	228
124	Uncompensated Horizontal Square Response for the RCA C21095 Image Isocon at Various Input Photocathode Irradiance Levels	229
125	Correction Factor to Atmosphere Attenuation Coefficient	237
126	Relative Contrast Versus Slant Range for Aircraft Altitude of 8,000 ft	239
127	The Spectral Responsivity of Two Photocathodes	245
128	Air Mass Versus Source Declination	246
129	Irradiance from 0.1 x Full Moon Plus Airglow	247

<u>Figure</u>		<u>Page</u>
130	Required Contrast at Sensor for 50 Percent Probability of Detection and Contrast at Sensor as a Function of Range	253
131	Range Versus Scene Irradiance for 50 Percent Probability of Detecting Truck Against Sand-Grass	255
132	Range Versus Scene Irradiance for 50 Percent Probability of Recognizing Panel	256
133	Detection Range Versus Visibility for Active System	257

LIST OF TABLES

<u>Table</u>		<u>Page</u>
I	Display Signal-to-Noise Ratio Required for 50 Percent Probability of Detection	21
II	Statistical Analysis for Experiment Involving Random Selection of Signal and Noise for Squares of Size 6 x 6 Scan Lines	26
III	Statistical Analysis for Experiment Involving Random Selection of Display S/N Ratio for Images of Size 6 x 6 Scan Lines	27
IV	Threshold SNR_D Required Using Equation 98 to Identify Bar Patterns of Various Height to Spacing Ratio, n_v as a Function of n_v . Dynamic Noise Assumed	74
V	Limiting Resolution for Two Signal Levels Using Two Different SNR_D Models	81
VI	Levels of Target Discrimination	100
VII	Johnson's Criteria for Resolution Per Minimum Target Dimension	100
VIII	Number of Bars Through Target for Various Targets	103
IX	Iris Diameter Versus Scene Luminance	116
X	Typical Photoemitter Parameters	129
XI	Incremental Radiance for a Blackbody Differing in Temperature by 1°K from a Background at 300°K in the Spectral Band 0 to λ Micrometers ⁵	142
XII	Incremental Radiance for a Blackbody Differing in Temperature by 1°K from a Background at 300°K in the Spectral Band 0 to λ Micrometers	143
XIII	MTF for an Aberration-Free Circular Aperture	145
XIV	Representative Values of Sky-Ground Ratio (K)	238
XV	Relationship Between Radiometric and Psychometric Quantities, Full Moon Plus Airglow With S-25 Photocathode	259
XVI	Relationship Between Radiometric and Psychometric Quantities, 0.3 Full Moon Plus Airglow With S-25 Photocathode	259

<u>Table</u>		<u>Page</u>
XVII	Relationship Between Radiometric and Psychometric Quantities, 0.1 Full Moon Plus Airglow With S-25 Photocathode	260
XVIII	Relationship Between Radiometric and Psychometric Quantities, 0.03 Full Moon Plus Airglow With S-25 Photocathode	260
XIX	Relationship Between Radiometric and Psychometric Quantities, Full Moon Plus Airglow With S-20-XR Photocathode	261
XX	Relationship Between Radiometric and Psychometric Quantities, 0.3 Full Moon Plus Airglow with S-20-XR Photocathode	261
XXI	Relationship Between Radiometric and Psychometric Quantities, 0.1 Full Moon Plus Airglow With S-20-XR Photocathode	262
XXII	Relationship Between Radiometric and Psychometric Quantities, 0.03 Full Moon Plus Airglow With S-20-XR Photocathode	262
XXIII	Scene and Sensor Parameters	263
XXIV	Calculation of Contrast Required at Sensor to Satisfy Equation 291 for $H_S = 10^{-3} \text{ W/m}^2$ Square Target, 10 ft Wide, MTF of 3-Stage Intensifier	264

SECTION I

INTRODUCTION AND SUMMARY

The objectives of the Performance Synthesis Study performed under Contract Number F33615-70C-1461 as part of Air Force Project 698DF are to determine the fundamental limitations of long-range air-to-ground detection, recognition, and identification of tactical military targets; to determine methods of realizing maximum range performance through optimum spatial, temporal, and electrical filtering of the received image signals; and to devise methods of predicting maximum range performance, taking into account the parameters of real targets, backgrounds, illumination sources, atmospheric conditions, and sensory systems. The results are to be applicable to all imaging sensors, whether passive or active, and are to include low-light-level television, forward-looking infrared scanners, and direct view light amplifiers.

The approach taken in this program was to devise analytical models to describe sensory system operation including the observer as an integral part of the system. Psychophysical experiments were performed to obtain the necessary constants required to quantitatively evaluate the analytical models devised. Using these models, performance of a wide variety of sensors was predicted and coincided closely with measured performance. It is felt that these studies have led to a better understanding of electro-optical sensors and their operation and will lead to improved sensors, improved methods of sensory system specification and a reduction of costly laboratory and flight testing of systems.

Although the prediction of sensory system performance must still be regarded as an art needing considerable development to achieve greater precision and to extend the results to more complicated and more

realistic imaging situations, we feel that the progress made in this study is substantial. Indeed, the results of this program as reported herein, exceeded our early expectations - particularly with regard to basic concepts.

In order to focus on fundamentals and to form a firm analytical basis, most of the test images used in the analyses and the experimentation in this program were of comparatively simple geometry such as regular squares, rectangles, and periodic sine waves and bar patterns although some efforts were made to determine the correlation between the detectability of these simple objects and real tactical targets such as tanks and trucks. In Sections II through IV, the test objects were simple squares and rectangles. In the initial analysis, it was assumed that the sensor was photoelectron or fluctuation noise limited and that the sensor's point spread function was essentially an impulse which corresponds to a uniform spatial frequency response of infinite extent. It was found to be possible to associate a signal-to-noise ratio with simple images produced by this ideal sensor. The possibility of synthetically generating images, such as would be produced by the ideal sensor on a television display with known signal-to-noise ratios was also disclosed. The experimental setup is as shown in figure 1. In one of many experiments discussed in Section II, the test images were rectangles of variable length-to-width ratio which could appear in any of 4 quadrants on the display. The observer was asked to specify their location as the test images were randomly moved about. Prior to display, the image signals were randomly selected and mixed with a known amount of band-limited white noise.

The probability of the observer detecting the test image is plotted as a function of the video-signal-to-noise ratio in figure 2. In the experiment, the test image size was specified in units of the television display's scan linewidths of which there were 490 active in the picture height.

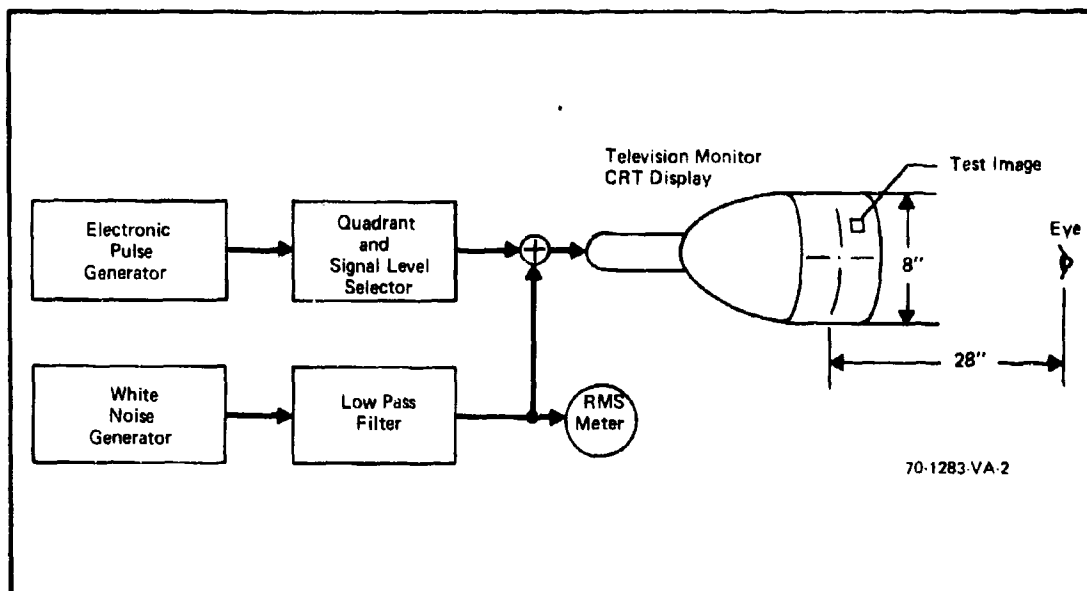


Figure 1. Display Signal-to-Noise Ratio Experiment

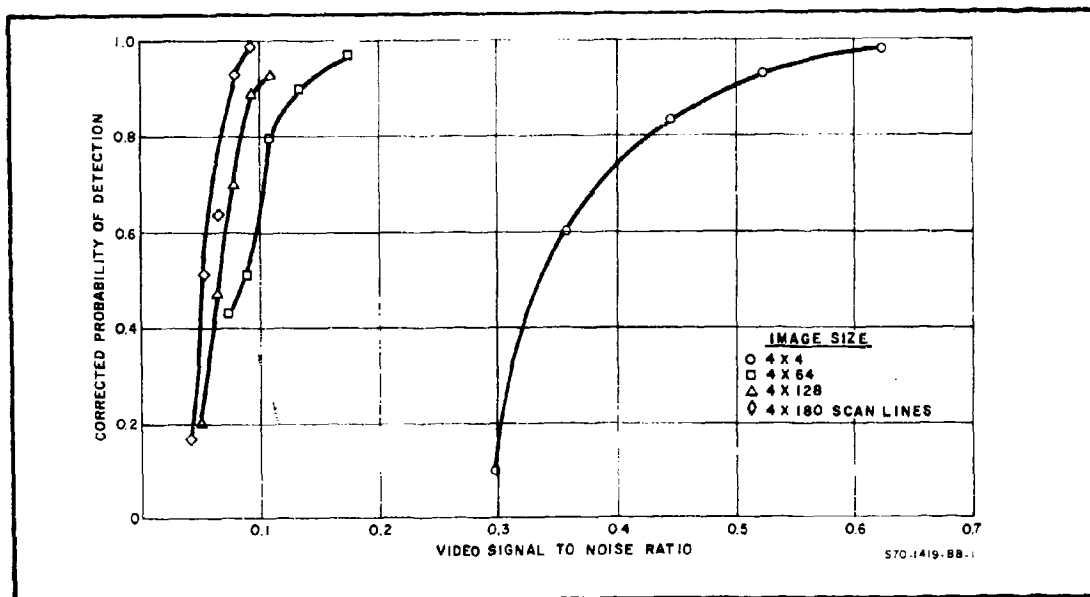


Figure 2. Measured Versus Predicted Probability of Detection

The video signal-to-noise ratio or SNR_V , is a measure of the image's SNR in a single scan line rather than over its entire area. In the analysis referred to earlier, it was found that the image's SNR (referred to as the display signal-to-noise ratio or SNR_D herein), could be related to the SNR_V analytically. The result is shown as a curve of probability of detection versus SNR_D in figure 3. It is seen that the SNR_D required for the detection of a rectangle is independent of the rectangles size over a large range. In the experiment, the smallest rectangle was 4×4 scan lines in size and the largest was 180×4 scan lines. The smallest subtended 0.13×0.13 degree at the observer's eye and the largest, 0.13×6.02 degrees. The eye can apparently integrate in space over angles of large extent. The extent recorded here is generally much larger than was previously thought and is one of the important results recorded in this study. In other experiments, the image sizes and contrasts were varied and the detectability of images in motion were studied. A probability of detection model was developed and fitted to the experimentally measured results.

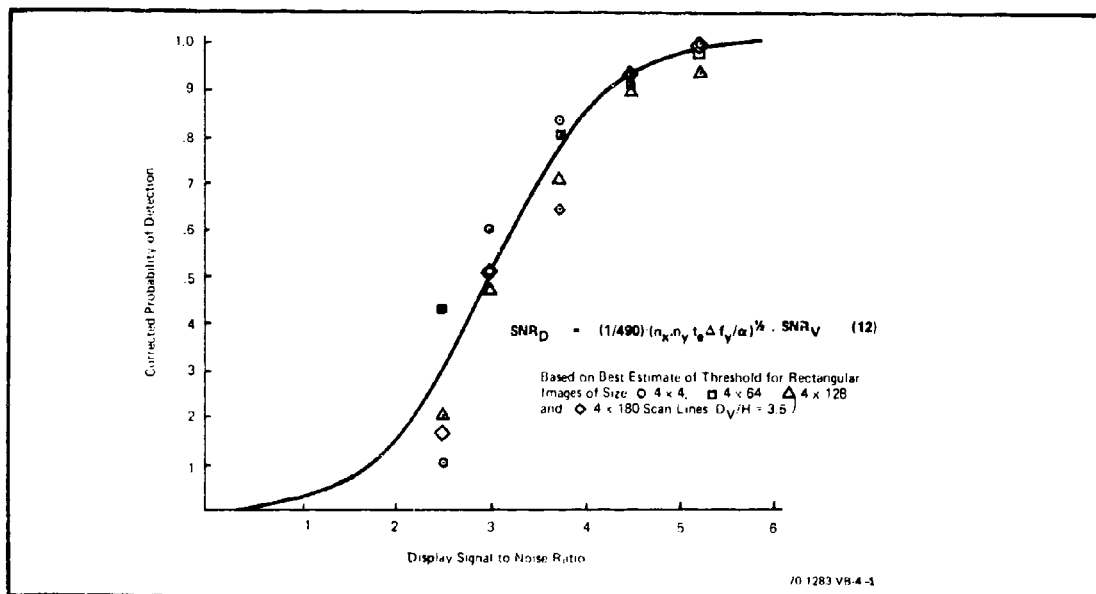


Figure 3. Measured Versus Predicted Probability of Detection

The elementary analytical model serves quite well in describing images developed by ideal sensors and has been widely used by other investigators. However, the imagery developed by real sensors are degraded by the sensor's finite apertures such as optical lenses, fiber optic transfer plates, electron lenses, finite phosphor particles, and electron reading beams. Over the past few years it has become routine to measure and report these apertures. (Usually in the form of a one-dimensional modulation transfer function or MTF.) However, the effect of the apertures on image detectability has often been more qualitative than quantitative. Sections III and IV demonstrate that the application of the elementary model to real sensors with finite apertures could lead to the conclusion that apertures improve the detectability of small aperiodic images since image signals remain unaltered while the noise in the signal is smoothed.

This result is unlikely. Thus, a new model is proposed which views the eye as an energy detector. In this new formulation, based on the Fourier integral energy theorem, the higher signal amplitudes are weighted more heavily than signals of lower amplitude which are buried in the noise. With this weighting, the effect of an aperture is found to be degrading, a condition much more likely to be the case. This result is felt to be the major contribution made to the art of imaging system prediction in this effort. The impact of the new model on the detectability of aperiodic images is studied in Section IV. Through its use, certain parameters such as noise equivalent irradiance for any imaging device can be defined. Previously, these quantities were well defined only for point detector systems.

In Section V, the detectability of periodic test patterns such as sine waves and bars is considered. These patterns are the most often used in evaluating the resolving power of sensors. The historical development of imaging models for the periodic test pattern case was reviewed. It was previously thought that the eye integrated signals from a repetitive pattern

along each bar or sine wave in the pattern and across a number of bars. However, it was found that while the eye can apparently integrate for long distances along the bar, the assumption that a number of bars are integrated appears unwarranted. Hence, it was postulated that the eye uses but a single bar in recognizing the presence of a bar or sine wave pattern. The earlier data from other investigators appears to support this contention when the data is viewed in this new light. Some preliminary data was taken and this data tends to support the new view.

A new analytical model was constructed to describe the resolution sensitivity characteristic of sensors viewing periodic test patterns and is employed to reevaluate a number of sensors in later sections. The new models overcome many objections raised in regard to the earlier models in that the noise filtering effects of apertures are included in addition to the signal degrading effects previously observed.

In Section VI, more complex targets and higher levels of target discrimination than detection such as recognition and identification are discussed. In this work, an effort was made to correlate the detectability and recognizability of standardized test patterns (such as bar patterns) with the same levels of discrimination for real targets such as tanks and trucks. This work proceeded along the lines suggested by John Johnson of the US Army's Warfare Vision Branch. In his analysis, visual levels of discrimination are correlated with the number of resolution bars through the minimum target dimension. In one experiment of Section VI, the SNR_D required to recognize tanks, trucks, etc, was determined and the results of the tank-truck experiment are shown in figure 4. For this experiment, Johnson's criteria of 8 bars through the minimum target dimension was assumed, and the calculation of SNR_D was based on the area of a single bar of an 8-bar pattern of area equal to the area of the tank, truck, etc. The value of SNR_D required for recognition of the real-world image is, within experimental accuracy, identical to that required theoretically in

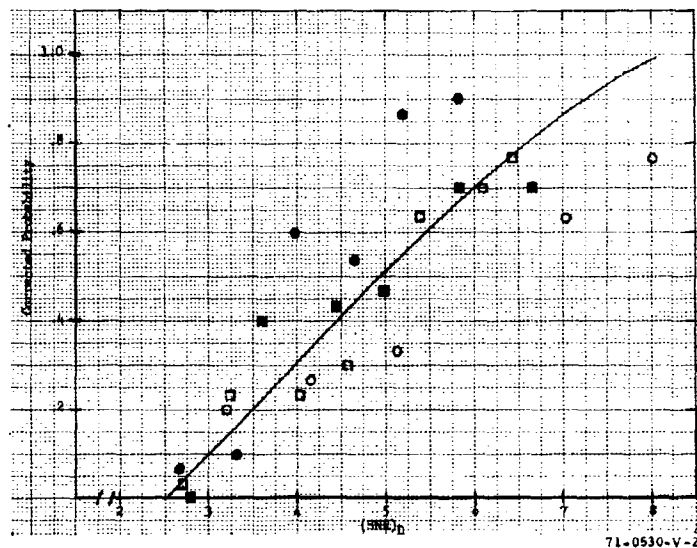


Figure 4. Probability of Recognition Versus (SNR_D) for
 ● Truck, ○ Tank, ■ Derrick, □ Radar Truck

Section V for recognizing of bar patterns. Furthermore, a measurement of SNR_D for a bar pattern of area equal to the tank yielded a value of SNR_D that was also equal to the theoretical value within experimental accuracy. The resolution results we obtained were consistent with those reported by Johnson which lends credence to the measurements, and, in addition, the results can be used directly in the analytical models developed in the earlier sections. Though these measurements were modest in scope, they represent an important first step in extending the prediction methods to encompass real imaging situations.

It has become even more evident that the display can become an important limitation to sensory system performance. This effect has been particularly noted in the case of FLIR equipment when wide intrascene temperature excursions are encountered which require that the display's dynamic luminance range. It was postulated that the performance

limitations noted are due to display luminance-fluctuation noise generated within retinal photo-conversion process of the observer's eye. The reduction in video gain causes small signals to drop below the display luminance fluctuation noise. While this hypothesis first seemed improbable when conceived, our calculations in Section VII indicate its possibility. In one of the experiments discussed in Section VII, very large video signal-to-noise ratios were used. The brightness of the display and the contrast (video gain) were randomly varied. For the larger values of display brightness, the observer was display luminance-fluctuation noise limited. The results of the experiment are shown in figure 5. The results from figure 5 show that at a fixed monitor brightness, an increase in video signal (corresponding to an increase in the video gain) increases the probability of detection; that is the minimum detectable contrast is less. Similarly, for a fixed video signal (that is for a fixed video gain) an increase in the display brightness corresponds to a decrease in the probability of

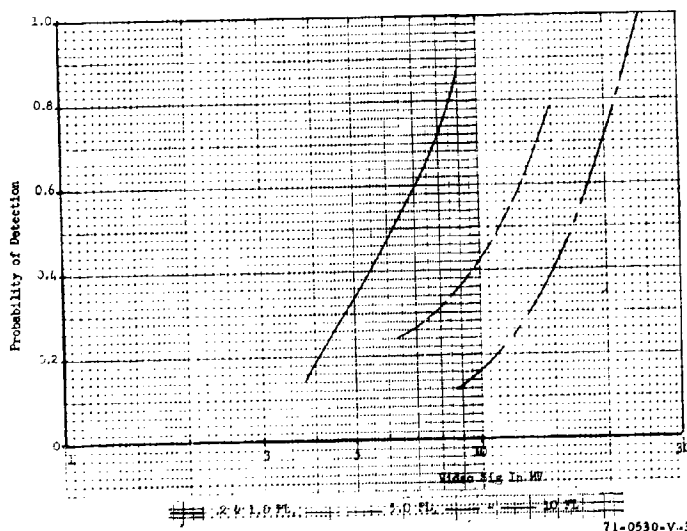


Figure 5. Probability of Detection Versus Video Signal

detection. In other words, an increase in the display brightness was accompanied by an increase in the minimum detectable contrast. The results, as reported in Section VII, confirm the hypothesis, and the same conclusions have been reached and reported by R. Sendall¹ at the January 1971 IRIS meeting of the Imaging Sensor Specialty Group in Dallas, Texas and by measurements at Wright Field.

Analytical models used in Sections VII through XV predict the threshold resolution versus sensitivity characteristics of a wide variety of sensors including the image dissector, forward-looking infrared scanners (or FLIR), direct view light amplifiers, and a number of television cameras based on the SEBIR, vidicon, lead oxide vidicon, silicon vidicon, SEC, and image orthicon camera tubes. Where appropriate, the combinations of these tubes with added stages of image intensification are analyzed. The Image Isocon is also discussed but its performance is not predicted because of the uncertainty regarding its modulation transfer characteristics. These analyses are all based on the new models developed. A sampling of the results obtained are shown in figure 6 wherein the threshold resolution of a number of television cameras are plotted versus the input photocathode current. The use of photocathode current in the analysis and reporting of results generalize the results to any arbitrary input photocathode type and diameter.

In Section XV, methods of predicting the range capability of sensors are devised. Using the elementary statistical model from Section II and the effect of apertures from Section IV, the range equation was significantly improved and refined. It is applicable for both the photoelectron-limited and the pre-amplifier-limited sensor in either the action or the passive mode. Included in the range equation are the target size and range, the sensor and target spatial frequency characteristics, the responsivity and area of the photocathode, the irradiance, the overall gain, the noise equivalent bandwidth and noise current of the preamplifier, the target background contrast as seen at

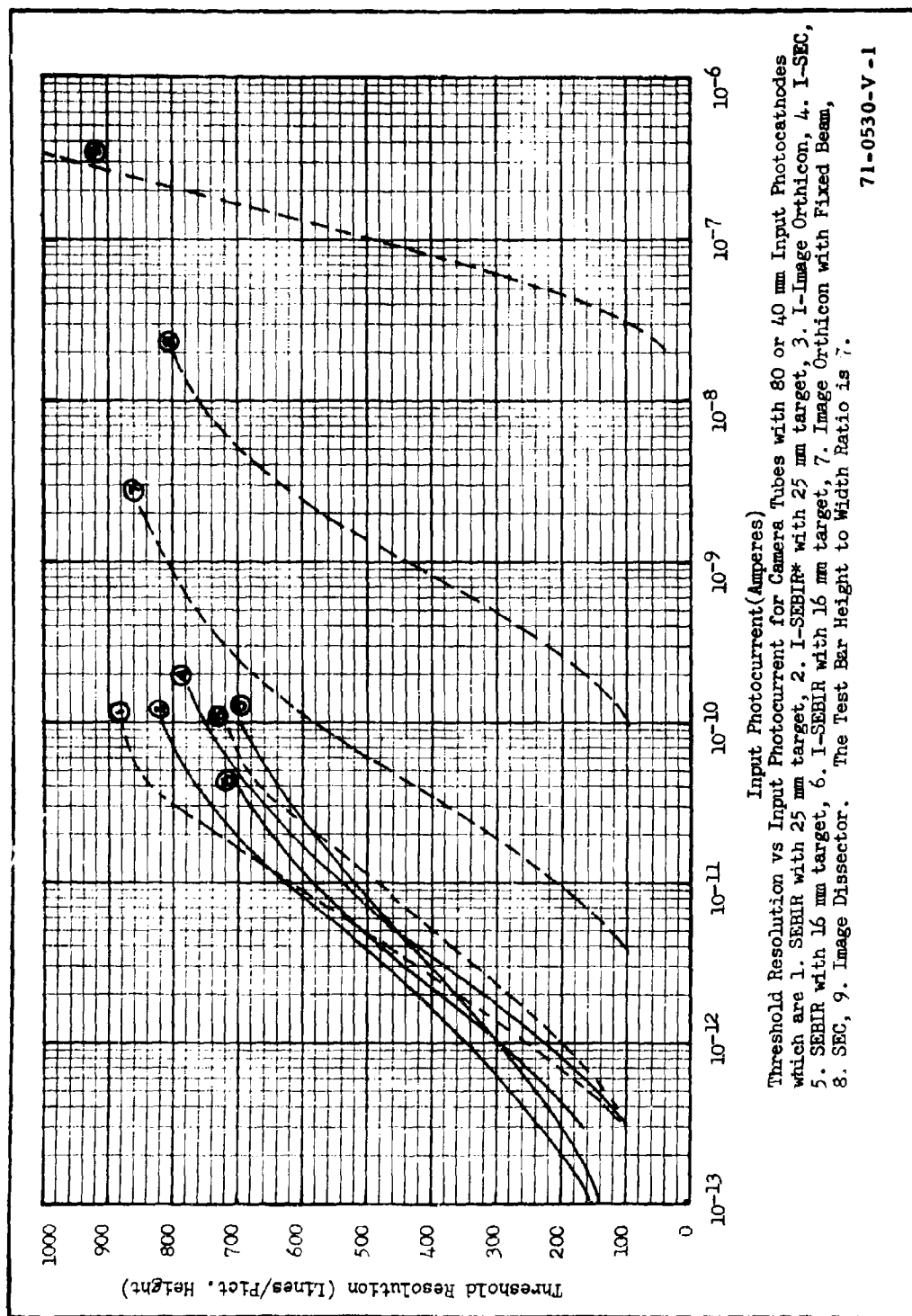


Figure 6. Threshold Resolution Versus Input Photocurrent
(Tubes with 80 or 40-mm Input Photocathodes)

the sensor, the integration time of the eye, and the required value of SNR_D for the given level of target discrimination. Atmospheric visibility and sky-ground ratio are used to calculate the degrading effect of the atmosphere on contrast for the passive case and, with the sensor on-off ratio contrast as a function of range and atmosphere was calculated for the active case. The methods were used to predict the performance of both active and passive low-light-level television cameras.

Finally, in Section XVI, we discuss the use of the new models in synthesizing, specifying, evaluating, and developing new sensory systems. It is seen that the models will have direct and immediate use in system measurement and specification since previously employed methods can lead to substantial error. It is seen that more prestorage gain can be used in photoelectron-noise-limited sensors than was previously thought to be the case and that the gain so provided leads to marked performance improvements. Possibilities of reducing display limitations are discussed. It is also readily seen that the methods of predicting range performance should lead to systems which more nearly meet mission requirements in their prototype stage.

In the course of the model development, it was found that the height-to-bar spacing ratios of the test patterns used in measuring camera performance can have considerable impact on sensory system performance. Currently, the test patterns used are not standardized either within government laboratories nor in industry. Although no compelling reasons for standardization are indicated other than for uniformity in reporting or for ease of data utilization, the test patterns used must as a minimum be reported, and, where practicable, performance correction factors from pattern to pattern should be devised.

BLANK PAGE

SECTION II

DETECTION OF ISOLATED RECTANGULAR IMAGES

In this section, we will treat one of the simpler visual tasks; detecting an isolated rectangular object as viewed against a uniform background of large extent by an electro-optical-sensor-augmented observer.

Consider the simple imaging geometry shown in figure 7. The scene, consisting of a rectangular object against a uniform background, is imaged on a photocathode by a lens. The photocathode converts the scene photon image to a photoelectron image. This image is then amplified and magnified in a signal processor and focused onto a phosphored display screen that, in turn, reconverts the photoelectron image to a visible light image. Next, photons from the displayed image are collected by the lens of the observer's eye and projected onto his retina. The retina converts the image to sensory impulses for subsequent processing and interpretation by the brain.

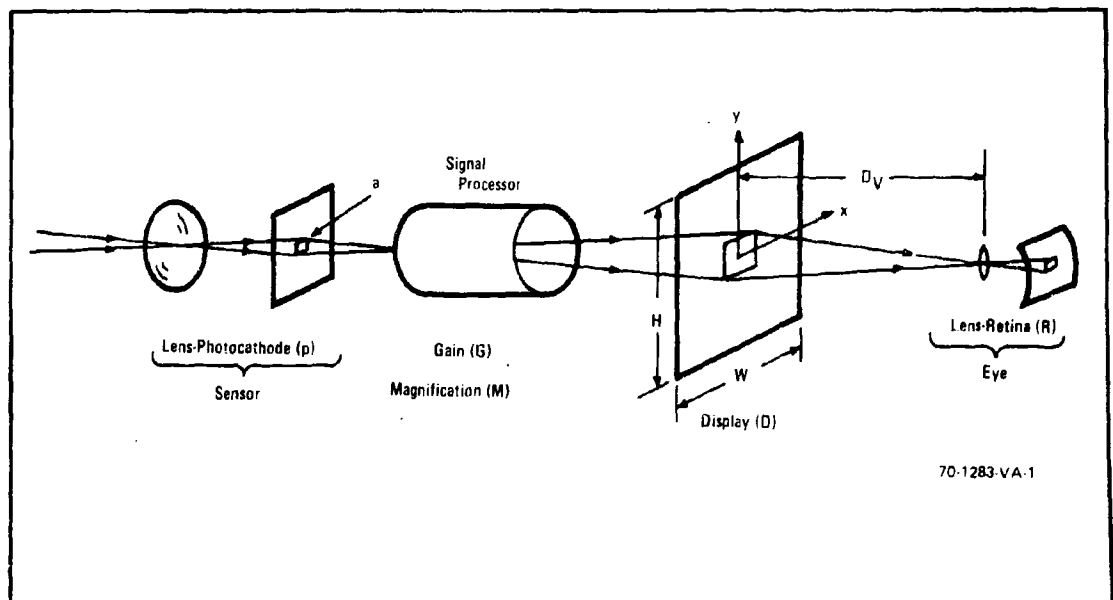


Figure 7. Electro-Optical Imaging Process

In effect, the sensor lens and photocathode replace the lens and retina of the eye as the primary phototransducer. The purpose of replacing the eye as the primary sensor is to provide it with some capability that it does not ordinarily have. For example, the sensor lens can have greater aperture and thus greater light-gathering capability. Longer focal lengths can be employed to increase scene resolution. Photocathodes of greater quantum efficiency than the retina can be obtained, and in addition, photo-response can be obtained at wavelengths beyond the visible. Even without these attributes, the sensor may be of aid, because it can be remotely located where the observer cannot or prefers not to be.

In many electro-optical sensory systems, the designer has some latitude in selecting the lens and the input photocathode type. For our present purposes, we may regard both the lens and the photocathode type as design parameters. Then, the beginning point of our analysis is at the photocathode, which is taken to be the source of a photoelectron image. System elements (including the observer) that follow it are generally unaware of the source of these photoelectrons. We further observe that the primary photoprocess in converting scene photons to electrons is noisy; thus, we can associate a signal-to-noise ratio with the photoelectron image generated.

The function of the signal processor is to amplify the photoelectron signal and, if necessary, to magnify the image. If the sensor were ideal, the signal and the noises would be equally amplified and magnified so that the signal-to-noise ratio at the phosphored screen would be identical to that at the photocathode. In real sensors, noise may be added in the processor, and in addition, the signals are distorted or smeared by the finite apertures of the signal processor and display elements. These apertures may include the effects of electron lenses, fiber-optic coupling plates, electron scanning beams, bandpass filters, finite phosphor particles, etc. The effect of these apertures can be measured and specified in terms of the system point spread function. So long as our rectangular image is large relative to the effective

diameter of the point spread function, we can neglect the effect of the apertures. We will temporarily assume this to be the case. Also, we will temporarily assume a noise-free signal processor.

The eye viewing the display also has limitations, depending on the display brightness, the image size, and the viewing distance. A fluctuation noise is associated with the conversion of display photons to sensory impulses and both the eye and the retina have finite apertures. However, we shall temporarily assume that the display brightness is high enough, the image is large enough, and the display viewing distance is either short enough or otherwise optimized so that either retinal fluctuation noise or acuity limitations to image detection are precluded. In addition, the angular extent of the image will not be so large as to exceed the spatial integration capability of the eye. Many of these restrictions will be lifted as the discussion proceeds. In any event, with the assumptions made, it is implied that the signal-to-noise (S/N) ratio at the display and at the retina are identical to that established by the sensor input photocathode. We also imply that all sensor and observer signal processes are linear. The purpose of making all of these initial assumptions is to show the fundamental limitations imposed by the input photocathode alone.

The elementary model describing the effect of photoprocess fluctuation noise on image detection is ordinarily attributed to Rose² who in turn attributes its origin to deVries,³ The basic notion is that the photon-to-photoelectron conversion process is random in space and time. It has been shown that this randomness can be characterized by the Poisson probability distribution law. Suppose that the photocathode emits \dot{n}_{xy} photoelectrons per unit area and time. According to Poisson statistics, the average or mean number, \bar{n} , emitted by an area, a , in a time, t , will be numerically equally to

$$\bar{n} = \dot{n}_{xy} at \quad (1)$$

where \dot{n}_{xy} is the average rate of photoemission.

Let the average number of photoelectrons emitted by an object be designated by \bar{n}_o , and suppose the average number emitted by the background in an equivalent area and time is \bar{n}_b . The elementary model then proposes that the signal will be equal to $\Delta\bar{n}$, where

$$\begin{aligned} S_p &= \Delta\bar{n} = \bar{n}_o - \bar{n}_b \\ &= \Delta\bar{n}_{xy} \text{ at } t \end{aligned} \quad (2)$$

If the signal and background photoelectrons follow Poisson statistics, then the standard deviation σ_p (or rms noise) due to fluctuations is proportional to the photoelectron number generated during the sampling period and time. In the Rose model, the noise is taken to be equal to $(\bar{n}_b)^{1/2}$ (i.e., equal to the background rate). In a later model by Coltman and Anderson⁴, it was suggested that the fluctuations from the signal and background can be added quadratically as follows:

$$\sigma_p = \left[\bar{n}_o + \bar{n}_b \right]^{1/2} \quad (3)$$

This noise model agrees better with the statistical model that will be described later.

It is well-known that the detectability of objects with positive contrast (objects brighter than their surroundings) is approximately equal to the detectability of objects with negative contrast (objects darker than their surroundings).⁵ For convenience, we will define the contrast of isolated objects to be always positive and to be numerically equal to

$$C = (\bar{n}_{xy \text{ max}} - \bar{n}_{xy \text{ min}}) / \bar{n}_{xy \text{ max}} \quad (4)$$

where $\bar{n}_{xy \text{ max}}$ and $\bar{n}_{xy \text{ min}}$ are the photoelectron rates due to scene highlights and lowlights, respectively.

Now, by combining equations 2, 3 and 4, the S/N ratio becomes

$$\text{SNR}_D = \Delta\bar{n}_{xy} / (\bar{n}_o + \bar{n}_b)^{1/2} = \Delta\bar{n}_{xy} \text{ at } t / (\bar{n}_o + \bar{n}_b)^{1/2} \quad (5)$$

$$= \Delta\bar{n}_{xy} \text{ at } t / \left[(\bar{n}_{xy \text{ max}} + \bar{n}_{xy \text{ min}}) \text{ at } t \right]^{1/2} \quad (6)$$

$$\text{SNR}_D = \bar{n}_{xy \text{ max}}^{\text{at}} / \left[(2-C) \bar{n}_{xy \text{ max}}^{\text{at}} \right]^{1/2} \quad (7)$$

We have arbitrarily chosen to designate the S/N ratio as being that at the display (D). By our assumptions, this is numerically equal to the S/N at the photocathode which is equal to the S/N ratio at the retina, provided that the reference sampling time period is taken to be that of the observer's eye. The reason for choosing the reference point as that of the display is that in later analysis, we will want to consider the effect of observer viewing distance.

Next, the elementary model exemplified by equation 5 postulates that to be detectable, the display S/N ratio, SNR_D , must exceed some threshold value SNR_{DT} , where the subscript T implies threshold. The definition of SNR_{DT} is such that a 50-percent probability of detection is implied. By examination of a large number of noisy photographs, Rose found that the threshold, SNR_{DT} , required for detection is constant over a wide range of conditions.

To continue, we will consider the specific case of a television camera tube considered ideal in the sense described above. Our first effort will be to convert equation 7 to a form that can be described in terms of readily measured sensor parameters. First, we note that the photoelectron rate can be written in terms of a photocurrent, i , as follows:

$$\bar{n}_{xy \text{ max}} = \frac{i_{\text{max}}}{eA} \quad (8)$$

where e is the charge of an electron (coul), and A is the effective raster area scanned by the electron beam. Now, equation 7 becomes

$$\begin{aligned} \text{SNR}_D &= \frac{C a i_{\text{max}} / (eA)}{\left[(2-C) a i_{\text{max}} / (eA) \right]^{1/2}} \\ &= (a t / A)^{1/2} \left[\frac{C i_{\text{max}}}{\left[(2-C) e i_{\text{max}} \right]^{1/2}} \right] \end{aligned} \quad (9)$$

Before proceeding, we note that the photocurrent is related to the image irradiance by the formula

$$i = \sigma_A A H_A \quad (10)$$

where σ_A is the photocathode responsivity in A/W to some specific test source, H_A , in W/m^2 , and A is the effective photocathode area as before. The σ_A should not be confused with the standard deviation, σ_p , of equation 3.

As the next step, we multiply the numerator and denominator of equation 9 by Δf_V the video bandwidth such that,

$$\text{SNR}_D = \left[at \cdot \Delta f_V / A \right]^{1/2} \left[\frac{C_{i_{\max}}}{[(2-c) e \Delta f_V i_{\max}]} \right]^{1/2} \quad (11)$$

The second bracketed term to the right represents the video S/N ratio for a sensor limited only by photo-electron noise. This formulation is convenient, because the video S/N ratio, SNR_V , can be directly measured in the signal processor electrical channel. Using SNR_V in equation 11, we have that SNR_D and SNR_V are related by

$$\text{SNR}_D = \left[(a/A) t \Delta f_V \right]^{1/2} \text{SNR}_V \quad (12)$$

Equation 12 suggests that the same value of SNR_D should be obtained for different size targets; that is, if the SNR_V value is chosen inversely proportional to the square root of the target area, a , then different size targets will have the same value of SNR_D . In the following experiment, the value of SNR_D required for a given probability of detection is determined for different size squares to test equation 12. If the equation is correct, the value of SNR_D should be independent of target size.

The experiment is shown schematically in figure 8. The signal pulse is electronically generated so that it will correspond as close as possible to a perfect square on the display. Prior to display, the signal is linearly mixed with band-limited white noise of Gaussian distribution. Initially, the spatial image

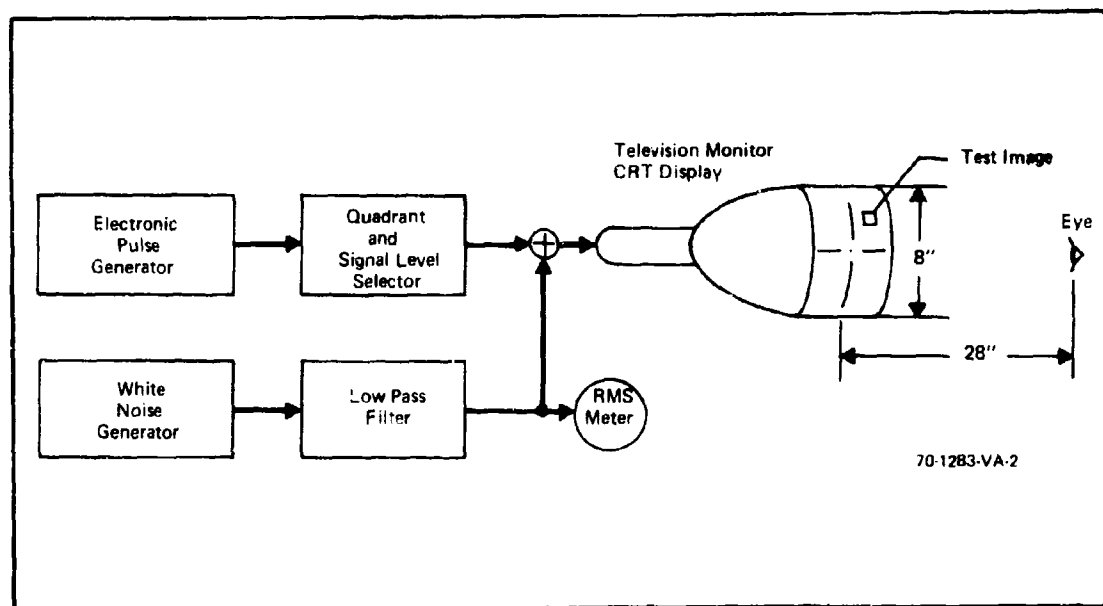


Figure 8. Display Signal-to-Noise Ratio Experiment

format chosen was a square that could be located in any of four different quadrants (but always at the same position in the quadrant selected). The observer is asked to specify which quadrant the image is located in as the display S/N ratios and the locations are randomly varied. The same SNR_D values were used for each target size. The responses were forced (i.e., the observer was required to specify the targets location whether he could see it or not). The probability of detection, so determined, was then corrected for pure chance. Each target was presented to the observer for 10 seconds and removed.

The results of the experiment are shown by the curves of figure 9, which are fitted to the measured data on a basis of a statistical model that will be discussed later. In the experiment, the image size n_x by n_y , was expressed in units of scan line widths assuming there were a total of 525 vertical scan lines with 490 active lines. Thus the ratio of the image size, a , to the total area, A , is

$$\frac{a}{A} = \frac{n_x n_y}{a(490)^2} = \frac{n_y^2}{a(490)^2} \quad (13)$$

where a is the display width-to-height aspect ratio, which was $4/3$ in this case and, $n_x = n_y$ since the target was square. Then, SNR_D is computed using

$$SNR_D = \frac{[t \Delta f_V / a]^{1/2} n_y}{490} \cdot SNR_V \quad (14)$$

The video noise bandwidth used was 7.1 MHz, and t , the observer integration time was taken to be 0.2 sec for the purposes of calculation.

The total experiment involved using five trained observers. For each observer, 4 different image sizes, 4 image positions (quadrants), 5 observations per size, and 2 complete sets of trials were used. In all, the experiment involved 800 observations. The display viewing distance to height ratio, D_V/H , was 3.5 as it was in all of the experiments that follow unless

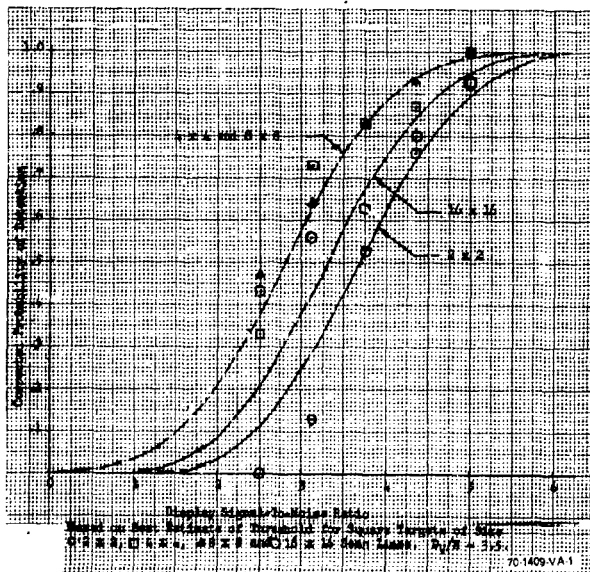


Figure 9. Measured Probability of Detection vs Predicted

otherwise specified. From the results shown in figure 9, SNR_{DT} is estimated to be as shown in table I below.

TABLE I
DISPLAY SIGNAL-TO-NOISE RATIO REQUIRED FOR 50 PERCENT
PROBABILITY OF DETECTION

Image Size ($n_x \times n_y$ Scan Lines)	SNR_{DT}
2 x 2	3.7
4 x 4	2.8
8 x 8	2.8
16 x 16	3.3

A statistical analysis of the data for the 4 x 4, the 8 x 8, and the 16 x 16-line targets indicated that target size was not statistically significant. But when the data for the 2 x 2 line target was included in the analysis, target size was then found to be statistically significant.

However, the increase in SNR_{DT} for the 2 x 2 and 16 x 16-line targets over that needed for the 4 x 4 and 8 x 8-line targets has been consistently noted in many experiments preceding and following the one discussed here, but it is not desired to speculate as to the causes at this time. In any event, for image sizes from 4 x 4 through 16 x 16, equation 14 holds.

In the next experiment, rectangular images of variable aspect ratio were employed. The image size was chosen to be 4 lines high and $4a_i$ wide, where a_i was varied in steps of 1, 16, 32 and 45. The SNR_D equation used was

$$SNR_D = (1/490) (n_x n_y t \Delta f_V / a_i)^{1/2} SNR_V \quad (15)$$

where the terms are as before except that $n_y = 4$ and $n_x = a_i n_y$. The results obtained are shown in figure 10. It can be seen that the above equation holds

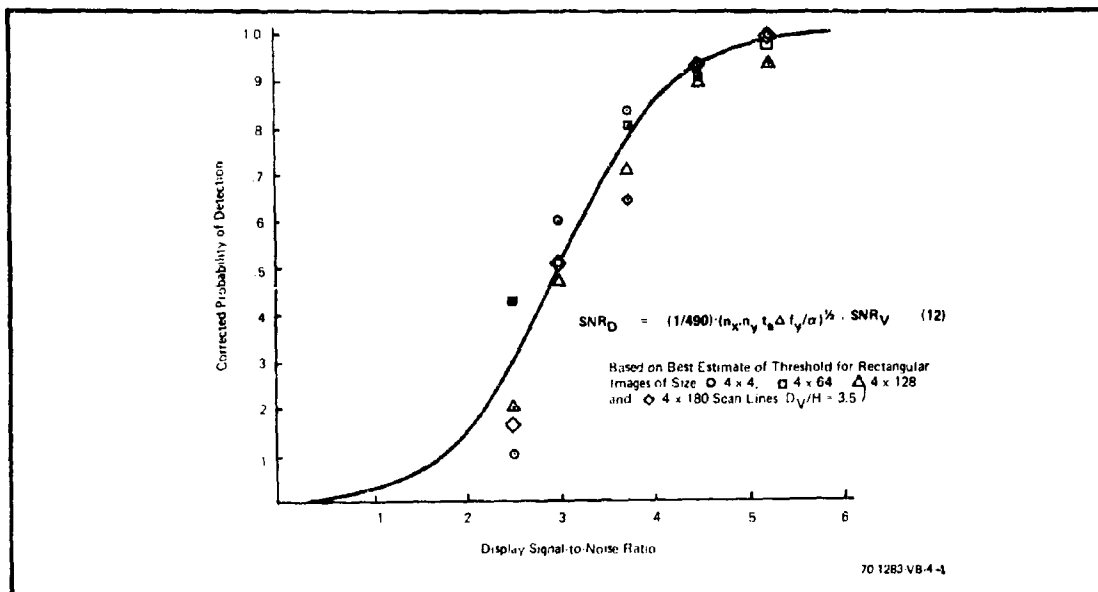


Figure 10. Measured Probability of Detection vs Predicted

over a large range of image aspect ratios. In the experiment, the angular extent of the image relative to the observer's eye varied from 0.133 x 0.133 degrees for the 1:1 rectangle to 0.133 x 6.02 degrees for the 1:45 rectangle. The aspect angle experiment involved a total of 800 observations by 5 observers.

Next, a series of preliminary experiments were performed to investigate the influence of image motion on detectability using square targets. Two speeds were used; 20 and 5 sec across about 93 percent of the picture width. For each experiment, 5 subjects were used, and 600 data points were taken. It was discovered that if the observer knew when to look in relation to the start of the target across the display, he could do much better than if he was not given start information. The data that will be shown reflects the random start case. The image could appear in three locations (upper third, middle third, lower third), and a forced response was required (i.e., if the image was not located, the observer was asked to guess). The data was again corrected for chance.

[illegible][illegible][illegible]

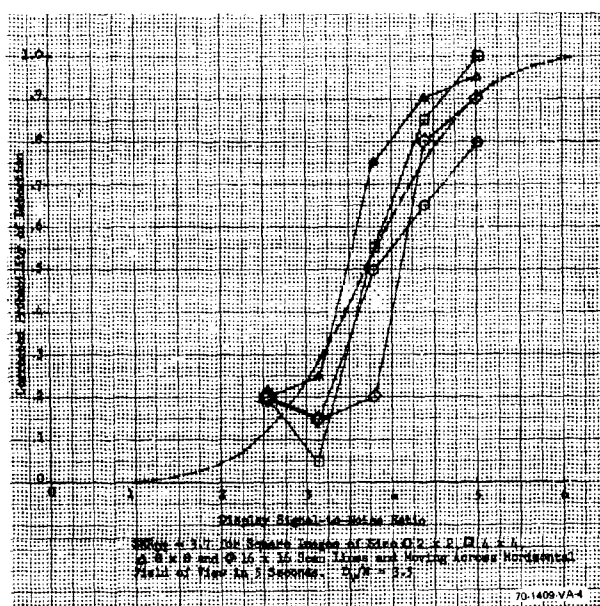


Figure 12. Measured Probability of Detection vs Predicted

of a minimum detectable contrast. While this representation is sometimes analytically convenient, it is noted that contrast is synonymous with signal. We feel that S/N ratio is more fundamental as a measure of observer performance and further, that over a wide range of conditions, detectability is a function of S/N ratio only. In other words, low-contrast and high-contrast images are equally detectable if their S/N ratios are equal.

To test this hypothesis, we repeated the square image detection experiment using a 6 x 6 line image. In the previous experiments, noise was held constant while signal was increased. The display monitor brightness was set at some reasonably constant level so that the noise was clearly evident. As the signal was varied, the image-to-noise background ratio varied, which in effect is a variation in the displayed image contrast (i.e., contrast was varied by both noise and signal). In the new experiment, the image signal and noise levels were randomly varied. Five subjects, three noise levels, and nine signal levels were employed. Again, four quadrant locations and

two trials per observer were employed; the total number of observations was 540.

The probability of detection obtained is plotted in figure 13 as a function of the SNR_D for the three noise levels. From the curves, no apparent effect of contrast (which is a function of signal and noise level) is noted.

To explore the interaction of contrast with detectability further, a statistical analysis based on the analysis of variance was performed. In this analysis, the "total variability in a set of data is reduced to components associated with possible sources of variability whose relative importance" one wishes to determine. For a particular source of variability, a calculation is made of the variance that is an estimate of the actual variance. A comparison of the actual with the estimate, together with a knowledge of the number of data points involved (or degrees of freedom plus 1), gives a measure by which the importance of the source of variability can be assessed. If the ratio of the two is large for the number of degrees of freedom involved, it is statistically

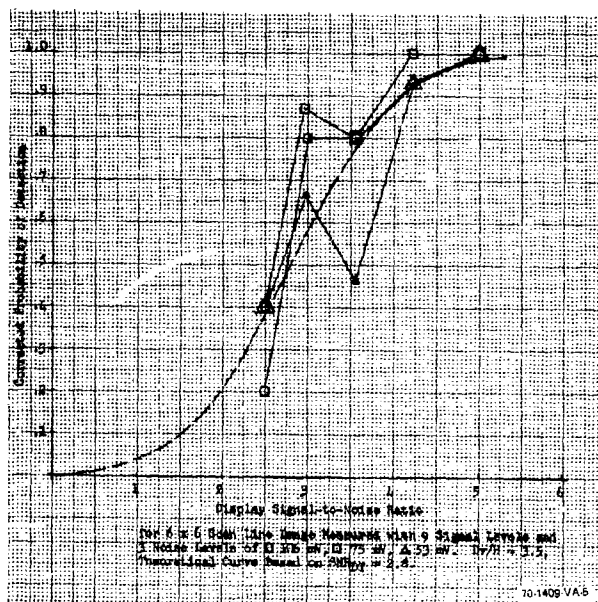


Figure 13. Probability of Detection vs Display S/N Ratio

unlikely that the variation was, in fact, due to random events; or in other words, the source of variability is said to be statistically significant.

For each source of variability in the experiment, such as the subject, signal level, noise level, signal and noise together, etc., an estimate of the variance and an estimate of the actual variance due to experimental error was calculated. The results of the calculations are shown in table II. The residual term in the table is taken to be the actual variance. The ratio of the variance estimate for the signals and noise together, to that for the residual is 5.61. Applying the F test⁷ for a ratio of 5.61:1, with 64 degrees of freedom for the 0.87 variance value and 16 degrees of freedom for the 4.88 variance value, we find that the level of significance is greater than 0.001. That is, the chance that a variation as large as 4.88 (due to the influence of signals and noise together) being due to random causes is less than one in 1000. In other words, signal and noise together cause significant variation

TABLE II
STATISTICAL ANALYSIS FOR EXPERIMENT INVOLVING RANDOM
SELECTION OF SIGNAL AND NOISE FOR SQUARES OF SIZE
6 x 6 SCAN LINES

<u>Source of Variance</u>	<u>Degree of Freedom</u>	<u>Variance Estimate</u>
Subjects	4	0.31
Signals	8	1.54
Subjects and Signals	32	1.18
Noises	2	1.81
Subjects and Noises	8	1.33
Signals and Noises	16	4.88
Residual	64	0.87

70-1409-T-6

in the data. This, of course, is not surprising since equation 14 predicts that SNR_D is a function of the video SNR_V .

With the numbers from table II, we can only infer that the variation due to signal and noise together is a significant variation. Because of the statistical significance of signal and noise together, it is not permitted to test either the signal or the noise dependence alone against the residual. However, the experiment was designed so that for each noise level, the same five SNR_D values were used. Further inference can be drawn if the analysis is done using SNR_D . The analysis of variance for this new arrangement, including SNR_D , subjects, and noise, together with second-order interactions is shown in table III. From the table, it is seen that only two sources of variations are significant, SNR_D and subjects. Using the F test, it is found that each source of variation is significant to better than the 0.001 level. That is, the chance was less than 1 in 1000 that the variation in each case was due to random cause.

TABLE III
STATISTICAL ANALYSIS FOR EXPERIMENT INVOLVING RANDOM SELECTION OF DISPLAY S/N RATIO FOR IMAGES OF SIZE 6 x 6 SCAN LINES

<u>Source of Variance</u>	<u>Degrees of Freedom</u>	<u>Variance Estimate</u>
Noise	2	0.81
Subjects	4	3.31
Noise and Subjects	8	0.51
SNR_D	4	9.55
Noise and SNR_D	8	0.50
Subjects and SNR_D	16	0.80
Residual	32	0.51

S70-1308-V-2

Applying the F test for noise, we found that the level of significance was greater than 0.2, which suggests that noise level was not a significant parameter. The noise level in the experiment performed alters the image contrast by making an increase in dc brightness level of the display and changes in the signal level necessary. Since the displayed image contrast and noise level are related, and since noise level is not significant with regard to probability of detection, it is inferred that contrast is also not significant.

A word of caution is in order. The range of contrast variation was not large, and very small contrast values were not considered. For high-contrast images, perhaps in the range of 10 or 20 to 100 percent, we feel that detectability does depend only on SNR_D , while at very low contrasts, the eye can become fluctuation-noise-limited, as will be discussed later.

Before concluding this section, we shall construct a model for the probability of detection along the lines suggested by Legault.⁸ First, we observe that as the mean number of photoelectrons in the spatial sampling interval and sampling time period becomes large, the Poisson probability density distribution approaches a Gaussian or normal probability density distribution given by

$$f_X(x) = \exp \left[-\frac{1}{2} \left[\frac{(x-m)}{\sigma} \right]^2 \right] / \left(\sigma (2\pi)^{1/2} \right) \quad (16)$$

where X is the random variable, x is the independent variable, m is the mean, and σ is the standard deviation.

Consider two photoelectron population densities, one representing the image with mean m_2 and standard deviation σ_2 and the second, being the background with mean m_1 and standard deviation σ_1 . We wish to know how the difference $m_2 - m_1$ (which represents the signal) is distributed statistically. To obtain the new distribution we use the concept of movement generating functions,⁹ which is defined by

$$M_X(\theta) = \int_{-\infty}^{\infty} \exp(\theta x) f_X(x) dx \quad (17)$$

and generate moments through the equation

$$\left. \frac{d^k [M_X(\theta)]}{d\theta^k} \right|_{\theta=0} = a_k \quad (18)$$

where a_k is the moment of order k . In the above, θ is a dummy variable. Other properties of interest are that for a sum of independent variables,

$$M_{(X_1 + X_2)}(\theta) = M_{X_1}(\theta) M_{X_2}(\theta) \quad (19)$$

and also

$$M_{cg(x)}(\theta) = M_{g(x)}(c\theta) \quad (20)$$

the moment generating function for a normal distribution is given by

$$M_X(\theta) = \exp \left[m\theta + \frac{1}{2} \sigma^2 \theta^2 \right] \quad (21)$$

In the mathematical detection model, we express the signal as being the difference between the true means, m_2 and m_1 , of the image and background signals, and on the average, this will be true. However, in any given sampling period determined by the integration in time and space by the eye, the difference may not be $m_2 - m_1$, but rather, it may be some different number, $x_2 - x_1$, where x_2 and x_1 are randomly distributed. Suppose next that we take a number of samples and take the average, \bar{X} , where

$$\bar{X} = \frac{1}{k} \sum_{i=1}^k x_i \quad (22)$$

In the limit as k , the number of samples taken increases to infinity, \bar{X} , becomes, m_1 , the mean. However, for finite sample numbers, \bar{X} is a random number equal to the mean of a sample of size k .

Since x_i is normally distributed with mean m_x and variance σ_x^2 , its moment generating function is given by equation 19 and using equations 20 and 22, it follows that,

$$\begin{aligned} M_{\bar{X}}(\theta) &= M_{\frac{1}{k} \sum_{i=1}^k x_i}(\theta) \\ &= M_{\sum_{i=1}^k x_i} \left[\frac{\theta}{k} \right] \\ &= \left\{ M_{x_i} \left[\frac{\theta}{k} \right] \right\}^k \end{aligned} \quad (23)$$

and using equation 21,

$$\begin{aligned} M_{\bar{X}}(\theta) &= \left[\exp \left[m_x \cdot \theta/k + \frac{1}{2} \sigma_x^2 \frac{\theta^2}{k^2} \right] \right]^k \\ &= \exp \left(m_x \theta + \frac{1}{2} \frac{\sigma_x^2}{k} \theta^2 \right) \end{aligned} \quad (24)$$

By comparison with equation 21, we recognize the above equation as the moment generating function of a normally distributed variable with mean m_x and variance σ_x^2/k . Having shown that \bar{X}_2 and \bar{X}_1 are normally distributed, we now inquire about the distribution of the difference $\bar{X}_2 - \bar{X}_1$. Again, this is found quite simply by using the moment generating functions for \bar{X}_2 and \bar{X}_1 , which are,

$$M_{\bar{X}_2}(\theta) = \exp \left[m_2 \theta + \frac{1}{2} \frac{\sigma_2^2}{k} \theta^2 \right]$$

and

$$M_{-\bar{X}_1}(\theta) = M_{\bar{X}_1}(-\theta)$$

$$M_{-X_1} = \exp \left[-m_1 \theta + \frac{1}{2} \frac{\sigma_1^2}{k} \theta^2 \right]$$

Thus

$$M_{\bar{X}_2 - \bar{X}_1}(\theta) = \exp \left[(m_2 - m_1) \theta + \frac{1}{2} \left(\frac{\sigma_2^2 + \sigma_1^2}{k} \right) \theta^2 \right] \quad (25)$$

By comparing the above equation with equation 21, we see that $(\bar{X}_2 - \bar{X}_1)$ is normally distributed with mean equal to $(m_2 - m_1)$ and standard deviation equal to

$$\left[(\sigma_2^2 + \sigma_1^2) / k \right]^{1/2}$$

The interpretation of k in the above equations for the specific case of television is that the eye takes several samples of the signal (it integrates over more than a single frame). Viewing noisy photographs, k would be unity.

Proceeding further, we will let Δn be the random variable $\bar{X}_2 - \bar{X}_1$ and $\Delta \bar{n}$ be the mean $m_2 - m_1$. The Δn is recognized as the number of signal photoelectrons as used in equation 2. In accord with our previous discussions, we will let $\left[(\sigma_2^2 + \sigma_1^2) / k \right]^{1/2}$ be equal to $\left[(2-C)\bar{n}_{\max} \right]^{1/2}$. We now define a new random variable

$$\begin{aligned} Z &= (x - m) / \sigma \\ &= (\Delta n - \Delta \bar{n}) / \left[(2-C)\bar{n}_{\max} \right]^{1/2} \end{aligned} \quad (26)$$

According to statistical theory, if x is a normally distributed random variable with mean m and standard deviation σ , then $z = (x-m)/\sigma$ is normally distributed with zero mean and unit standard deviation.

Also, observe that the probability of detection is equal to the cumulative probability that Z will fall in the range $-\infty$ and some value z_2 is expressed by the integral

$$P_d (-\infty < Z < z_2) = \frac{1}{2\pi^{1/2}} \int_{-\infty}^{z_2} \exp(-z^2/2) dz \quad (27)$$

The normal probability curve and its integral are plotted in figure 14. Specific values of the integral are found in standard tables.¹⁰ We note further that when $z = 0$, the probability of detection is 0.5. We have previously defined the threshold display S/N ratio SNR_{DT} as being that value at which $P_d = 0.5$. Thus, since $P_d = 0.5$ when $z = 0$ and

$$z = \frac{\Delta n - \Delta \bar{n}}{\bar{n}^{1/2}} = 0 \quad (28)$$

Then

$$\frac{\Delta n}{\bar{n}^{1/2}} = \frac{\Delta \bar{n}}{\bar{n}^{1/2}} = SNR_{DT} \quad (29)$$

Therefore, we interpret $\Delta n/\bar{n}^{1/2}$ as being the actual S/N ratio (and a random variable) and $\Delta \bar{n}/\bar{n}^{1/2}$ as being the threshold display S/N ratio. Then, we can rewrite z

$$z = SNR_D - SNR_{DT} \quad (30)$$

Now we can fit the measured P_d curve with a calculated theoretical curve simply by overlaying the latter at the best estimate of the measured $P_d = 0.5$ point. This was the procedure used in the previous figures. The fit is quite good as can be seen in figure 15, in which the data of figure 9 for the 4 x 4 and 8 x 8 line square is plotted along with the theoretical curve.

Before continuing on to the next section, we wish to observe that in the experiments performed, the imagery was displayed on a television screen with a frame rate of 30 per second and a field rate of 60 per second interlaced 2:1. We have presumed the integration time of the eye to be 0.2 seconds, so that 6 frames of signal and noise are integrated. Some dispute centers about the eye's time constant, with some claims that it is variable¹¹ with light level.

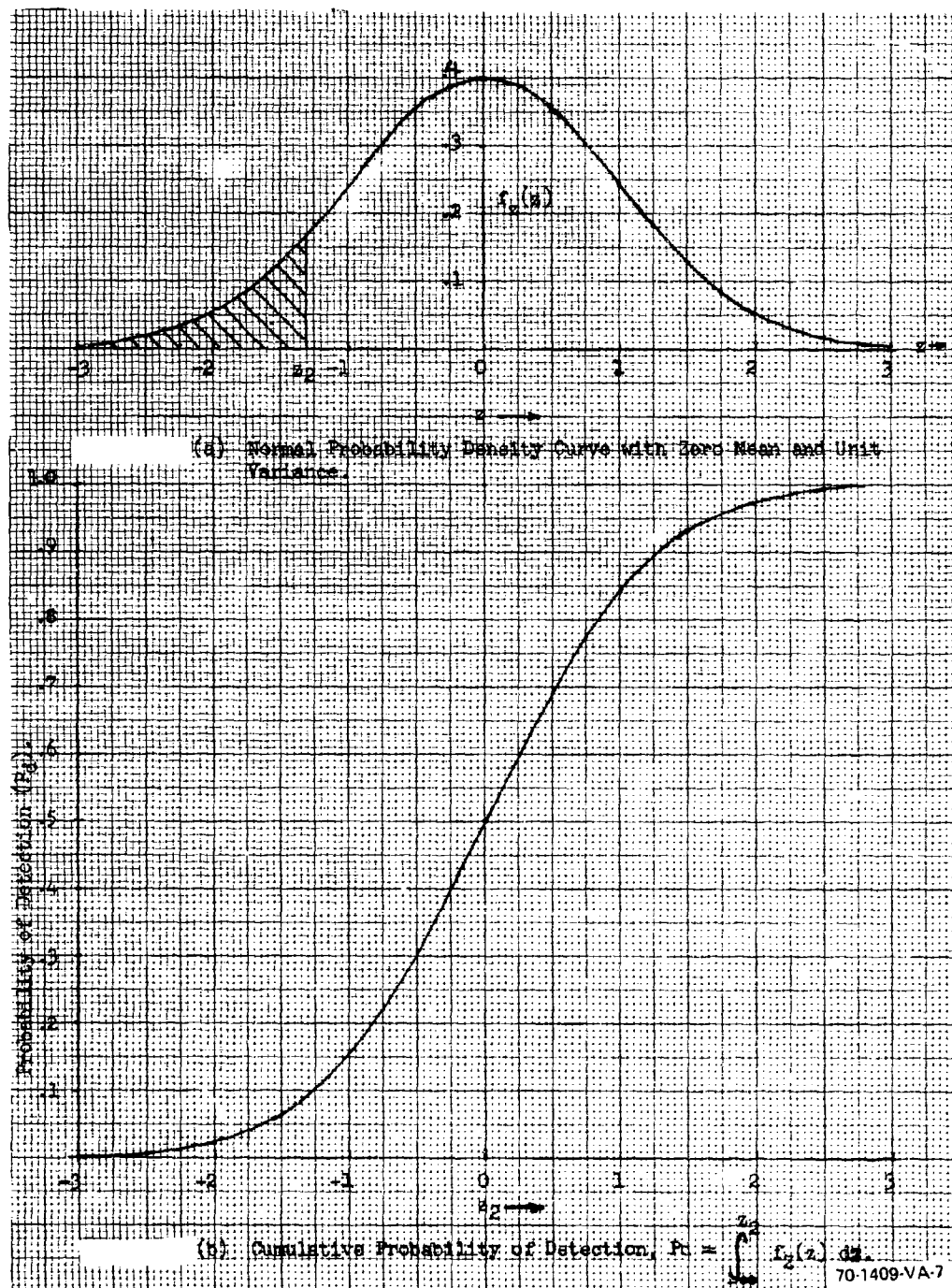


Figure 14. Normal and Cumulative Probability

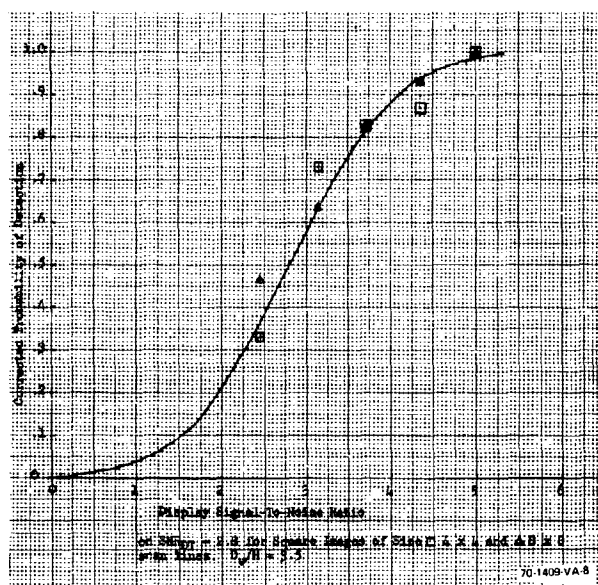


Figure 15. Measured Probability of Detection vs Predicted

The noise as viewed on a TV monitor is varying from frame to frame. For want of a better name, we shall refer to it as dynamic noise, as opposed to static noise, which would be the case when viewing a photograph. For the static noise case, the threshold S/N ratio value has been commonly accepted to be between 4 and 5, which is between 1.4 and 1.8 times larger than for the dynamic case. Viewed in terms of samples, the eye then apparently integrates between 2 and 3 frames (1.4^2 to 1.8^2) rather than 6, as implied by the 0.2-second integration time. In turn, a 0.1-second integration time would seem more appropriate. This is purely conjecture at this point, and it will not be belabored further, except to note that for the present purposes, it is of no great concern, because if 0.1 second is a better number, it would change the value of SNR_{DT} to a lower value as well, with no net change in the results. It would be of concern in certain integration experiments or in correlating results where the noise is static as opposed to dynamic.

SECTION III SPATIAL FREQUENCY ANALYSIS, ELEMENTARY MODEL

The detection model used in Section II is based on an elementary statistical model that does not lend itself readily to more detailed systems analysis. However, as many authors have noted,¹² direct analogies can be drawn between imaging systems and communications systems, and very powerful mathematics have been evolved for the latter. Thus, we shall attempt to reconstruct the elementary statistical model along the lines used in communication theory. Whatever model is adopted however, must be consistent with the elementary model.

In proceeding, we shall make heavy use of Fourier analysis, wherein images can be quantitatively described either in terms of their distribution in image space or their distribution in spatial frequency.¹³ Suppose the image is a function, $f(x, y)$ of the two independent variables x and y . Then, the spatial frequency spectrum, $F(\omega_x, \omega_y)$, is given by the Fourier transform of $f(x, y)$,

$$\begin{aligned} F(\omega_x, \omega_y) &= \mathcal{F}[f(x, y)] \\ &= \iint_{-\infty}^{\infty} f(x, y) \exp \left[-j(\omega_x x + \omega_y y) \right] dx dy \end{aligned} \quad (31)$$

where \mathcal{F} denotes the taking of the Fourier transform, j is the complex operator $[= (-1)^{1/2}]$, and ω_x, ω_y are referred to as spatial frequencies. The transform as defined above is a complex-valued function of two independent variables ω_x and ω_y . Given the function $F(\omega_x, \omega_y)$, the original spatial image distribution can be recovered through use of the inverse Fourier transforms (\mathcal{F}^{-1}) where

$$\begin{aligned} f(x, y) &= \mathcal{F}^{-1} \left[F(\omega_x, \omega_y) \right] \\ &= \frac{1}{4\pi^2} \iint_{-\infty}^{\infty} F(\omega_x, \omega_y) \exp \left[j(\omega_x x + \omega_y y) \right] d\omega_x d\omega_y \end{aligned} \quad (32)$$

To be transformable, $f(x, y)$ must satisfy the existence conditions

- a. $f(x, y)$ must be absolutely integrable over the infinite x, y plane.
- b. $f(x, y)$ must have only a finite number of discontinuities and a finite number of maxima and minima in any finite rectangle.
- c. $f(x, y)$ must have no infinite discontinuities.

For real linear systems, transforms must exist.¹⁴ However, some of the idealized mathematical functions created to represent the waveforms of interest will not meet the existence theorems. Fortunately, it is possible, in many cases, to find meaningful transforms that do not strictly satisfy the existence conditions, but that can be written as the limit of transformable functions. The limit of the transform of this new sequence is called the generalized Fourier transform, and these functions can be manipulated in the same manner as conventional transforms.

The first function we shall consider is the Dirac delta function, or unit impulse. This function fails to satisfy existence theorem c. above. Its immediate use will be to define mathematically the generation of a single photoelectron at point x_1, y_1 through the equation

$$\delta_0(x-x_1, y-y_1) = \lim_{N \rightarrow \infty} N^2 \exp \left[-N^2 \pi (x-x_1)^2 (y-y_1)^2 \right] \quad (33)$$

which has the property of being infinite at $x = x_1, y = y_1$ and zero everywhere else. Also, it is defined that,

$$\int_{-\infty}^{\infty} \int_{-\infty}^{\infty} \delta_0(x-x_1, y-y_1) dx dy = 1.0 \quad (34)$$

The Fourier transform of equation 33 has a transform given by

$$\mathcal{F} \left\{ N^2 \exp \left[-N^2 \pi (x^2 + y^2) \right] \right\} = \exp \left[\frac{-\pi (f_x^2 + f_y^2)}{N^2} \right] \quad (35)$$

for $f_x, f_y = \omega_x/2\pi, \omega_y/2\pi$. The generalized Fourier transform of the Dirac delta function then becomes

$$\mathcal{F}\{\delta_0(x-x_1, y-y_1)\} = \lim_{N \rightarrow \infty} \left\{ \exp \left[\frac{-\pi(f_x^2 + f_y^2)}{N^2} \right] \right\} \quad (36)$$

$$= 1.0$$

From the above, we infer that a point image has infinite amplitude, but finite volume in x, y space, as shown in figure 16(a) and a uniform distribution in spatial frequency space over all frequencies, as shown in figure 16(b). This is sometimes referred to as a "white" frequency spectrum.

Suppose that the sensor input photocathode is uniformly irradiated with photons which are converted to photoelectrons. The exact number emitted in any given sampling area or time period is subject to statistical fluctuation, but has a well-defined average or mean. Next, we apply an image that has the effect of weighting the mean number emitted over a specified area and time. Let the

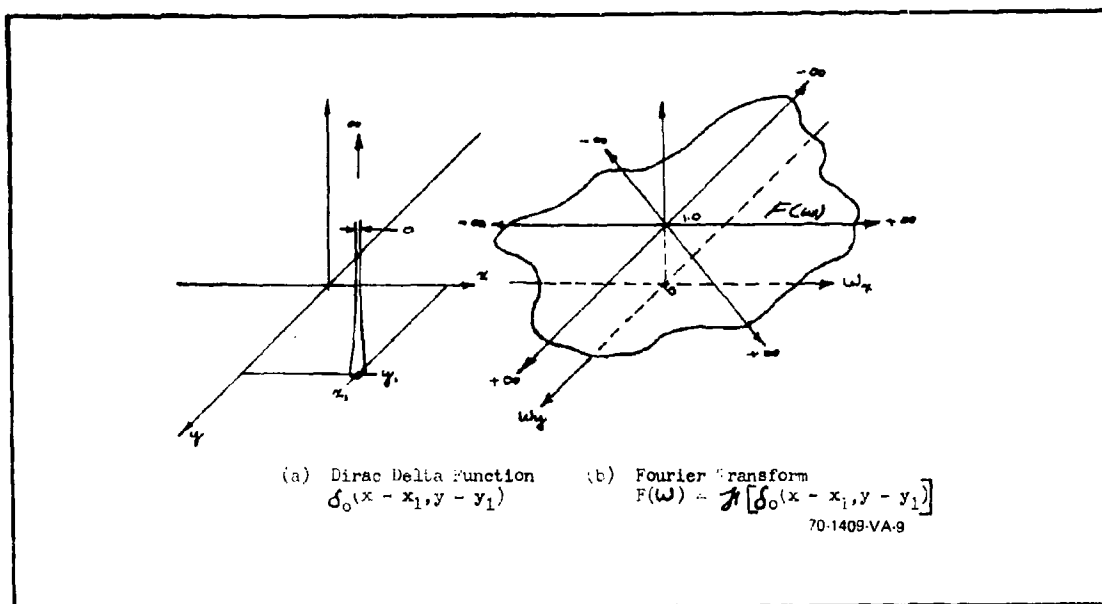


Figure 16. Dirac Delta and Fourier Transform

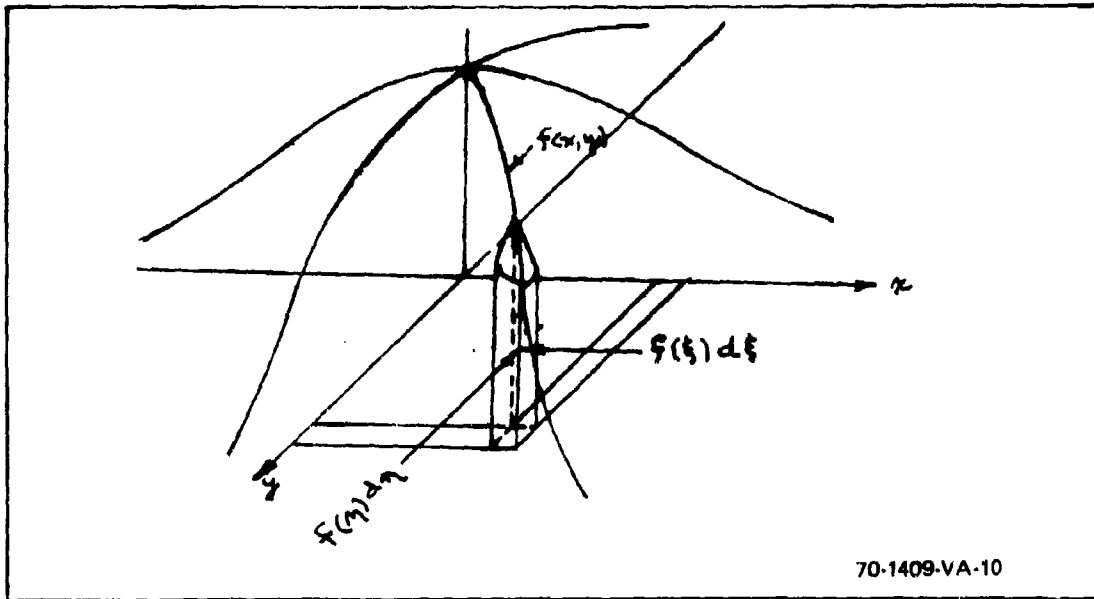


Figure 17. Image $f(x, y)$ as a Weighting Function of Volume $f(\xi, \eta) d\xi d\eta$

image function be $f(x, y)$ as shown in figure 17 and consider a narrow slice at $x = \xi, y = \eta$. This little slice may be thought of as an impulse at $x, y = \xi, \eta$ of weighted area $f(\xi, \eta) d\xi d\eta$. We then consider the image signal to be a linear superposition of all possible infinitesimal slices of the form $f(x, y) f(x, y) dx dy \delta(x - \xi, y - \eta)$. In other words, we sum over all ξ, η to obtain

$$f(x, y) = \int_{-\infty}^{\infty} \int_{-\infty}^{\infty} f(\xi, \eta) \delta_0(x - \xi, y - \eta) d\xi d\eta \quad (37)$$

This result is known as the superposition integral or in mathematical terms as the convolution of f and δ_0 . As is well known, convolution in the space domain is equivalent to multiplication in the frequency domain, i. e., $f(x, y)$ can be found either by equation 37 or by taking the inverse Fourier transform of the product of the frequency responses.

$$f(x, y) = \int_{-\infty}^{\infty} \int_{-\infty}^{\infty} F(\omega_x, \omega_y) (\mathcal{F}(\delta_0(x, y))) \exp[j(\omega_x x + \omega_y y)] d\omega_x d\omega_y. \quad (38)$$

This suggests that we can think of the image weighting function as a simple two-dimensional filter which alters the frequency spectrum of the impulse noise, (which is white), to some other band-limited spectrum as shaped by the image.

The elementary statistical model is defined only for a simple image of uniform average amplitude and fairly regular shape such as disks or rectangles. Recalling equation 6 which states

$$\text{SNR}_D = \Delta \bar{n}_{xy} \text{ at } \left[(\bar{n}_{xy \text{ max}} + \bar{n}_{xy \text{ min}}) \text{ at} \right]^{1/2}$$

and therefore, suggests the simple formulation called Model A₁ in terms of the spatial formulation

$$\text{SNR}_D = \frac{t^{1/2} \iint_{\infty} f_1(x, y) dx dy}{\left[\iint_{\infty} f_2(x, y) dx dy \right]^{1/2}} \quad \text{Model A}_1 \quad (39)$$

In frequency formulation, Model A₁ becomes

$$\text{SNR}_D = \frac{t^{1/2} \frac{1}{4\pi} \iint_{-\infty}^{\infty} F_1(\omega_x, \omega_y) \exp j(\omega_x x + \omega_y y) d\omega_x d\omega_y}{\left[\frac{1}{4\pi} \iint_{-\infty}^{\infty} F_2(\omega_x, \omega_y) \exp j(\omega_x x + \omega_y y) d\omega_x d\omega_y \right]^{1/2}} \quad \text{Model A}_2 \quad (40)$$

which can be inferred from equation 38. Both $f_1(x, y)$ or $F_1(\omega_x, \omega_y)$ and $f_2(x, y)$ or $F_2(\omega_x, \omega_y)$ have the same shape, but they differ in amplitude, because the signal is proportional to the difference in means, while the noise is proportional to the rms deviations due to the sum of background and signal.

For reasons to be discussed, an alternate model will be considered wherein the eye is considered to be an energy detector responsive to the mean square image signal envelope. In this new formulation use is made of Parseval's relation, which states that for independent nonperiodic variables with dc term excluded, the energy contained within $f(x, y)$ is equal to

$$\iint_{-\infty}^{\infty} f^2(x, y) dx dy = \frac{1}{4\pi^2} \iint_{-\infty}^{\infty} |F(\omega_x, \omega_y)|^2 d\omega_x d\omega_y = \frac{1}{\pi^2} \int_0^{\infty} \int_0^{\infty} |F(\omega_x, \omega_y)|^2 d\omega_x d\omega_y \quad (41)$$

In the above, $|F(\omega_x, \omega_y)|^2$ represents an energy spectral density and it is assumed to be symmetrical. The equation serves to further relate the space and frequency representation of real functions and is a statement of the equality of the energy term in either the space or frequency domain. Equation 44 is also referred to as Plancherel's theorem.¹⁵ Using this representation, the alternate model becomes

$$SNR_D = \frac{t^{1/2} \iint_{-\infty}^{\infty} f_1^2(x, y) dx dy}{\left[\iint_{-\infty}^{\infty} f_2^2(x, y) dx dy \right]^{1/2}} \quad \text{Model B}_1 \quad (42)$$

in terms of the spacial distributions, or

$$SNR_D = \frac{\left[t^{1/2} / \pi^2 \right] \iint_0^{\infty} |F_1(\omega_x, \omega_y)|^2 d\omega_x d\omega_y}{\left[(1/\pi^2) \iint_0^{\infty} |F_2(\omega_x, \omega_y)|^2 d\omega_x d\omega_y \right]^{1/2}} \quad \text{Model B}_2 \quad (43)$$

in terms of the frequency characteristics. The rationale for choosing the alternate models (B₁ and B₂) is that they give greater weight to high amplitudes in both space and frequency at the expense of low amplitudes. This feature will be discussed in some detail in the following sections.

We will first show that both A models and both B models give the same result as the elementary statistical model if constants are appropriately adjusted. Consider the rectangular image pulse of figure 12, which can be mathematically described by

$$x \begin{cases} = 0, & -\infty < x < -x_0/2 \\ = A, & -x_0/2 < x < x_0/2 \\ = 0, & x_0/2 < x < \infty \end{cases} \quad \text{and } y \begin{cases} = 0, & -\infty < y < -y_0/2 \\ = A, & -y_0/2 < y < y_0/2 \\ = 0, & y_0/2 < y < \infty \end{cases} \quad (44)$$

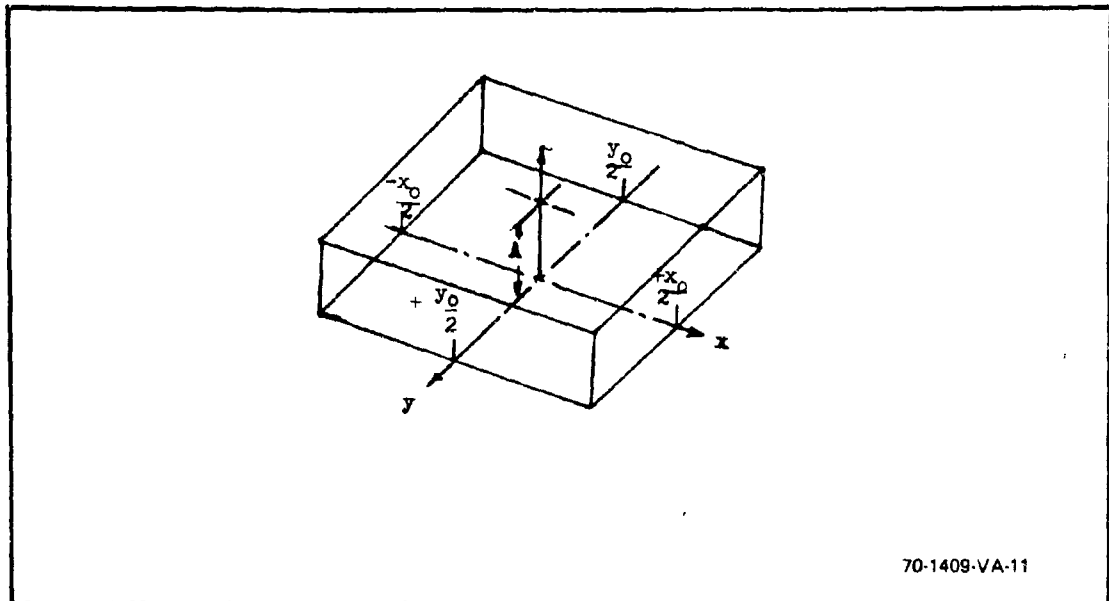


Figure 18. Rectangular Image Distribution

We will assume for the minute that the background of the image is zero.

Now using Model A₁,

$$\begin{aligned}
 \text{SNR}_D &= \frac{t^{1/2} A \int_{-x_0/2}^{x_0/2} \int_{-y_0/2}^{y_0/2} dx dy}{\left[A \int_{-x_0/2}^{x_0/2} \int_{-y_0/2}^{y_0/2} dx dy \right]^{1/2}} \\
 &= \frac{A x_0 y_0 t}{\left[A x_0 y_0 t \right]^{1/2}}
 \end{aligned}$$

Model A₁ (45)

which gives equation 6 if $A = \Delta \bar{n}_{xy} = \bar{n}_{xy}$ (for 100-percent contrast) and if $a = x_o y_o$.

Using Model A_2 , we first observe that since x and y are independent variables,

$$\mathcal{F}[f(x, y)] = \mathcal{F}[f(x)] \cdot \mathcal{F}[f(y)]$$

and then

$$\begin{aligned} \mathcal{F}[f(x)] &= \int_{-x_o/2}^{x_o/2} (\Delta \bar{n}_{xy} t)^{1/2} \exp[-j\omega_x x] dx \\ &= (\Delta \bar{n}_{xy} t)^{1/2} \left[\exp(-j\omega_x x_o/2) - \exp(j\omega_x x_o/2) \right] / j\omega_x \end{aligned} \quad (46)$$

$$\text{but since, } \left[\exp(-j\omega_x x_o/2) - \exp(j\omega_x x_o/2) \right] / j = 2 \sin(\omega_x x_o/2) \quad (47)$$

we have

$$F(\omega_x) = (\Delta \bar{n}_{xy} t)^{1/2} \frac{x_o \sin \omega_x x_o/2}{\omega_x x_o/2} \quad (48)$$

Since $F(\omega_y)$ is of the same form, we may write

$$F(\omega_x, \omega_y) = \frac{(\Delta \bar{n}_{xy} t)^{1/2} x_o y_o \sin(\omega_x x_o/2) \sin(\omega_y y_o/2)}{(\omega_x x_o/2) (\omega_y y_o/2)} \quad (49)$$

This function is sketched in figure 19, and we can observe that the original space function can be obtained either by taking the inverse of equation 43, using equation 38, or through use of standard tables of Fourier transform pairs.¹⁰

Using alternate Model B_1 , we again assume the same image as shown in figure 18. Using equations 42 and 44, we obtain

$$\begin{aligned} \text{SNR}_D &= \frac{t \int_{-y_o/2}^{y_o/2} \int_{-x_o/2}^{x_o/2} A^2 dx dy}{\left[t \int_{-y_o/2}^{y_o/2} \int_{-x_o/2}^{x_o/2} A^2 dx dy \right]^{1/2}} = \frac{t A^2 x_o y_o}{\left[t A^2 x_o y_o \right]^{1/2}} \end{aligned} \quad (50)$$

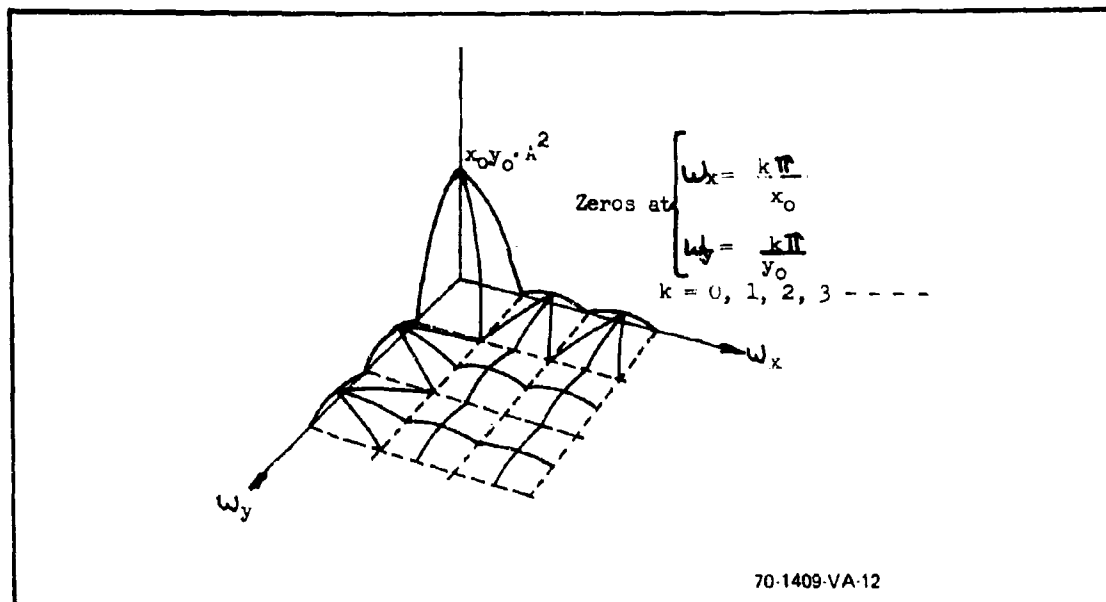


Figure 19. Spatial Frequency Spectrum of Rectangular Image

We will then conform to the elementary model if $A^2 = \bar{n}_{xy}$ and $a = x_0 y_0$.

Using the alternate frequency description, we observe that

$$F_1(\omega_x, \omega_y) = \frac{(\bar{n}_{xy} t)^{1/2} x_0 y_0 \sin \omega_x x_0 / 2 \sin \omega_y y_0 / 2}{(\omega_x x_0 / 2) (\omega_y y_0 / 2)} \quad (51)$$

and the integral in the numerator of equation 43 is

$$\iint_{-\infty}^{\infty} |F_1(\omega_x, \omega_y)|^2 d\omega_x d\omega_y = \frac{\bar{n}_{xy} t (x_0 y_0)^2}{\pi^2} \int_0^{\infty} \left[\frac{\sin \omega_y y_0 / 2}{\omega_y y_0 / 2} \right]^2 d\omega_y \int_0^{\infty} \left[\frac{\sin \omega_x x_0 / 2}{\omega_x x_0 / 2} \right]^2 d\omega_x \quad (52)$$

Performing the last integral to the right, we let $x = \omega_x x_0 / 2$ and

$d\omega_x = dx / (x_0 / 2)$. Then, from tables of definite integrals we obtain

$$\frac{2}{x_0} \int_0^{\infty} \frac{\sin^2 x}{x^2} dx = \frac{\pi}{x_0} \quad (53)$$

Similarly,

$$\frac{2}{y_o} \int_0^{\infty} \frac{\sin^2 y}{y^2} dy = \frac{\pi}{y_o}$$

and

$$\frac{1}{\pi^2} \iint_0^{\infty} |F_1(\omega_x, \omega_y)|^2 d\omega_x d\omega_y = \bar{n}_{xy} t x_o y_o \quad (54)$$

which confirms the result obtained in the numerator of equation 50 (after insertion of the appropriate constants).

We see that either Model A or B fits the elementary statistical model. We note, however, that Model B gives a result for the noise that is more consistent with the noise expressions ordinarily used in communications system analysis, and in the next section we will show that the signal analysis seems more reasonable as well.

SECTION IV

EFFECT OF A FINITE APERTURE

In the perfect imaging sensor considered heretofore, a point image on the photocathode is assumed to appear as a point image on the display. In short, all images are transmitted through the sensor with perfect fidelity. In real sensors, the images at the display may be distorted in amplitude, shape, or phase (position), or all three. These distortions are due to finite imaging apertures such as the objective lens, any fiber-optic face-plates, geometrical defocusing, electron scanning beams, finite phosphor particles, electrical bandwidth limitations, etc. The effect of these apertures is to smear image detail in a manner analogous to the filtering of electrical signals by electrical filter networks. This analogy can be put to good use.

To illustrate the effect of apertures, consider the point source object of figure 20(a). Due to diffraction, chromatic and geometric aberrations, and imperfect focusing, the point will be imaged by the lens as a blur. Similarly, a line source is imaged as a line-spread function as shown in figure 20(b). The line-spread case corresponds most directly to the case most commonly encountered in communications systems, wherein the signals vary only in amplitude and time. Where an image is very long in one dimension compared to the other, it can usually be considered a one-dimensional image, varying only in intensity and a single spatial dimension.

In any event we will, for the moment, consider an aperture to be analogous to a linear electrical filter, except that it may be two-dimensional. Where two dimensions are involved, we will initially assume that the two

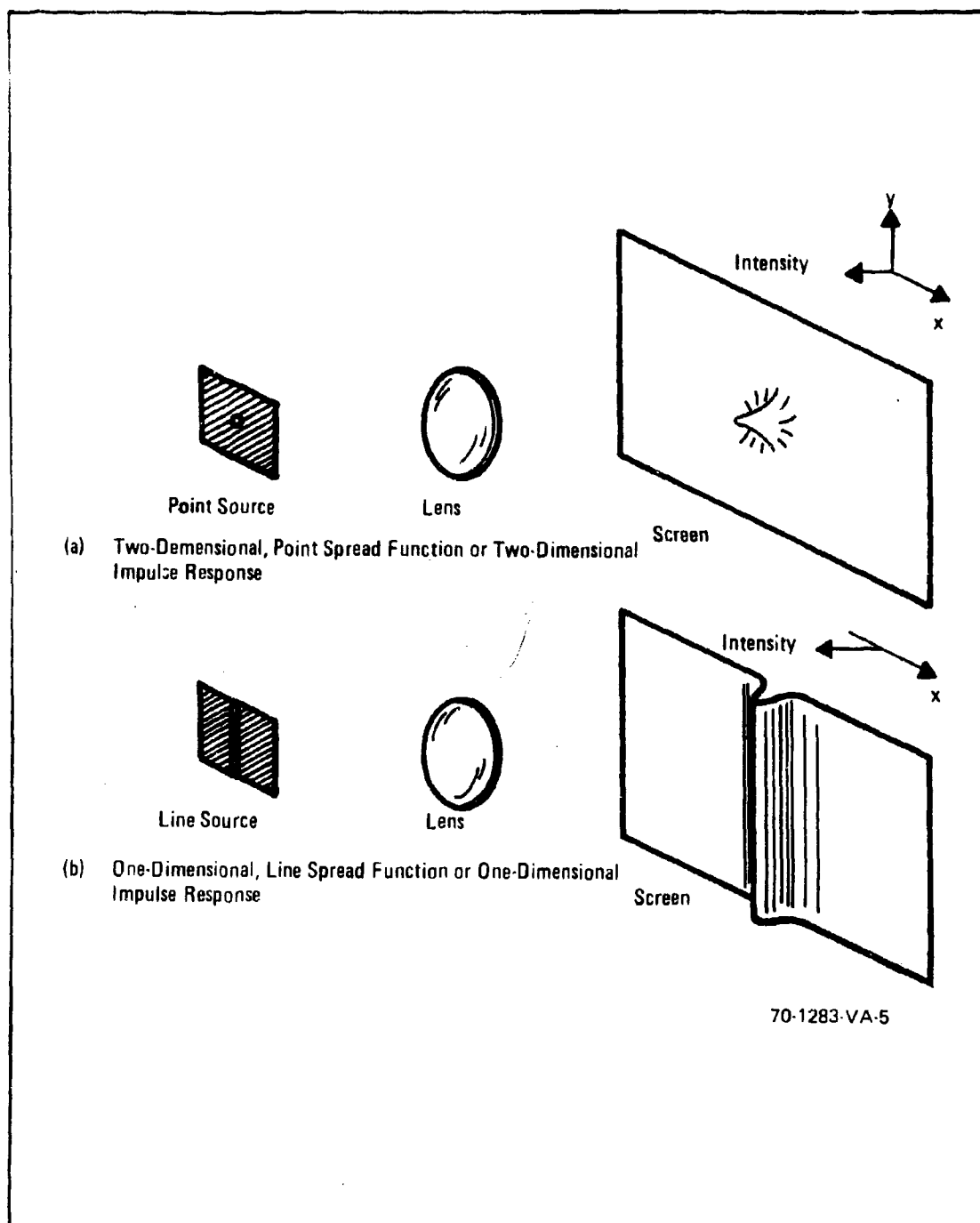


Figure 20. Impulse Response

dimensions are either independent (so that they can be treated separately) or that they possess radial symmetry (so that they become essentially one-dimensional in character). Many of the apertures that appear in nature are found to have a response to several input stimuli acting simultaneously that is identical to the sum of the responses that each stimuli would produce individually. A system of this type is a linear system. The property of linearity leads to an enormous simplification in the mathematical description of such phenomena. In particular, it becomes possible to decompose complicated input signals to simpler signals for which the system response is known and then, to find the total response by summing the individual responses in linear combination. Furthermore, we can then use Fourier analysis, in which signals are decomposed to sine and cosine waves.

The statement of linearity implies that the system response to any stimulus can be described by the solution to some appropriate set of simultaneous linear differential equations. The restriction to constant coefficients rules out consideration of linear systems with time or space-varying parameters, but it permits us to apply the principle of superposition.

In general, the linear systems we will deal with are considered to be space and time invariant (sometimes called isoplanatic). By this, it is meant that the system impulse response $r_o(x_1, y_1, \xi, \eta)$ depends only on the distances $(x_1 - \xi)$, $(y_1 - \eta)$ in which case,

$$r_o(x_1, y_1, \xi, \eta) = r_o(x - \xi, y - \eta). \quad (55)$$

In the case of an imaging system, it is said to be space invariant if the image of a point source changes only in position, but not in functional form, as the image moves about the image plane. In a television sensor, this would imply that corner resolution is the same as center resolution. This

is seldom the case, but for analytical purposes, we can divide the image plane into small areas (or isoplanatic patches) within which the system is spatially invariant. The assumption of linearity results in many simplifications.

To proceed, we have observed that image signals in passing through a sensor may be distorted by the various optical elements and re-imaging steps involved. Depending on the degree and nature of the distortion, signal strength may be degraded. To analyze these signal effects, we assume that the sensory system is linear in the interval of interest. Further, as we previously noted, we assume that both the input signal $f(x, y)$ and the system impulse response $r_o(x, y)$ are functions of independent variables x and y and are separable. In this case, we can draw the block diagram of figure 21 to represent the signal processes. As we have previously observed, the assumption of separability permits us to write

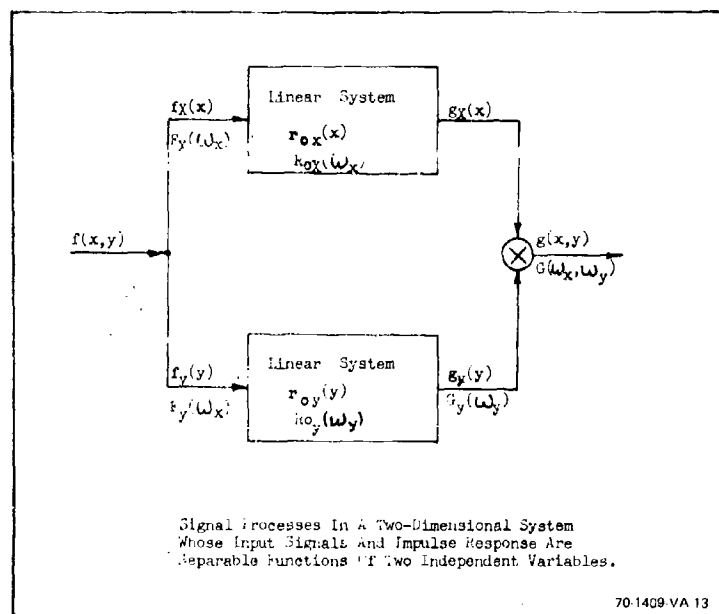


Figure 21. Signal Processor Block Diagram

the arbitrary function $g(x, y)$ as,

$$g(x, y) = g_X(x) \cdot g_Y(y) \quad (56)$$

and its Fourier transform as,

$$\mathcal{F}\{g(x, y)\} = \mathcal{F}_x\{g(x)\} \mathcal{F}_y\{g(y)\} \quad (57)$$

Therefore, the transform is separable into a product of two factors, one a function of f_x only, and the second, a function of f_y only. Thus the process of two-dimensional transformation simplifies to a succession of more readily calculated and manipulated one-dimensional transforms.

In Fourier analysis, it is convenient to employ a certain set of test signals known as the singularity test functions. The most useful input singularity function is the unit area (or volume) impulse already described as $\delta_0(x, y)$. The system response for this input is designated $r_0(x, y)$. The Fourier transform of the impulse response is designated $R_0(\omega_x, \omega_y)$ and is known as the complex steady-state frequency response. The usefulness of $R_0(\omega_x, \omega_y)$ is that for systems with apertures that are independent in x and y , the response can be measured through use of sinewave image patterns as the input. The output signal amplitude is then measured, and a plot of these amplitudes (as the pattern frequency is varied) represents the magnitude of $|R_0(\omega_x)|$ or $|R_0(\omega_y)|$. This function is variously known as the sinewave response or the modulation transfer function (MTF) (when the output amplitudes are normalized to its magnitude at zero frequency).

To illustrate, a typical experimentally measured MTF curve for a three-stage image intensifier is shown in figure 22. To make use of this curve, we first assume a zero phase shift characteristic, which implies that the output image is in correct 1:1 spatial correspondence at all frequencies. Then $|R_0(\omega_x)|$ becomes $R_0(\omega_x)$, and in principle, we have sufficient information to find the response of the intensifier to any one-



Figure 22. Error Curve (---) Fit to Measured (—) MTF of a 3-Stage Image Intensifier and Equivalent Bandwidth, (N_{LPB}) of the Error Curve

dimensional input test pattern varying in the x coordinate. While comparatively simple in principle, these calculations can be tedious in practice.

A somewhat simpler approach, which will be used here for illustration, will be to fit a well-behaved analytical expression to that experimentally measured. In particular, the function we will fit as a first trial will be the error curve that is also known as the normal or Gaussian error distribution. In form it is identical to that used for the probability density function (Section III). For this analysis, spatial frequency will be expressed in terms of N_{LP} (line pairs/mm), and the distance will be in mm.

The error curve to be fitted to the experimental response is given by,

$$R_o(N_{LP}) = \exp \left[- \left(2 \pi N_{LP} \right)^2 .5 a^2 \right] \quad (58)$$

where a is equal to

$$a = \left[-2 \ln \left(R_o(N_{LP}) \right) \right]^{-1/2} / (2\pi N_{LP}) \quad (59)$$

Substituting $R(N_{LP}) = 0.45$ at $N_{LP} = 8.75$ lp/mm, we obtain
 $4\pi^2 a^2/2 = 1.044 \cdot 10^{-2}$ and $a = 2.31 \cdot 10^{-2}$ mm.

The fit of the error curve to the experimental curve is shown in figure 22, together with the equivalent bandwidth of the error curve which is defined by the width of a rectangle with the same area as that under the error curve.

Numerically, if Ω_B is the equivalent bandwidth in radians/mm,

$$\begin{aligned} 2\Omega_B R_o(o) &= \int_{-\infty}^{\infty} R_o(\omega) d\omega \\ &= \int_{-\infty}^{\infty} \exp \left[-(a\omega)^2/2 \right] d\omega \\ &= \frac{(2)^{1/2}}{a} \int_0^{\infty} \exp \left[-\theta^2 \right] d\theta \end{aligned}$$

and by standard tables of definite integrals

$$2\Omega_B R_o(o) = (\pi/2)^{1/2}/a \quad (60)$$

Since $\Omega_B = 2\pi N_{LP}$ and $R_o(O) = 1.0$,

$$N_{LPB} = \frac{1}{2(2\pi)^{1/2} a} = 8.65 \text{ lp/mm} \quad (61)$$

One of the interesting features of the error curve filter is that its impulse response, as determined from

$$r_o(x) = \frac{1}{2\pi} \int_{-\infty}^{\infty} \exp \left[-(a\omega)^2/2 \right] \exp \left[j\omega x \right] d\omega$$

is itself an error curve. While the above equation can be directly integrated, the derivation is lengthy,¹⁶ and we will simply state the result, which is

$$r_o(x) = \exp \left[-(x^2/2a^2) \right] / (2\pi a^2)^{1/2} \quad (62)$$

This function, which is plotted in figure 23 represents the line spread function shown schematically in figure 20(b) for the error curve filter. The equivalent duration of the impulse response is defined as a rectangle of height equal to $r_o(0)$ and area equal to that under the impulse curve and is given by

$$D_o = \left[\int_{-\infty}^{\infty} r_o(x) dx \right] / r_o(0) \quad (63)$$

$$= [2\pi a^2]^{1/2}$$

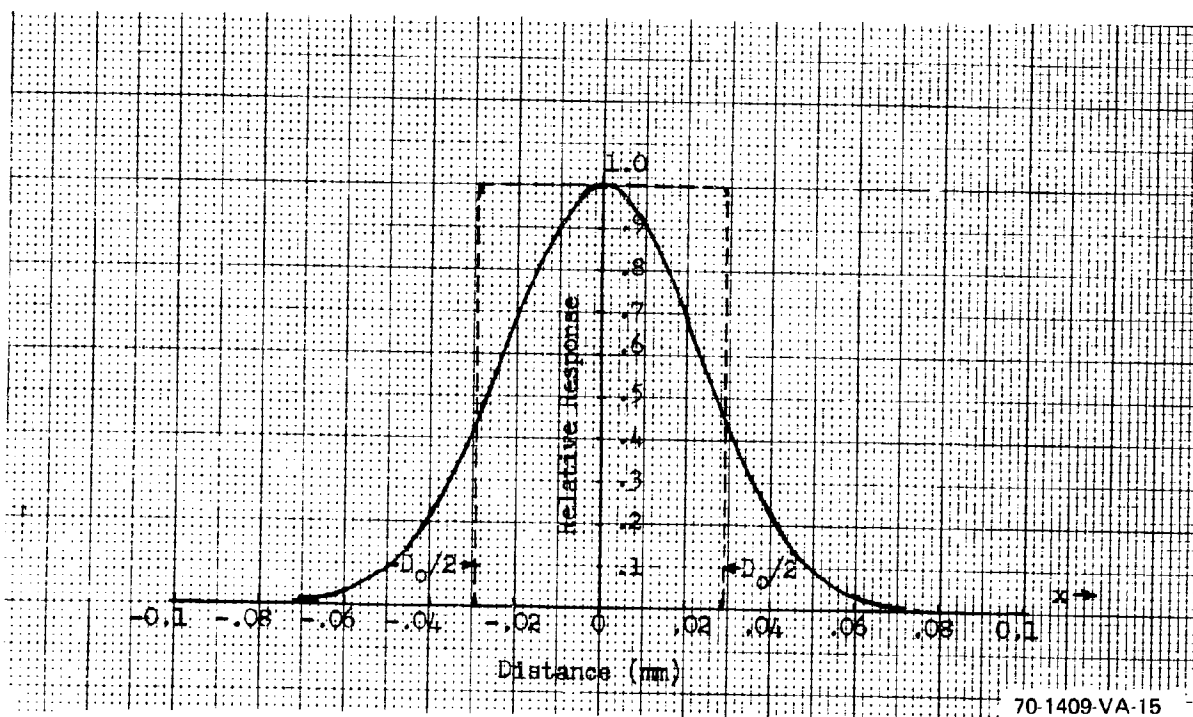


Figure 23. Impulse Response of Error Curve (figure 15) and Equivalent Pulse Duration

Using equations 60 and 61, we see that

$$D_o = \frac{\pi}{\Omega_B} = \frac{1}{2 \Delta N_{LPB}} \quad (64)$$

Thus, the wider the equivalent bandwidth, the narrower the equivalent impulse duration and conversely. This is the well-known reciprocal spreading effect between the space and frequency domain. Also, the interpretation of the impulse response is that as the input pulse is decreased to zero width, the output pulsewidth decreases only to the width of that given by the impulse response and no further.

The input impulse is of unit area. The area of the output pulse is also unity as can be seen from equations 62 and 63, i.e.,

$$D_o \cdot r_o(o) = (2\pi a^2)^{1/2} / (2\pi a^2)^{1/2} = 1.0 \quad (65)$$

This result might have been foreseen, because the filter is dissipationless. All of the electrons flowing into the filter, glow out. This is quite often true of sensor apertures. We shall have occasion to return to this result.

In the above, the method of fitting the error curve to the experimentally measured MTF curve was shown. In the following, it is desired to generalize the analysis by use of the dimensionless parameter x/a . To this end, the error curve frequency response is replotted in figure 24, and the impulse response is replotted in figure 25. Note that the frequency response is shown as a two-sided spectrum (as is more customary in analysis), but it is quite immaterial when the spectrum is symmetrical.

The unit step function designated $\delta_{-1}(x)$ is perhaps the second most useful singularity test signal. It is defined by

$$\delta_{-1}(x) = \begin{cases} 0, & x < 0 \\ 1, & x > 0 \end{cases} \quad (66)$$

and also,

$$\delta_{-1}(x) = \int_{-\infty}^x \delta_o(x) dx \quad (67)$$

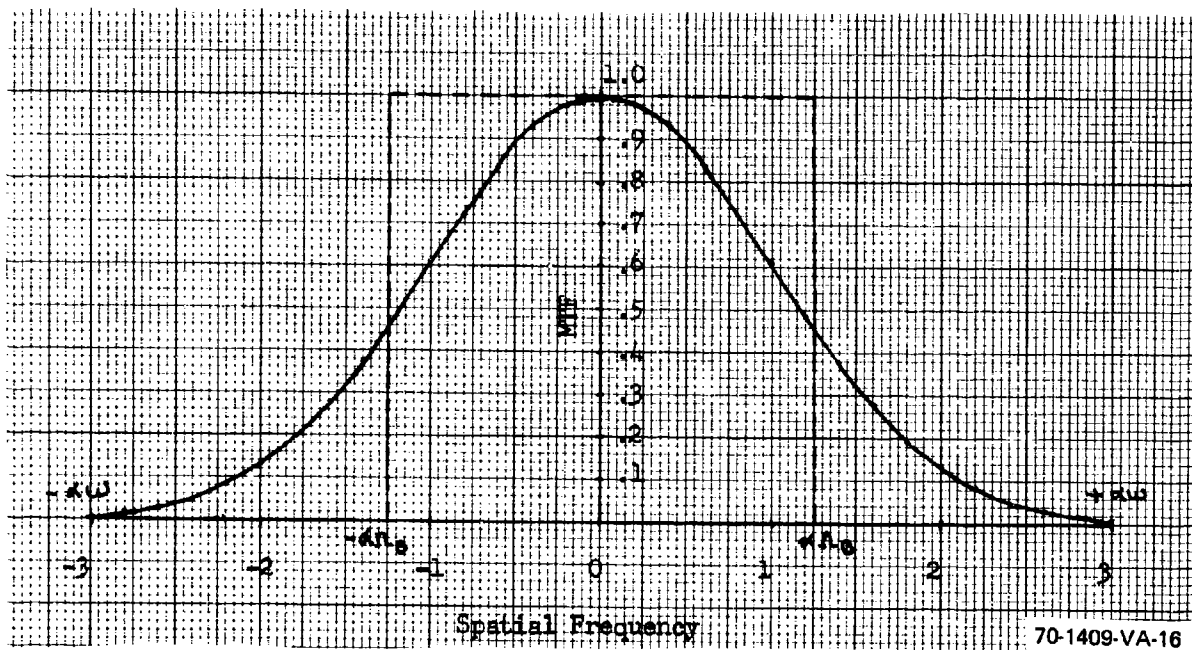


Figure 24. Modulation Transfer Function and Effective Bandwidth for Error Curve Filter in Dimensionless Coordinates

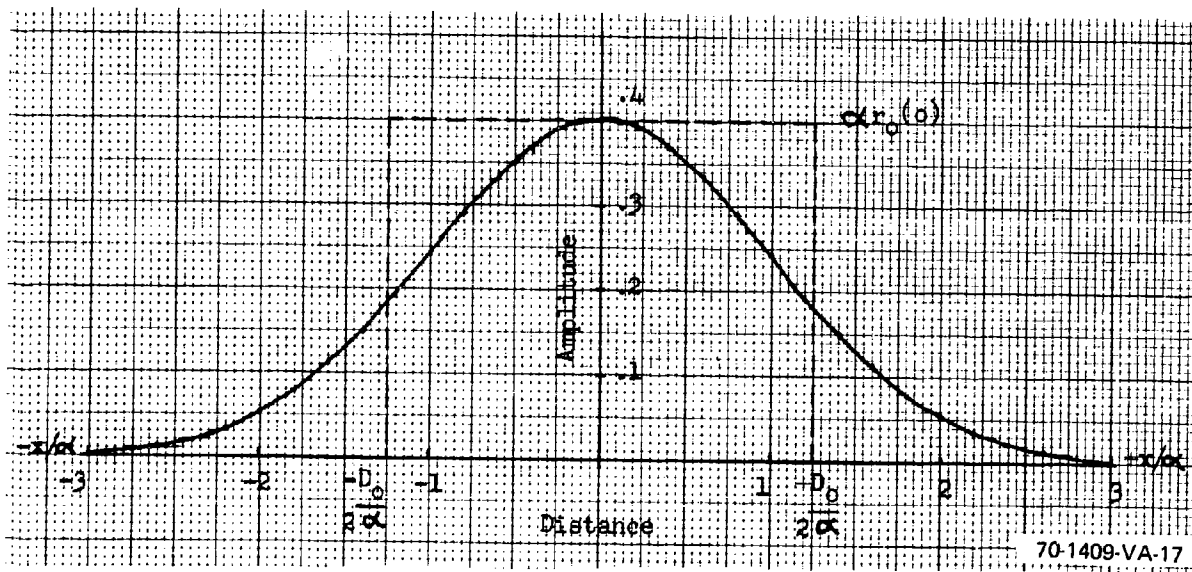


Figure 25. Unit Area Impulse Response and Effective Duration for Error Curve Filter in Dimensionless Units

Similarly, the unit step response of a filter is given by $r_{-1}(x)$ and can be obtained from

$$r_{-1}(x) = \int_{-\infty}^x r_0(x) dx \quad (68)$$

For our error curve filter,

$$r_{-1}(x) = \frac{1}{(2\pi a^2)^{1/2}} \int_{-\infty}^x \exp \left[-(x/a)^2/2 \right] dx$$

With the change of variable $z = (x/a)^2/2$,

$$\begin{aligned} r_{-1}(x) &= \frac{1}{\pi^{1/2}} \int_{-\infty}^0 \exp \left[-z^2 \right] dz + \int_0^z \exp \left[-z^2 \right] dz \\ &= 1/2 + \frac{1}{\pi^{1/2}} \int_0^z \exp \left[-z^2 \right] dz \\ &= 1/2 + 1/2 \operatorname{erf} \frac{x}{(2a^2)^{1/2}} \end{aligned} \quad (69)$$

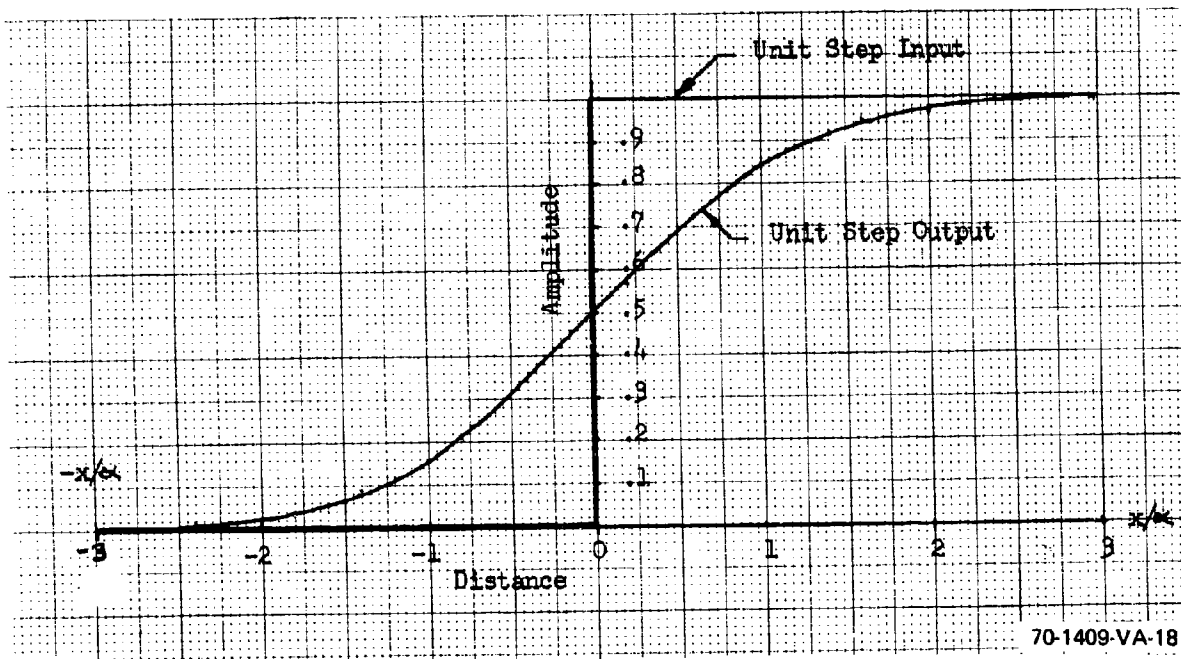
The error function (erf) is not obtainable in closed form, but it is widely available in tabular form.¹⁰ The unit step response, $r_{-1}(x)$, is plotted in figure 26. In optical tests, the unit step test is similar to the knife edge test.

Suppose next, that the input pulse is a unit area rectangle as shown in figure 27 of width x_0/a . By superposition, this input can be considered to be described by two unit-step inputs shifted by $\pm x_0/2$. Thus, the input becomes

$$f(x) = \delta_{-1} \left[\frac{x + x_0/2}{a} \right] - \delta_{-1} \left[\frac{x - x_0/2}{a} \right] \quad (70)$$

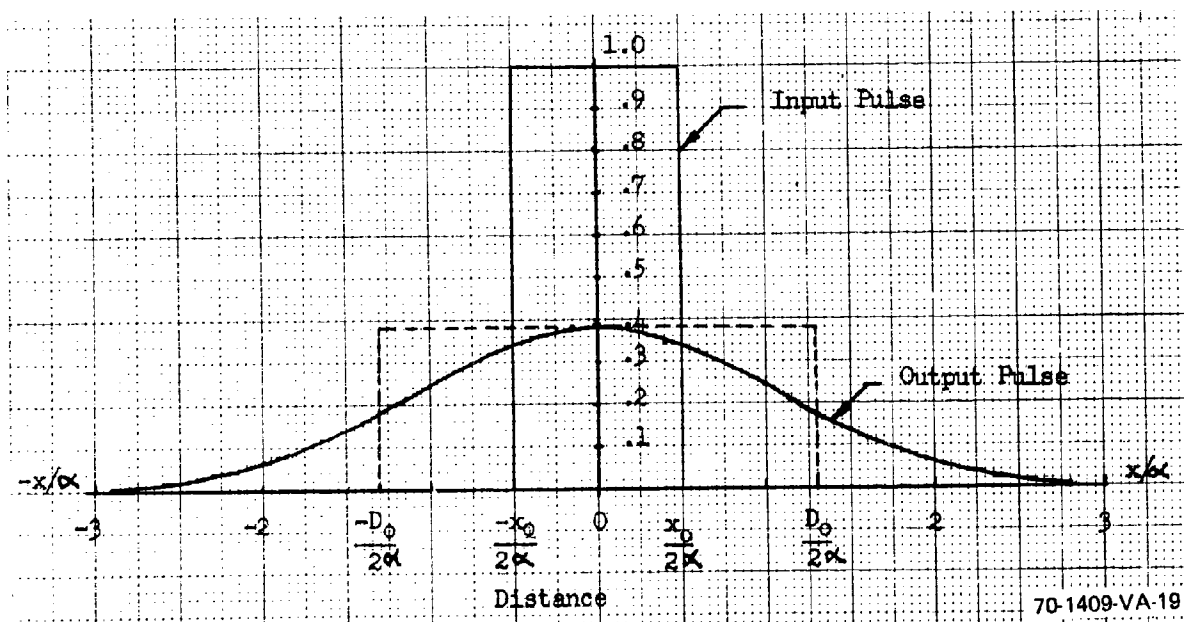
and the corresponding output of the filter is then,

$$\begin{aligned} g(x) &= r_{-1} \left[\frac{x + x_0/2}{a} \right] - r_{-1} \left[\frac{x - x_0/2}{a} \right] \\ &= \left[1/2 \operatorname{erf} \left[\frac{x + x_0/2}{(2a^2)^{1/2}} \right] - 1/2 \operatorname{erf} \left[\frac{x - x_0/2}{(2a^2)^{1/2}} \right] \right] \end{aligned} \quad (71)$$



70-1409-VA-18

Figure 26. Unit Step Response of Error Curve Filter in Dimensionless Units



70-1409-VA-19

Figure 27. Response of Error Curve Filter to Rectangular Input Pulse of Duration $(x_0/a)=1.0$ and Effective Output Pulse Duration

This function is plotted in figure 27. As can be seen, the output pulse is stretched in distance and reduced in amplitude. The amplitude is a maximum at $x = 0$, for which,

$$g(0) = \text{erf} \left[x_0 / 2 (2a^2)^{1/2} \right] \quad (72)$$

Using this equation, the ratio of output pulse amplitude to input pulse amplitude is plotted in figure 28. The effective duration D_0/a can be found by the conservation of signal notion described in connection with equation 65. That is,

$$g(0)/(D_0/a) = A(x_0/a) \quad (73)$$

where A is the input pulse amplitude which is equal to unity for the case discussed. D_0/a is plotted vs. x_0/a in figure 29. Observe that as the input pulse width approaches zero, the effective output pulse width approaches the effective duration of the impulse response as it should.

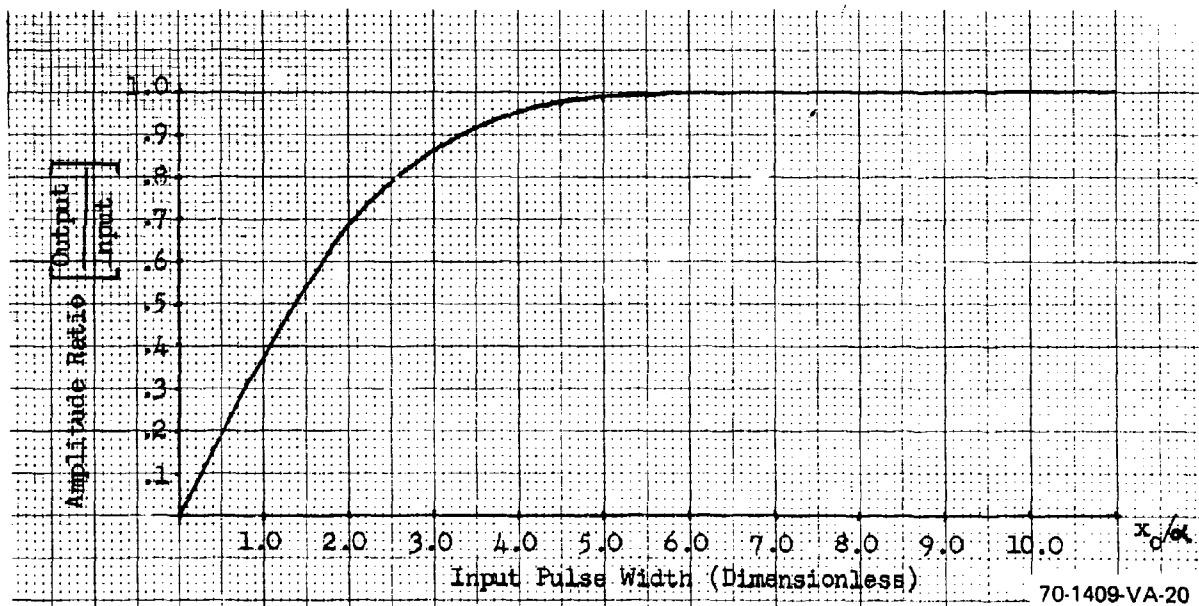


Figure 28. Output-Input Pulse Amplitude vs Pulse Width Ratio (Input Rectangular with Unit Amplitude)

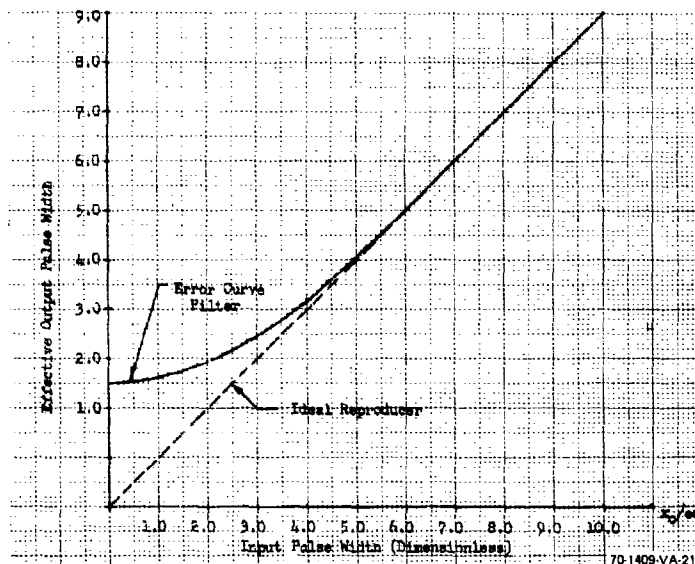


Figure 29. Effective Output vs Input Pulse Width (Input Rectangular with Unit Amplitude)

The effect of the error curve filter on the unit amplitude rectangular pulse as the input pulse is made progressively wider, is shown in figure 30. Once again, we note that the area under the output pulse curve is identical to the area under the input pulse curve. If we now apply the Model A_1 of equation 37, we would find that the SNR_D after filtering is identical to that before filtering. In other words, as the pulse is smeared out by the filter, the eye would presumably integrate over wider spatial limits and recover all of the signal.

However, when the pulse is smeared out, the amplitude of the signal in the tails becomes very small, and intuitively, we might expect this signal to be less effective than the higher amplitudes near the peak. As observed in Section III, Model B_1 of equation 42 weights the higher amplitude terms at the expense of the lower. To illustrate, we shall apply this equation to the output pulse of the error curve filter. If the input pulse is of unit amplitude

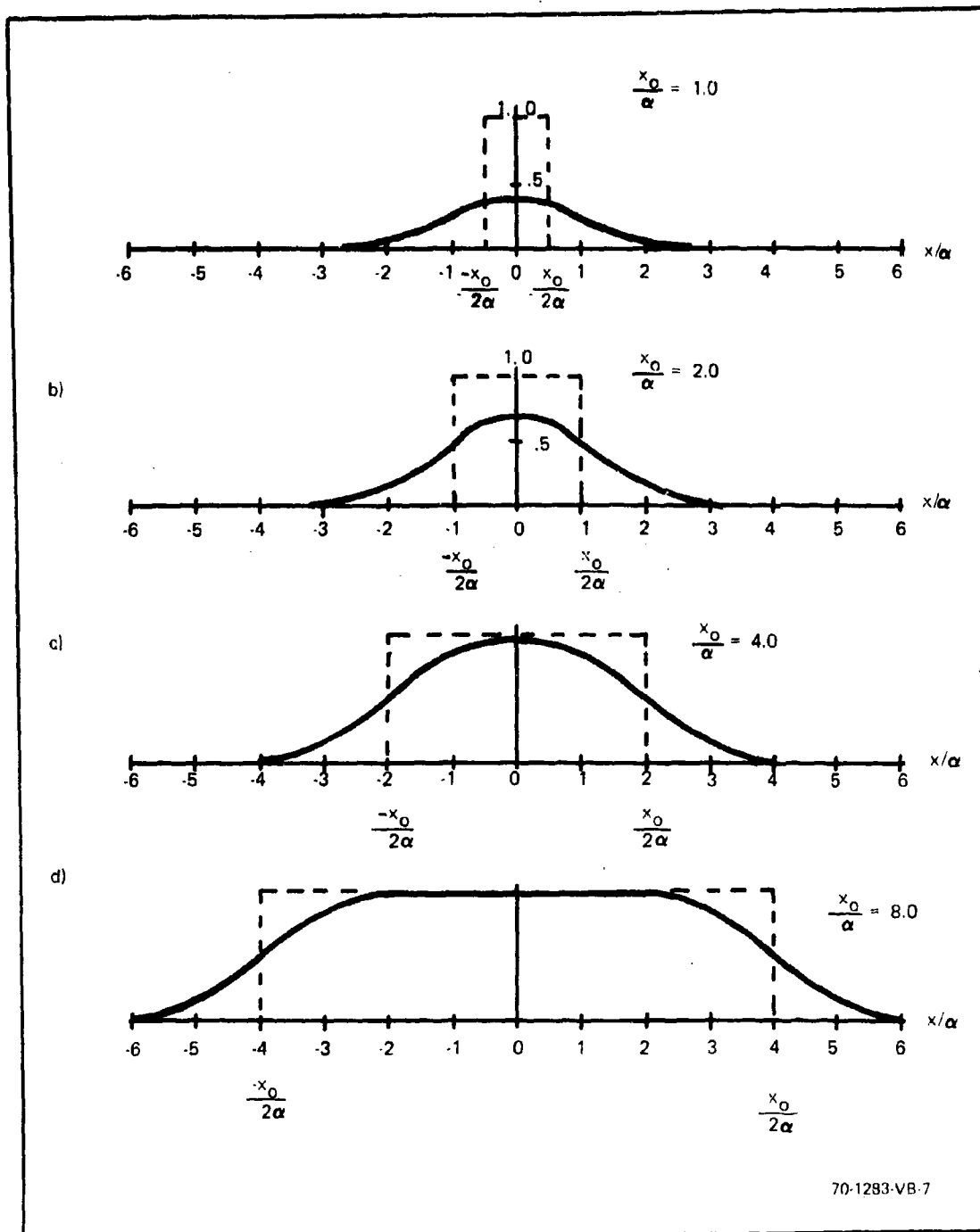


Figure 30. Output Pulse (-) for an Error Curve Filter as the Width of a Unit Amplitude Rectangular Input Pulse (---) Varies

and duration x_o/a , then the output signal using Model A_1 becomes simply x_o/a and the noise is simply $(x_o/a)^{1/2}$ such that

$$SNR_{DA} = t^{1/2} (x_o/a)^{1/2} \quad \text{Model } A_1 \quad (74)$$

Using Model B_1 ,

$$SNR_{DB} = \frac{t^{1/2} \int_{-x_o/2}^{x_o/2} g^2(x) dx}{\left[\int_{-x_o/2}^{x_o/2} g^2(x) dx \right]^{1/2}} \quad \text{Model } B_1 \quad (75)$$

where $g(x)$ is given by equation 71. In both of the above conditions, a one-dimensional pulse (a bar of infinite length) is assumed, image contrast is unity, and the sensor is presumed to be photoelectron-noise-limited.

Before proceeding, we will define a factor R_K , which is the amount by which the signal energy is reduced. Numerically,

$$R_K = \frac{\int_{-x_o/2}^{x_o/2} g^2(x) dx}{\int_{-x_o/2}^{x_o/2} f^2(x) dx} = \frac{\int_{-x_o/2}^{x_o/2} g^2 \left(\frac{x}{a} \right) \frac{dx}{a}}{x_o/a} \quad (76)$$

where $f(x)$ is simply the input pulse.

R_K is plotted vs x_o/a in figure 31. Also plotted are $R_K^{1/2}$, and R_K^2 . The interpretation of these quantities is as follows. For a one-dimensional bar,

$$\frac{SNR_{DB}}{SNR_{DA}} = \frac{R_K}{(R_K)^{1/2}} = R_K^{1/2} \quad (77)$$

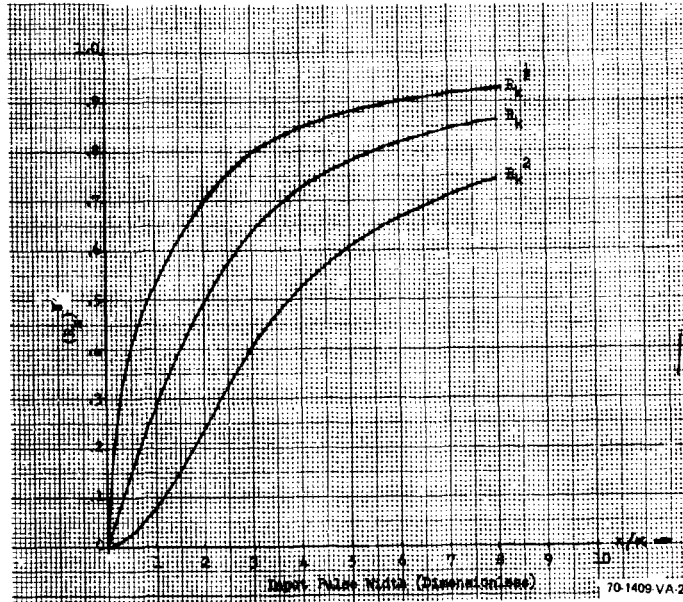


Figure 31. Signal and S/N Ratio Reduction Factors Due to Spreading of Input Pulses by Error Curve Filter

and for a two-dimensional image, (a square) where the horizontal and vertical MTF's are independent and separable,

$$\frac{\text{SNR}_{\text{DB}}}{\text{SNR}_{\text{DA}}} = \frac{R_K^2}{R_K} = R_K \quad (78)$$

Thus, since $R_K^{1/2}$ and R_K are numbers smaller than unity, the effect of the apertures is to reduce the S/N ratio.

To make use of these results, we will calculate the minimum detectable irradiance and the minimum detectable power for a photoelectron-noise-limited sensor viewing a square target. These quantities are of interest to astronomers and to system designers who wish to detect small sources such

as rescue beacons or laser illuminated spots. Suppose first that the MTF is unity. Then, from equations 7 and 10,

$$\text{SND}_D = \frac{C(\bar{n}_{xy} at)^{1/2}}{(2-C)^{1/2}} = C \left(\frac{iat/eA}{(2-C)} \right)^{1/2} = C \left(\frac{\sigma_A a H_A t/e}{(2-C)} \right)^{1/2}$$

If H_A , the photosurface irradiance is given in W/m^2 , and a is given in mm^2 , then

$$\text{SNR}_D = C \left[\frac{\sigma_A a H_A t 10^{-6}}{(2-C) e} \right]^{1/2} \quad (79)$$

The threshold SNR_{DT} for squares has been determined to be 2.8 for 50 percent probability of detection. Thus, we can solve the above equation for either minimum detectable irradiance H_{Amin} ,

$$H_{Amin} = \frac{(2.8)^2 (2-C)}{C^2} \left[\frac{10^6 e}{\sigma_A at} \right] \quad (80)$$

or minimum detectable power, P_{Amin} ,

$$\begin{aligned} P_{Amin} &= H_{Amin} a \\ &= \frac{(2.8)^2 (2-C)}{C^2} \left[\frac{10^6 e}{\sigma_A t} \right] \end{aligned} \quad (81)$$

As can be seen, H_{Amin} is proportional to $1/a$, and P_{Amin} is a constant for sensors that are photoelectron-noise-limited and have unity MTF. We plot equation 71 on figure 32, assuming that $C = 1.0$ and $\sigma_A = 4 \cdot 10^{-3} \text{ A/W}$, which is typical of S-25 photocathodes irradiated by tungsten test sources. Similarly, P_{Amin} is calculated and plotted in figure 33.

Suppose that we have the three-stage intensifier of figure 22, which is approximated by the error curve as shown in the same figure. For this

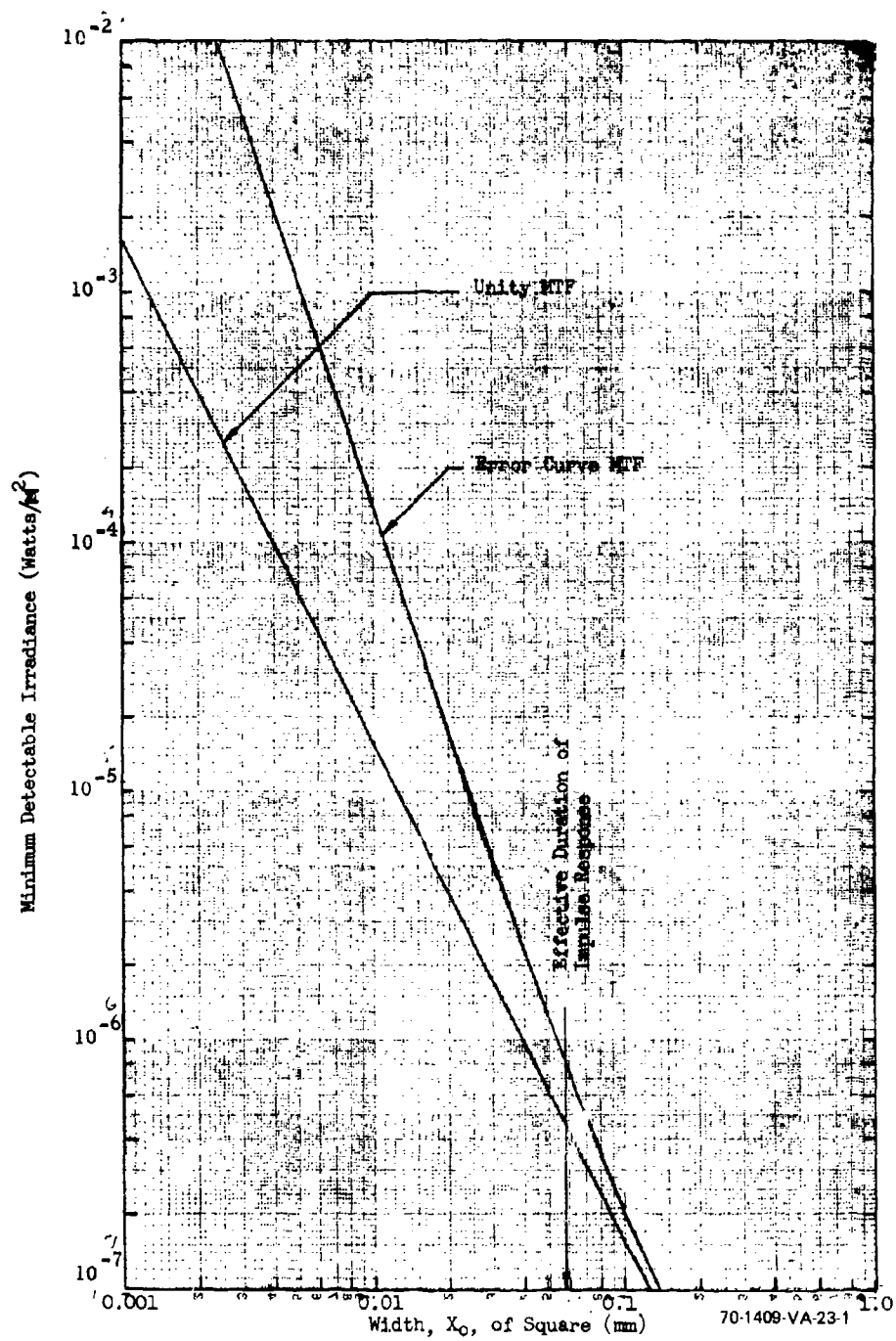


Figure 32. Minimum Detectable Irradiance for Square of Width X_0

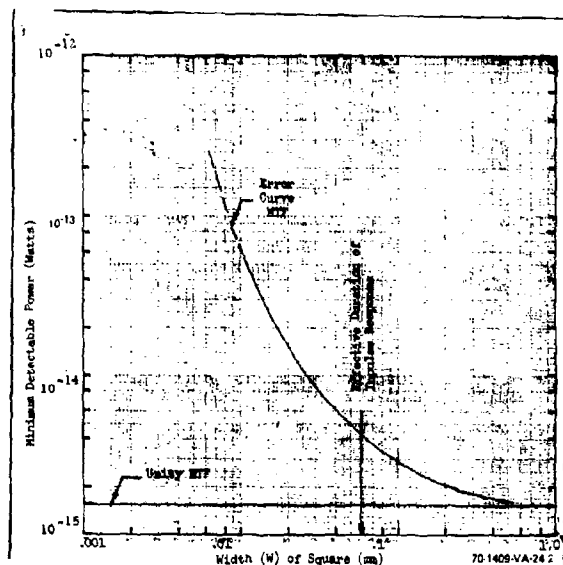


Figure 33. Minimum Detectable Power for Square of Width W for 3-Stage Intensifier (figure 22)

curve, $a = 2.31 \cdot 10^{-2}$ mm. Assuming a square image of unity contrast and horizontal and vertical MTF's that are equal, independent and separable,

$$\begin{aligned} \text{SNR}_D &= \left[\frac{\sigma_A a H_A t \cdot 10^{-6}}{e} \right]^{1/2} \cdot \frac{R_K^2}{R_K} \\ &= \left[\frac{\sigma_A a H_A t \cdot 10^{-6}}{e} \right]^{1/2} \cdot R_K. \end{aligned} \quad (82)$$

Now, we see that H_{\min} increases as $1/R_K^2$ and P_{Amin} is no longer constant, but it also increases in the same manner. The effect of R_K on H_{Amin} and P_{Amin} is shown in figures 32 and 33. The effect of the aperture is seen to be small for images of size about 4 to 5 times the effective duration of the impulse response.

SECTION V

PERIODIC SIGNALS AND FINITE WAVETRAINS

In the past two decades, the use of periodic image patterns has found widespread use in the testing and specification of image forming sensors.^{17, 18} These test patterns take various forms from sine wave patterns, to bar pattern wedges, to bursts of bar patterns¹⁹ as shown in figure 34. Whatever their form, the notion is to project patterns of various spatial frequencies onto the sensor. Then the response of the sensor to the pattern is judged by various means. In the case of television sensors, two methods of judging response are used. In one, the amplitude of a bar pattern of spatial frequency N_{TV} lines/picture height is measured in the electrical channel (the video amplifier), and a plot of the measured amplitude relative to the

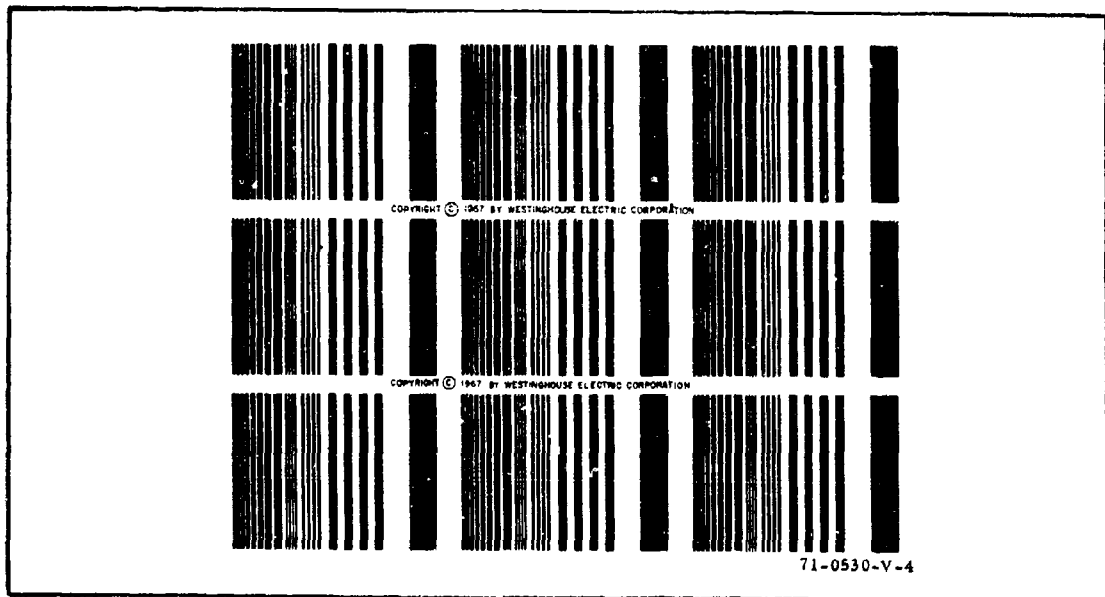


Figure 34. Resolution Test Chart Developed by Limansky for Calculation of Sine Wave MTF

amplitude measured at some low spatial frequency constitutes the square wave amplitude response $R_{SQ}(N_{TV})$. In another test, an observer is asked to determine the pattern of highest spatial frequency, which can be barely detected as the pattern's signal-to-noise ratio, is varied by increasing or decreasing its irradiance. The resolution so measured is called the sensor's "limiting resolution," and it is plotted versus the pattern's highlight irradiance.

The limiting resolution versus photocathode irradiance characteristic is now used by nearly all the major sensor manufacturers to specify and compare the performance of their products with others. Test procedures have been standardized after a fashion and surprisingly the limiting resolution versus irradiance characteristic has come to be a fairly reliable method of comparison even though the measurements (which are subjective and statistically variable) are usually made by a single observer in a very limited number of trials and using test patterns of widely different parameters. Observers must, of course, be experienced. The measuring of sensors in this manner can be extremely costly — particularly where new developmental sensors or combinations of sensors, such as television pickup tubes with cascaded intensifiers, are involved. Rosell²⁰ found that, given certain data of the type ordinarily supplied by sensor manufacturers, the limiting resolution versus absolute irradiance level could be calculated with fair-to-good accuracy. This model will be reviewed in the following and improved.

The earlier analysis proceeds along the lines discussed in Section II. The bar pattern image being viewed is divided into square elements of size $\Delta y \cdot \Delta y$ where Δy is numerically equal to the bar spacing (which is also equal to the bar width). Then SNR_D is calculated for this single square element which eventually results in equation 10. Next, we note that if we define the bar spacing Δy in terms of the number, N_{TV} , of squares which can be fitted into a picture height, then,

$$N_{TV} = \frac{Y}{\Delta y} . \quad (83)$$

Also, if X is the picture width which is equal to aY where a is the picture aspect ratio, then $A = aY^2 = \Delta y^2 \cdot N_{TV}^2/a$. Note further that $a = \Delta y^2$ such that equation 10 becomes

$$SNR_D = \frac{[t \Delta f_V / a]^{1/2}}{N_{TV}} \cdot SNR_V \quad (84)$$

This equation was derived for the photoelectron noise limited case where the noise is white and for the case where the sensor's MTF is unity. This situation can be simulated in the laboratory and was by Coltman and Anderson.⁴ Their formulation was somewhat different in that they set up the equation in the form

$$N_{TVP/W} = k [\Delta f_V']^{1/2} \cdot SNR_{VR} \quad (85)$$

and then evaluated k experimentally for "threshold identification" of the pattern. Their value was found to be equal to 615 when $\Delta f_V'$ is given in MHz, $N_{TVP/W}$ is given in line pairs/picture width, and the SNR_{VR} is in terms of an rms signal-to-rms noise. Converting the Coltman and Anderson nomenclature to that used here, we have that,

$$N_{TV} = \frac{N_{TVP/W} \times 2}{4/3} \frac{\text{lines}}{\text{picture height}} \quad (86a)$$

$$SNR_V = 2.82 SNR_{VR} \frac{\text{peak signal}}{\text{rms noise}} \quad (86b)$$

and

$$\Delta f_V = 10^{-6} \Delta f_V' \text{ (Hz)}. \quad (86c)$$

Inserting these results along with the constant $k = 615$ into equation 85, we find that

$$N_{TV} = 3.27 (\Delta f_V')^{1/2} \cdot SNR_V \quad (87)$$

Next, we solve equation 84 for N_{TV} ,

$$N_{TV} = \frac{[t/a]^{1/2}}{SNR_D} (\Delta f_V')^{1/2} \cdot SNR_V \quad (88)$$

By comparison of equations 87 and 88, equality would result if,

$$\frac{\left[\frac{t}{a} \right]^{1/2}}{\text{SNR}_D} = 3.27. \quad (89)$$

If $t = 0.2$ seconds and $a = 4/3$, then,

$$\text{SNR}_D = 1.18 \quad (90)$$

The inference is that SNR_D is a constant and equal to about 1.18.

Somewhat later, Parton and Moody gave an equation which, rewritten in the nomenclature used in this report and rearranged, is²¹

$$\text{SNR}_D = \left[\frac{t}{a} \right]^{1/2} \frac{C}{N_{TV}} \left[\frac{\sigma AH}{e} \right]^{1/2}. \quad (91)$$

By multiplying the numerator and denominator by Δf_V , and noting that

$$\left[\frac{\sigma AH}{e \Delta f_V} \right]^{1/2} = \text{SNR}_V, \text{ we find that}$$

$$\text{SNR}_D = \frac{\left[\frac{t \Delta f_V}{a} \right]^{1/2}}{N_{TV}} C \cdot \text{SNR}_V \quad (92)$$

which for unity contrast becomes equation 84. Parton and Moody gave a value of 1.2 for threshold SNR_{DT} . This number has been used since that time although incorrectly as will be seen.

Coltman and Anderson also suggested that the effect of the sensor's MTF could be taken into account by simply modifying the SNR_V obtainable from the photocathode by the MTF.⁴ In the nomenclature of this report, this modification becomes

$$\text{SNR}_D = \frac{\left[\frac{t \Delta f_V}{a} \right]^{1/2}}{N_{TV}} \cdot R_\omega(N_{TV}) \cdot \text{SNR}_{V,0,1} \quad (93)$$

where $R_\omega(N_{TV})$ is the sensor's sine wave response or MTF and $\text{SNR}_{V,0,1}$ is the video SNR at zero frequency and unit contrast. This equation has been used extensively by the authors and others to calculate the limiting resolution of sensors, and the results so computed are in very good agreement with measured results. We will see that this is so not because the

equation is right, but because it is not too far wrong and because of compensating errors.

The fact that equation 93 holds so well is surprising for several reasons. First, SNR_D derived is for a single element of size $1/N_{TV} \times 1/N_{TV}$, where N_{TV} is the width of a single bar and the results appear to hold for the "detection" of the entire bar pattern. The height of the bar pattern is stipulated to be large with respect to the bar spacing, but, otherwise, no account is taken of it. The threshold SNR_{DT} is supposedly a constant independent of the height which would imply that the height is of no moment. A bar pattern is presumably a one-dimensional pattern if the bars are very long compared to their spacing, yet, the derivation assumes a two-dimensional element which does not seem physically reasonable.

To show the impact of reducing the number of bars available to the observer, Coltman and Anderson devised the experiment shown in figure 35. The displayed pattern "was left fixed and a series of cardboard apertures were employed to vary the number of lines seen by the observer." * The mask was presumably of square aspect ratio. The results, as shown in figure 35, "show that the observer probably uses no more than seven line pairs in making an identification. As the number which he is permitted to see is decreased, the signal required rises rapidly being greater by a factor of four when only one line pair is presented."

Schade also notes that "the sampling aperture of the eye for lines and edges is its line image, limited in length to 14 equivalent point image diameters." These two observations give a possible explanation for the use of the elemental image of size, $1/N_{TV} \times 1/N_{TV}$. However, to hold over a wide range of spatial frequencies, it is necessary to conclude that as the pattern spacing changes, then the eye's ability to integrate along the line changes in direct proportion. This is at considerable variance with the results obtained in Section II where, figure 10, it was shown that the eye

* Quotes are from Ref 4, page 862 and Ref 11, page 731.

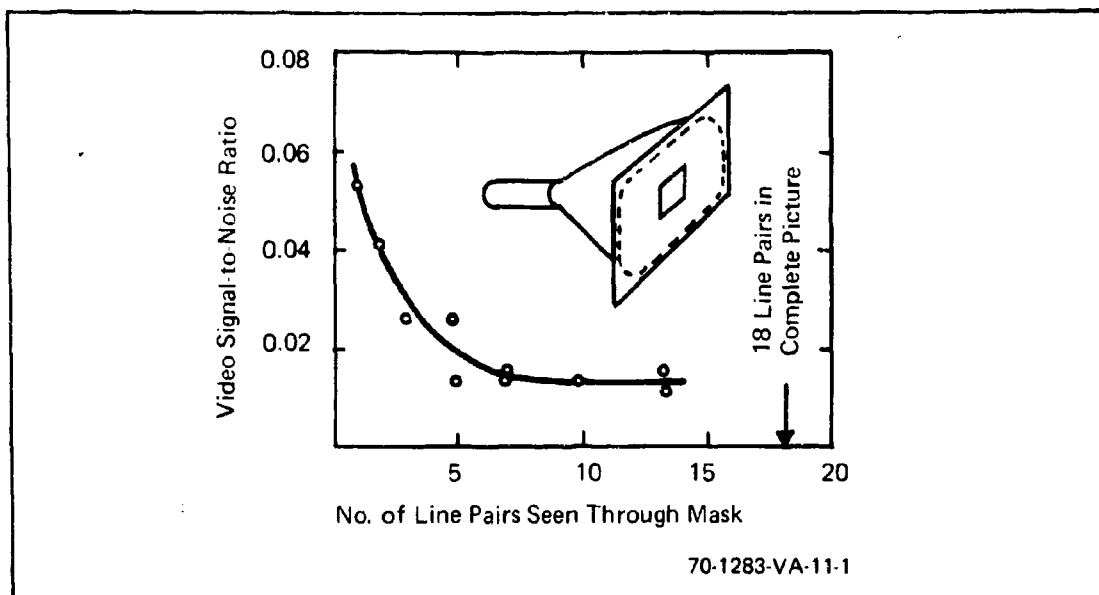


Figure 35. Video S/N Ratio Required to Detect Pattern as a Function of the No. of Line Pairs Visible Through Mask

could integrate a line of length to width aspect ratio from 1:1 to at least 45:1 (or 22 line pairs) and perhaps even more since no end point was determined.

Since the notion of using an elemental image to describe a one-dimensional bar pattern conflicts with physical intuition and since the notion of a limited but variable integrating capability for the eye conflicts with measured data, it was decided to take a new approach. First, we define detection. By detection, it is implied that the observer must be able to determine that a bar pattern is actually present. We will further stipulate that the observer makes this determination on the basis of a single line (or line pair). Thus, the problem reduces to the two-dimensional rectangle detection problem of Section II except that we feel that a higher signal-to-noise ratio is needed because the identification must be positive. For this reason and because the result will be found to fit well, we will assume that the bar must be detected

with near 100 percent probability. Reference to figure 15 shows 100 percent probability will require an SNR_{DT} of 5.3. Let the dimensions of the bar be given in terms of the reciprocal distance $N_V \cdot N_H$ where

$$N_H = \frac{Y}{\Delta y} \quad (94a)$$

$$N_V = \frac{Y}{n_v \cdot \Delta y} \quad (94b)$$

where Y is the picture height, Δy is the linear dimension of the bar width, and n_v is the length of the bar measured in terms of a number of bar widths. The image area relative to the total effective photocathode area is equal to

$$\frac{a}{A} = \frac{n_v \Delta y^2}{a Y^2} \quad (95c)$$

$$= \frac{1}{a N_V \cdot N_H} \quad (95b)$$

$$= \frac{n_v}{a N_{TV}^2} \quad (95c)$$

where $N_{TV} = Y/\Delta y$ lines/picture height. With this result, equation 12 becomes either,

$$SNR_D = \frac{[t \Delta f_V / a]^{1/2}}{[N_V \cdot N_H]^{1/2}} \cdot SNR_V \quad (96)$$

or,

$$SNR_D = [t \Delta f_V / a]^{1/2} \cdot \frac{n_v^{1/2}}{N_{TV}} \cdot SNR_V \quad (97)$$

which becomes the new models for the recognition of bar patterns (with unity MTF and image contrast). The SNR_{DT} required is taken to be 5.3 as previously discussed.

Next, we focus our attention on equation 97 which is very similar to equation 84 and which was previously used for pattern detection. The right sides of the two equations would in fact be identical if equation 97 were divided by $n_v^{1/2}$ which results in the formula,

$$\frac{SNR_D}{n_v^{1/2}} = \frac{[t \Delta f_v / \alpha]^{1/2}}{N_{TV}} \cdot SNR_V. \quad (98)$$

Consider $SNR_D / n_v^{1/2}$ to be a new display signal-to-noise ratio which has a threshold value for bar patterns of frequency N_{TV} of $SNR_{DT}(N_{TV})$ equal to

$$SNR_{DT}(N_{TV}) = \frac{SNR_{DT}(N_{TV}, n_v)}{n_v^{1/2}}, \quad (99)$$

which is plotted in figure 36. We note that $SNR_{DT}(N_{TV})$ drops quickly to a value of about 1.2 at about 14 lines (or 7 line pairs) and then slowly decreases thereafter. This, we believe, is the origin of the value of 1.2 for

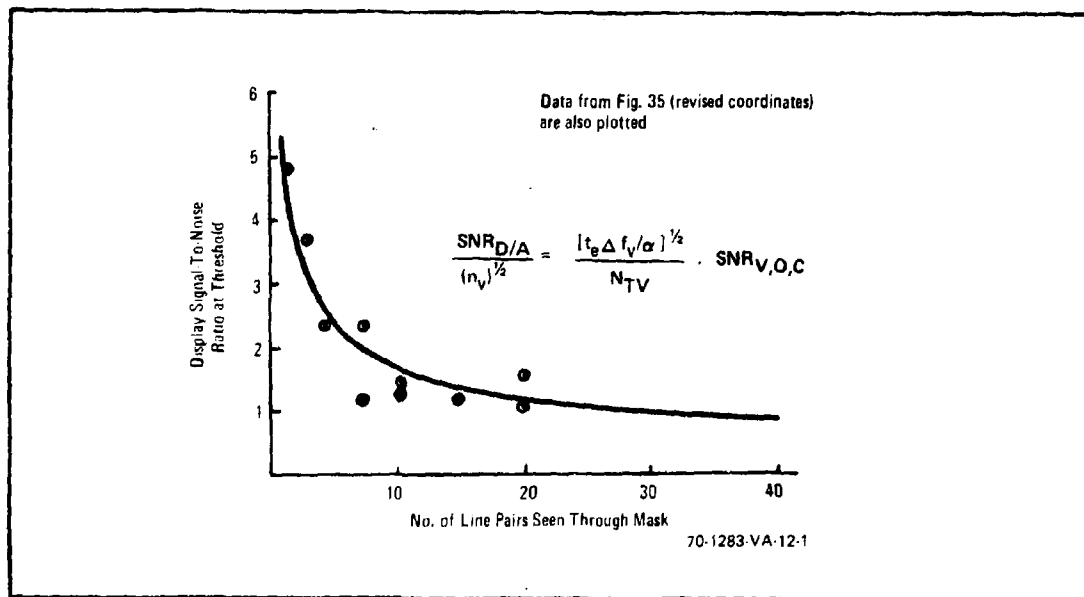


Figure 36. Threshold Display S/N Ratio Required to Identify Bar Patterns as a Function of Bar Length-to-Width Ratio

SNR_{DT} for bar patterns. It is not 1.2 but nearly so over a fairly broad range of bar heights. When other effects are taken into account, the range of validity of $SNR_{DT} = 1.2$ will probably be even larger as will be discussed later.

However, before going on to this subject, we will replot the data of figure 35 on figure 36 using the relation

$$SNR_D = \frac{[0.15 \Delta f_V]^{1/2}}{N_{TV}} SNR_{VM} \quad (100)$$

where now SNR_{VM} is the measured value of threshold video SNR and the conversion factors of equations 86a, b, and c are applied to the data. The fit of the data to the predicted curve using equation 99 is seen to be well within experimental measurement errors. It is tentatively concluded that the effect of the cardboard apertures was only to decrease the bar height over which the eye can integrate.

The premise that the eye can integrate only over a small portion of the bar length which is some small multiple of the bar width (such as 14 elements) is evidently not correct. Per the experiments of Section II, the eye can integrate up to a 6-degree angle on the display and perhaps more since we apparently had not reached the limit in the experiment. With normal observer distance to display height ratios of 3 to 5, the eye appears to be able to fully integrate bars which are of length $1/4$ to $1/2$ the display height and perhaps more.

In the usual data supplied by the sensor manufacturer, the bar pattern height to spacing ratio is not specified. To be precise, this ratio must be supplied. To a certain extent, the problem could be avoided by using patterns of constant height to spacing ratio (which is numerically equal to n_V). In this case, the SNR_{DT} required would be as given in table IV if equation 98 is used.

TABLE IV

THRESHOLD SNR_D REQUIRED USING EQUATION 98 TO IDENTIFY
 BAR PATTERNS OF VARIOUS HEIGHT TO SPACING RATIO,
 n_v AS A FUNCTION OF n_v . DYNAMIC NOISE ASSUMED

n_v	$SNR_{DT}/n_v^{1/2}$
2	3.72
3	3.05
5	2.36
7	2.0
9	1.77
11	1.6
13	1.47
19	1.21

The notion that the eye's ability to integrate is limited to only rather small angles has been rather commonly accepted, but it appears to not be the case. This important result bears further investigation. As a preliminary step, we performed the following experiment. A 70 TV line per raster height pattern was electronically generated, mixed with white noise and displayed on a monitor of 8-inch picture height. An observer was seated 28 inches from the display. The pattern height to width ratio was varied over a range of 70:1 in steps of 1, 2.67, 6.67, 18.18, and 70.8:1.

The observer was asked to state whether or not he could determine the presence of the pattern as the pattern height and signal-to-noise ratio was varied. No chance was involved because the pattern was always present. Because of the nature of the electronics involved, the patterns of small height were very bright and the patterns of large height were dim. Over the range of heights, the pattern brightness varied by about 10:1. Although display brightness is only a second order effect, one cannot ignore the possibility of it being a factor. With noise, the brightness of the display only varied by 5 percent.

To do a proper series of experiments, which are beyond the scope of the current effort, display brightness must be more rigidly controlled, observer viewing distance must be varied, and an element of chance must be introduced. In short, the experiment performed is felt to be inadequate, but it serves the useful purpose of showing that further effort should be expended as will be seen.

The fraction of patterns detected is plotted versus the display signal-to-noise ratio for the various display heights in figures 37 and 38 using equation 98. We had expected the SNR_D curves to be identical for the various heights except perhaps for the larger heights wherein the eye's ability to integrate might fall off. At the observer distances involved, the highest pattern (70:1) subtends an angle of 16.2 degrees. However, as can be seen, the SNR_D required to detect the pattern increased somewhat as the height increased. Observe that we designated the ordinate as the "fraction of patterns identified" rather than "probability of detection" because the pattern was always present.

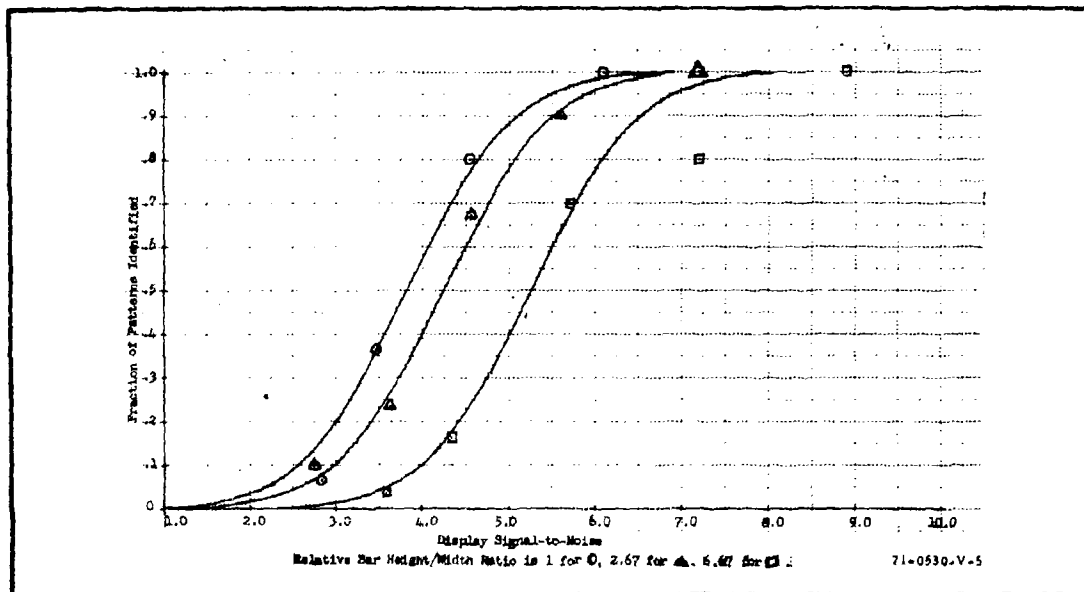


Figure 37. Fraction of Bar Patterns Identified Versus Display S/N Ratio Calculated on Basis of the Area of a Single Bar

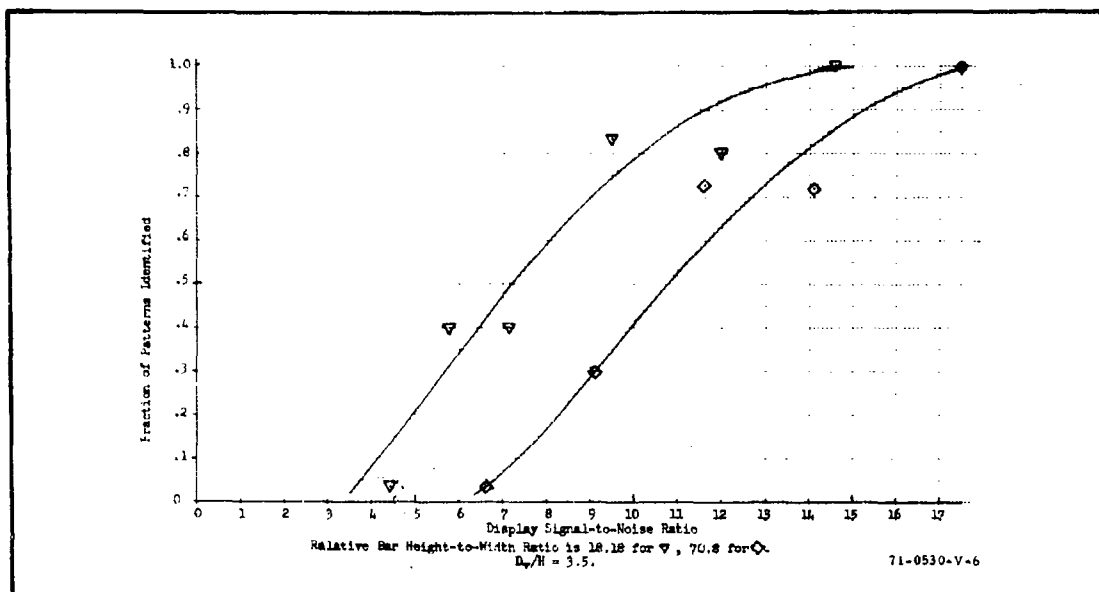


Figure 38. Fraction of Bar Patterns Identified Versus Display S/N Ratio Calculated on the Basis of the Area of a Single Bar

SNR_D versus bar height to width ratio is plotted in figure 39. In this curve, the SNR_D plotted is for the fraction of patterns identified equal to 0.5. Note that SNR_D required increases slowly with length. Although there is a suggestion of a knee in the curve near a length-to-width ratio of 2 to 3, SNR_D is a straight line function from 3 to 70. The implication of this data is that the eye's ability to integrate a bar pattern falls off with length, but that the fall off is gradual rather than abrupt as has been suggested. Also, over a 70:1 change in length, the SNR_D required increases only by about 2.5:1.

The data of figure 39 was also plotted in figure 40 using the "per element" concept of equation 99. It is seen that the actual curve is of lesser slope than that predicted. The dashed curve represents the result obtained when it is assumed that the eye integrates only up to a bar length 14 times longer than its width.

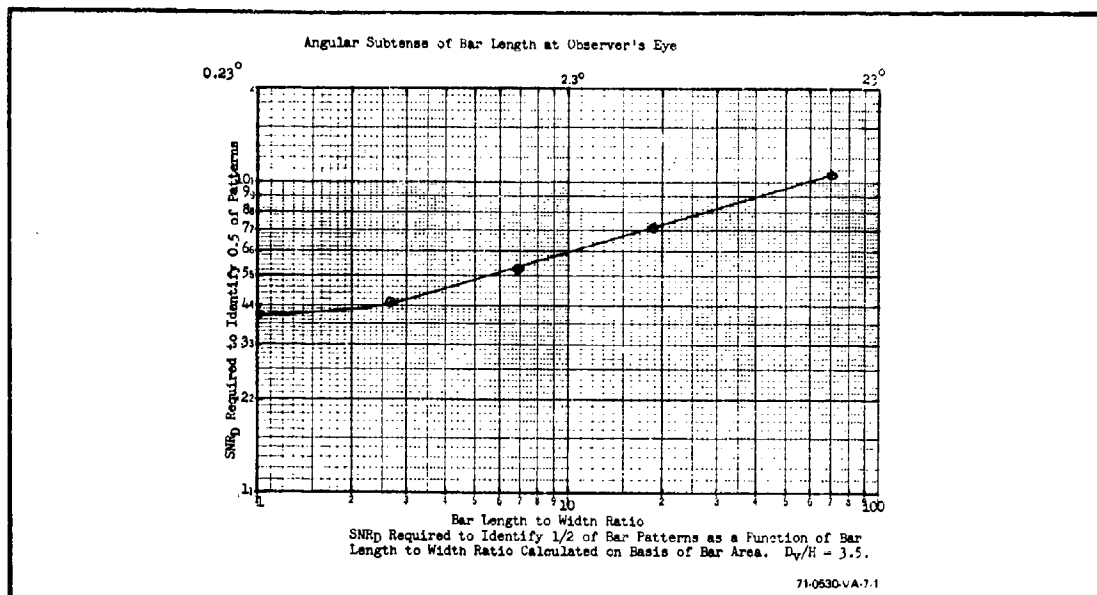


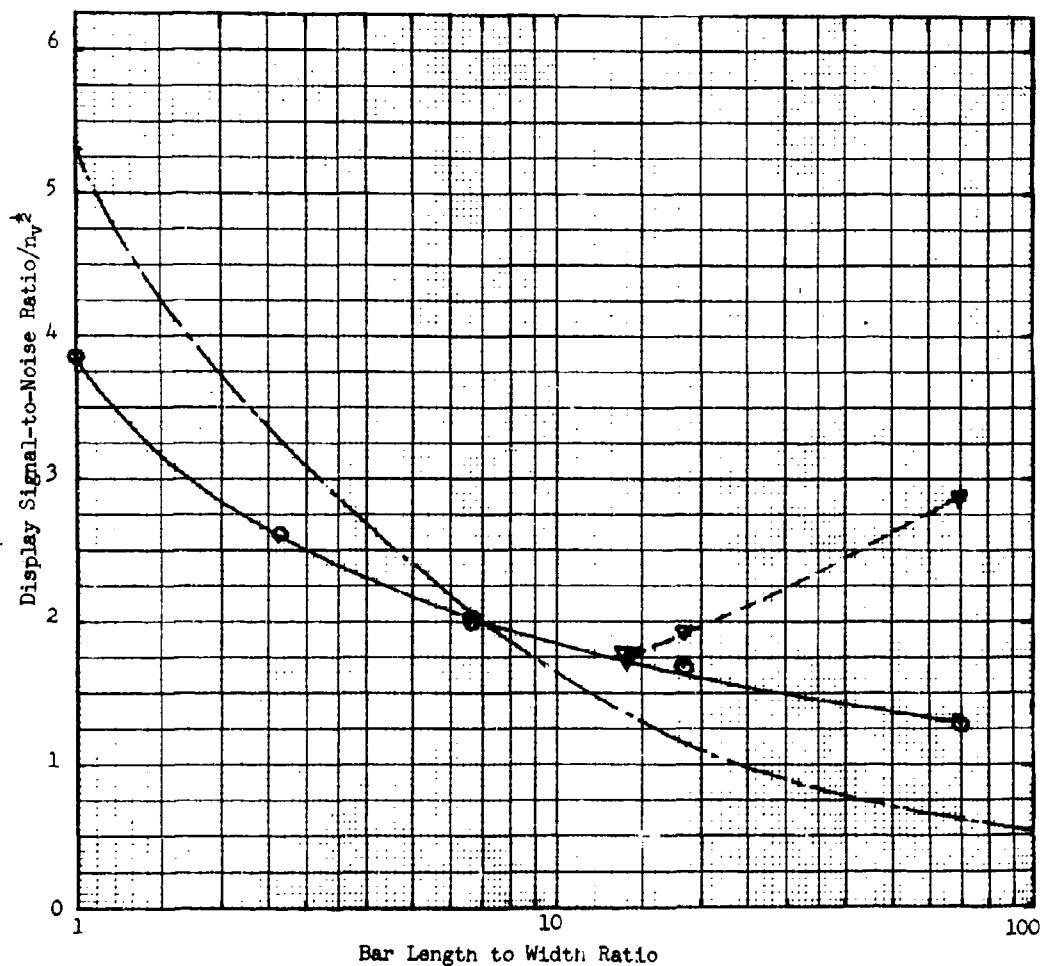
Figure 39. SNR_D Required to Identify 1/2 of Bar Patterns

The results obtained in this experiment conflict somewhat with the rectangle experiment of Section II and the Coltman and Anderson experiment results as we interpreted them in figure 36. In general, we feel that the experiment just described was not sufficient to give decisive answers for the reasons cited. Further effort is urged.

Before proceeding, the method of determining "limiting resolution" will be briefly discussed. Assume first that equation 98 holds. We shall refer to this as the area model since the bar area is used for calculation and we emphasize the area concept by writing

$$\text{SNR}_{D/A} = \left[t \Delta f_{V/a} \right]^{1/2} \cdot \frac{n_v^{1/2}}{N_{TV}} \cdot \text{SNR}_V \quad (101)$$

Next, suppose the bar patterns used for test purposes are of the type shown in figure 34. That is, each subgroup of bars within one of the nine major



SNR_D Required to Identify $\frac{1}{2}$ of Bar Patterns as Function of Bar Length to Width Ratio Calculated on Basis of Square Element of Size Equal to Bar Width. Measured Curve (—), Computed Curve (-----), Computed Curve Assuming Limited Eye Integration (-·-·-·-). $D_v/H = 3.5$

71-0530-V-8

Figure 40. SNR_D Required to Identify $\frac{1}{2}$ of Bar Patterns

groups has a different spatial frequency, but all are of the same height. If this height is L and the display height is Y , then,

$$\frac{L}{Y} = \text{constant} = \frac{n_v \Delta y}{Y} = \frac{n_v}{N_{TV}} = k_v \quad (102)$$

and since $n_v = k_v \cdot N_{TV}$, equation 101 becomes,

$$\text{SNR}_{D/A} = \left[t \Delta f_{V/a} \right]^{1/2} \cdot \left[\frac{k_v}{N_{TV}} \right]^{1/2} \cdot \text{SNR}_V \quad (103)$$

(for bars of constant height)

This equation is plotted as the two parallel straight lines on figure 41 and represent two arbitrary signal levels. The purpose of the curve is to show the functional relationships between $\text{SNR}_{D/A}$ and N_{TV} . The threshold signal-to-noise ratio required by the observer at any line number is assumed to be 5.3. With this value for $\text{SNR}_{D/A-T}$, limiting resolution can be calculated directly from equation 103 or graphically as on figure 41 by noting the line number at which the calculated $\text{SNR}_{D/A}$ curve crosses the $\text{SNR}_{D/A-T}$ curve.

In the above method, a unity MTF is assumed in both the vertical and the horizontal. Suppose that k_v is large enough such that the vertical MTF is essentially unity and assume further that*

$$\text{SNR}_{D/A} = \left[t \Delta f_{V/a} \right]^{1/2} \cdot \left[\frac{k_v}{N_{TV}} \right]^{1/2} \cdot |R_o(N_{TV})| \cdot \text{SNR}_{V,0,1} \quad (104)$$

where $|R_o(N_{TV})|$ is assumed to be the sensor's MTF and $\text{SNR}_{V,0,1}$ is assumed to be independent of $R_o(N_{TV})$ which would be the case where photo-electron noise is small compared to that of the preamplifier. A typical $|R_o(N_{TV})|$ is shown in the insert of figure 41 and its effect on $\text{SNR}_{D/A}$ is shown by the dashed curves. Note that with unity MTF, $|R_o(N_{TV})| = 1$, that limiting resolution is 580 and 140 lines at the two signal levels which are

* A sine wave pattern is presumed in this analysis.

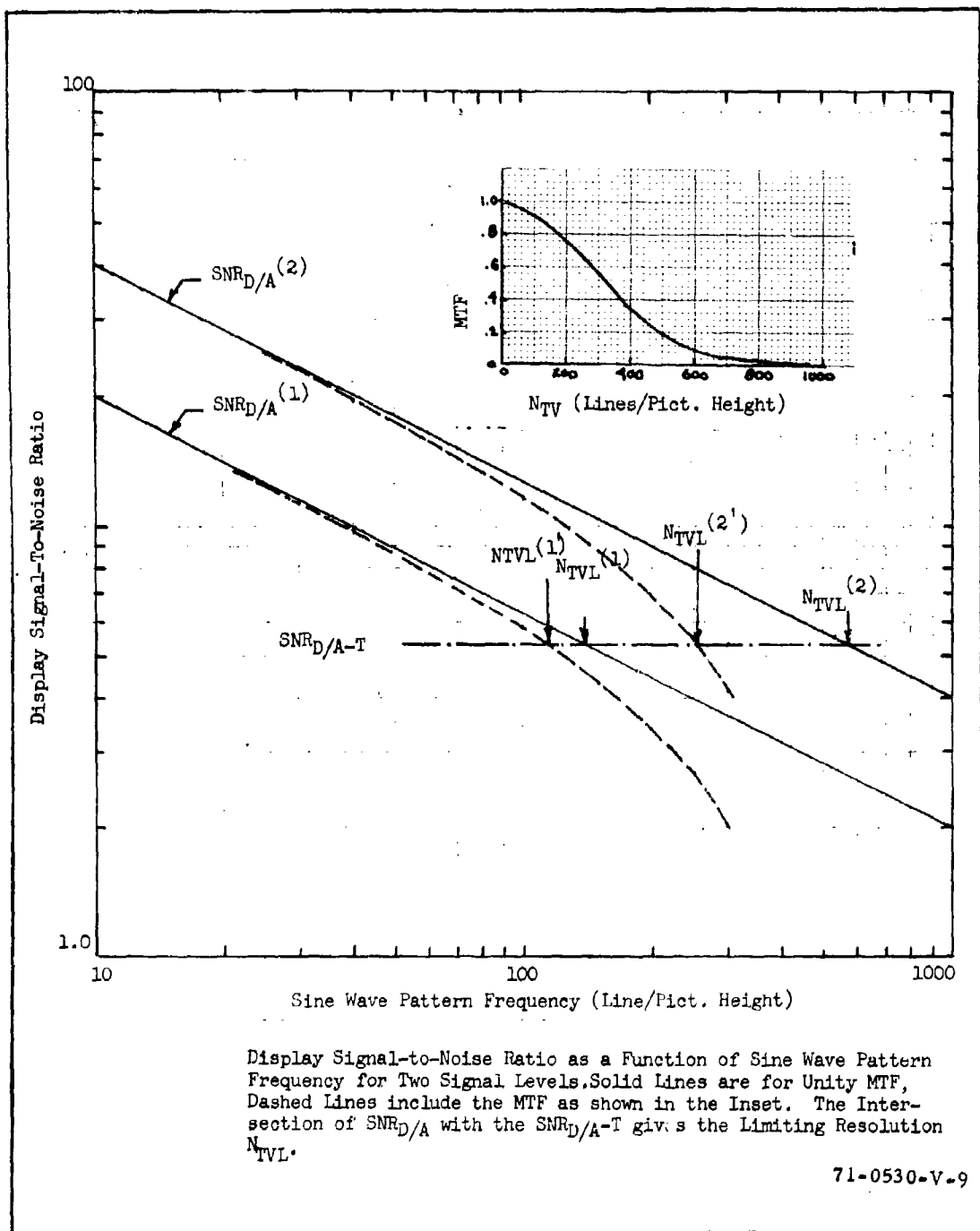


Figure 41. Display S/N Ratio as a Function of Sine Wave Pattern Frequency

reduced to 250 and 115 lines respectively by the assumed modulation transfer curve. Thus, the MTF has a strong effect on limiting resolution.

Next, the "per element" display signal-to-noise ratio is defined by

$$\text{SNR}_{D/E} = \left[t \Delta f_V / a \right]^{1/2} \frac{|R_o(N_{TV})|}{N_{TV}} \cdot \text{SNR}_{V,0,1} \quad (105)$$

and plotted on figure 42 for the same conditions as were used in figure 41.

For comparison, the $\text{SNR}_{D/A}$ of the latter figure is plotted on figure 42.

When $\text{SNR}_{D/E}$ is used, the threshold $\text{SNR}_{D/E-T}$ becomes 1.2. It can be readily seen that with unity MTF, equations 104 and 105 give widely different values for limiting resolution as can be seen in table V.

TABLE V
LIMITING RESOLUTION FOR TWO SIGNAL LEVELS USING
TWO DIFFERENT SNR_D MODELS

Signal Level	Area Model	Limiting Resolution (N_{TVI})		
		MTF = 1		Including MTF
		Element Model	Area Model	Element Model
1	140	115	112	105
2	580	275	250	210

However, when the MTF is included, the two models give results which are much closer together. When other effects are included such as the eye's aperture response, the results will probably be even closer.

That the two models give nearly the same result for sine wave bar patterns of constant height is a fortuitous result but not a correct one as we now believe. In this early stage of model development, we do not yet have sufficient data to define a "correct solution," but it is clear that in the interim, we must, as a minimum, specify the exact pattern parameters — its height as well as its spatial frequency.

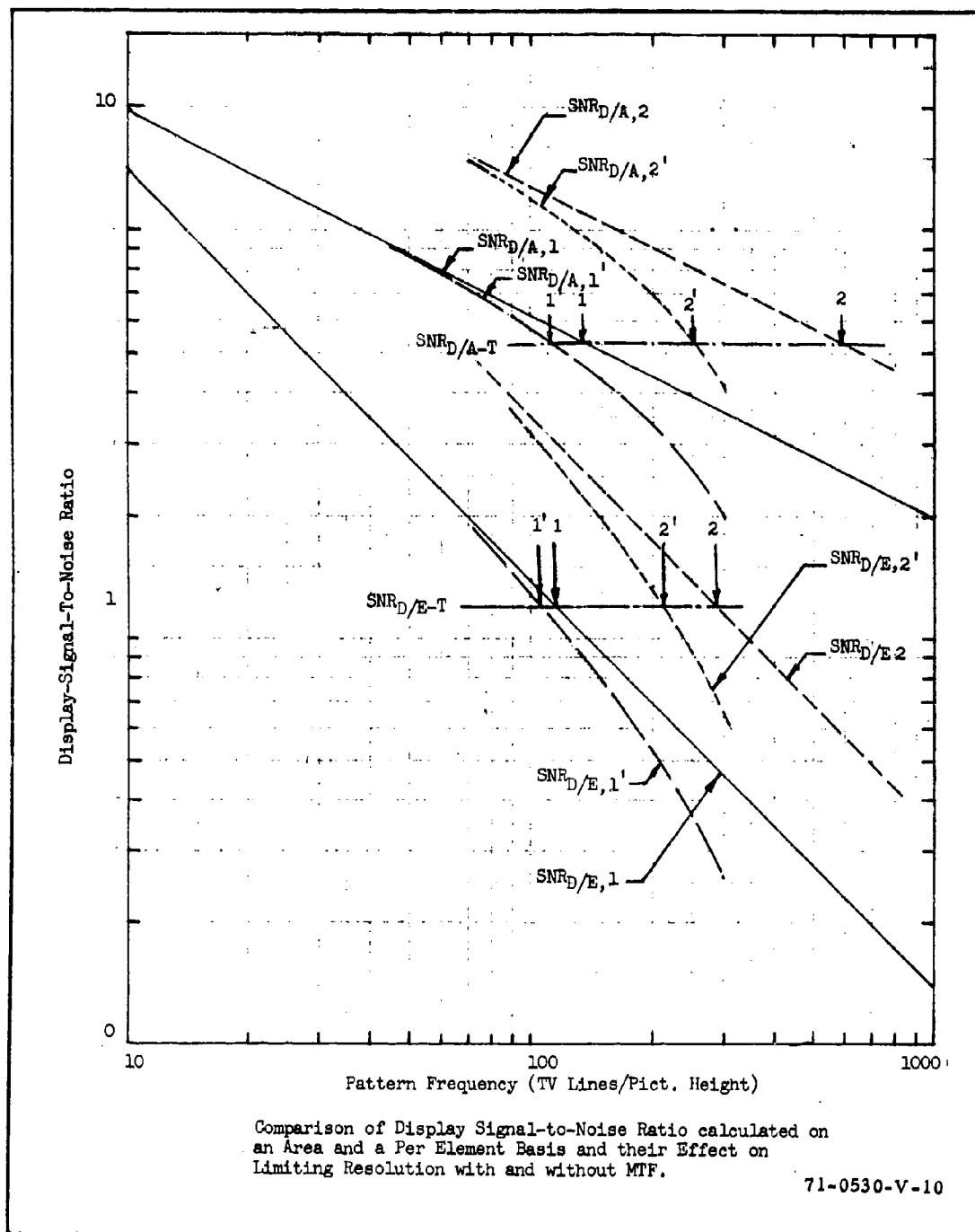


Figure 42. Comparison of Display S/N Ratio

Until we have further information to the contrary the preferred model will be the area model as exemplified by equation 104 for the calculation of the $SNR_{D/A}$ provided by the sensor. As we noted in the experiment, the threshold $SNR_{D/A-T}$ may not be a constant but may be a function of the visual subtense of the bars. However, this effect is an observer phenomena and should be kept separate from the sensor characteristics. Obviously, more work is needed in this area.

We next turn to the matter of MTF or modulation transfer function which is the primary method of describing the loss of resolving power due to finite sensor apertures. MTF, in the communications sense is synonymous with the magnitude of the sensor's complex steady state response $R_o(\omega)$ where,

$$R_o(\omega) = |R_o(\omega)| \exp [j \phi(\omega)] \quad (106)$$

In the above, $\phi(\omega)$ represents a phase or position shift and has been designated by the International Commission for Optics (ICO) as the phase transfer function. The ICO also refers to $R_o(\omega)$, the complex steady state response as the optical transfer function which seems only partially appropriate to sensors. The ICO recommends changing the word function to curve when referring to curves representing the functions. Also for specific values of the function at a given frequency, the word function is replaced by factor; e.g., the modulation transfer factor.

MTF is also synonymous with sine wave amplitude response. In the testing of sensors, sine wave amplitude response can be directly measured although the machinery required can be quite complex and costly. Thus, in current practice, it is more usual to employ bar patterns in making tests. The quantity measured is then the square wave amplitude response $|R_{SQ}(\omega)|$. If $R_o(\omega)$ is known, then $R_{SQ}(\omega)$ can be determined directly from

$$R_{SQ}(\omega) = Sq(\omega) \cdot R_o(\omega) \quad (107)$$

where $Sq(\omega)$ is the Fourier spectrum of a square wave wavetrain. As will be seen, the inverse operation

$$R_o(\omega) = \frac{R_{SQ}(\omega)}{Sq(\omega)} \quad (108)$$

cannot be performed because $Sq(\omega)$ is not a well behaved function.

Periodic functions such as an infinitely long train of square waves can be decomposed into a sum of simpler sine and cosine waves through the use of Fourier series. The trigonometric form of the Fourier series is given by,

$$f(x) = \frac{a_0}{2} + \sum_{n=-\infty}^{\infty} (a_n \cos 2n\pi k_1 x + b_n \sin 2n\pi k_1 x) \quad (109)$$

where

$$\frac{a_0}{2} = k_1 \int_{-x_0/2}^{x_0/2} f(x) dx_1 \quad (110)$$

$$a_n = 2k_1 \int_{-x_0/2}^{x_0/2} f(x) \cos 2n\pi k_1 x dx, \quad (111)$$

$$b_n = 2k_1 \int_{-x_0/2}^{x_0/2} f(x) \sin 2n\pi k_1 x dx_1 \quad (112)$$

$$\omega_1 = 2\pi k_1 = 2\pi/x_0. \quad (113)$$

Another form is the complex Fourier series,

$$f(x) = \sum_{n=-\infty}^{\infty} c_n \exp [j2n\pi k_1 x] \quad (114)$$

where

$$c_n = 2k_1 \int_{-x_{0/2}}^{x_{0/2}} f(x) \exp [j2n\pi k_1 x] dx \quad (115)$$

In both forms, the interval is implied to be $-x_{0/2} < x < x_{0/2}$. Also, if the series is to hold outside the interval, $f(x)$ must be periodic; i. e.,

$$f(x) = f(x + x_0).$$

The fourier transform of a periodic function written in the form of a Fourier series is found as follows:

$$\begin{aligned} F(k) &= \sum_{n=-\infty}^{\infty} c_n \int_{-\infty}^{\infty} \exp [-2\pi j(k - n k_1) x] dx \\ &= \sum_{n=-\infty}^{\infty} c_n \delta_0(k - k_1) \end{aligned} \quad (116)$$

This is recognized as a sum of impulses at integral multiples of the fundamental frequency with strengths or areas equal to the corresponding Fourier coefficients. The consistency of this result can be checked by taking the inverse transform to obtain

$$\begin{aligned} f(x) &= \sum_{n=-\infty}^{\infty} c_n \int_{-\infty}^{\infty} \exp [2\pi j k x] \delta_0(k - n k_1) dk \\ &= \sum_{n=-\infty}^{\infty} c_n \exp [2n\pi j k_1 x] \end{aligned} \quad (117)$$

If spatial frequency is expressed in terms of ω instead of k , similar reasoning will show that

$$F(\omega) = \sum_{n=-\infty}^{n=+\infty} c_n 2\pi \delta_0(\omega - n\omega_1) \quad (118)$$

The periodic square wave of figure 43 can be described either by the sine series

$$Sq(x) = \frac{4A}{\pi} \left[\sin 2\pi k_1 x - \frac{\sin 2\pi 3k_1 x}{3} + \frac{\sin 2\pi 5k_1 x}{5} - \dots \right] \quad (119)$$

if the origin is at $\frac{N_o}{2}$ or, by the cosine series

$$Sq(x) = \frac{4A}{\pi} \left[\cos 2\pi k_1 x + \frac{\cos 2\pi 3k_1 x}{3} + \frac{\cos 2\pi 5k_1 x}{5} - \dots \right] \quad (120)$$

If the origin is at 0', the Fourier transform $\mathcal{F}(sq(x)) = sq(k)$ can be found to be

$$Sq(k) = \frac{4A}{\pi} \left[\frac{\delta_o(R - R_1)}{2} + \frac{\delta_o(k + k_1)}{2} - \frac{\delta_o(k - 3k_1)}{6} - \frac{\delta_o(k - 3k_1)}{6} + \frac{\delta_o(k - 5k_1)}{10} - \frac{\delta_o(k - 5k_1)}{10} - \dots \right] \quad (121)$$

which is plotted in figure 44. The difficulty with equation 108 can now be visualized. $Sq(k)$ is zero nearly everywhere except at the harmonic frequencies $k_1, 3k_1, 5k_1$, etc. where it is infinite.

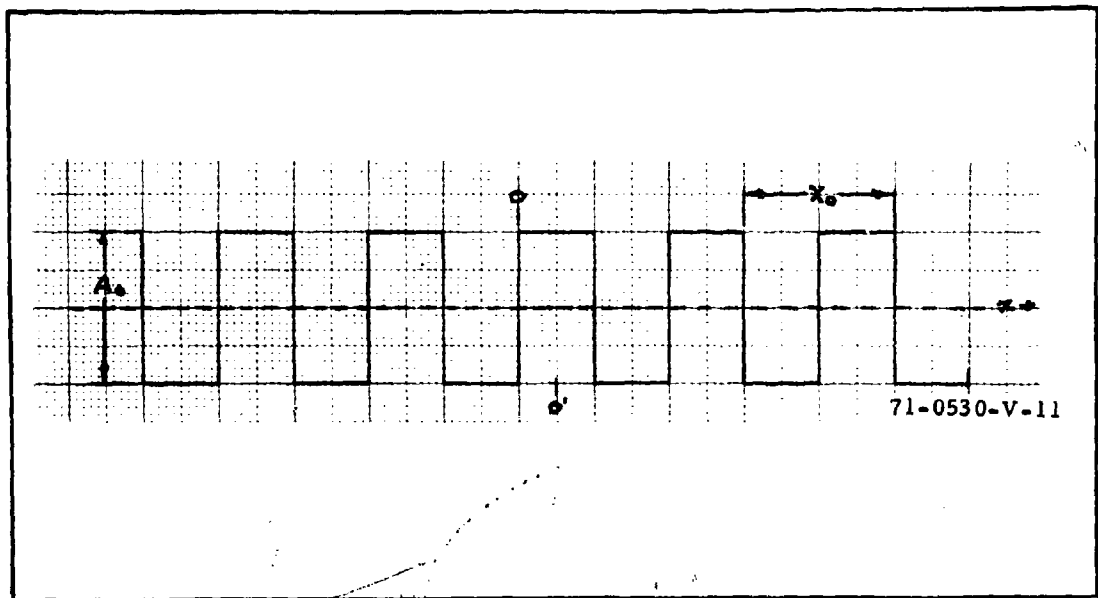


Figure 43. Periodic Sine Wave

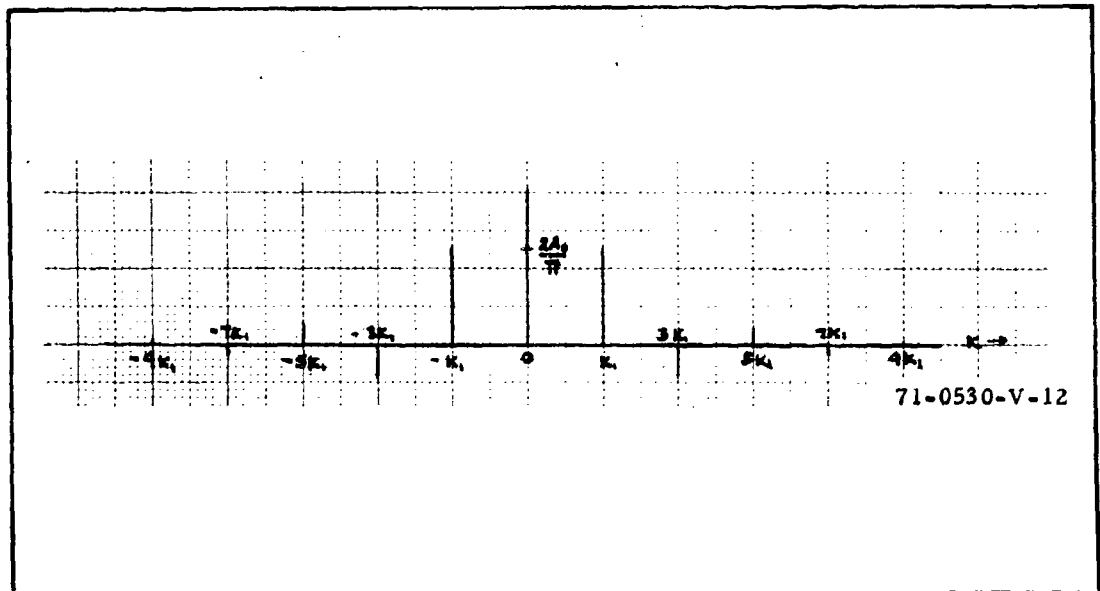


Figure 44. Fourier Spectrum of a Periodic Square Wave

We previously noted that if the complex frequency response $R_o(k)$ is known, we can find the complex square wave frequency response $R_{SQ}(k)$ from equation 102. The inverse of this equation is simply

$$g_{sq}(x) = \frac{4A}{\pi} \left[R_o(k_1) \cos 2\pi k_1 x - \frac{R_o(3k_1)}{3} \cos 2\pi 3k_1 x + R_o(5k_1) \cos 2\pi 5k_1 x - \dots \right] \quad (122)$$

The function $g_{sq}(x)$ is understood to mean the response of the devices to a square wave input of frequency k_1 .

Before proceeding, it is desired to note that the sensor's total complex frequency response $R_o(\omega)$ may be due to a number of apertures with response $R_{o1}(\omega)$, $R_{o2}(\omega)$, etc. If the apertures are linear, then

$$R_o(\omega) = R_{o1}(\omega) \cdot R_{o2}(\omega) \dots \quad (123)$$

Observe that,

$$\begin{aligned} R_{sq}(\omega) &= Sq(\omega) \cdot R_{o1}(\omega) \cdot R_{o2}(\omega) \dots \\ &= [Sq(\omega) \cdot R_{o1}(\omega)] \cdot R_{o2}(\omega) \dots \\ &= [Sq(\omega) \cdot R_{o2}(\omega)] \cdot R_{o1}(\omega) \dots \end{aligned} \quad (124)$$

which implies that the overall complex square wave response of a series of linear devices can be found by multiplying the sine wave responses of all but anyone of the devices with the complex square wave response of the remaining device.

Although the inverse process of finding the complex frequency response from the complex square wave response cannot be found directly, it is possible, according to Coltman¹⁷, to estimate it from the relation

$$\begin{aligned}
R_o(\omega) = \frac{\pi}{4} \left[R_{sq}(\omega) + \frac{R_{sq}(3\omega)}{3} - \frac{R_{sq}(5\omega)}{5} + \frac{R_{sq}(7\omega)}{7} \right. \\
+ 0 + \frac{R_{sq}(11\omega)}{11} - \frac{R_{sq}(13\omega)}{13} - \frac{R_{sq}(15\omega)}{15} \\
\left. + \frac{B_r R_{sq}(r\omega)}{r} \right] \quad (125)
\end{aligned}$$

In the general term, r , takes on the odd values 1, 3, 5, etc, and B_r is 1, 0, or -1 according to the formulas,

$$\begin{aligned}
B_r &= (-1)^m \cdot (-1) \cdot (k-1)/2 \quad \text{if } r = m \\
B_r &= 0 \quad \text{if } r < m
\end{aligned} \quad (126)$$

where m is the total number of primes into which k can be factored and r is the number of different prime factors in k .

Ordinarily, sensor manufacturers specify only the MTF or the square wave amplitude response $|R_{sq}(\omega)|$ in their catalogs. Given one, the other may be estimated. A third type of response, the square wave flux response function is favored by Schade for use in system performance calculations.²²

This concept is made necessary according to Schade, because the square wave amplitude response of a sensor bears no fixed relationship to the average value of flux in the half-waves of the variational flux as is the case with sine waves but instead depends on the harmonic components of the waveform.

For example, a typical output waveform given a square wave input is shown in the solid curve in figure 45. The equivalent square wave representing this output waveform is shown by the dashed curve. The square wave's amplitude is given by A_s , and the equivalent square wave flux amplitude is given by A_F in figure 45. Quantitatively, the square wave flux response is given by

$$R_{SQF}^{(k)} = \frac{8}{\pi} \sum_{n=0}^{\infty} \frac{1}{n} R_o(nk) \quad (127)$$

($n = 1, 3, 5, \dots$)

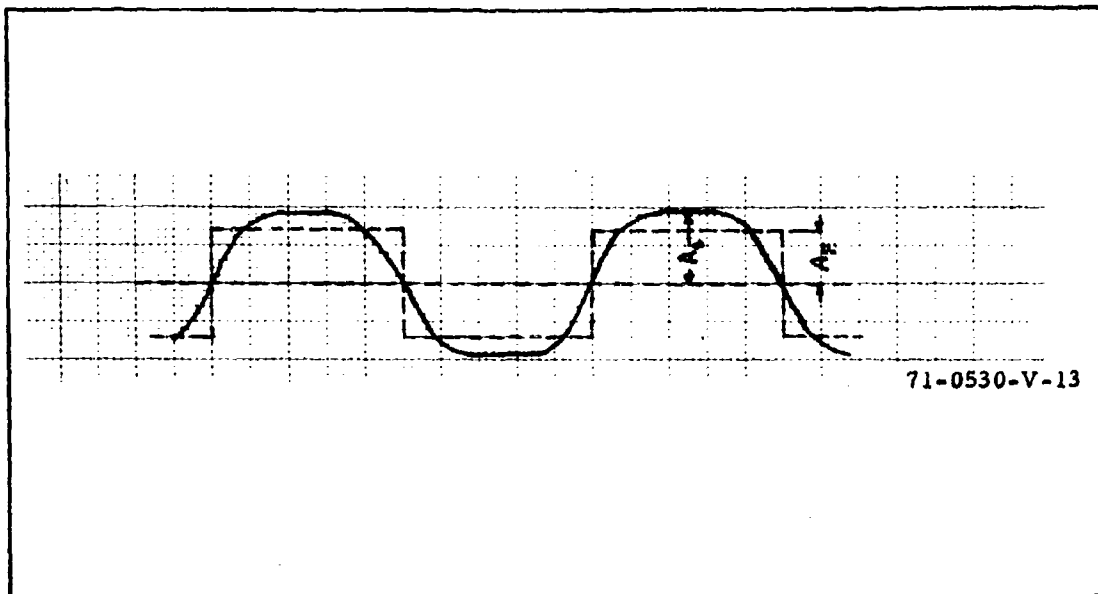


Figure 45. Equivalent Square Wave Flux Amplitude

where $R_o(nk)$ represents the values of the complex steady state frequency response at frequencies nk .

The relationships between the three types of responses are shown in figures 46 and 47. The square wave amplitude response is seen to be the highest while the square wave flux response is the lowest.

We next turn to the formulation of a model that, though it will require considerable modification and verification, represents the most accurate representation of the fundamentals of imaging as we know them and is felt to be the best point of departure for further model development. In the beginning of this model development, it is assumed that the input test pattern is a sine wave and that the sensor MTF is unity.

Recall that we have hypothesized that the eye uses only a single line, or line pair, in identifying a bar pattern. For this analysis, the displayed pattern is taken to be an infinitely long train of cosine waves in the x'

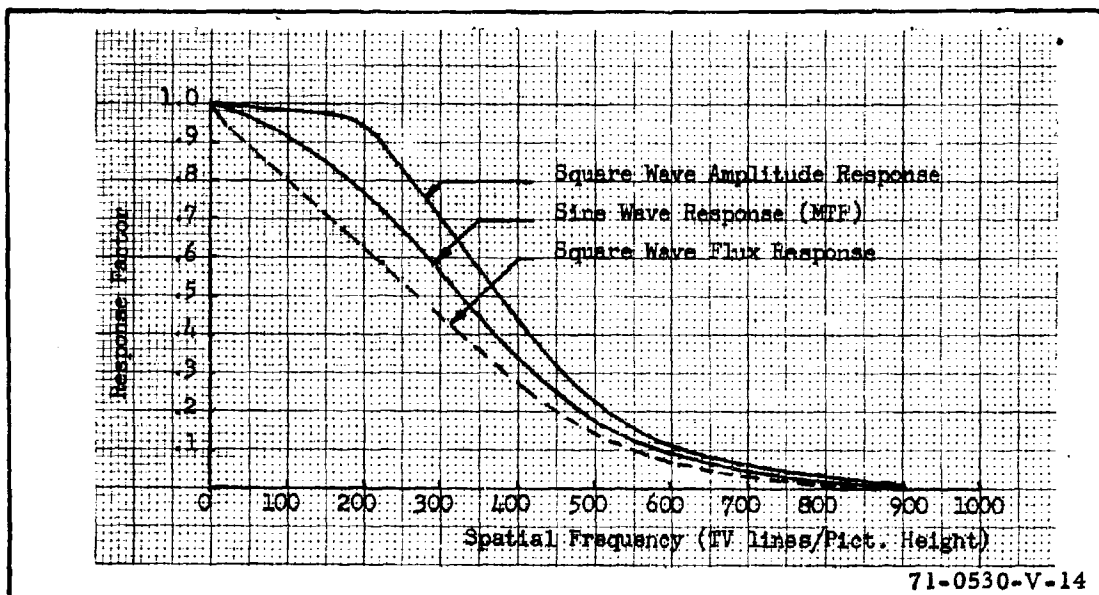


Figure 46. Relationship Between Various Sensor Response Factors for an Assumed MTF

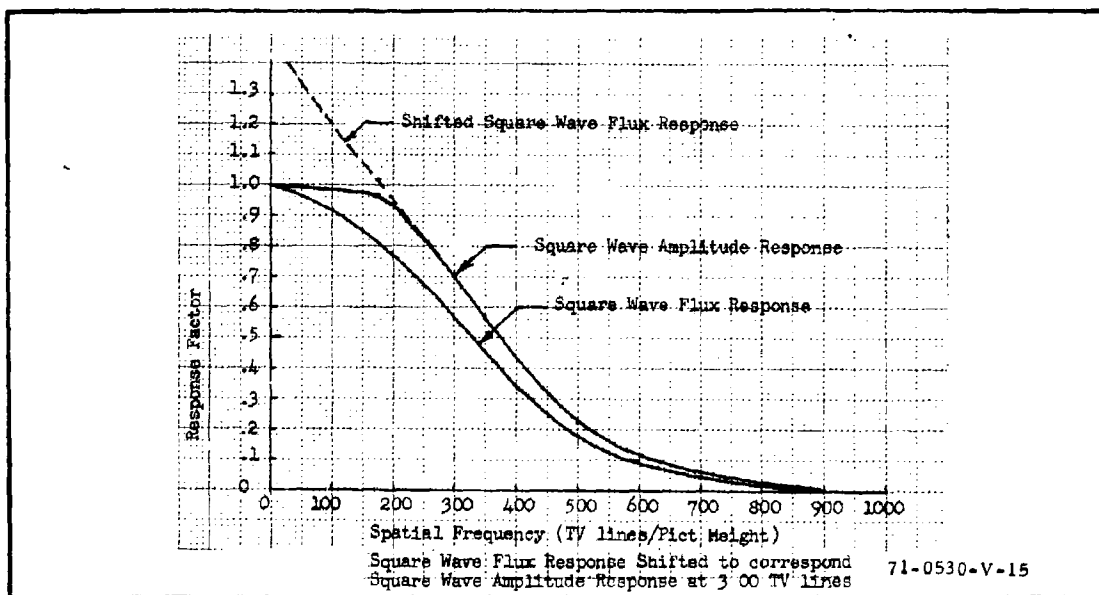


Figure 47. Relationship Between Various Sensor Response Factors

direction and a rectangle in the y direction, but only the single cycle shown in figure 48 is used for the pattern identification. Quantitatively, the waveform used by the eye will be assumed to be

$$g_o(x) = \begin{cases} 0 & -\infty < x < -x_o \\ 1/2 (1 + \cos \pi x/x_o) & -x_o \leq x \leq x_o \\ 0 & x_o < x < \infty \end{cases} \quad (128)$$

$$g_o(y) = \begin{cases} 0 & -\infty < y < -y_o/2 \\ 1 & -y_o/2 \leq y \leq y_o/2 \\ 0 & y_o/2 < y < \infty \end{cases} \quad (129)$$

and that

$$g_o(x, y) = g_o(x) \cdot g_o(y) \quad (130)$$

The basic $\text{SNR}_{D/A}$ expression to be used will be equation 9 rearranged to read,

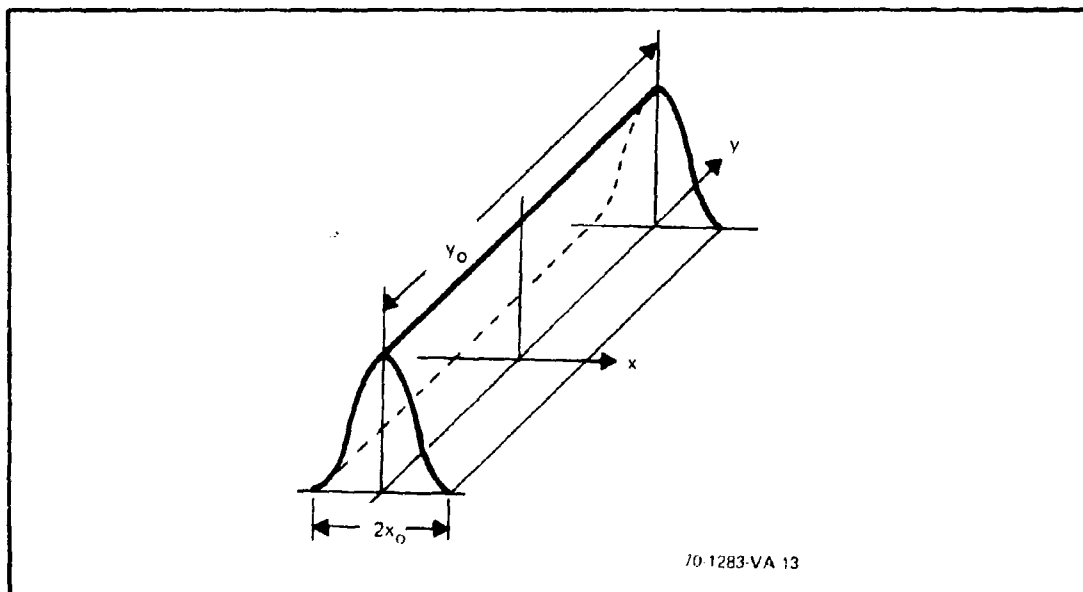


Figure 48. Portion of Wavetrain Assumed Used by the Eye to Recognize Wave Pattern

$$\text{SNR}_{D/A} = \left[\frac{t}{A} \right]^{1/2} \frac{C i_{\max} a}{\left[(2-C) i_{\max} a \right]^{1/2}} \quad (131)$$

$$= \left[\frac{t}{a Y^2} \right]^{1/2} \frac{C i_{\max} a}{\left[(2-C) i_{\max} a \right]^{1/2}}$$

where A, the effective photocathode area is equal to $a Y^2$ as previously noted. The area, a, in equation 131 will be treated according to the Fourier energy integral of equation 93. Thus,

$$a = \iint_{-\infty}^{\infty} g_o^2(x, y) dx dy \quad (132)$$

and because of the independence and separability assumption,

$$a = \int_{-\infty}^{\infty} g_o^2(x) dx \cdot \int_{-\infty}^{\infty} g_o^2(y) dy \quad (133)$$

The appeal of this formulation is that it is identical to that used for the aperiodic rectangle detection problem, that it eliminates the problem of deciding what to do about images that have both positive and negative components, that it treats signals and noise alike, that integration limits become fairly well defined, that it gives results that are in good agreement with those obtained by other investigators, and that the results predicted using this concept correlate well with measured results.

The result of applying equation 133 to equations 128 and 129 is that

$$a = 3 y_o x_o / 4$$

and equation 131 becomes

$$\text{SNR}_{D/A} = \left[\frac{t/a}{Y^2/x_o y_o} \right]^{1/2} \frac{0.75 C i_{\max}}{\left[0.75 (2-C) e^{i_{\max}} \right]^{1/2}} \quad (134)$$

Also, since $N_v = (Y/y_o)$ and $N_h = (Y/x_o)$ where N_v and N_h are expressed in TV lines per picture height, then

$$\text{SNR}_{D/A} = \left[\frac{t/a}{N_v \cdot N_h} \right]^{1/2} \frac{0.75 C i_{\max}}{\left[0.75 (2-C) e^{i_{\max}} \right]^{1/2}} \quad (135)$$

Suppose next that the sensor MTF is either unity in the y direction or that the image is so long in the vertical that it can be considered to be unity. In the x direction, let the MTF be $|R_o(N_h)|$. Then equation 135 is revised to read

$$\text{SNR}_{D/A} = \left[\frac{t/a}{N_v \cdot N_h} \right]^{1/2} \frac{0.75 C |R_o(N_h)| i_{\max}}{\left[0.75 (2-C) |R_o(N_h)| e^{i_{\max}} \right]^{1/2}} \quad (136)$$

The use of $|R_o(N_h)|$ in this form is somewhat unusual for sine wave inputs. It stems from the following reasoning. If the input image to a linear filter (or optical aperture) is a one-dimensional train of sine or cosine waves, then the output waveform will be a train of sine or cosine waves of identical spatial frequency but of reduced amplitude. The image waveshape weighting function, $g_o(x)$, remains unchanged. The effect of the aperture is decreasing the signal and mean square noise equally in the sampling area. However, in other cases, the waveshape is altered, as, for example, in the case of square wave (or bar pattern) image inputs.

For the case of a square wave input, suppose that the sensor MTF is unity once again. Also, let $g_o(y)$ be given by equation 128 as before, but $g_o(x)$ is,

$$g_o(x) = \begin{cases} 0 & -\infty < x < -x_o/2 \\ 1 & -x_o/2 < x < x_o/2 \\ 0 & x_o/2 < x < \infty \end{cases} \quad (137)$$

Proceeding as before, we find that

$$a = x_o y_o = Y^2 / (N_h \cdot N_v) \quad (138)$$

and

$$\text{SNR}_{D/A} = \left[\frac{t/a}{N_v \cdot N_h} \right]^{1/2} \frac{C i_{\max}}{\left[(2-C) e i_{\max} \right]^{1/2}} \quad (139)$$

(for square wave image inputs)

Thus, for a photoelectron-noise-limited sensor, the area form of the display signal-to-noise ratio is larger for a unit amplitude square wave image than for a unit amplitude sine wave by a factor of $1/(0.75)^{1/2}$, or 1.15, presuming both to be of equal spatial frequency. Intuitively, we would expect square waves to be more detectable.

To consider the effects of the MTF on a periodic square wave, we will first decompose the square wave input image to a series of sine waves, using the Fourier series representation

$$S_q(x) = \frac{4}{\pi} \sum_k \frac{\sin \pi k N_h x}{k} \quad (140)$$

$$k = 1, -3, -5, -7, 9, - \dots$$

where N_h is the spatial frequency of the square wave in half-cycles per picture height and is equal to

$$N_h = 1/x_o \quad (141)$$

for x_o measured in units of picture heights. If the sine wave response or MTF is given by $|R_o(N_h)|$, the square wave amplitude response may be written as

$$R_{SQ}(N_h) = \frac{4}{\pi} \sum_k R_o(N_h)/k \quad (142)$$

$$k = 1, -3, 5, -7, 9, - \dots$$

The MTF of a typical sensor is plotted in figure 49, along with the square wave amplitude response. The MTF curve is seen to cut off at $N_{hc} = 900$ TV lines. Referring to equation 40 we see that for spatial frequencies, N_h

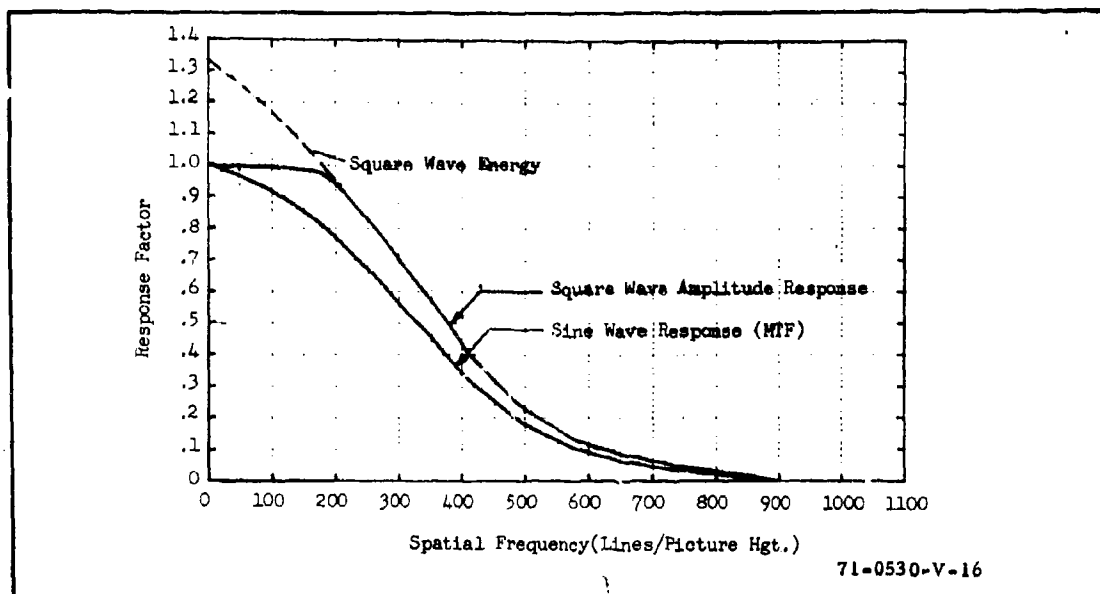


Figure 49. MTF, Square Wave Amplitude Response and Square Wave Energy Factor for a Typical Sensor

(larger than $N_{hc}/3$) the square wave response becomes a sine wave, and indeed, this result holds with fair accuracy down to spatial frequencies of $N_{hc}/4$ or $N_{hc}/5$. At these higher spatial frequencies, the square wave amplitudes are $4/\pi$ times the value of the MTF.

At lower spatial frequencies, the square wave amplitude response approaches unity. However, the square wave energy keeps increasing being $4/3$ that of a unit amplitude sine wave at zero frequency. This effect is shown as the dashed curve in figure 49. We see the following interesting result. At spatial frequencies above $N_{hc}/3$, a square wave input yields a sine wave output of amplitude $4/\pi$ times the input amplitude; below $N_{hc}/3$, the energy is about $4/3$ of that in a sine wave. Thus, we can treat the square wave as a sine wave but the square wave's equivalent amplitude will be higher by a factor of about $4/3$. Thus, we can use equation 136 modified slightly to read

$$\text{SNR}_{D/A} = \left[\frac{t/a}{N_v \cdot N_h} \right]^{1/2} \frac{C R_o(N_h) i_{\max}}{\left[(2-C) \left| R_o(N_h) \right| e i_{\max} \right]^{1/2}} \quad (143)$$

(for square wave inputs)

Equations 136 and 143 will be used to evaluate sensors in later sections.

BLANK PAGE

SECTION VI

LEVELS OF DISCRIMINATION

In the previous sections, various aspects of target detection were discussed, and equations were derived for calculating the display signal-to-noise ratio for detecting aperiodic laboratory targets such as squares and rectangles as well as periodic patterns such as bar patterns. It was shown that for a given detection probability that a specific value of display signal-to-noise ratio was required and that this value was independent of target size for aperiodic targets and line number for periodic patterns. To perform higher levels of target discrimination than detection, such as target recognition or identification, we would intuitively expect that higher signal-to-noise ratios will be needed since greater target detail must be discerned. Target detail can be expressed in terms of resolution lines through the target. In work by Johnson, a criterion has been set up which expresses image discrimination in terms of the number of lines through the minimum target dimension.²³ This criterion has been widely used. (Johnson's original data was in line pairs, but to be consistent with our symbology, we will use lines.)

Johnson has classified the levels of target discrimination as detection, orientation, recognition and identification; and his definition of each of these categories is listed in table VI. In table VII the required resolution in lines through the minimum target dimension are given for the various discrimination levels.

TABLE VI
LEVELS OF TARGET DISCRIMINATION

<u>Classification of Discrimination Level</u>	<u>Meaning</u>
Detection	An object is present
Orientation	The object is approximately symmetrical or unsymmetrical and its orientation may be discerned
Recognition	The class to which the object belongs may be discerned (e.g., tank, truck, man, etc).
Identification	The target can be described to the limit of the observer's knowledge (e.g., T-34 tank, friendly jeep, etc).

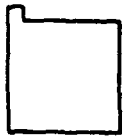
TABLE VII
JOHNSON'S CRITERIA FOR RESOLUTION PER MINIMUM
TARGET DIMENSION

<u>Discrimination Level</u>	<u>Resolution per Minimum Target Dimension (TV Lines)*</u>	
Detection	2	+1.0 -0.5
Orientation	2.8	+0.8 -0.4
Recognition	8.0	+1.6 -1.4
Identification	12.8	+3.2 -2.8

* Plus and minus values taken from the maximum spread in the data from Johnson's Table I.

In Section II it was shown that $(\text{SNR})_D$ is calculated on the basis of the total area of the square or rectangle for detecting an isolated square or rectangle. In Section V it was shown that in detecting periodic patterns, such as bar patterns, essentially the same model held as that for aperiodic targets if $(\text{SNR})_D$ is calculated on the basis of the total area of a single bar. Furthermore, the detection of a single bar in a bar pattern, with a higher $(\text{SNR})_D$ than that required for an isolated bar, corresponded to detection of the bar pattern, which is a higher order visual task than just detection of an isolated square or rectangle. It seems reasonable, therefore, to calculate $(\text{SNR})_D$ on the basis of the area of a bar which corresponds to the visual discrimination level and this will be done in the following. In the cases where the resolution across the minimum target dimension is not known, we will assume that Johnson's data applies. Indeed, it will be shown that for recognition of tanks and trucks that our data for the required $(\text{SNR})_D$ calculated on the basis of the area of a resolution rectangle (as in the bar pattern case), is consistent with Johnson's resolution criteria. In the following, some preliminary experiments will be discussed with a view toward determining some insight into the interrelation between target discrimination, resolution, and $(\text{SNR})_D$.

The first experiment, requiring a higher level of discrimination than detection, utilized two touching squares as shown in figure 50. Two sizes of large squares were used, 16×16 and 8×8 raster lines. With the largest square (16×16), three small squares were used 2×2 , 4×4 , and 8×8 as shown in figure 50a, whereas for the smaller of the large squares (8×8), two small squares were used, 2×2 and 4×4 , as shown in figure 50b. The number of bars through the target dimension was calculated by dividing the width of the large square by the width of the small square and these values are listed in table VIII as numbers of bars through the target dimension. For the experiment, the position of the small square was randomly varied, and the subject was asked to say where the small square was. Even if he



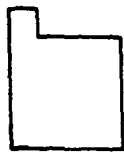
A) SMALL SQUARE ON LARGEST SQUARE
SMALL SQUARE: RASTER LINES HIGH

2

4

8

LARGE SQUARE: RASTER LINES HIGH
16



B) SMALL SQUARE ON LARGE SQUARE
SMALL SQUARE: RASTER LINES HIGH

2

4

LARGE SQUARE: RASTER LINES HIGH
8



70-1308-VB-5

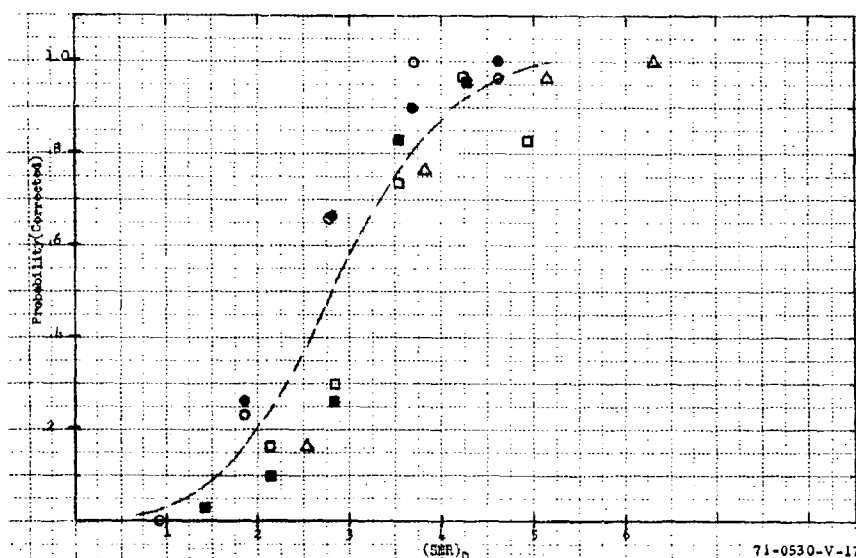
Figure 50. Geometry for Two Square Experiment

TABLE VIII
NUMBER OF BARS THROUGH TARGET FOR VARIOUS TARGETS

<u>Large Square Size</u>	<u>Small Square Size</u>	<u>Number of Bars Through Target Dimension</u>
16 x 16	2 x 2	8
16 x 16	4 x 4	4
16 x 16	8 x 8	2
8 x 8	2 x 2	4
8 x 8	4 x 4	2

didn't know, he was asked to guess. The probability was then corrected for chance. For the largest square case (figure 50a), a total of 600 data points were taken, whereas for the smaller larger square case (figure 50b), 500 data points were taken. For each experiment, five subjects were used and each subject was run through the experimental conditions twice. $(\text{SNR})_D$ was calculated for a bar of width equal to the width of the small square and of length such that the area of the bar times the number of bars through the target dimension was equal to the total area of the target. In the following, rectangles of this type will be called resolution rectangles. Before proceeding, it will be useful to determine the resolution rectangle for a particular target to further clarify our definition. Specifically, consider the target to consist of the large square (16 x 16 lines) with the medium size square (4 x 4 lines) on it. The width of the resolution rectangle is 4 (16 divided by 4) and the length, L , is 17 ($4 \times 4 \times L = (16)^2 + (4)^2$).

In figure 51 the results of the experiment are shown as corrected probability versus $(\text{SNR})_D$, calculated for a resolution rectangle, and it is seen that to a good approximation (± 10 percent at the 50 percent probability point) that the dashed curve fits the data independent of resolution. The dashed curve was calculated using the probability model which was derived for the detection of squares in Section II with $(\text{SNR})_{D/T} = 2.8$. Thus, for this experiment, the specification of the threshold $(\text{SNR})_D$ value, together with



71-0530-V-17

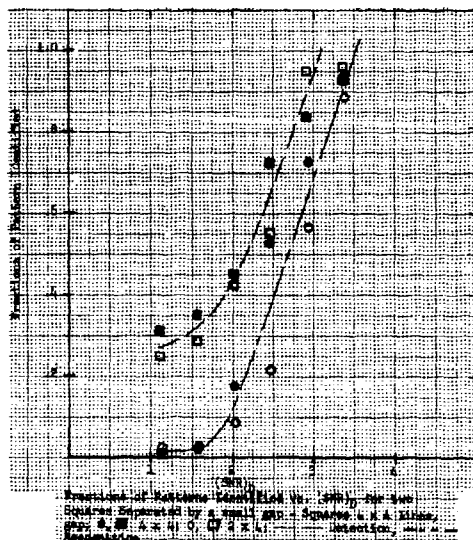
Figure 51. Probability of Recognition Versus $(SNR)_D$ for Square on Square

Δ 2 x 2 on 16 x 16, 8 Resolution Rectangles; ● 4 x 4 on 16 x 16, 4RR;
○ 2 x 2 on 8 x 8, 4RR; □ 8 x 8 on 16 x 16, 2RR; ■ 4 x 4 on 8 x 8, 2RR

the number of resolution rectangles, completely specify the conditions necessary for recognition of the target. The word "recognition" was put in quotation marks because the visual level of discrimination here is different than that used by Johnson. By recognition Johnson meant determining the class of the target. Here, the subject was asked to determine where the small square was, and the visual level of discrimination using Johnson's criteria was smaller for some of the targets than others. Indeed, visual level of discrimination as specified by lines of resolution is the highest for the target with the smallest and largest squares (8 lines resolution), and the visual level of discrimination was the smallest for the target with the largest of the small squares (the resolution was 2 lines). Nevertheless, over this resolution range, $(SNR)_D$ per resolution rectangle was constant. Furthermore, the threshold value of $(SNR)_D$ per resolution rectangle at the higher

discrimination levels is the same as that required for detection of an isolated single square or rectangle.

A second series of experiments were performed with two squares, each 4 x 4 raster lines but separated by a gap of either 4 x 4 or 2 x 4 lines. The target was put in one of four quadrants and the subject was asked to detect the target (that is, say where the target was) and to discriminate at a higher level by saying if he could see the two separate squares. The pattern was always present so chance, at the higher level of discrimination, could not be corrected for. The experimental results are shown in figure 52 as fractions of patterns identified versus $(SNR)_D$ per resolution rectangle (per square in this case) for target detection and for target recognition. Over the whole range for recognition, the influence of the smaller gap (2 x 4) was to require larger $(SNR)_D$ values for a given fraction of patterns identified than that for the larger gap (4 x 4). The variation about the average was less than the experimented error and only one curve has been drawn through the data. For target detection with 2/3 of the $(SNR)_D$ values, the smaller gap



71-0530-V-18

Figure 52. Fractions of Patterns Identified Versus $(SNR)_D$

corresponded with larger $(\text{SNR})_D$ values. It should be noted that for detection $(\text{SNR})_D$ was calculated on the basis of the area of a resolution rectangle that was appropriate for recognition instead of using the total area of the target which makes more sense for detection. The use of the same resolution rectangle area in the two cases allows one to plot the data for detection and recognition on the same scale and for this reason it has been done.

A third set of experiments was performed using a 1-1/2-inch-diameter, 826-line vidicon camera to generate the target video signal. The signals were added as in the previous experiment and filtered by an 11.6-MHz bandwidth filter. The target consisted of a rectangle 0.28 x 0.15 inch with 9 bars from a 500-line pattern inscribed across the minimum dimension. Four transparencies were made, each with the rectangle in a different quadrant. The picture height, as viewed by the camera was 6.4 inches. The subject was asked if he could see the individual bars. The pattern was always there and no correction was made for chance. For the experiment, there were 5 subjects and 5 $(\text{SNR})_V$ values, and the target was placed randomly in 1 of 4 quadrants. Each subject was run through the experimental conditions 3 times which yielded a total of 300 data points. As in the previous experiment, $(\text{SNR})_D$ was calculated using the area of a resolution rectangle, one of the bars in this case.

The results of the experiment are shown in figure 53 as fractions of patterns identified versus $(\text{SNR})_D$ using the area of the resolution rectangle as the area in the $(\text{SNR})_D$ calculation. In Section V, it was postulated that an $(\text{SNR})_D$ value of 5.3 for a single bar of a bar pattern would be appropriate for detecting the bar pattern where detecting the bar pattern was taken to mean resolving individual bars. The value of 5.3 corresponded to a near 100 percent probability of detecting an isolated bar. In the present experiment, the bar pattern consisted of 9 bars, and the threshold value of $(\text{SNR})_D$ for a single bar is seen, from figure 53, to be 4.6. This value is

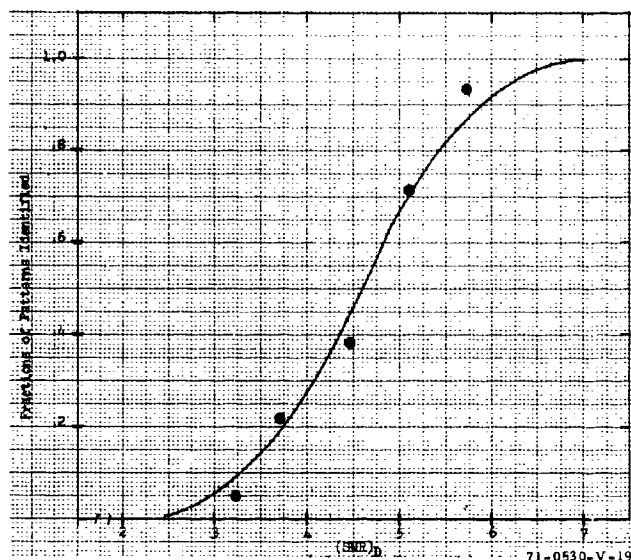


Figure 53. Fractions of Patterns Identified Versus $(SNR)_D$ for Rectangles With Nine Inscribed Bars

within 13 percent of the predicted value, and within experimental accuracy is consistent with 5.3.

If the value of $(SNR)_D$ for a resolution rectangle is a constant, independent of the number of bars in the pattern, then we would have the same value of $(SNR)_D$ for an 8-bar pattern. The theory of Section V indicates that this is, in fact, the case, and the value of $(SNR)_D = 4.6$ obtained here for the 9-bar pattern will be used for comparison with that obtained for recognition of lower resolution targets.

The last experiment that will be discussed in this section utilized real-world-like images. High-quality photographs were taken of models of a tank, a van truck, a half-truck with a radar antenna on top, and a derrick-bulldozer on a tread base. The area of each was adjusted to be approximately equal to that of the rectangle with the inscribed bars. Each target was randomly placed in one of four quadrants, and 6 $(SNR)_V$ values were used for each.

As before, 5 subjects were used and each subject went through the experimental conditions twice giving a total of 960 data points. Each subject was asked to say which target he saw and in which quadrant he saw it. In every case the subject gave the correct quadrant response.

The results of the experiment are plotted in figure 54 as corrected probability versus $(SNR)_D$. Johnson's required resolution for recognition was used; that is, it was assumed that 8 bars are required through the minimum target dimension and the area used in calculating $(SNR)_D$ was that of a single bar of an 8-bar pattern whose area is equal to the target area.

From figure 54 it is seen that the threshold value of $(SNR)_D$ is 5.0. This value is within 6 percent of the assumed value of 5.3, and, furthermore, it is within 8 percent of that determined in the previous experiment of the rectangle with the inscribed bars. This is well within the experimental accuracies of the two experiments. Thus, to within the accuracies of the experiments, the same $(SNR)_D$ value is required to recognize a truck from

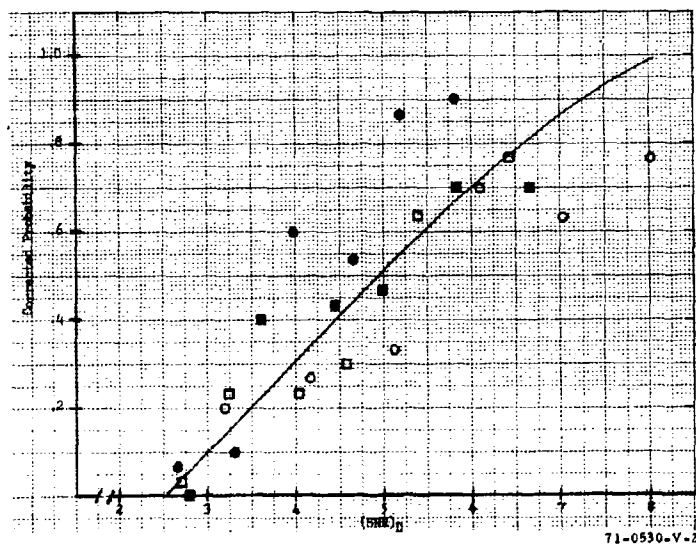


Figure 54. Probability of Recognition Versus $(SNR)_D$ for ● Truck, ○ Tank, ■ Derrick, □ Radar Truck

a tank, etc, as is required in order to be able to see individual bars in a 9-bar pattern of the same area. This would suggest that one could work with segments of bar patterns to model real-world targets in laboratory tests, but much more work must be done to confirm or deny this. Further experiments should be done with more real-world targets and with bar patterns of different numbers of bars. Also, the accuracy of the experiment should be increased.

BLANK PAGE

SECTION VII

DISPLAY LIMITATIONS

7.1 INTRODUCTION

It has become ever more evident that the eye can become limited by an electro-optical sensor's cathode ray tube display luminance, and that this effect does impact on the performance of certain systems. To illustrate the plausibility of this limitation, we first consider the principle of display operation as shown in figure 55. Ordinarily, there are two controls used by the observer in adjusting the CRT's operating point. The first is the "brightness" control which adjusts the average level of display luminance β . The second control is usually referred to as a contrast control, but is actually a video gain control. This is not a complete misnomer, however, since this control determines the swing of the display luminance about the steady state luminance, β_0 , and, therefore, increases or decreases the contrast of the displayed image.

In the analysis of imaging sensor performance, we ordinarily assume that the operator is limited only by the image's signal-to-noise ratio as established by the sensor and not by display brightness nor viewing distance. However, a fluctuation noise is associated with the display's background brightness and if video gain is sufficiently reduced, the signal will fall below the fluctuation noise. In this case, the observer will be said to be display-luminance-fluctuation-noise limited rather than sensor noise or photoelectron-noise limited.

Ordinarily, the operator would not turn the gain down to the point where the signal falls below the fluctuation noise, but a situation can arise where it becomes a necessity. For example, when the scene high light-to-low

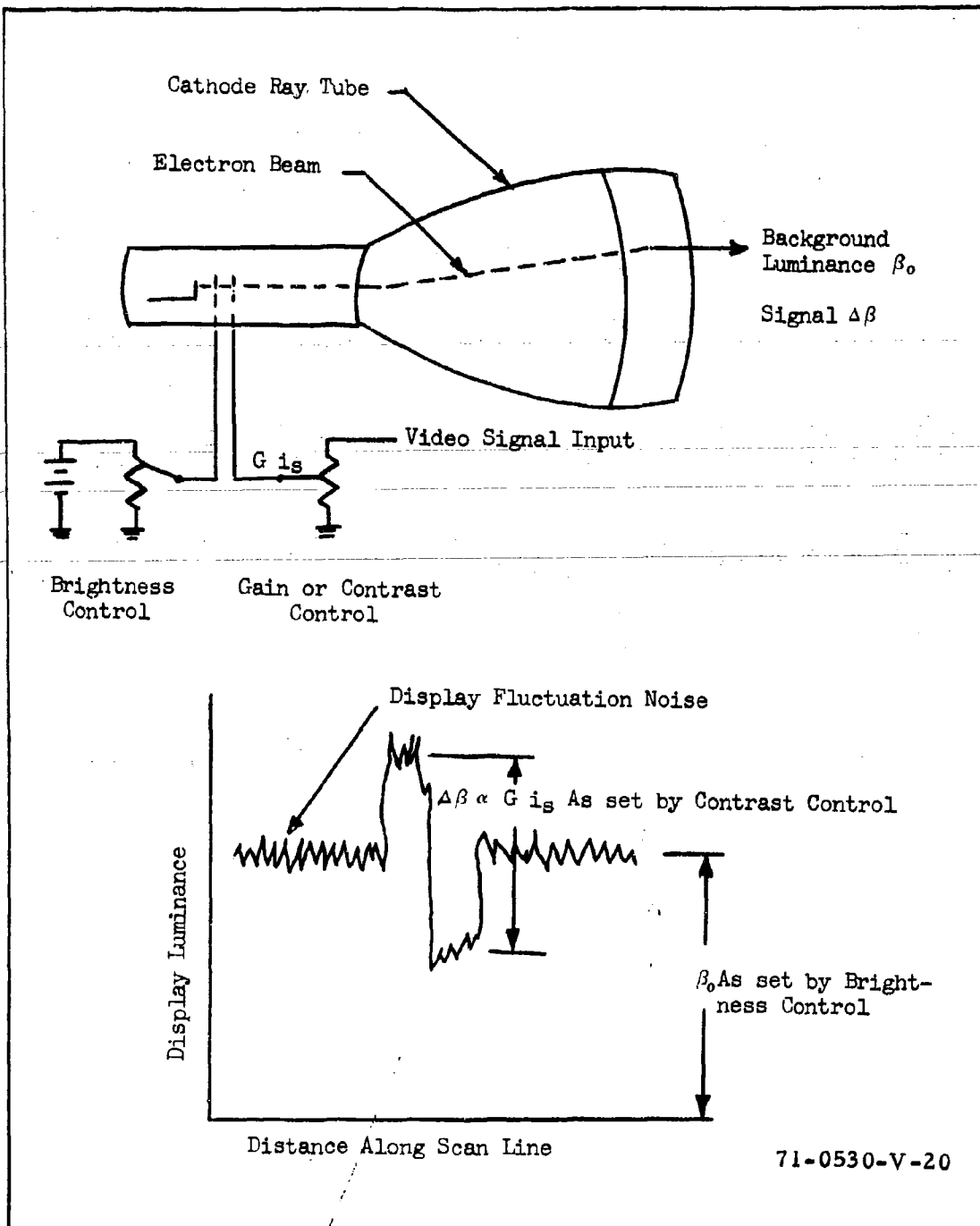


Figure 55. Effect of Display Controls on Output Image Brightness and Contrast

light irradiance range becomes very large, the operator may first need to increase (or decrease) average display brightness and then decrease gain to keep the highlight signals within bound. In this way, the small signals which were previously detectable may now drop below the display noise fluctuations.

In the following analysis, it will be assumed that the gamma of the display is unity. Many simplifying assumptions regarding the eye will be made for which revision will most certainly be needed as our understanding improves.

7.2 THE FLUCTUATION-NOISE-LIMITED EYE

The incremental signal at the output of the eye's retinal photo process is assumed to be

$$S_R = q (\dot{P}_{\max} - \dot{P}_{\min}) t \quad (144)$$

where q is the retinal conversion efficiency in sensory impulses per photon (or trolands), \dot{P}_{\max} and \dot{P}_{\min} are the high-light and low-light photo rates per second per "resolution" area, and t is the sampling period or integration time of the observer. A fluctuation noise will be assumed to be associated with the primary photoprocess whose magnitude is equal to

$$N_R = \left(q (\dot{P}_{\max} + \dot{P}_{\min}) t / 2 \right)^{1/2} \quad (145)$$

Recalling that the image contrast was defined as

$$C = \frac{\dot{P}_{\max} - \dot{P}_{\min}}{\dot{P}_{\max}} \quad (146)$$

and letting \dot{P}_o be the average photon rate,

$$\dot{P}_o = \frac{\dot{P}_{\max} + \dot{P}_{\min}}{2} \quad (147)$$

we may then write the retinal signal-to-noise ratio as

$$SNR_R = \frac{C \dot{P}_{\max} q t}{(\dot{P}_o q t)^{1/2}} \quad (148)$$

Now write the retinal flux in terms of the retinal illumination, E_{ro} , and the resolution element area A_r , as

$$\begin{aligned} \dot{P}_o &= E_{ro} A_r \\ &= \frac{E_{ro}}{4 N_{LP}^2} \end{aligned} \quad (149)$$

where A_r is assumed to be a square of dimensions $(1/(2 N_{LP}))^2$. Here, N_{LP} is expressed in line pairs/mm which is a common description of spatial resolution.

We have that the SNR_R relation is

$$SNR_R = \frac{C \dot{P}_{max} q t}{\left(q t \frac{E_{ro}}{4 N_{LP}^2} \right)^{1/2}} \quad (150)$$

For small contrasts, $\dot{P}_o \approx \dot{P}_{max} \approx \dot{P}_{min}$ and the retinal signal-to-noise ratio is

$$SNR_R = \frac{C \left(E_{ro} / (4 N_{LP}^2) \right) q t}{\left(E_{ro} q t / (4 N_{LP}^2) \right)^{1/2}} \quad (151)$$

The retinal illumination E_{ro} can be related to scene luminance for objects of large angular extent as

$$E_{ro} = \tau \delta^2 \beta_o / (4 F_L^2) \quad (152)$$

where τ is the transmission of the eye's lens and δ is its iris opening in mm, β_o is the average scene luminance in foot-lamberts and F_L is the eye's equivalent focal length in air (in mm).

To evaluate equation 152 numerically, we assume that the display is a 5400°K blackbody (essentially white). One lumen of this source is equivalent

to a photon rate of 1.3×10^{16} per second.²⁴ Using a value of 17 mm for the eye's equivalent focal length in air, we see that

$$E_{ro} = \frac{\beta_o \tau \delta^2}{4(17 \text{ mm})^2} \frac{\text{lumens-ft}^2}{\text{ft}^2 144 \text{ in.}^2} \frac{\text{in.}^2}{645 \text{ mm}^2} \frac{1.3 \times 10^6 \text{ photons}}{\text{lumen-sec}} \quad (153)$$

$$= 1.19 \times 10^8 \beta_o \tau \delta^2 \text{ photons/m}^2\text{-sec}$$

Inserting these results in equation 150,

$$\text{SNR}_R = \frac{t^{1/2} C (1.19 \times 10^8 \beta_o \tau \delta^2 q)}{2 N_{LP} (1.19 \times 10^8 \beta_o \tau \delta^2 q)^{1/2}} \quad (154)$$

In the above discussion, a broad area image was specified. Of course, as the image becomes smaller and more detailed, the apertures (MTF) distort the image in both amplitude and shape. The effects of apertures were discussed, for electro-optic sensors, in sections IV and V, and it will be assumed here that the same model used in those sections applies for the eye. Thus, using n_v as the length to width ratio of a single bar of a bar pattern and $R_o(N)$ the MTF of the eye we may then write equation 152 for bar patterns, as

$$\text{SNR}_R = \frac{(tn_v)^{1/2} R_o(N_{LP})^{1/2} C (1.19 \times 10^8 \beta_o \tau \delta^2 q)}{2 N_{LP} (1.19 \times 10^8 \beta_o \tau \delta^2 q)^{1/2}} \quad (155)$$

For a first estimate, we will let $\tau q t = 5 \times 10^{-3}$, $\text{SNR}_R = 5.3$ and $n_v = 7$.

For low-contrast images we thus have that

$$\text{SNR}_R = \frac{n_v^{1/2} C R_o(N_{LP})^{1/2} 385 \delta \beta_o^{1/2}}{N_{LP}} \quad (156)$$

and solving for the contrast we obtain

$$C = \frac{\text{SNR}_R N_{LP}}{n_v^{1/2} R_o(N_{LP})^{1/2} 385 \delta \beta_o^{1/2}} \quad (157)$$

The iris diameter, δ , is a function of β_o , the display luminance as shown in Table IX.

TABLE IX
IRIS DIAMETER VERSUS SCENE LUMINANCE

Scene Luminance Foot-Lamberts	Iris Diameter (mm)	(mm) ²
1×10^{-6}	7.1	50.2
4×10^{-6}	7.1	50.2
1×10^{-5}	7.0	49.1
4×10^{-5}	6.86	47.2
1×10^{-4}	6.7	45.0
4×10^{-4}	6.55	41.9
1×10^{-3}	6.34	40.2
4×10^{-3}	5.95	35.4
1×10^{-2}	5.7	32.4
4×10^{-2}	5.33	28.4
1×10^{-1}	5.1	26.0
4×10^{-1}	4.66	21.8
1	4.35	19.0
4	3.94	15.5
10	3.6	13.0
40	3.04	9.3
100	2.76	7.62
400	2.34	5.47
1,000	2.11	4.47

Before proceeding, it is useful to derive a relation between the spatial frequency N_{LP} on the retina of the eye to the displayed image frequency N_{TV} lines/picture height and then to determine the MTF of the eye in terms of N_{TV} . Suppose that the eye is viewing a television screen of vertical height V at a distance of d . Let the displayed pattern be a sine wave pattern

with spatial frequency N_{TV} lines (or half cycles) per picture height. Then the angular subtense of one line at the eye will be approximately

$$\Delta\theta = \frac{V}{N_{TV} d} \quad (158)$$

On the observer's retina, the corresponding angle is

$$\Delta\theta = \frac{\Delta y}{F_L} \quad (159)$$

Where Δy is the dimension of 1/2 cycle of the pattern, and F_L is the equivalent focal length of the eye in air (17 mm). Resolution on the eye's retina is ordinarily expressed in terms of N_{LP} line pairs/mm where

$$N_{LP} = \frac{1}{2\Delta y} \quad (160)$$

and thus

$$\Delta\theta = \frac{1}{2 N_{LP} F_L} = \frac{V}{N_{TV} d} \quad (161)$$

and

$$N_{TV} = \frac{V}{d} 2 N_{LP} F_L \quad (162)$$

The sine wave response of the eye as given by Campbell²⁵ is shown in figure 56 as a function of pupil diameter and pattern resolution. Pupil diameter was listed as a function of scene luminance in table IX. Normal display viewing luminances are between 0.1 to 100 foot-lamberts which means that pupil diameter will vary from about 2.8 to 5.1 mm. Suppose next that the display height is 8 inches, and the viewing distance is 28 inches. The equivalent focal length of the eye in air is 17 mm as previously noted so we have that

$$N_{TV} = \frac{8}{28} \cdot 2 \cdot 17 N_{LP} = 9.7 N_{LP} \quad (163)$$

which is the relation between TV lines on the display and line pairs per mm on the retina. With this relationship, we can replot the sine wave response of the eye as a function of display pattern resolution and this was done for figure 57.

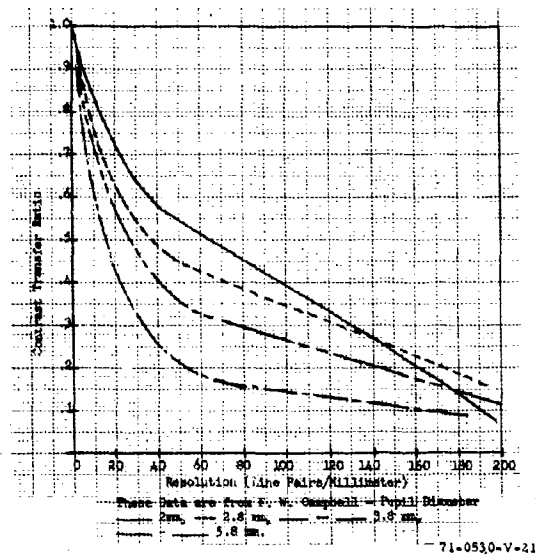


Figure 56. Contrast Transfer Function for an Infocus Eye

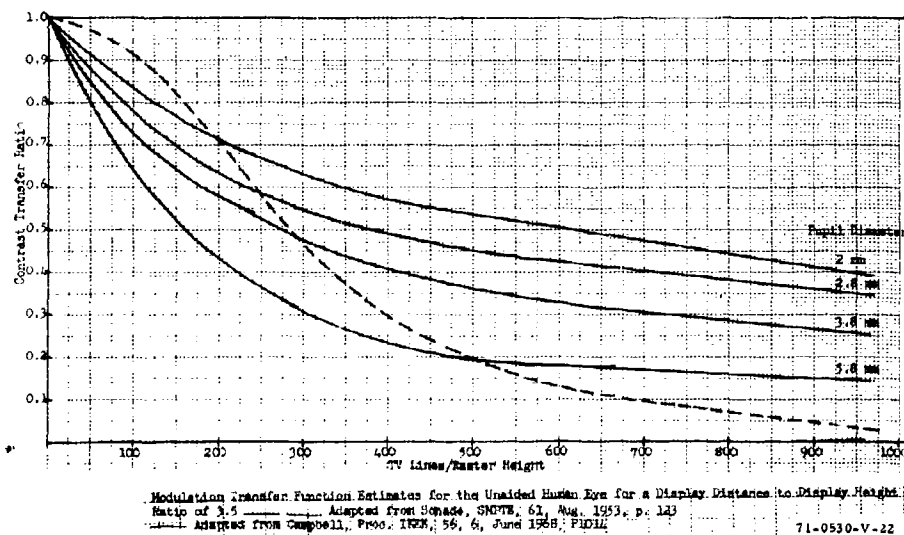


Figure 57. Modulation Transfer Function Estimates for the Unaided Human Eye

Also shown for comparison purposes is the curve assumed by Schade²⁵ which, in general, has higher response at low line numbers and lower response at the higher numbers. Schade's curves were said to correspond to average field luminances of 4 to 10 foot-lamberts. Note that Schade's curves were corrected for the d/V ratio of 3.5 rather than 4.0 as used in his paper.

We can now write the contrast equation 157 in terms of N_{TV} as

$$C = \frac{SNR_R N_{TV} d}{\left(n_v^{1/2} 34 V \cdot 385 \beta_o^{1/2} R_o (N_{TV})^{1/2} \right)} \quad (164)$$

and using $SNR_R = 5.3$, $n_v = 7$, $V = 8$ inches and $d = 28$ inches, we can calculate the minimum detectable contrast as a function of display brightness and this was done, for two brightness values, 0.41 and 32 foot-lamberts, and the results of the calculation are plotted in figure 58.

For comparison some results obtained by Schober and Hilz²⁷ are also plotted in figure 58. It should be noted in the comparison that the resolution units used by Schober and Hilz were given in terms of "lines" per unit angle. Unfortunately, it is unclear whether "lines" meant individual lines counting black and white separately or whether it meant line pairs. In figure 58, it was assumed that Schober and Hilz meant line pairs, as is usually the practice in optical journals.

In any event, the agreement between the first cut computed data and that measured is not unreasonable and is good enough for this preliminary analysis. It is quite clear that display fluctuation noise can be a problem. For example, in order to detect a 300-line pattern, the smallest detectable contrast at 0.41 foot-lambert is 40 percent, and 32 foot-lamberts, the smallest detectable contrast is 3.3 percent (from the measured data).

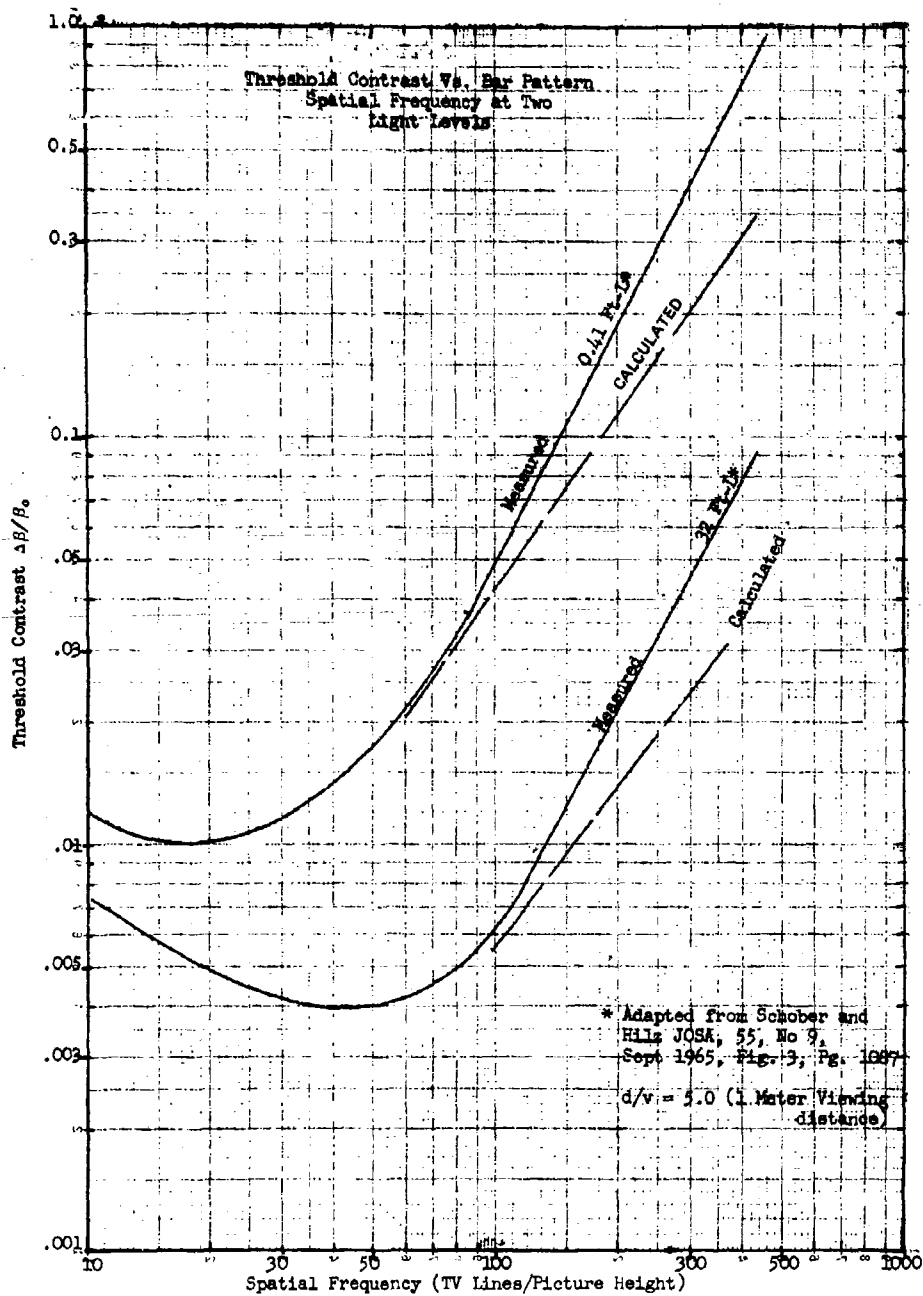


Figure 58. Threshold Contrast Versus Bar Pattern Spatial Frequency at Two Light Levels

7.3 IMPACT ON SENSORY SYSTEM PERFORMANCE

As can be seen, smaller image contrasts can be seen as display brightness increases. However, as will be seen, image contrast may also decrease with such an increase. Suppose equation 157 is rewritten as

$$C_I = \frac{\Delta\beta}{\beta_o} = \frac{SNR_R N_{TV} d}{\left(n_v^{1/2} 34 V \delta \beta_o^{1/2} R_o^{1/2}\right)} \quad (165)$$

Now $\Delta\beta$ is related to incremental signal current Δi_s by the proportionality

$$\Delta\beta \propto G_c \Delta i_s \quad (166)$$

Where G_c is the gain of the contrast control and is in the range of 0 to 1.0. The value of β_o is proportional to the maximum signal current expected and nominally will be proportional to

$$\beta_o \propto \frac{i_{s \max}}{2} \quad (167)$$

Hence, equation 162 may be written as equation 168

$$\Delta i_s \propto \frac{(i_{s \max}) SNR_R N_{TV} d}{G_c \left(n_v^{1/2} 34 V \delta \beta_o^{1/2} R_o^{1/2}\right)} \quad (168)$$

We see now that the smallest incremental signal which can be seen increases as the highlight signal increases and as G_c , the video gain or contrast control is decreased. This effect has been observed in forward-looking infrared systems (FLIRS).²⁷ In such systems, the minimum resolvable temperature difference as shown in figure 59 increases as gain is reduced. The same effects are seen in LLLTV, where video gain is reduced because of bright lights in the field of view.

7.4 EXPERIMENTAL RESULTS

7.4.1 Influence of Monitor Brightness and Contrast With Noise in the Video Line

With a 4 raster line high square, an experiment was performed using three different $(SNR)_D$ values in which the contrast and brightness of the

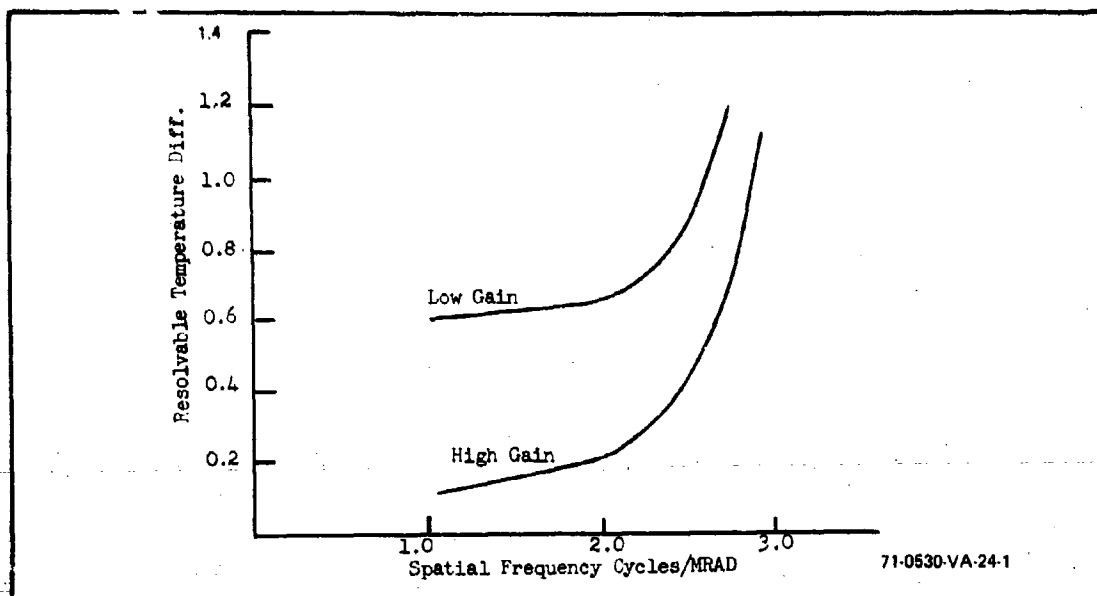


Figure 59. Resolvable Temperature Difference for High- and Low-Gain CRT Contrast Control Settings

display were randomly varied. Three brightness levels (with no video noise) of 0.2, 1, and 5 foot-lamberts and three contrast (gain) levels, 0, 3, and 17 dB were used. The results of the experiment are plotted in figure 60 as corrected probability versus total monitor brightness, and it is seen that over a range of about 10:1 the brightness and contrast level (setting) have no influence on the $(SNR)_D$ value when the noise is set by that in the video. Beyond about 5 to 8 foot-lamberts, the curves rapidly drop.

7.4.2 Influence of Monitor Brightness and Contrast - No Noise in the Video Line

As discussed above theoretically, the eye can become limited by an electro-optical sensor's cathode ray tube display luminance. The following experiment was performed to confirm this.

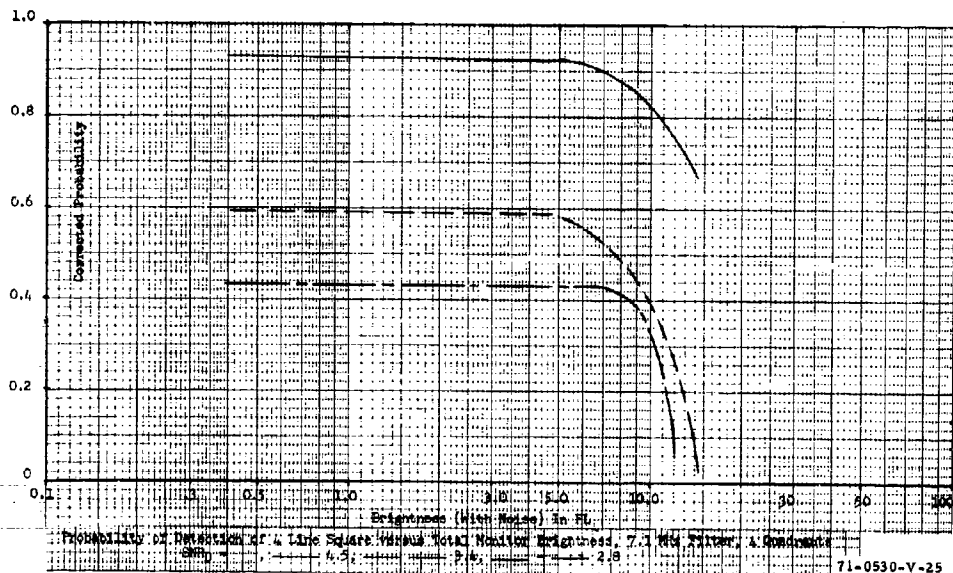


Figure 60. Probability of Detection of 4-Line Square Versus Total Monitor Brightness

Again, using the 4 raster line high square, the experiment was performed by randomly varying the signal level of the target (corresponding to varying the video gain) and monitor brightness. Four brightness levels and five signal levels were used. The target was randomly placed in one of three different positions. Five subjects participated in the experiment and a total of 900 data points were taken. In figure 61, the experimental results are shown. The data for a monitor brightness of 0.2 and 1 foot-lambert are very similar and a single curve has been drawn through this data. Higher signal levels are required, for a given probability, for both the 5- and the 10-foot-lambert cases. For a 50 percent probability of detection, at 0.2- or 1-foot-lambert brightness levels, a signal of 6.2 mv high was required; at a 5-foot-lambert brightness level, the signal must be 10.1 mv; and at 10 foot-lambert level, the signal must be 17.2 mv.

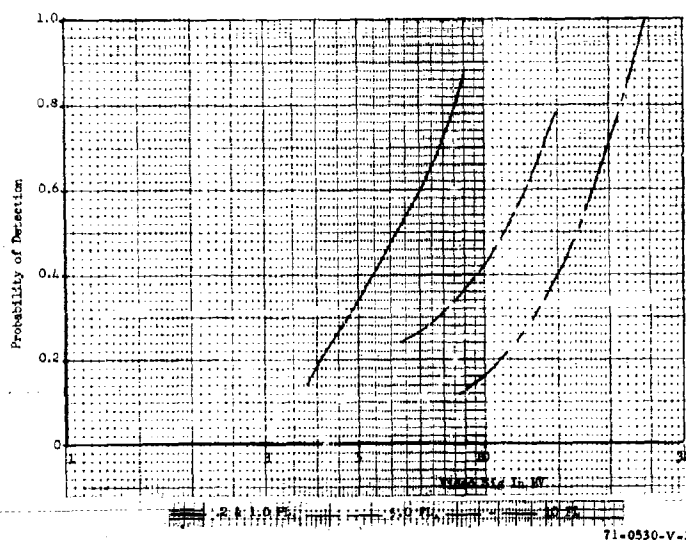


Figure 61. Probability of Detection Versus Video Signal

Thus, we see that at a fixed monitor brightness, an increase in the video signal (video gain) increases the probability of detection; that is, the minimum detectable contrast is less. Likewise, for a fixed video signal level (video gain), an increase in the display brightness corresponded to a decrease in the probability of detection; that is, to an increase in the minimum detectable contrast. Thus, the experimental results are consistent with the theory discussed above.

SECTION VIII IMAGE DISSECTOR

The first sensor to be analyzed is the image dissector which is schematically illustrated in figure 62. This sensor can provide extremely high resolution, good gray scale rendition, and an absence from lag making it ideal for microfilm readout, TV film cameras, and high-speed flying spot scanning. It is also used in conjunction with lasers that sequentially illuminate incremental scene areas while the image dissector views the same small area by scanning in synchronism with the laser beam. Since the image dissector has no target or hot cathode, it is inherently rugged and long-lived, and circuitry is simple because there is no electron scanning beam to form or deflect.

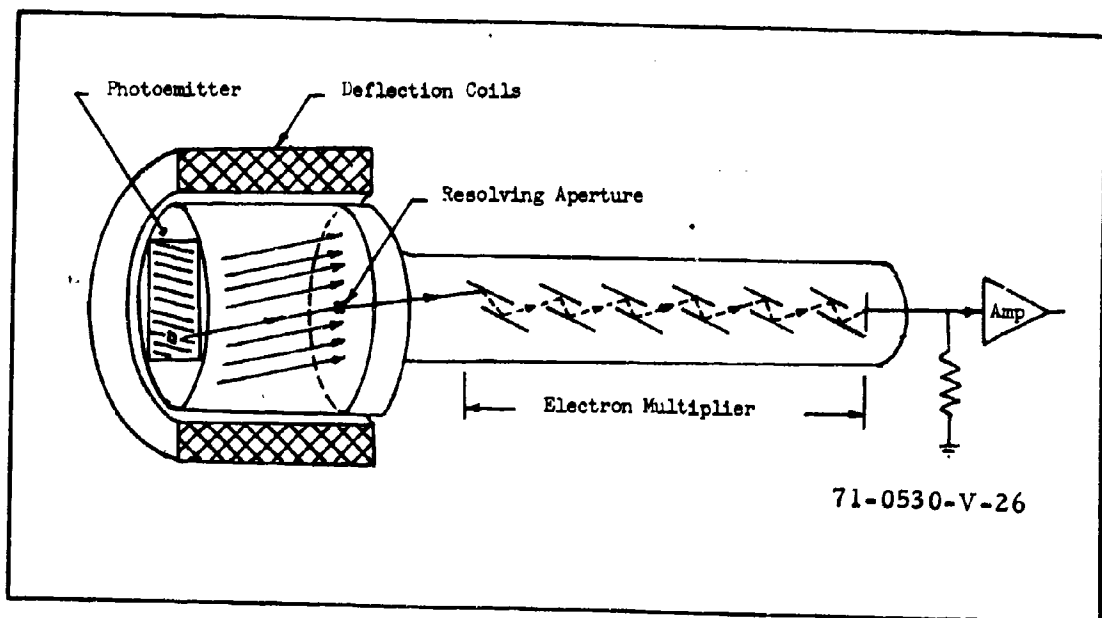


Figure 62. Schematic of an Image Dissector

As shown in figure 62, the image dissector consists of a photoemissive photocathode followed by a resolving aperture and an electron multiplier. In operation, the photoelectron image generated by the input photocathode is swept past the small resolving aperture so that the entire image is sequentially scanned in a manner similar to that used in television. In the following, the aperture is assumed to be a square of size $\beta \times \beta$, although in practice, it is more usual to use round apertures. Photoelectrons which pass through this small aperture or hole constitute the signal. These photoelectrons are amplified by a multistage secondary emission multiplier (or electron multiplier), processed, and displayed on a cathode ray tube. No signal storage is involved in the dissector and scene photo utilization is therefore inefficient.

Various photoemitters can be used. The absolute spectral responsivity of the most commonly used photoemitters is shown in figure 63. Except for the S-20 VR, (very red), these photocathodes are standardized, type classified, and available from a number of manufacturers. The S-10 is mainly used in commercial broadcast use where the similarity of its spectral response to that of the human eye is prized. The S-20, which is the forerunner of the S-25 and S-20 VR photocathodes, is still used when it is desired to spectrally match the output of a modified P-20 phosphor as is used on most image converters (or image intensifiers). The S-20 VR and S-25 are particularly suited to the imaging of man-made objects against vegetation backgrounds. The S-1 still finds some use in conjunction with covert auxiliary illuminators since it has some response at wavelengths far beyond the visible.

In addition to absolute spectral responsivity, it has become customary to specify the sensitivity of these photocathodes to certain standard test sources. In particular, one favorite is a tungsten bulb operated at a temperature of 2854°K. For this source, the sensitivity, σ_T is given by the formula,

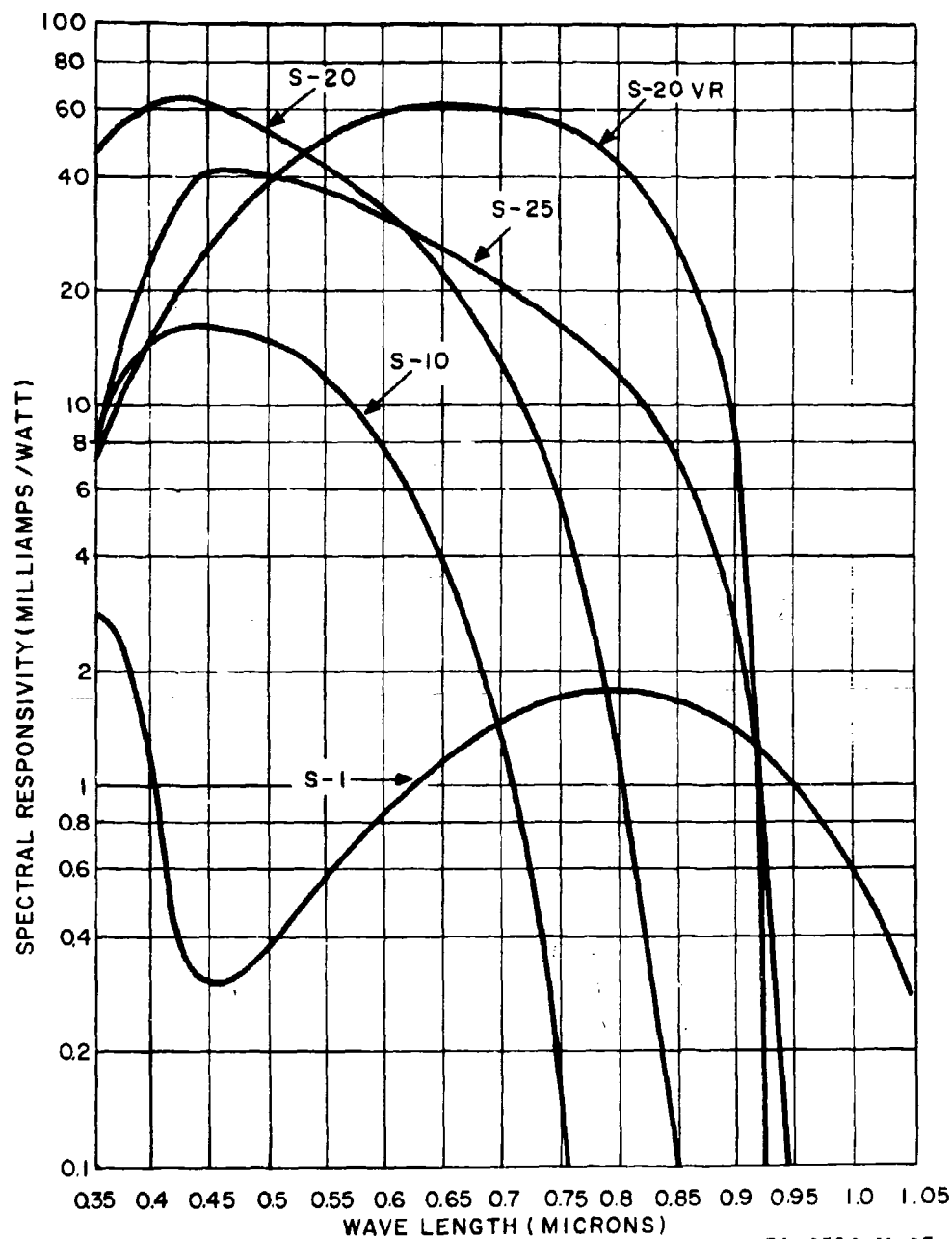


Figure 63. Spectral Responsivity Versus Wavelength for Several Photoemissive Photocathodes

$$\sigma_T = \frac{\int_{-\infty}^{\infty} R_{\lambda} W_{\lambda} (2854^{\circ}\text{K}) d\lambda}{\int_{-\infty}^{\infty} W_{\lambda} (2854^{\circ}\text{K}) d\lambda} \quad \frac{\text{amperes}}{\text{watt}} \quad (169)$$

where R_{λ} is the absolute spectral responsivity of the photoemitter in amperes/watt-micrometer, $W_{\lambda} (2854^{\circ}\text{K})$ is the radiant emittance of the 2854°K source in watts, and λ is the wavelength in micrometers. The photocurrent i_T obtainable from a photocathode of effective area A is

$$i_T = \sigma_T A H_T \quad (170)$$

where H_T is the image irradiance due to the specified source.

Although the above measures of sensitivity are preferred, much of the data in the past and even some current data is reported using the same 2854°K test source, but the irradiance is reported in terms of luminous equivalents. These units, which strictly speaking are relevant only to the unaided human eye, are inappropriate to the description of physical sensors, but their use is so widespread that they cannot be entirely avoided. The precise definition of equivalent luminous sensitivity is quantitatively given by

$$S_T(2854^{\circ}\text{K}) = \frac{\int_{-\infty}^{\infty} R_{\lambda} W_{\lambda} (2854^{\circ}\text{K}) d\lambda}{680 \int_{-\infty}^{\infty} \bar{y}_{\lambda} W_{\lambda} (2854^{\circ}\text{K}) d\lambda} \quad \frac{\text{amperes}}{\text{lumen}} \quad (171)$$

where 680 is the peak sensitivity of the "standard observer's" eye in lumens/watt and \bar{y}_{λ} is the eye's relative spectral sensitivity. With the above definition the photocurrent is given by

$$i_T = S_T A E_T \quad (172)$$

where E_T is the photocathode illuminance in lumens/ft² or footcandles.

One can also convert from equivalent luminous sensitivity to radiant sensitivity by noting that the luminous efficiency of 2854°K tungsten light is

approximately 20 lumens/watt. The rule of thumb for tungsten light is to divide footcandles by 2 to obtain watts/meters².

A dark current is also associated with a photoemitter. At room temperature, the S-1 has the most severe problem, necessitating cooling in many cases to achieve high-quality imaging. The S-10 is much superior in this regard, but still a factor of 10 less than that of the S-20 and its derivatives, the S-20 VR and S-25.

These various photoemitter parameters are summarized in table X.

TABLE X
TYPICAL PHOTOEMITTER PARAMETERS

Parameter	S-1	S-10	S-20	S-25	S-20VR
Long Wavelength Limit (micrometers)	1.1	0.75	0.85	0.94	0.92
Radiant Sensitivity (amperes/watt)*	0.4	0.8	3-4	4-6	6-9
Luminous Sensitivity ($\frac{\mu\text{amps}}{\text{lumen}}$)	10	20	40	200 to 300	300 to 450
Dark Current at 20°C (amperes/cm ²)	10^{-11}	10^{-12}	10^{-13}	10^{-14}	10^{-15}

* To a 2854°K tungsten source

In general, photoemission is linear with irradiance, and the MTF of the photocathode may be neglected relative to the other apertures within the sensor.

To proceed with the analysis suppose the sampling area to be of size β by β meters. Initially, we assume that the sensor MTF is unity. Then, the photoelectron image signal current is equal to

$$i = \sigma \beta^2 H e_v \cdot e_h. \quad (173)$$

where σ is the photoemitter responsivity (amperes/watt), H is its irradiance (watts/m²), and $e_v e_h$ are the vertical and horizontal scan efficiencies respectively. Here, the scan efficiency is numerically equal to the ratio of the actual time spent in scanning the effective photocathode area to the total time before repeating the scan. Suppose that $\beta = 0.0006$ inch or $1.524 \cdot 10^{-5}$ meter, $e_v e_h = 0.79$, and that $\sigma = 4 \cdot 10^{-3}$ (ampere/watt). Then, $i_{\max} = 7.35 \cdot 10^{-13} H$ ampere. This current is independent of scanning rate unless scan efficiency is affected thereby. Suppose the input test image to be a square wave bar pattern. Then, the starting point for this analysis is equation 139 (Section V) which is repeated below,*

$$\text{SNR}_{D/A} = \frac{\left[\frac{t}{a} \right]^{1/2}}{\left[N_v \cdot N_h \right]^{1/2}} \frac{C i_{\max}}{\left[(2-C) e i_{\max} \right]^{1/2}} \quad (139)$$

This equation must be modified to include sensor gains and other sensor or system noises. In particular, the signal current, i_{\max} , at the output of the photomultiplier becomes

$$i_{\max} = G_M \sigma \beta^2 H_{\max} \cdot e_v \cdot e_h \quad (174)$$

where G_M is the overall electron-multiplier gain which is typically 10^6 for 12 stages of electron multiplication. The mean square photoelectron noise generated per unit video bandwidth is equal to

$$\frac{i_e^2}{\Delta f_V} = (2-C) G_M^2 e i_{\max} \quad (175)$$

and the mean square noise generated by the first electron multiplier dynode is

$$\frac{i_D^2}{\Delta f_V} = (2-C) (G_{D1} - 1) G_{D11}^2 e i_{\max} \quad (176)$$

where G_{D1} is the gain of the first dynode (equal to about 3.16), and G_{D11} is the gain of all the dynodes which follow the first (equal to about 316,000).

*In the image dissector analysis the $(2-C)$ term in the noise is retained but will be dropped for the sensors that will be discussed in Section X.

The noises of equations 175 and 176 add in quadrature so that equation 173 as modified now reads

$$\text{SNR}_{D/A} = \left[\frac{t/a}{N_v \cdot N_h} \right]^{1/2} \frac{C}{(2-C)^{1/2}} \frac{[i_{\max/e}]^{1/2}}{\left[1 + (G_{D1}-1) G_{D11}^2 / G_M^2 \right]^{1/2}} \quad (177)$$

If we suppose the bars in the test pattern to be long relative to their spacing, then the effect of the MTF in the vertical can be neglected and only the MTF in the horizontal or $|R_o(N_h)|$ need be considered. Using the formulation of equation 143 (Section V), equation 177 becomes

$$\text{SNR}_{D/A} = \left[\frac{t_e/a}{N_v \cdot N_h} \right]^{1/2} \frac{C}{(2-C)^{1/2}} \frac{[i_{\max} |R_o(N_h)| / e]^{1/2}}{\left[1 + (G_{D1}-1) G_{D11}^2 / G_M^2 |R_o(N_h)| \right]^{1/2}} \quad (178)$$

In the above, it is assumed that the first dynode noise is white and unaffected by the scanning apertures. To evaluate the above, we will use the numbers previously discussed and will let $t = 0.2$ second and $a = 4/3$. In this calculation, it is presumed that the sensor is imaging in real time after the fashion of a conventional television camera. Then, for the image dissector with 0.0006-inch resolving aperture,

$$\text{SNR}_{D/A} = \frac{0.387}{[N_v]^{1/2}} \cdot \frac{C}{(2-C)^{1/2}} \left[\frac{R_o(N_h)}{N_h} \right]^{1/2} \frac{2140 (H_{\max})^{1/2}}{\left[1 + 0.21/R_o(N_h) \right]^{1/2}} \quad (179)$$

We next turn to the subject of MTF in the horizontal. If the sampling aperture plate is $\beta = x_o$ picture heights high and wide, then, the spatial frequency domain,

$$|R_o(N_h)| = \left| \frac{\sin \pi N_h x_o / 2}{\pi N_h x_o / 2} \right| \quad (180)$$

which has zeros at $N_h = 2k/x_o$; k being an integer. This MTF out to the first zero is plotted in figure 64 for three resolving apertures of 0.0006, 0.0012 and 0.0024 inch.

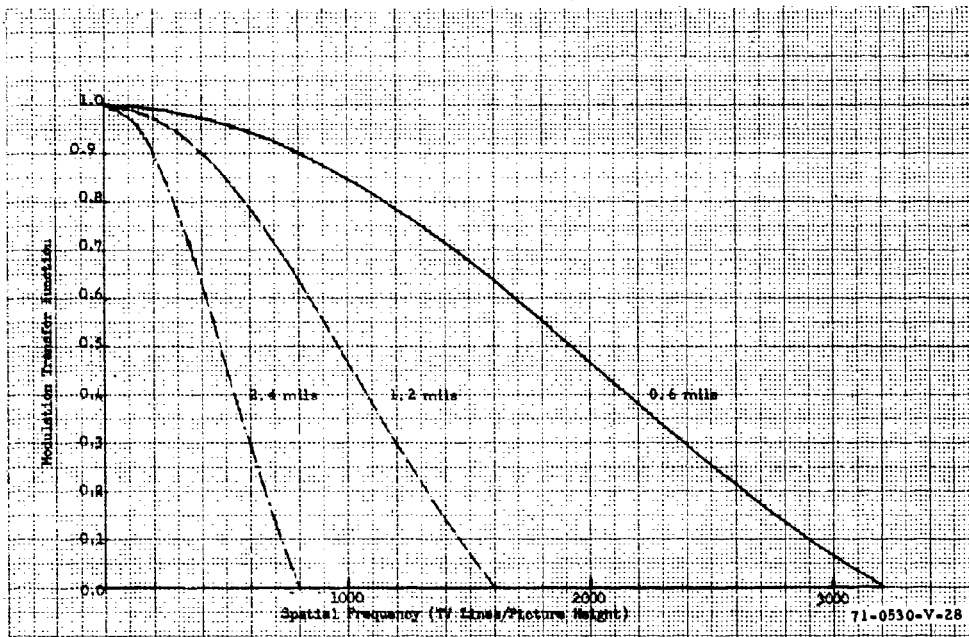


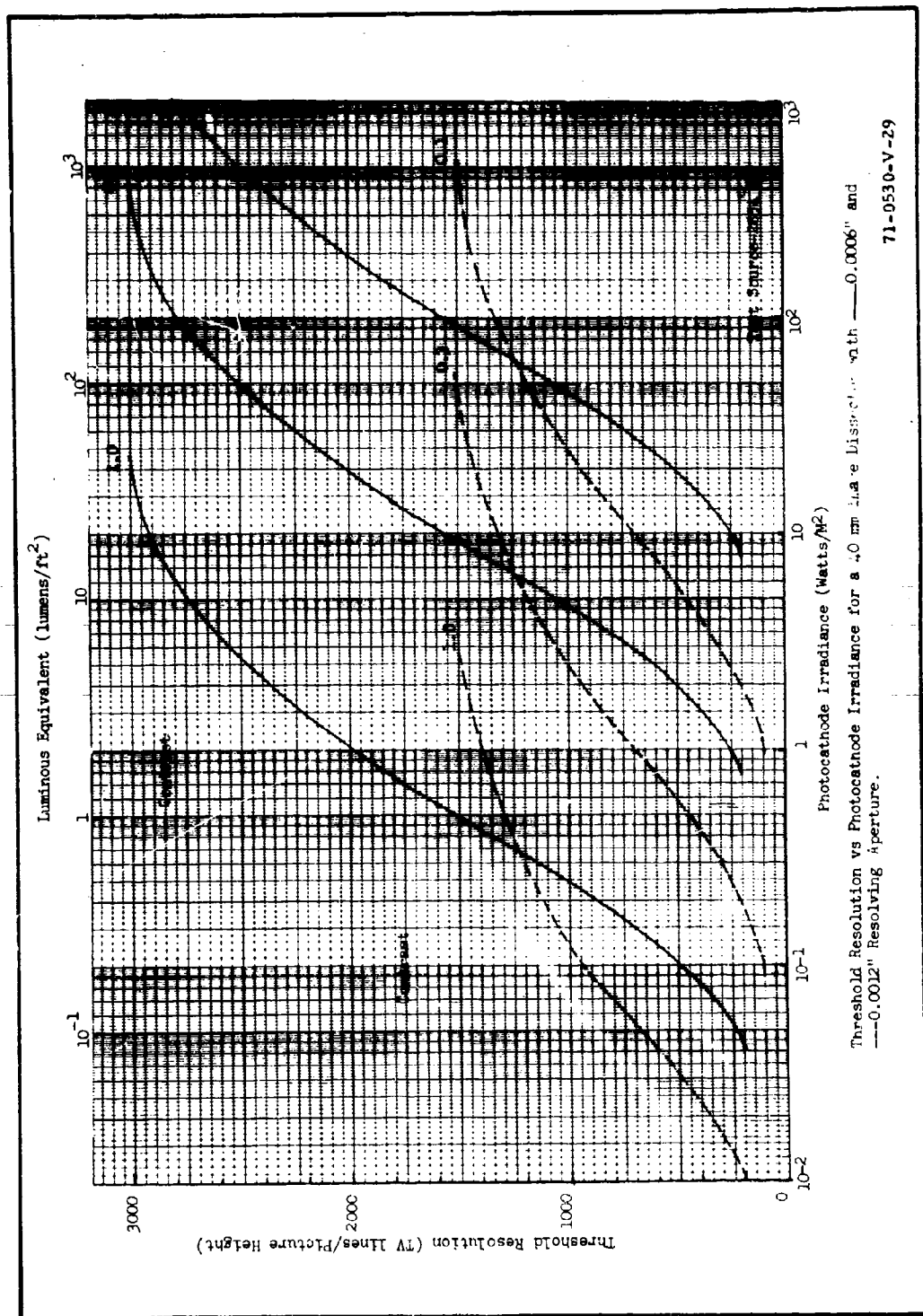
Figure 64. Modulation Transfer Function for a 40-mm Image Dissector

Equation 179 is next solved for highlight irradiance H_{\max} , obtaining

$$H_{\max} = (\text{SNR}_{D/A})^2 \cdot N_V \left[\frac{2-C}{C^2} \right] \frac{N_h}{|R_o(N_h)|} \frac{[1 + 0.21/|R_o(N_h)|]}{(827)^2} \quad (181)$$

The threshold value of H_{\max} is obtained when $\text{SNR}_{D/A} = 5.3$. Also, we will assume that the test pattern bar heights are maintained constant as their spatial frequency is increased. Let the bar height be L and the display height be Y . Then, $L/Y = K_V$, a constant. Also $N_V = Y/L = 1/K_V$. Using $K_V = 0.25$, equation 181 is next evaluated and plotted in figure 65 as a function of test pattern spatial frequency.

To illustrate the effect of a larger resolving aperture, the threshold value of H_{\max} was also computed for an aperture of size 0.0012×0.0012 inch. As can be seen, the larger aperture causes resolution at high irradiance levels to be sacrificed for greater sensitivity at the lower irradiance levels.



71-0530-V-29

Figure 65. Threshold Resolution Versus Photocathode Irradiance for a 40-mm Dissector

BLANK PAGE

SECTION IX

FORWARD-LOOKING INFRARED SCANNER

The next sensor to be considered is a forward-looking infrared scanner commonly referred to as a FLIRS or more simply as a FLIR. These systems are very similar to an image dissector; the principal difference being that the scene is scanned with an array of detectors such as shown in figure 66. Also, in a dissector, the photoelectron stream is magnetically deflected past the scanning aperture, whereas in a FLIR, the photon image is mechanically scanned past the detector array in the horizontal by a mirror or prism. As shown in figure 66, the detector elements need not be contiguous, but may be spaced by one or more elements per detector to provide an interlace feature similar to that used in television practice.

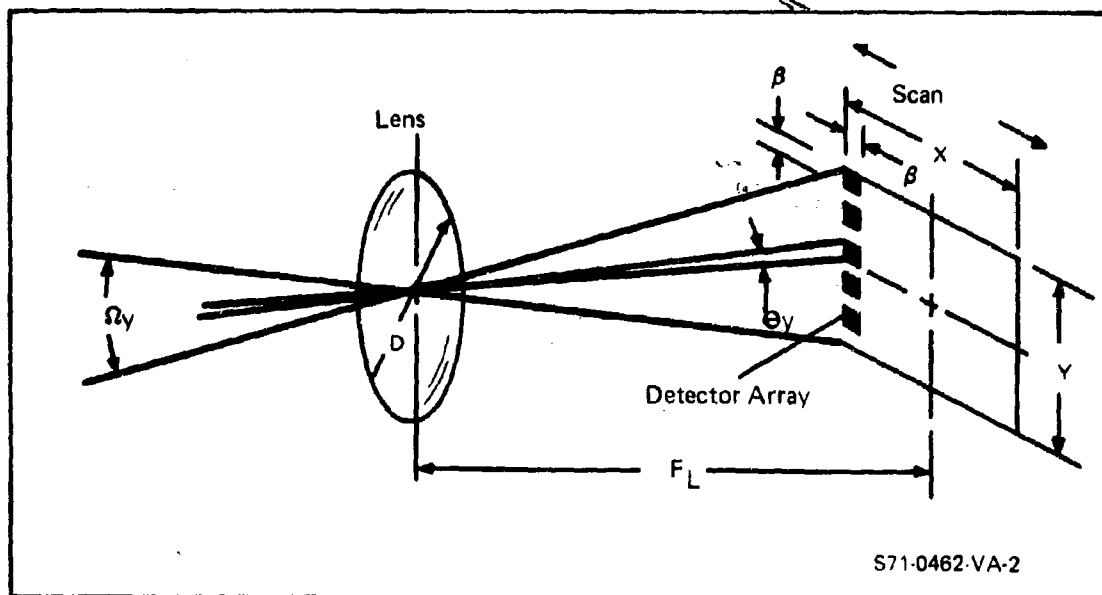


Figure 66. FLIRS Schematic

The detectors may number several hundred, with each detector having a preamplifier whose function is to build up the detected signal prior to multiplexing the channels in the vertical. The use of scene photons is much larger for the FLIR than for the image dissector because of the large number of detectors, but it is still far less than that of a TV camera tube incorporating signal storage. On the other hand, a FLIR senses only differential scene radiation, but a TV camera tube must store the entire background flux. In the far infrared, the background is many orders of magnitude larger than the differential signal. In a TV camera tube, this background uses up nearly all the signal storage capability of the storage element, which severely restricts the sensor's dynamic range. Thus, the FLIR will generally outperform a camera tube in the middle and far infrared spectra.

In multiplexing, the output of each detector element is sampled at least twice during the time required for the detector to move one detector element width. This multiplexing is needed to generate a signal analogous to the video signal generated by a television camera so that it can be displayed on a cathode ray tube with a single electron beam. These complexities do not appreciably affect the analysis of FLIR, which is virtually identical to that for any other sensor, except perhaps for terminology. To proceed, we first consider a single channel and as before, we initially assume the MTF to be unity. The photoelectron current for the single channel by analogy to equation 172 (Section VIII) is given by

$$i = \sigma \beta^2 \Delta H \cdot e_v e_h \quad (182)$$

where the terms are as before, except that only incremental irradiance is of interest. Contrast loses its meaning for a FLIR because of the signal differentiation prior to the video preamplifier. In general, the FLIR scan efficiency, $e_v e_h$ is less than that for electronic devices because of the finite mass of the mechanical scan elements. Typically, $e_v e_h$ is about 0.6 for a sinusoidal scan at the picture center.

The broad-area, peak signal-to-rms noise ratio or $SNR_{C,O}$ in an individual detector channel is given by

$$SNR_{C,O} = \frac{\Delta i_C}{\left[e \Delta f_C i_{nC} \right]^{1/2}} \quad (183)$$

$$= \frac{\sigma \beta^2 \Delta H e_v e_h}{\left[e \sigma \beta^2 H_B \Delta f_C e_v e_h \right]^{1/2}} \quad (184)$$

where Δf_C , the channel bandwidth required to pass the highest signal frequency of interest is inversely proportional to the time that the detector dwells on a detector sized element on the focal plane, or,

$$\begin{aligned} \Delta f_C &= \frac{kX}{2 e_v \cdot e_h \beta t_f} \\ &= \frac{k a Y}{2 e_v \cdot e_h \beta t_f} \end{aligned} \quad (185)$$

where k is the interlace ratio, X is the focal plane width, a is the picture aspect ratio, Y is the picture height, and t_f is the frame time.

The primary noise limiting a FLIR sensor is that due to the conversion of thermal background photons to electrons within the detector elements and this noise is a constant. The thermal background irradiance leading to this noise is given by H_B in equation 184. Ordinarily, the detector sensitivity is reported in terms of its noise equivalent power (NEP) or its inverse, detectivity (D). Usually, both are normalized to unit area and bandwidth in which case NEP becomes NEP* and D becomes D*. The value of NEP is numerically determined by setting the scan efficiency and channel signal-to-noise ratio of equation 184 equal to unity and solving for ΔH which becomes by definition ΔH_{min} , the minimum detectable irradiance. Thus,

* Interlace ratio is the number of fields scanned per frame time.

$$\Delta H_{\min} = \left[e H_B \Delta f_C / \beta^2 \sigma \right]^{1/2} \quad (186)$$

Next, ΔH_{\min} is normalized with respect to channel bandwidth and detector area such that

$$\text{NEP}^*(2\pi) = \frac{\Delta H_{\min}}{\left[\beta^2 \Delta f_C \right]^{1/2}} = \left[\frac{e H_B}{\sigma} \right]^{1/2} \quad (187)$$

Note that NEP* is denoted NEP* (2 π) which is done to indicate that the detector is viewing a 2 π Steradian background. In practice, the amount of background which the detector views can be decreased by cold shielding and the background noise is reduced in turn. With perfect cold shielding, the NEP* (2 π) becomes NEP* (2 π)/2f# where f# is the lens focal ratio. In line array or mosaic detector systems, perfect cold shielding cannot be achieved but substantial improvements are possible.

To continue, we now write equation 184 in the form

$$\begin{aligned} \text{SNR}_{C,O} &= \frac{\beta^2 \Delta H e_v e_h}{\left[\Delta f_C \beta^2 e_v e_h \right]^{1/2} \text{NEP}^*(\Omega)} \\ &= \frac{\beta^2 \Delta H e_v e_h}{\left[k a Y \beta / 2 t_f \right]^{1/2} \cdot \text{NEP}^*(\Omega)} \end{aligned} \quad (188)$$

by using the NEP expression of equation 187 but writing it as NEP* (Ω) to indicate that cold shielding is employed.

To form a two-dimensional image, the outputs of the individual channels are amplified and multiplexed to form a signal that can be used to modulate the cathode ray tube display. In such multiplexing, the output of each detector is sampled at least once during each dwell time. The video bandwidth after sampling becomes

$$\Delta f_V = \frac{k n_d}{2 e_v \cdot e_h \beta t_f} \quad (189)$$

which is larger than the channel bandwidth by an amount equal to the number of detectors, n_d .

We will assume that the multiplexing process neither degrades signal nor adds noise. In this event, the incremental broad area signal current in the video channel becomes

$$\Delta i_V = \sigma n_d \beta^2 \Delta H e_v \cdot e_h / k \quad (190)$$

which is also larger than the signal current in the channel because, in multiplexing, the rate of charge readout is increased. Similarly, the noise current is increased such that the video signal-to-noise ratio becomes

$$\begin{aligned} \text{SNR}_{V,O} &= \frac{n_d \beta^2 \Delta H e_v \cdot e_h}{\left[\Delta f_V n_d \beta^2 \cdot e_v \cdot e_h \right]^{1/2} \cdot \text{NEP}^*(\Omega)} \\ &= \frac{\beta^2 \Delta H e_v \cdot e_h}{\left[k a Y \beta / 2 t_f \right]^{1/2} \cdot \text{NEP}^*(\Omega)} \end{aligned} \quad (191)$$

By comparison with equation 188, we see that the video and channel signal-to-noise ratios are identical; i.e.,

$$\text{SNR}_{V,O} = \text{SNR}_{C,O} \quad (192)$$

The display signal-to-noise ratio expression for bar patterns of large height to width ratio is given by

$$\begin{aligned} \text{SNR}_{D/A} &= \left[\frac{t n_v \Delta f_V}{a} \right]^{1/2} \cdot \frac{|R_o(N_h)|^{1/2}}{N_h} \cdot \frac{n_d \beta^2 \Delta H e_v \cdot e_h}{\left[\Delta f_V n_d \beta^2 e_v e_h \right]^{1/2} \text{NEP}^*(\Omega)} \\ &= \left[\frac{t n_v n_d k Y}{e_v e_n \beta t_f} \right]^{1/2} \cdot \frac{|R_o(N_h)|^{1/2}}{N_h} \cdot \frac{\beta^2 \Delta H e_v \cdot e_h}{\left[k a Y \beta / t_f \right]^{1/2} \text{NEP}^*(\Omega)} \\ &= \left[\frac{t n_v n_d}{a} \right]^{1/2} \cdot \frac{|R_o(N_h)|^{1/2}}{N_h} \cdot \frac{\beta \Delta H (e_v \cdot e_h)^{1/2}}{\text{NEP}^*(\Omega)} \end{aligned} \quad (193)$$

In the analysis of a FLIR, it has become customary to specify the sensor sensitivity in terms of the total system capability (including the lens) to detect or differentiate between two objects differing only slightly in temperature. For this analysis, it is customary to write the incremental irradiance in the form

$$\begin{aligned}\Delta H &= \pi N_k \tau_o D^2 \Delta T / 4 F_L^2 \\ &= W_k \tau_o D^2 \Delta T / 4 F_L^2\end{aligned}\quad (194)$$

where N_k is the incremental object radiance expressed in watts/cm²-sr-°K, W_k is the incremental object irradiance in watts/cm²-°K, τ_o is the lens transmittance, D is its diameter, $f\#$ is its focal ratio, and ΔT is the incremental object temperature. Using equation 194, equation 193 becomes

$$SNR_{D/A} = \left[\frac{t_{n_v n_d}}{2a} \right]^{1/2} \frac{|R_o(N_h)|^{1/2}}{N_h} \frac{\beta W_k \tau_o D^2 \Delta T (e_v e_h)^{1/2}}{4 F_L^2 NEP^* (\Omega)} \quad (195)$$

In the above, we must also include the MTF of the lens in $R_o(N_h)$. Before continuing, we will briefly discuss W_k , the incremental object irradiance. By Plank's equations, the irradiance of a black body is given by

$$W(\lambda, T) = \frac{C_1}{\lambda^5} \left[(\exp C_2/\lambda T) - 1 \right]^{-1} \quad (196)$$

where $C_1 = 3.7412 \cdot 10^{-4}$ watt-micrometers², $C_2 = 14,388$ micrometer degrees, λ is the wavelength in micrometers and T is the absolute temperature in degrees Kelvin. For temperatures of the order of 300°K and wavelengths shorter than 20 micrometers, it is approximately true that

$$W(\lambda, T) = \frac{C_1}{\lambda^5} \exp (-C_2/\lambda T) \quad (197)$$

Now integrating with respect to λ , we find that

$$\int_{\lambda_1}^{\lambda_2} W(\lambda, T) d\lambda = \frac{C_1 e^{-C_2/\lambda T}}{\lambda^4} \left[\frac{\lambda T}{C_2} + \frac{3(\lambda T)^2}{C_2^2} + \frac{6(\lambda T)^3}{C_2^3} + \frac{6(\lambda T)^4}{C_2^4} \right] \Bigg|_{\lambda_1}^{\lambda_2} \quad (198)$$

With Lambert law radiators, the differential amount of radiant emittance obtained when the object differs by a small amount ΔT can be found approximately by differentiating the above equation with respect to temperature with the result

$$W_k = \frac{dW(T, \lambda)}{dT} = \frac{C_1 T^3 \exp(-C_2/\lambda T) \left[C_2^4 + 4C_2^3 \lambda T + 12C_2^2 (\lambda T)^2 + 24C_2 (\lambda T)^3 + 24(\lambda T)^4 \right]}{C_2^4 (\lambda T)^4} \quad (199)$$

This equation is evaluated (in terms of object radiance) in tables XI and XII for $T = 300^\circ\text{K}$. The lower limit is assumed to be zero micrometers and values of energy for a spectral bandpass can be determined by simple subtraction of the emittance at the upper and lower spectral limits.

Next, we observe that it is more usual to describe FLIR resolution in cycles per milliradian rather than "TV lines/picture height." For this purpose, both N_h and $R_o(N_h)$ must be revised to these units. This can be accomplished by noting that if $\Delta\theta$ is the angular extent of one bar at the focal plane relative to the plane of the lens, then N_θ measured in cycles/milliradian is equal to

$$N_\theta = \frac{1}{2,000 \Delta\theta} = \frac{N_h \cdot F_L}{2,000 Y} = \frac{N_h F_L}{2,000 k n_d \beta} \quad (200)$$

Using the above equation together with equation 175 there results,

TABLE XI

INCREMENTAL RADIANCE FOR A BLACKBODY DIFFERING IN TEMPERATURE BY 1°K FROM A BACKGROUND AT 300°K IN THE SPECTRAL BAND 0 TO λ MICROMETERS⁵

λ (Micrometers)	N_k (W/cm ² -sr-°K)	λ (Micrometers)	N_k (W/cm ² -sr-°K)
2.0	1.136.10 ⁻¹⁰	5.0	6.840.10 ⁻⁶
2.1	2.956	5.1	7.702
2.2	6.993	5.2	8.623
2.3	1.524.10 ⁻⁹	5.3	9.603
2.4	3.093	5.4	1.064.10 ⁻⁵
2.5	5.896	5.5	1.174
2.6	1.064.10 ⁻⁸	5.6	1.289
2.7	1.828	5.7	1.409
2.8	3.008	5.8	1.535
2.9	4.763	5.9	1.666
3.0	7.285	6.0	1.801
3.1	1.080.10 ⁻⁷	6.1	1.941
3.2	1.557	6.2	2.085
3.3	2.189	6.3	2.234
3.4	3.006	6.4	2.386
3.5	4.044	6.5	2.542
3.6	5.037	6.6	2.702
3.7	6.921	6.7	2.864
3.8	8.833	6.8	3.029
3.9	1.11.10 ⁻⁶	6.9	3.197
4.0	1.378	7.0	3.367
4.1	1.689	7.1	3.539
4.2	2.046	7.2	3.713
4.3	2.452	7.3	3.889
4.4	2.090	7.4	4.066
4.5	3.421	7.5	4.244
4.6	3.998	7.6	4.423
4.7	4.613	7.7	4.603
4.8	5.296	7.8	4.783
4.9	6.038	7.9	4.964

TABLE XII
INCREMENTAL RADIANCE FOR A BLACKBODY DIFFERING IN TEM-
PERATURE BY 1°K FROM A BACKGROUND AT 300°K IN THE
SPECTRAL BAND 0 to λ MICROMETERS

λ (Micrometers)	N_k (W/cm ² -sr-°K)	λ (Micrometers)	N_k (W/cm ² -sr-°K)
8.0	5.145. 10 ⁻⁵	11.1	1.020. 10 ⁻⁴
8.1	5.326	11.2	1.033
8.2	5.507	11.3	1.047
8.3	5.687	11.4	1.060
8.4	5.867	11.5	1.072
8.5	6.046	11.6	1.085
8.6	6.225	11.7	1.097
8.7	6.402	11.8	1.197
8.8	6.579	11.9	1.122
8.9	6.755	12.0	1.134
9.0	6.929	12.1	1.145
9.1	7.102	12.2	1.157
9.2	7.274	12.3	1.168
9.3	7.444	12.4	1.179
9.4	7.613	12.5	1.190
9.5	7.780	12.6	1.200
9.6	7.945	12.7	1.211
9.7	8.109	12.8	1.221
9.8	8.271	12.9	1.231
9.9	8.431	13.0	1.241
10.0	8.589	13.1	1.251
10.1	8.746	13.2	1.261
10.2	8.900	13.3	1.270
10.3	9.052	13.4	1.279
10.4	9.203	13.5	1.288
10.5	9.351	13.6	1.297
10.6	9.498	13.7	1.306
10.7	9.642	13.8	1.347
10.8	9.785	13.9	1.323
10.9	9.925	14.0	1.331
11.0	1.006. 10 ⁻⁴		

$$\begin{aligned}
\text{SNR}_{D/A} &= \left[\frac{t n_v n_d}{a} \right]^{1/2} \frac{D^2 \tau_o}{8,000 F_L} \frac{1}{k n_d} \frac{|R_o(N_\theta)|^{1/2}}{N_\theta} \frac{\pi N_k \Delta T (e_v e_h)^{1/2}}{\text{NEP}^* (\Omega)} \\
&= \left[\frac{t n_v}{a n_d} \right]^{1/2} \frac{D^2 \tau_o}{8,000 k F_L} \frac{|R_o(N_\theta)|^{1/2}}{N_\theta} \frac{\pi N_k \Delta T (e_v e_h)^{1/2}}{\text{NEP}^* (\Omega)}
\end{aligned} \tag{201}$$

At the longer wavelengths to which a FLIR is sensitive, diffraction forms an important limitation to the MTF of the lens. For a lens which is aberration-free, the one dimensional MTF as limited by diffraction effects is given by

$$\text{MTF}(\Phi) = \frac{2}{\pi} \left[\cos^{-1} \phi - \phi (1 - \phi^2)^{1/2} \right] \quad 0 \leq \phi \leq 1 \tag{202}$$

where

$$\phi = \lambda f\# \cdot N_{LP} \tag{203}$$

if spatial frequency is given in line pairs/mm,

$$\phi = \lambda f\# N_h / 2Y \tag{204}$$

if spatial frequency is given in TV line/picture height, or

$$\phi = 1,000 \lambda f\# \cdot N_\theta / F_L \tag{205}$$

If N_θ is given in cycles/milliradian. The MTF (Φ) is listed in table XIII for various values of ϕ .

The lens MTF is plotted in figure 67 using equation 205 and $\lambda = 10^{-2}$ mm (10 micrometers) and a lens of focal ratio 2.0 (diameter of 150 mm and focal length 300 mm).

The MTF of the detector itself is given by

$$R_{Od}(N_\theta) = (\sin \pi N_\theta \theta_o) / (\pi N_\theta \theta_o) \tag{206}$$

TABLE XIII
MTF FOR AN ABERRATION-FREE CIRCULAR APERTURE

ϕ	MTF (ϕ)	ϕ	MTF (ϕ)
0	1.0000	0.55	0.3368
0.05	0.9364	0.60	0.2848
0.10	0.8729	0.65	0.2351
0.15	0.8097	0.70	0.1881
0.20	0.7471	0.75	0.1443
0.25	0.6850	0.80	0.1041
0.30	0.6238	0.85	0.0681
0.35	0.5636	0.90	0.0374
0.40	0.5046	0.95	0.0133
0.45	0.4470	1.0	0
0.50	0.3910		

where

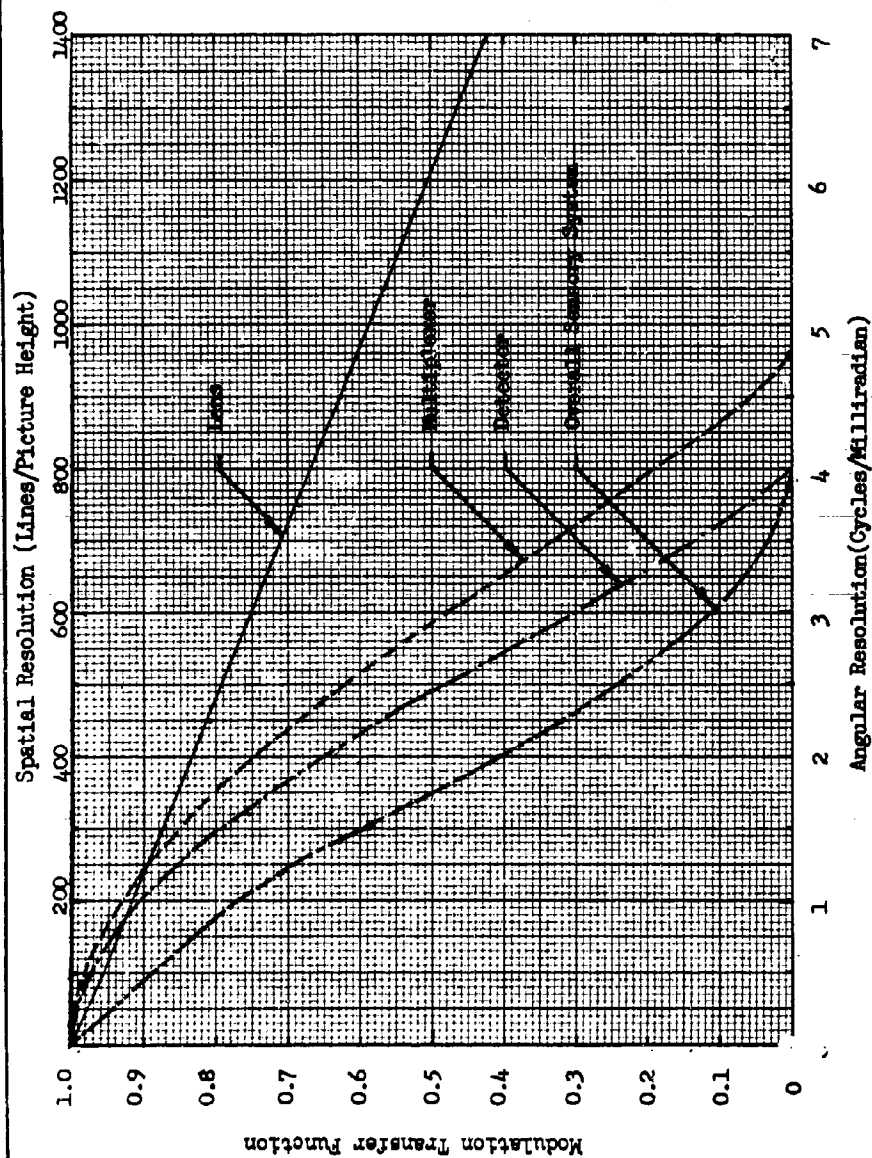
$$\theta_o = \frac{1,000 \beta}{F_L} \quad (207)$$

This MTF is plotted in figure 67 using $\beta = 0.075$ mm and $F_L = 300$ mm. The MTF for the multiplexer shown on the same figure is an assumed response. The overall system MTF is found as the product of the individual elements and is also plotted.

Finally, we solve equation 200 for ΔT as

$$\Delta T = \text{SNR}_{D/A} \left[\frac{\alpha n_d}{n_v t} \right]^{1/2} \frac{8 \cdot 10^3 k F_L}{D^2 \tau_o} \frac{N_\theta}{|R_o(N_\theta)|^{1/2}} \cdot \frac{\text{NEP}^*(\Omega)}{\pi N_k (e_v e_h)^{1/2}} \quad (208)$$

When $\text{SNR}_{D/A}$ equals 5.3, ΔT becomes the minimum resolvable temperature or MRT. This is calculated for our hypothetical sensor using $t = 0.2$ second, $n_v = 7$, $D = 15$ cm, $F_L = 30$ cm, $\tau_o = 0.6$, $W_k = 7.27 \times 10^{-5}$ watts/cm² - °K, $k = 2$, $\alpha = 4/3$, $n_d = 200$, $e_v e_h = 0.6$, and $\text{NEP}^*(\Omega) = 2 \times 10^{-11}$ (watts/cm-Hz)^{1/2}. The result is plotted in figure 68.



Modulation Transfer Function for Various FLIR Elements and Combined Sensory System Response (Detector is 0.075 mm on a Side and Lens is of Diameter 150 mm and Focal Length 300 mm.)

71-0530-V-30

Figure 67. Modulation Transfer Function for Various FLIR Elements and Combined Sensory System Response

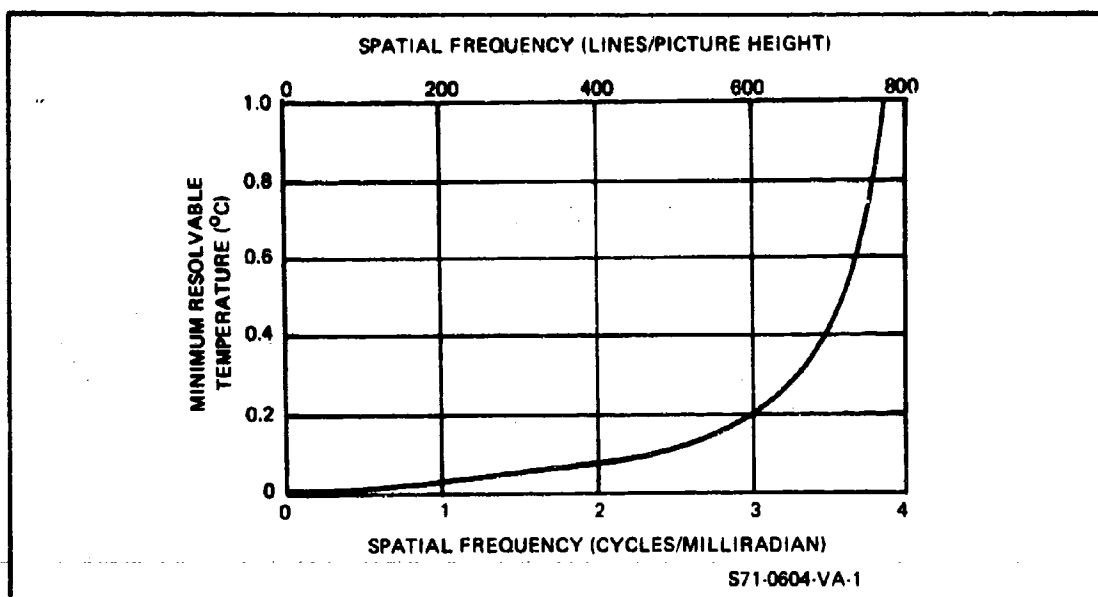


Figure 68. Threshold Resolution Versus Minimum Resolvable Temperature for the Assumed FLIR Parameters

It should be observed that the results are calculated for a rather idealized FLIR and also, the results apply only for small temperature excursions near 300°K. When the scene temperature excursions become large, the system may become display fluctuation noise limited rather than thermal scene background limited.

BLANK PAGE

SECTION X

DIRECT VIEW IMAGE CONVERTERS AND IMAGE INTENSIFIERS

An image converter is a sensor whose function is to detect a two-dimensional, photon-image, convert it to a photoelectron image, and then reconvert the photoelectron image back to a photon-image. An image intensifier is a special case of an image converter. This term is used to describe an image converter whose input and output images are primarily in the visible spectrum and whose output images are much brighter than those at the input. The output of an image intensifier may be viewed directly or it may be coupled to other image intensifiers to provide even larger image brightness gains. Image intensifiers may be coupled by means of lenses interposed between individual intensifier stages, but the efficiency of such coupling is usually less than 5 percent. In modern intensifiers, the input photocathodes and output phosphors are deposited on fiber-optic plates such that tubes can be directly coupled by simply butting one against the next. The coupling efficiency in this case can be as high as 50 to 80 percent depending on the type, diameter, and cladding of the fibers used. In addition to brightness gains, image intensifiers can be used to provide viewfield zoom by simple electronic means. They are also coupled to television pickup tubes to increase their sensitivity.

A typical electrostatically focused image intensifier is shown in figure 69. It consists of an evacuated glass envelope with a photocathode on the inner surface of one fiber-optic endplate and a phosphor on the other. The inner surfaces of the endplates are curved to minimize image distortion. The photoelectron image is greatly accelerated and focused onto the phosphor which recreates the original image in correct spatial correspondence except

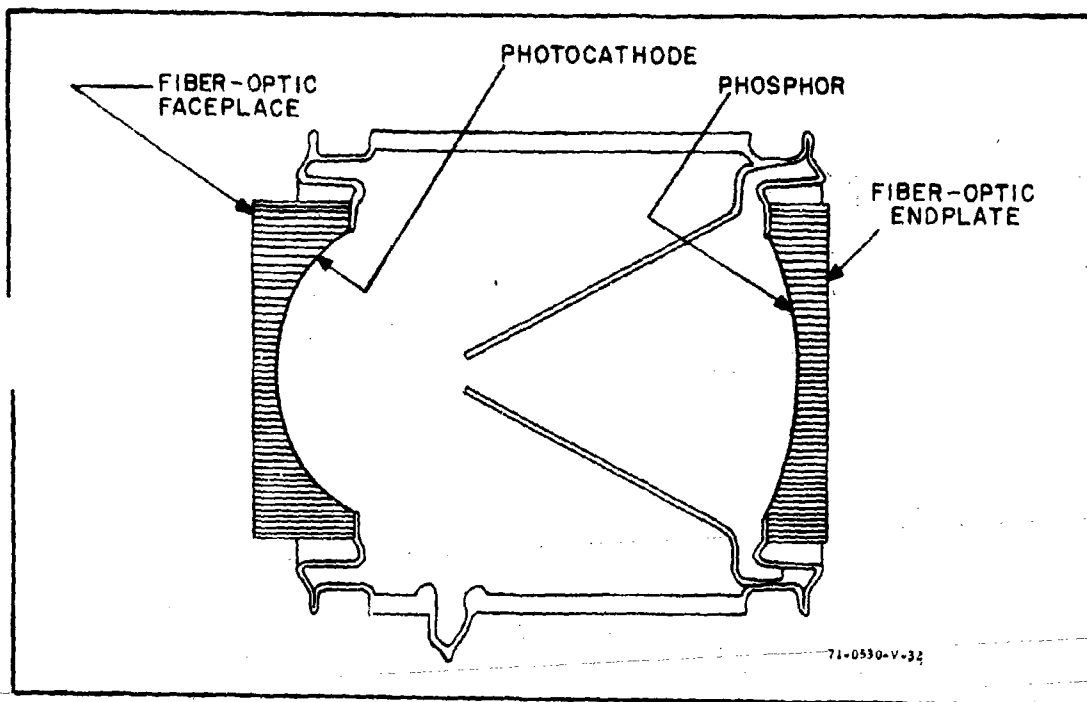


Figure 69. Schematic of a Single-Stage Image Intensifier

that the image is inverted top for bottom and right for left. To prevent feedback of phosphor light to the photocathode, the internal cone shaped electrode is blackened and the inner surface of the phosphor is aluminized. The light which emanates from the output endplate is diffused such that, when coupling to other intensifiers, both first stage output and second stage input endplates must be optically flat and tightly joined.

The maximum accelerating voltage is typically 15 kV. At higher voltages, the dark current rapidly increases, and difficulties with positive ion bombardment of the photocathode may be encountered. Some control over image brightness can be achieved by reducing the accelerating voltage (about 10 to 15:1), but at voltages much below 2 to 3 kV, the image will lose focus and rotate.

To proceed with the analysis, we note first that the input photocathode current, i , due to an input photocathode irradiance of $H(\lambda)$ is given by

$$i = A_I \sigma_p \int R(\lambda) H(\lambda) d\lambda \quad (209)$$

where A_I is the effective photocathode area, σ_p is its absolute sensitivity at the peak of its relative response $R(\lambda)$. Alternatively, when the source is a tungsten lamp operated at 2854°K, we may write the simpler equation

$$I = \sigma_T A H_T \quad (210)$$

The photocurrent is accelerated to the phosphor which recreates an image of radiant power distribution equal to

$$H_p(\lambda) = i k_p Z(\lambda) / A_p \quad (211)$$

where k_p is the radiant power conversion gain of the phosphor at peak λ in watts/ampere, A_p is the phosphor area, and $Z(\lambda)$ is the relative spectral distribution of the phosphor's output radiation. $Z(\lambda)$ is shown for a typical modified P-20 phosphor as is used in most modern intensifiers in figure 70. The modified P-20 phosphor represents a good spectral match with both the human eye and with S-20 and S-25 photoemitters, and in addition it is a good compromise between high gain and resolving power. When the eye views the output of the phosphor directly, we are concerned with brightness gain which is the ratio of output to input image brightness and can be a factor of 100 or more for intensifiers of equal input and output image areas. This high gain is due in part to the phosphor's green color to which the eye is most sensitive.

The apparent light gain (G_L) due to adding an intensifier in front of a second intensifier will be different than the brightness gain because the spectral response of second stage photocathode is different than that of the eye. In the cascaded intensifier case, it is convenient to define the light gain relation as

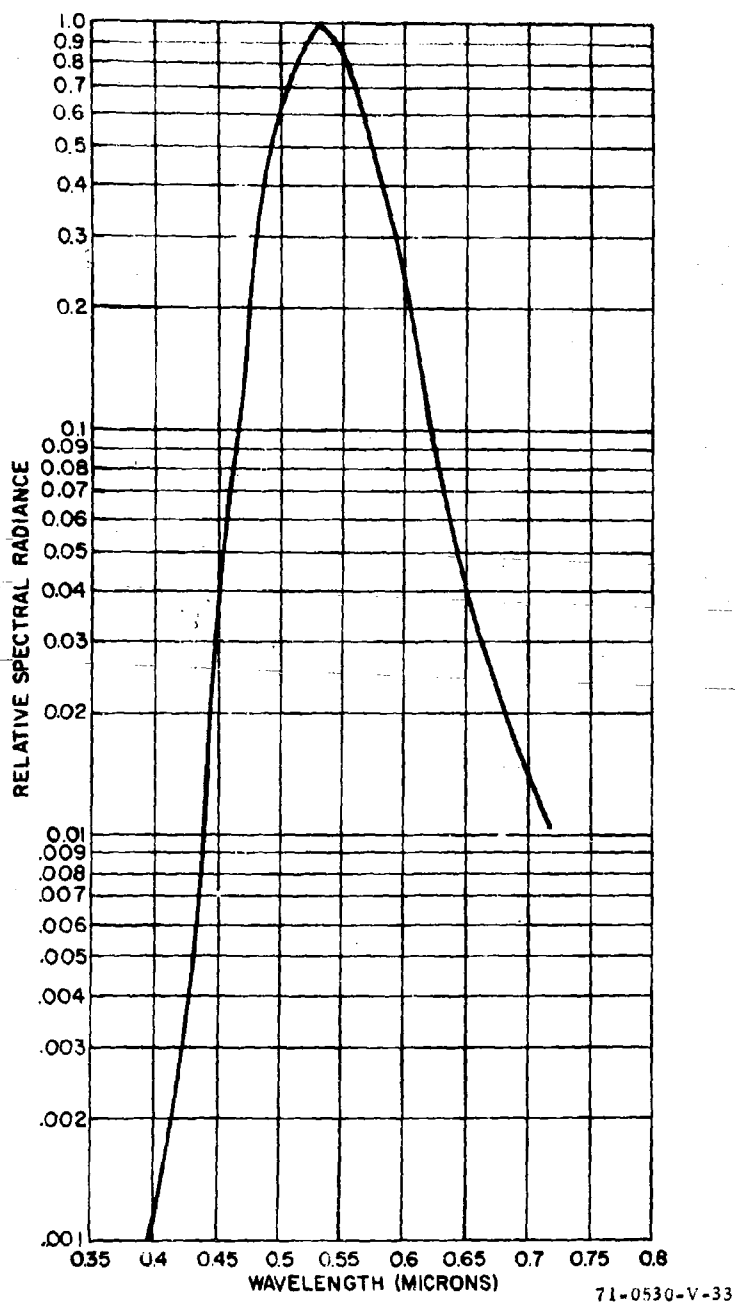


Figure 70. Relative Spectral Radiance of a Modified P-20 Phosphor

$$G_L = \frac{A_1}{A_2} \frac{\sigma_{T1}}{\sigma_{T2}} G_{E12} \quad (212)$$

where the subscripts 1 and 2 refer to the input and output stages, respectively. The quantity A_1/A_2 is the ratio of first to second stage photocathode areas; σ_{T1}/σ_{T2} is the ratio of photocathode radiant sensitivities; and G_{E12} is the electron gain at the input-intensifier's phosphor/output-intensifier's photocathode. Specifically, the electron gain is equal to the ratio of photocurrents in stage 1 to that in stage 2. Thus,

$$G_{E12} = \frac{i_2}{i_1} = K_{p1} \int Z_1(\lambda) \cdot \sigma_2 R_2(\lambda) d\lambda. \quad (213)$$

In this formulation K_{p1} includes any coupling losses which may take place between the two intensifiers. The value of G_E is variable from tube to tube, but is usually in the range of 30 to 50 with 40 being typical for tubes with P-20/S-20 phosphor/photocathode combinations.

In equation 212, we observe first that the electron gain should correlate with the value of σ_{T2} ; i.e., a high value for σ_{T2} should result in a high value of G_{E12} . This is not necessarily the case because the phosphor's output radiance is quite narrow spectrally and centered at about 0.51 to 0.55 micrometer. Therefore, only the sensor sensitivity near the peak phosphor wavelength is of concern. The more sensitive photocathodes gain their sensitivity mainly by a wider spectral bandpass which is of no use when coupling to a phosphor. Indeed, the old S-20 may be somewhat superior to the S-20 VR in this regard as can be seen by comparing figures 63 and 70.

We observe next that while the input-intensifier's phosphor must match the photocathode which follows it in size, the input photocathode need not. This is shown as the area ratio gain A_2/A_1 . A zoom intensifier in which the input photocathode area is variable is shown in figure 71. In this tube, the amount of photocathode which is imaged on the phosphor is electronically

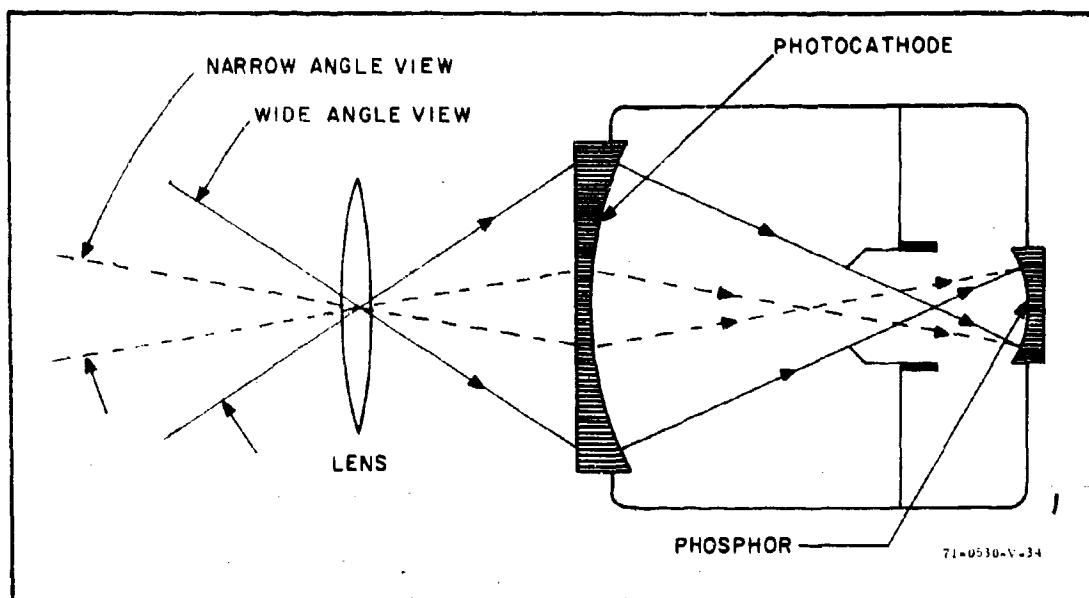


Figure 71. Schematic of an Electronic Zoom Intensifier

variable by changing the potentials on various internal focus electrodes. In current practice, up to a 3:1 viewfield zoom can be provided while maintaining the image on the phosphor at full size. As will be discussed, an increase in viewfield through electronic zoom is generally accompanied by an increase in sensitivity and field of view and a decrease in scene resolving power.

In the process of detecting the image, converting it to electrons, focusing it onto the phosphor, and in recreating a visible image; resolving power is lost at each step. As in the previous cases, the overall loss in resolution is specified in terms of the sensor's sine wave response $R_o(N_{LP})$. Note that spatial frequency in the case of an intensifier is ordinarily given in terms of cycles (or line pairs) per millimeter rather than TV lines per raster height as in the case of television cameras.

The sine wave response of a typical intensifier is shown in figure 72. Also shown is the sine wave response of two and three intensifiers in cascade assuming unit magnification (equal input photocathode and phosphor diameters in each stage). These responses are calculated from the relation

$$R_o(N_{LP}) = R_{o1}(N_{LP}) \cdot R_{o2}(N_{LP}) \dots R_{on}(N_{LP}), \quad (214)$$

where $R_o(N_{LP})$ is the overall sine wave response and $R_{on}(N_{LP})$ are the sine wave responses of the individual intensifiers. When combining responses in this form, it is necessary to reference the spatial frequency to the area where the individual elements are physically cascaded in each case. For two intensifiers in cascade, the appropriate area is the phosphor/photocathode interface. Where the intensifiers are of unit magnification, the point of reference is of no concern, but where zoom intensifiers are involved, care must be exercised.

The special case of a zoom intensifier merits some attention. If the intensifier were of unlimited resolving power which implies a unit sine wave

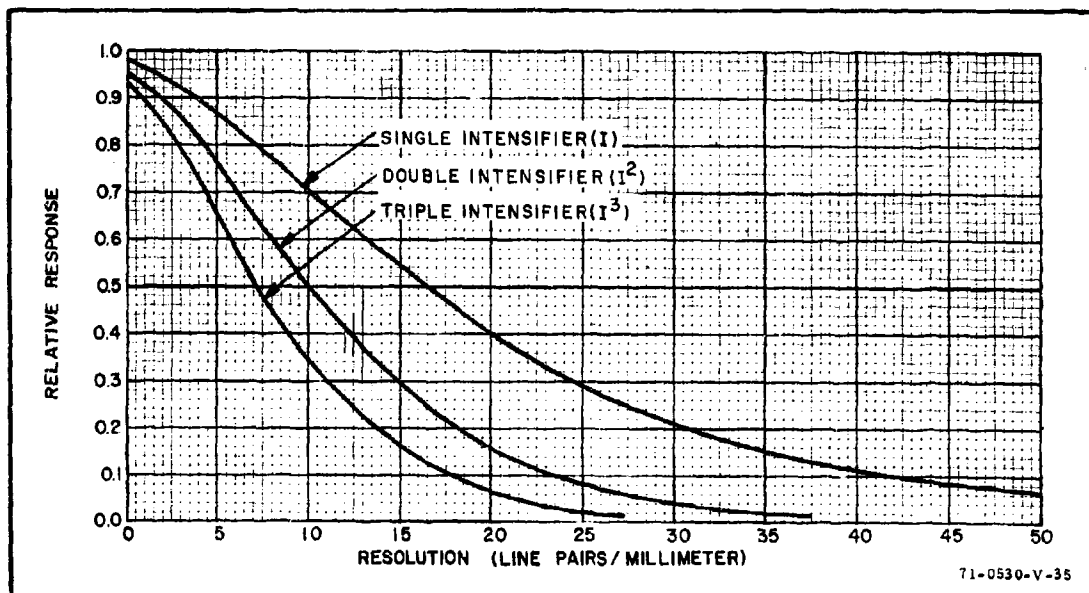


Figure 72. Sine Wave Amplitude Response for a Single, Double, and Triple Intensifier (These Curves are Independent of Intensifier Size to a First Approximation)

response, the scene resolution would be the same in both the wide-angle and narrow-angle modes. Since the wide angle mode also covers more viewfield as well, there would then be little point to zoom. As a practical matter, the intensifier's resolving power is limited by the phosphor particle sizes.

Thus, as viewfield is increased, the amount of scene area per phosphor particle increases. When the detail becomes smaller than the particles, the detail must inevitably be lost. The consequence is that a viewfield increase is accompanied by a loss in scene detail. On the other hand, the photoelectron density per particle increases with increase in photocathode size, and hence the smaller, less detailed scene objects, become brighter.

To illustrate this result more graphically, the sine wave response of a zoom intensifier is plotted in figure 73 referenced to the input photocathode. It is interesting to observe that the photocathode is ordinarily of very high resolving power compared to that of the phosphor. Hence, the sine wave response referenced to the phosphor is the same in either the wide-angle or narrow-angle view.

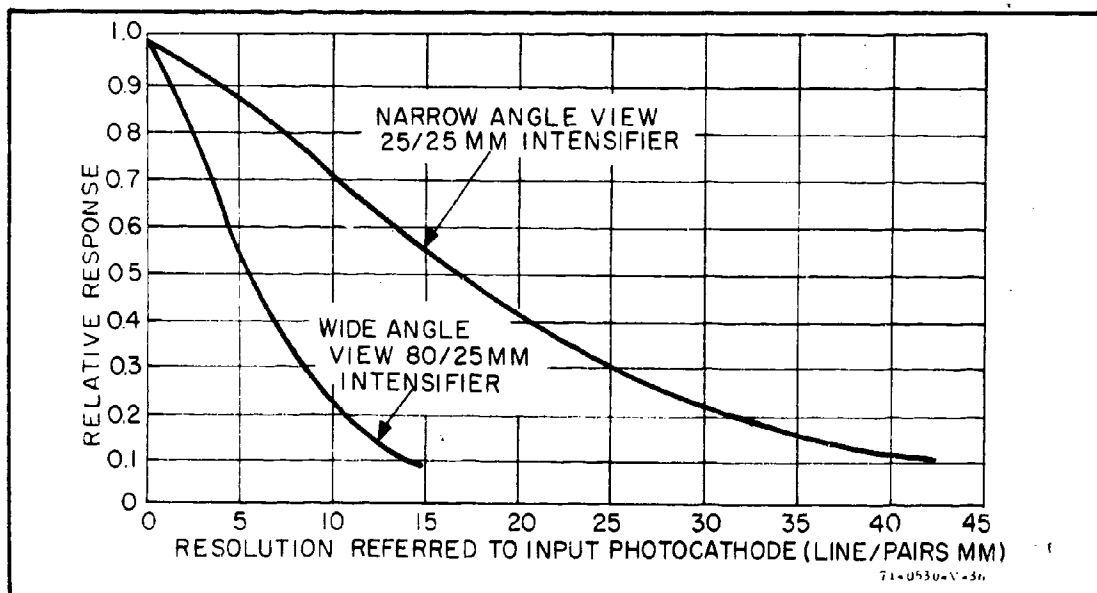


Figure 73. Sine Wave Response of a Zoom Intensifier Referred to the Input Photocathode

We will now turn our attention to the performance prediction of a direct view light amplifier consisting of an objective lens followed by three fiber-optically coupled intensifiers in cascade as shown in figure 74. The output phosphor is directly viewed through a magnifier or ocular. In this sensor, the objective lens focuses scene photons onto the photocathode with an efficiency of about 10 percent (for a T/1.5 lens). A typical S-25 photocathode has an average conversion efficiency of about 5 to 10 percent in its spectral band. These photoelectrons are accelerated to a phosphor that recreates the original image in the visible light spectral band. The phosphor has a gain of about 1,000 photons/electron so that the output image is perhaps tenfold brighter than that of the scene. This is insufficient for viewing of scenes at low-light levels. As a next step, a second intensifier is coupled to the first via fiber-optics. The photocathode of the second intensifier has a quantum efficiency of only about 5 to 10 percent, but the photocurrent in the second stage intensifier is still 40 to 50 times larger than in the first. The net

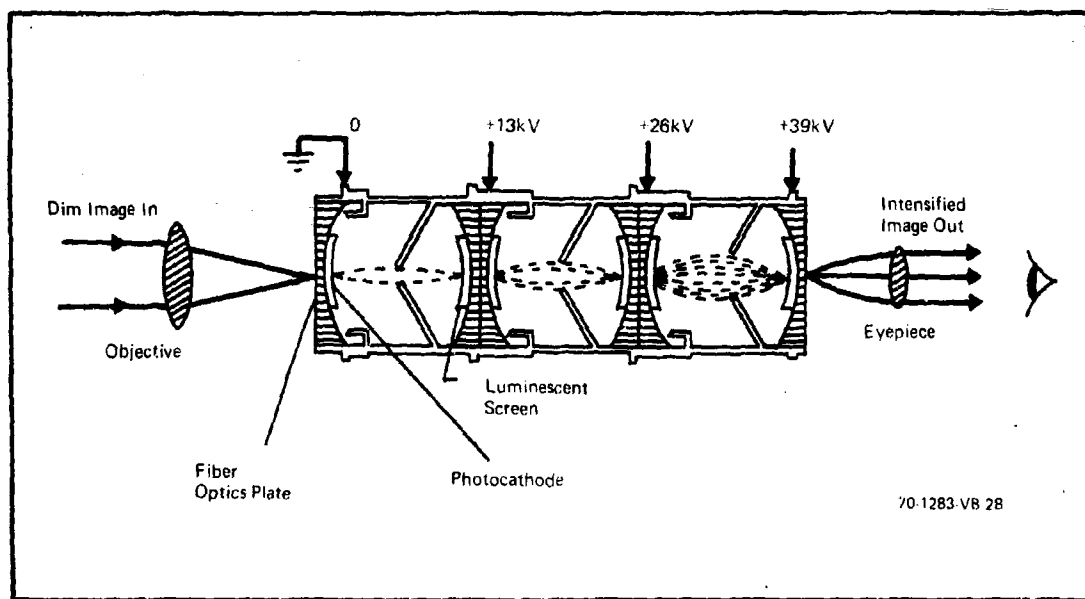


Figure 74. Modular Type Cascade Image Intensifier

"light gain" is perhaps 500 over that of the scene for the combined first and second stages — still insufficient for night viewing. A third stage provides an additional gain of 50, which gives the eye considerable added capability. Overall, a scene "brightness gain" of 2,500 to 5,000 is achieved, including the initial tenfold loss in the objective lens. The output phosphored screen is quite small and must be viewed with a magnifying glass or ocular if the full resolving power potential of the intensifier is to be realized.

With three image intensifiers in cascade, the direct view light amplifier is essentially photoelectron-noise-limited, and for a square wave bar pattern input of bar height to width ratio, n_v , the $\text{SNR}_{D/A}$ equation reads

$$\text{SNR}_{D/A} = \left[\frac{n_v t}{a} \right]^{1/2} \cdot \frac{C |R_o(N_h)|^{1/2}}{N_h} \cdot \left[\frac{\sigma A H_{\max}}{e} \right]^{1/2} \quad (215)$$

Or if resolution is given in line pairs/mm as is usually the case,

$$\text{SNR}_{D/A} = \left[n_v t \right]^{1/2} \cdot \frac{C |R_o(N_{LP})|^{1/2}}{2 N_{LP}} \cdot \left[\frac{\sigma H_{\max} \cdot 10^{-6}}{e} \right]^{1/2} \quad (216)$$

In the above, the quantity 10^{-6} is inserted to convert H_{\max} from units of watts/mm² to watts/m². In this formulation, it is implicitly assumed that the output intensifier phosphor is sufficiently bright and the image to be viewed is sufficiently large so as to preclude the possibility of the eye being acuity limited by light level. This is usually the case for three stage devices. We may now solve equation 216 for H_{\max} and set $\text{SNR}_{D/A}$ equal to 5.3 in order to calculate the threshold resolution versus irradiance characteristic. The result is shown in figure 75 for an intensifier of unit magnification and radiant sensitivity 4×10^{-3} ampere/watt.

In the figure, the equivalent illumination is shown in addition to a scale showing input photocathode current density computed from

$$\frac{i}{A} = \sigma_T H \quad (217)$$

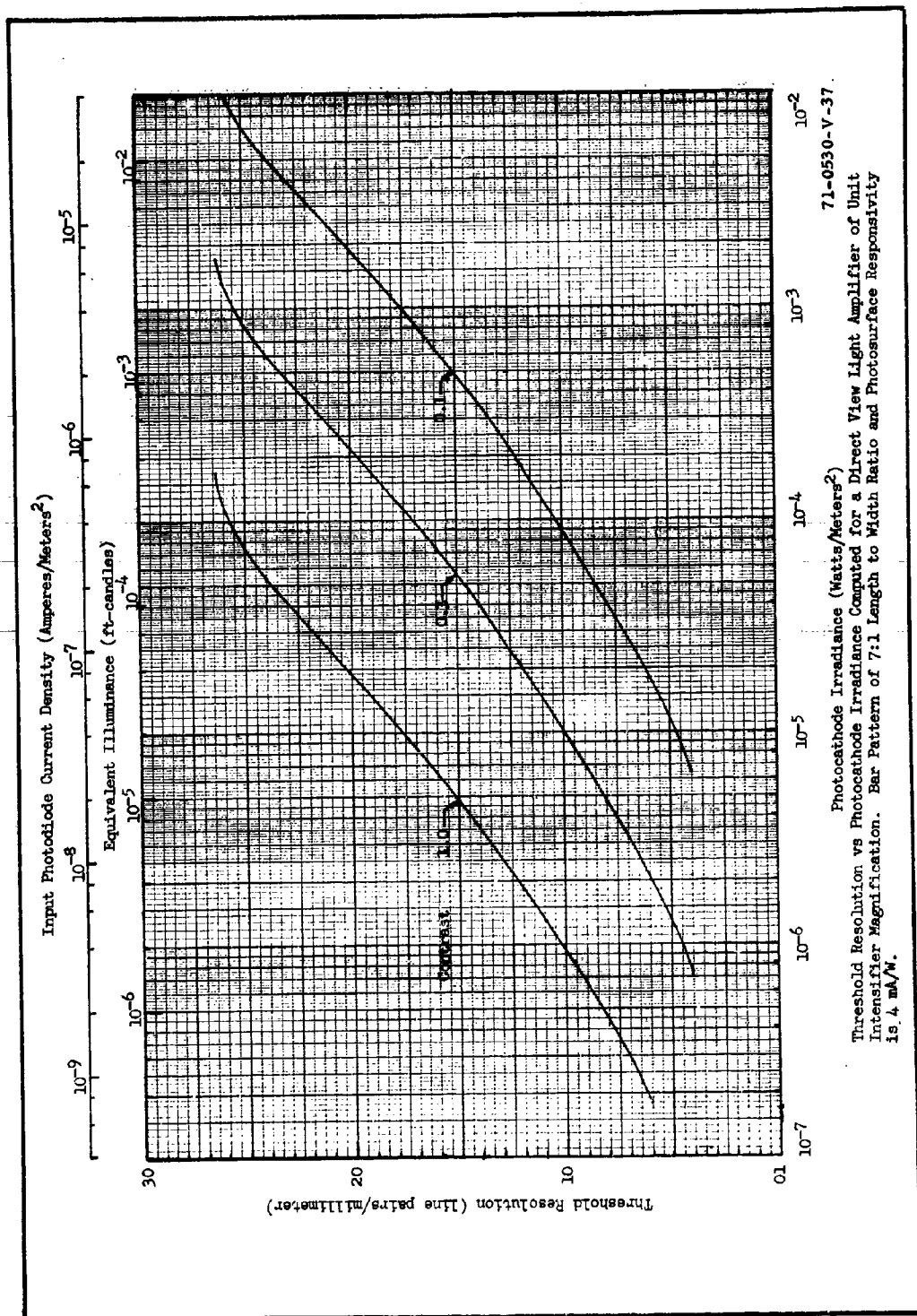


Figure 75. Threshold Resolution Versus Photocathode Irradiance

This scale is very convenient if the designer wishes to predict performance using a photocathode of greater or lesser sensitivity or of a different type altogether. In general, current density is computed from

$$\frac{i}{A} = \sigma \int_{\lambda} R(\lambda) H(\lambda) d\lambda \quad (218)$$

where σ is the peak responsivity of the photocathode, $R(\lambda)$ is its relative response, and $H(\lambda)$ is its irradiance.

Before proceeding, we wish to observe that the (2-C) term usually present in the noise calculation has been dropped from equation 215. The (2-C) term stems from the elementary model, which required that the eye compare an elemental area containing signal to some other similar area containing noise but no signal. The noise from the areas containing signal and no signal were then added in quadrature. We feel that this assumption is questionable, and in the new model it is necessary since the integral is over the waveform of the signal. The noise from areas adjacent to the image is, we feel, integrated over a much longer area than the signal and can, therefore, be neglected in most cases. The further rationale is that a better fit between experimentally measured and analytically predicted threshold resolution vs irradiance characteristic is observed when the (2-C) term is dropped.

SECTION XI

SILICON-EBIR TELEVISION CAMERAS

The silicon-electron-bombardment induced response or SEBIR television camera is the most capable sensor now available for most low-light-level imaging applications. The SEBIR camera tube is also known as the electron bombarded silicon or EBS camera tube (Westinghouse Electric Corporation) and as the silicon-intensified-target or SIT camera tube (Radio Corporation of America). Aside from constructional details, these various tubes are similar in principle and performance.

A typical SEBIR camera tube is shown schematically in figure 76. The photocathode is usually an S-20 photoemitter followed by an electrostatically focused image section and the SEBIR target. This target amplifies and stores

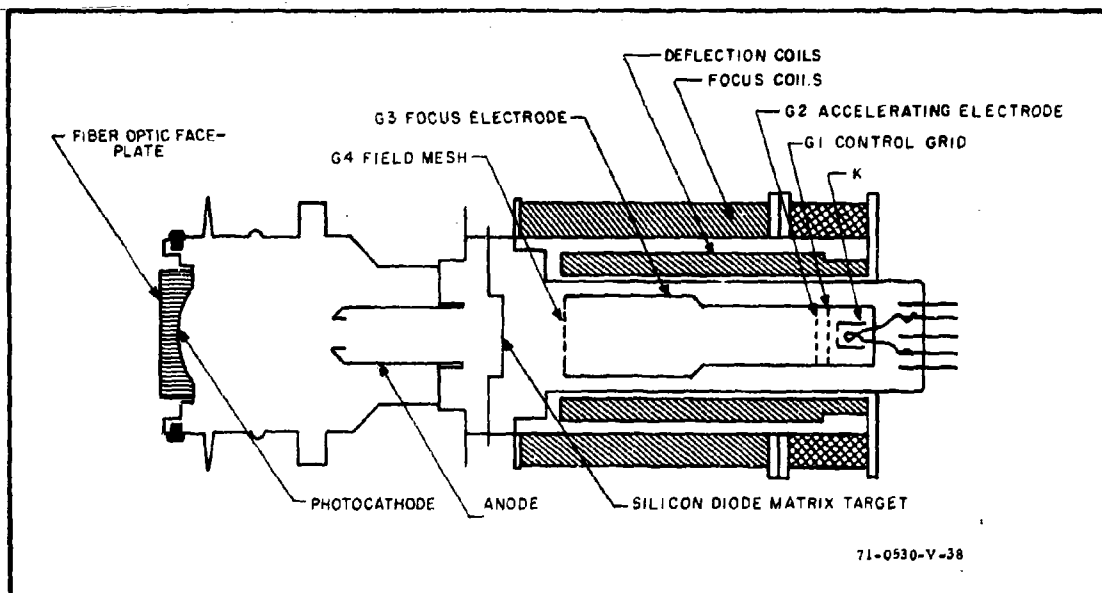


Figure 76. Cross Section of a Silicon EBIR Camera Tube

the image prior to readout by the scanning-electron-beam readout section. The gain of the SEBIR target is very high so that the SEBIR camera is of quite high sensitivity even without added image intensifiers. A SEBIR camera is simple to operate and can tolerate very large irradiance overloads without target burn or damage. With an intensifier, the SEBIR becomes photo-electron-noise limited since overall gain is then more than sufficient to make the preamplifier and all other system generated noises negligible.

The SEBIR target consists of a two-dimensional matrix of silicon diode elements. The amplification of signal current is due to an electron bombardment induced response, or EBIR effect, which takes place within the target. The maximum resolving power (or amplitude response) of the matrix is mainly limited by the density of diodes which in current practice is about 650 by 850 or 550,000 elements in a 3/8- by 1/2-inch area. Larger matrices are, however, becoming available.

The silicon diode matrix target is also used as a photoconductor in the silicon vidicon. In this mode, the silicon matrix array converts scene photons to electrons, and stores the image for subsequent readout, but provides no gain. As used in the SEBIR tube, the silicon diode matrix target amplifies and stores the photoelectron signal generated by an entirely separate photoemitter. The silicon vidicon discussed in Section XII, should not be confused with the silicon EBIR tube; the latter tube is many factors of 10 more sensitive.

The SEBIR camera tube's semitransparent photocathode shown in figure 76 is deposited on the inner surface of the plano-concave, fiber-optic faceplate. As in the case of the image intensifier, the photoemitter emits photoelectrons when irradiated, but instead of being accelerated to a phosphor, they are accelerated to the SEBIR target where they are brought to focus by the electrostatic lens formed between the photocathode surface and the anode cone.

Target operation is described by reference to figure 77. Suppose the n-type silicon slice is biased approximately 10 volts positive with respect to the cathode of the reading-electron-beam cathode. By scanning the back surface

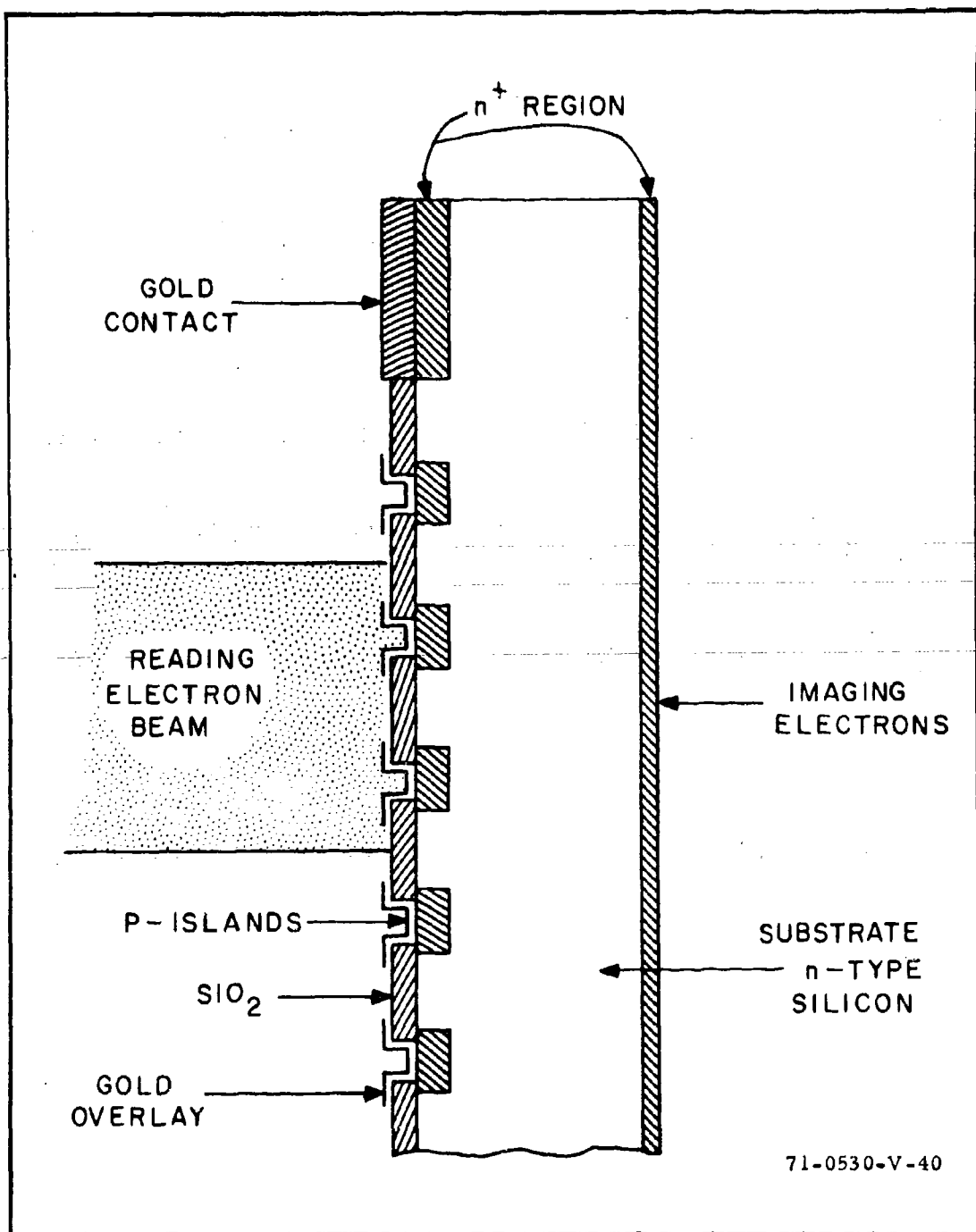


Figure 77. Schematic of Silicon-EBIR Target

of the target with the electron-beam, the p-type islands and the SiO_2 surface are charged to the read gun cathode potential and the p-n junctions become reversed biased. A junction capacitor is formed at each diode. Because of the low leakage current, this bias is retained during the frame time period when no signal photoelectrons are incident. When a photoelectron image is incident on the target, holes are generated in the n-type silicon which diffuse to the p-type islands and alter the charge on the diodes. The input photoelectrons are accelerated to the target with relatively high energy (about 10 keV). For each 3.4 eV of electron energy, one hole-electron pair is formed in the n-type silicon on the average. Theoretically, 2,930 hole-electron pairs are generated within the n-type silicon for each 10-keV photoelectron. This is equivalent to a signal amplification of the same amount. The actual gain is somewhat less and is controlled by the loss of holes due to recombination at the front surface and in the bulk of the target material. However, gains of 1,500 to 2,000 are readily obtainable. The video signal is developed directly from the portion of the electron beam which lands on the target and which flows in the target lead resistor as the beam scans the target point by point.

The plot of a camera tube's signal current output as a function of the input phototransducers irradiance level is known as the signal current versus photosurface irradiance transfer characteristic or more simply as the signal transfer characteristic. In measuring this characteristic, the input image is made very large relative to the camera tube's point image spread function so that MTF effects are not included. The signal current versus photocathode irradiance curves for the current state-of-the-art SEBIR tube are shown in figure 78 for three photocathode diameters, 16, 25, and 40 mm. The gamma of the signal transfer curve is essentially unity. No knee in the signal transfer curve is reported although eventually the signal output current available will be beam current limited. As a practical matter, some semblance of a knee will be introduced by means of an electronic target gain

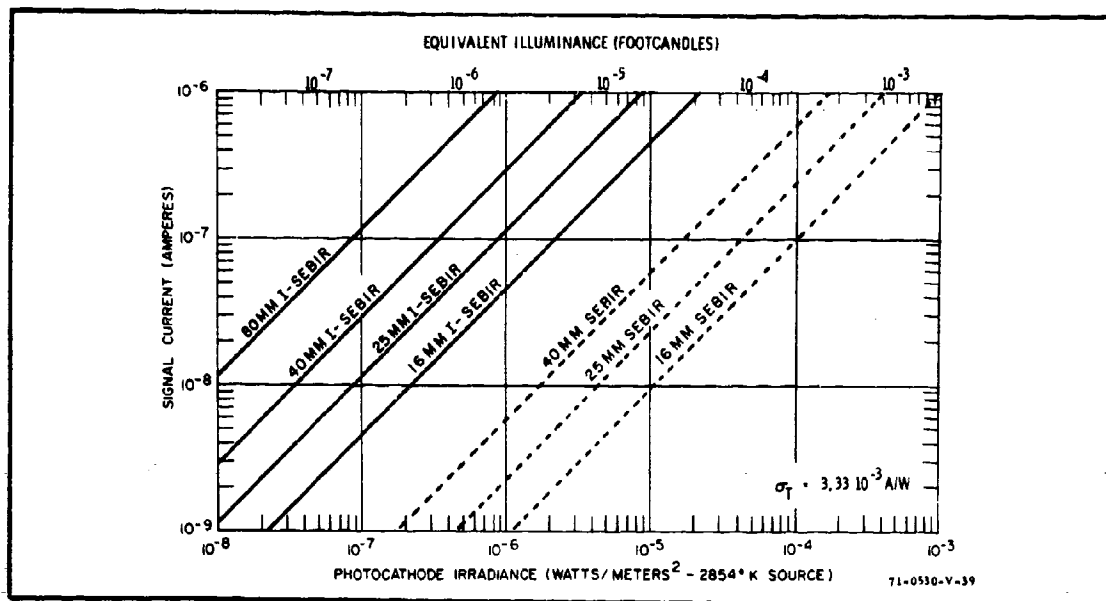


Figure 78. Signal Current Versus Photocathode Irradiance Characteristic for the Silicon-EBIR and Intensifier-Silicon-ERIR Cameras for Various Input Photocathode Diameters

control whereby the potential between the photocathode and target is reduced as light level increases.

The gain of the SEBIR target is primarily a function of the photocathode voltage as shown in figure 79. With current tubes, an absolute maximum voltage of -15 kV is specified with typical operation being in the range of -12 to -3 kV. This places maximum gain in the area of 2,500 to 3,000 and minimum gain a factor of about 10 lower. Above 15 kV, excessive dark current and positive ion bombardment of the photocathode can be expected to be a problem. At voltages below 3 kV, some image defocusing and rotation will occur although this may be tolerable in some instances. For the signal transfer curves shown in figure 78, a photocathode radiant sensitivity of 3.2×10^{-3} ampere/watt and a SEBIR target gain of 1,890 is assumed for calculation purposes.

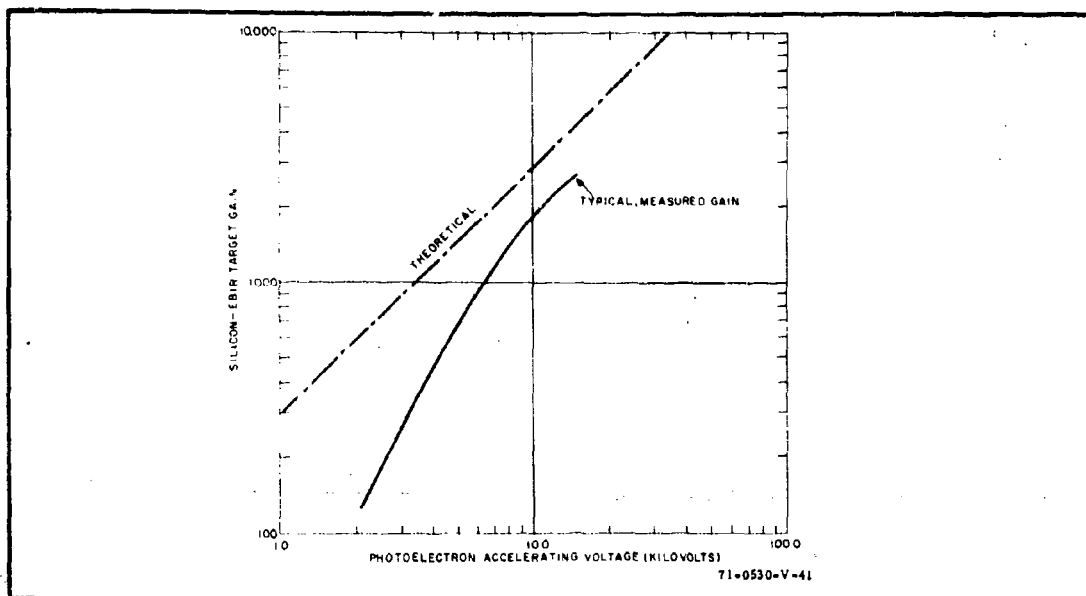


Figure 79. Silicon-EBIR Target Gain Versus Photoelectron Accelerating Voltage

The modulation transfer curves for two versions of the SEBIR camera tube are shown in figure 80. One version incorporates a silicon matrix target of 16-mm diameter while the other has a 25-mm target. The SEBIR camera tubes with 16-mm targets are currently available with input photocathodes of diameter 16, 25, and 40 mm. The SEBIR camera tubes with 25-mm targets are currently available only with a 40-mm photocathode, but a version with a 25-mm photocathode is in the offing and will be considered below. Ordinarily, the MTF is principally a function of the diameter of the silicon target and not the photocathode. Hence, one MTF curve suffices to describe the performance of several tubes with the same diameter target but different diameter photocathodes.

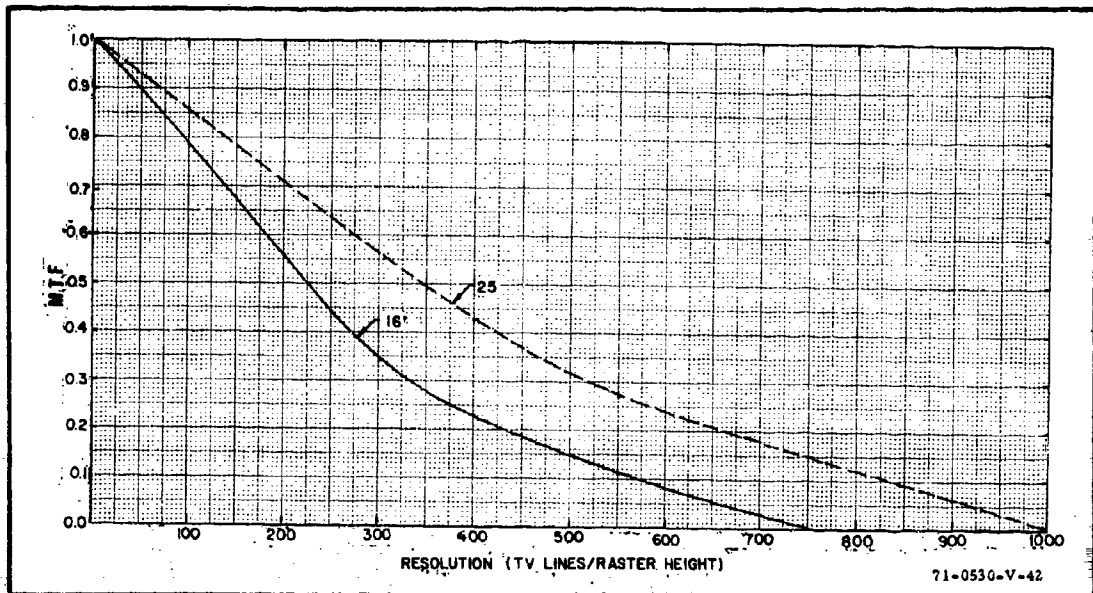


Figure 80. Modulation Transfer Curves for the Silicon-EBIR Camera With Silicon Targets of Diameter 16 and 25 mm

The display signal-to-noise ratio is calculated from the relation

$$\text{SNR}_{D/A} = \left[\frac{t \Delta f_V / a}{N_V N_h} \right]^{1/2} \frac{G_T |R_o(N_h)| i_{\max} / e_v e_h}{\left[G_T^2 e \Delta f_V i_{\max} |R_o(N_h)| / e_v e_h + I_P^2 \right]^{1/2}} \quad (219)$$

which applies to square wave test patterns as discussed in Section V. In the above, G_T is the gain of the silicon target, e_v and e_h are the horizontal and vertical scan efficiencies respectively, and I_P^2 is the mean square pre-amplifier noise. A reduction in scan efficiency is seen to increase photocurrent because the rate of charge readout is increased. Note also that the (2-C) term in the photoelectron noise expression (the term which quadratically

adds to I_p^2) has been dropped as discussed in Section X. It is presumed that the bar length to width ratio in the test pattern is 7 to 1 in which case $N_v = N_h/7$. The rms preamplifier noise is taken to be 3×10^{-9} ampere, and the video bandwidth is 10^7 Hz.

By writing the $SNR_{D/A}$ expression in terms of the photocurrent, the result is independent of the photocathode type, area, and absolute sensitivity. For specific photocathodes, the $SNR_{D/A}$ can be found as a function of irradiance through use of the relation

$$i_{\max} = \sigma A H \quad (220)$$

as previously noted. The $SNR_{D/A}$ obtainable from the sensors calculated as a function of i_{\max} and plotted for the SEBIR with 16-mm target is shown in figure 81 and for the SEBIR with 25-mm target in figure 82. Using the $SNR_{D/A-T}$ curves, threshold resolution versus photocurrent is plotted in figure 83 for three input image contrasts. Scales are also provided for high-light photocathode irradiance using a photocathode sensitivity of 3.33×10^{-3} ampere/watt and for equivalent illuminance using a sensitivity of 167 micro-amperes/lumen. The scale selected must be matched to the photocathode diameter used as noted to the right of the scales.

The effect of adding a single intensifier to the I-SEBIR on output signal current is shown in figure 78. These intensifiers may be of the unit magnification type or the zoom type as previously discussed. The gain provided by the added intensifier is assumed to be 40 times the ratio of input photocathode area (the intensifier) to that of the TV camera tube (the SEBIR). The overall gain of the intensifier-SEBIR camera tube is sufficient to ensure that the sensor will be photoelectron noise limited rather than preamplifier noise limited which permits a considerable simplification in the analysis as can be seen from the $SNR_{D/A}$ expression.

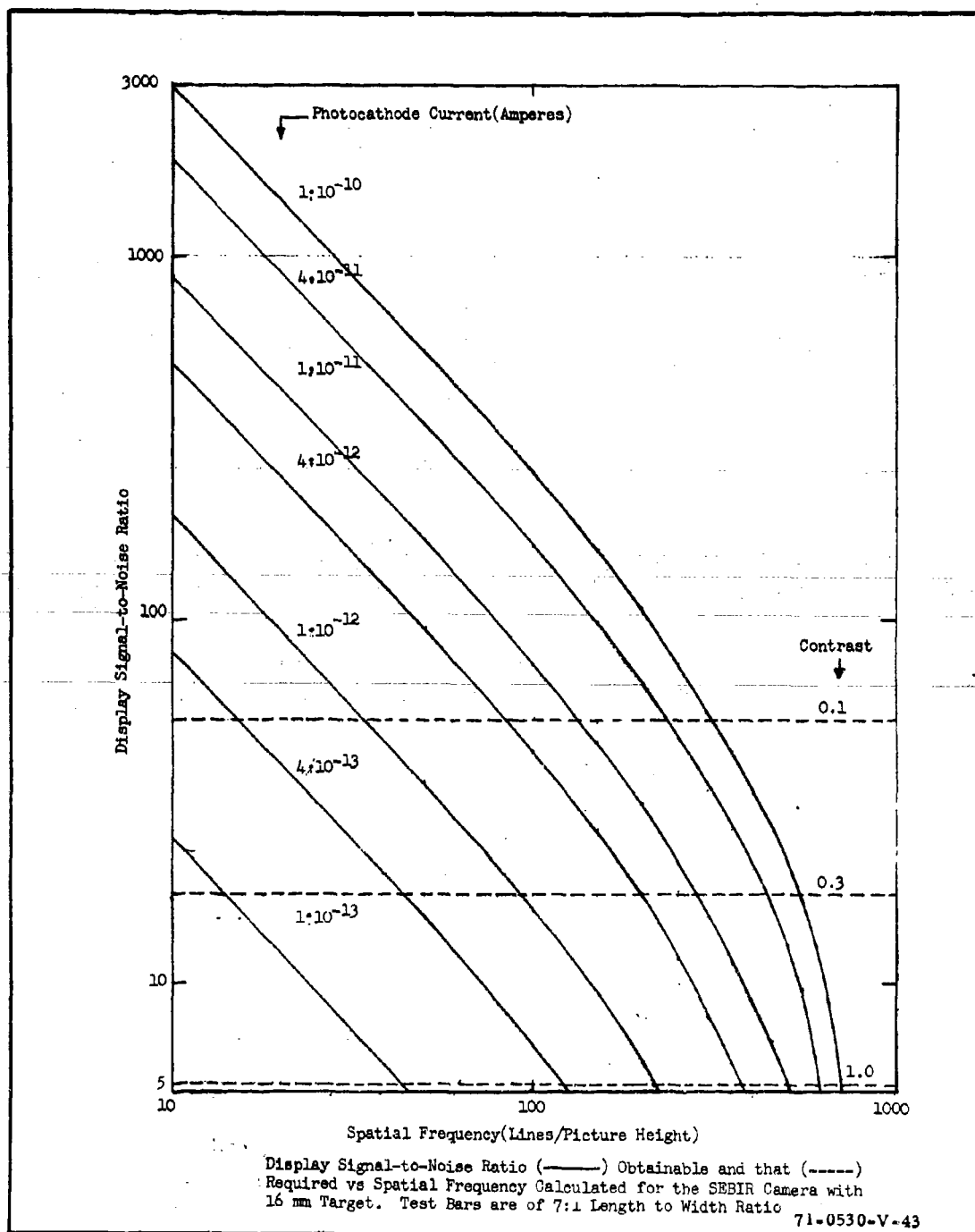


Figure 81. Display Signal-to-Noise Ratio for SEBIR Camera with 16-mm Target

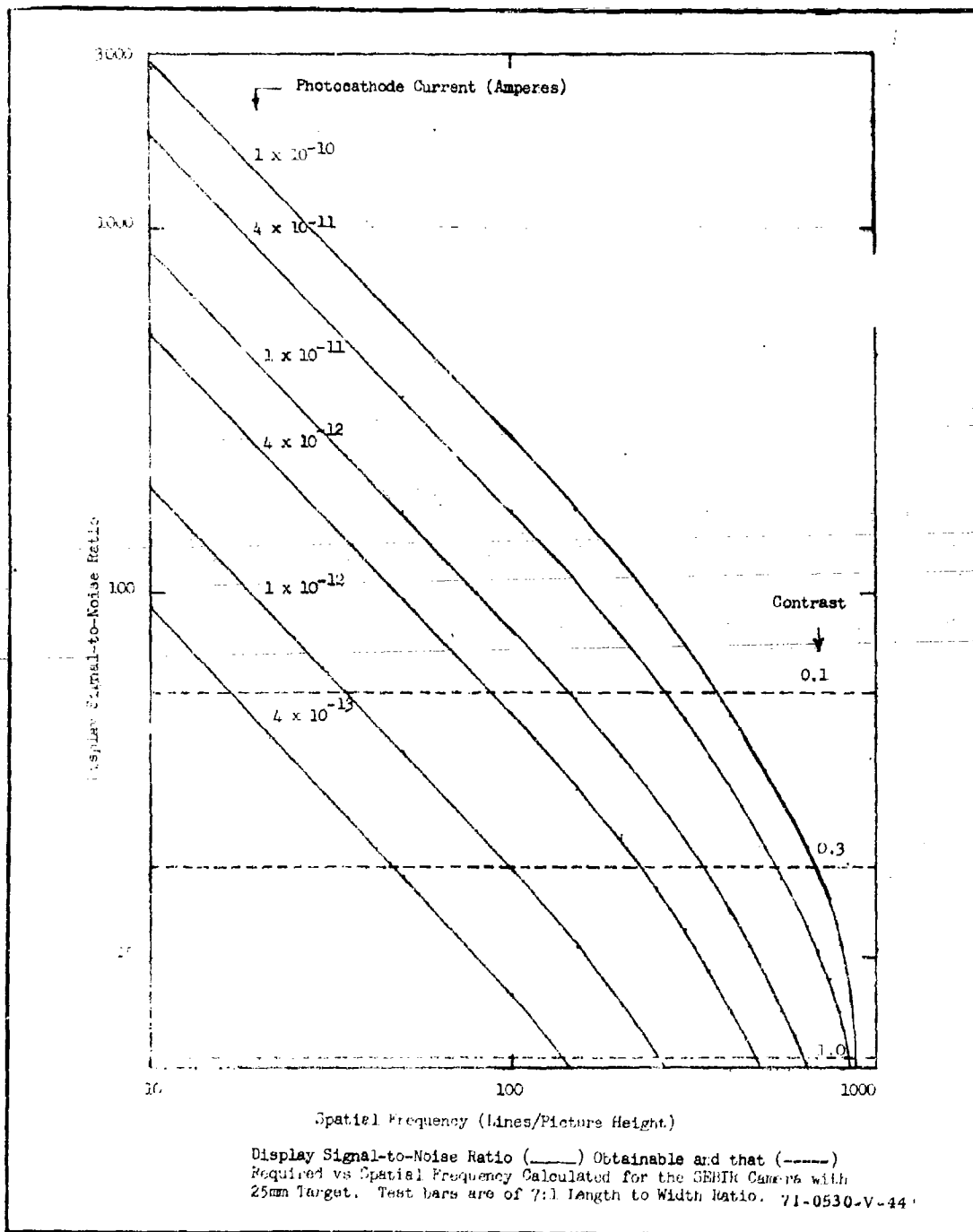


Figure 82. Display Signal-to-Noise Ratio for SEBIR Camera with 25-mm Target

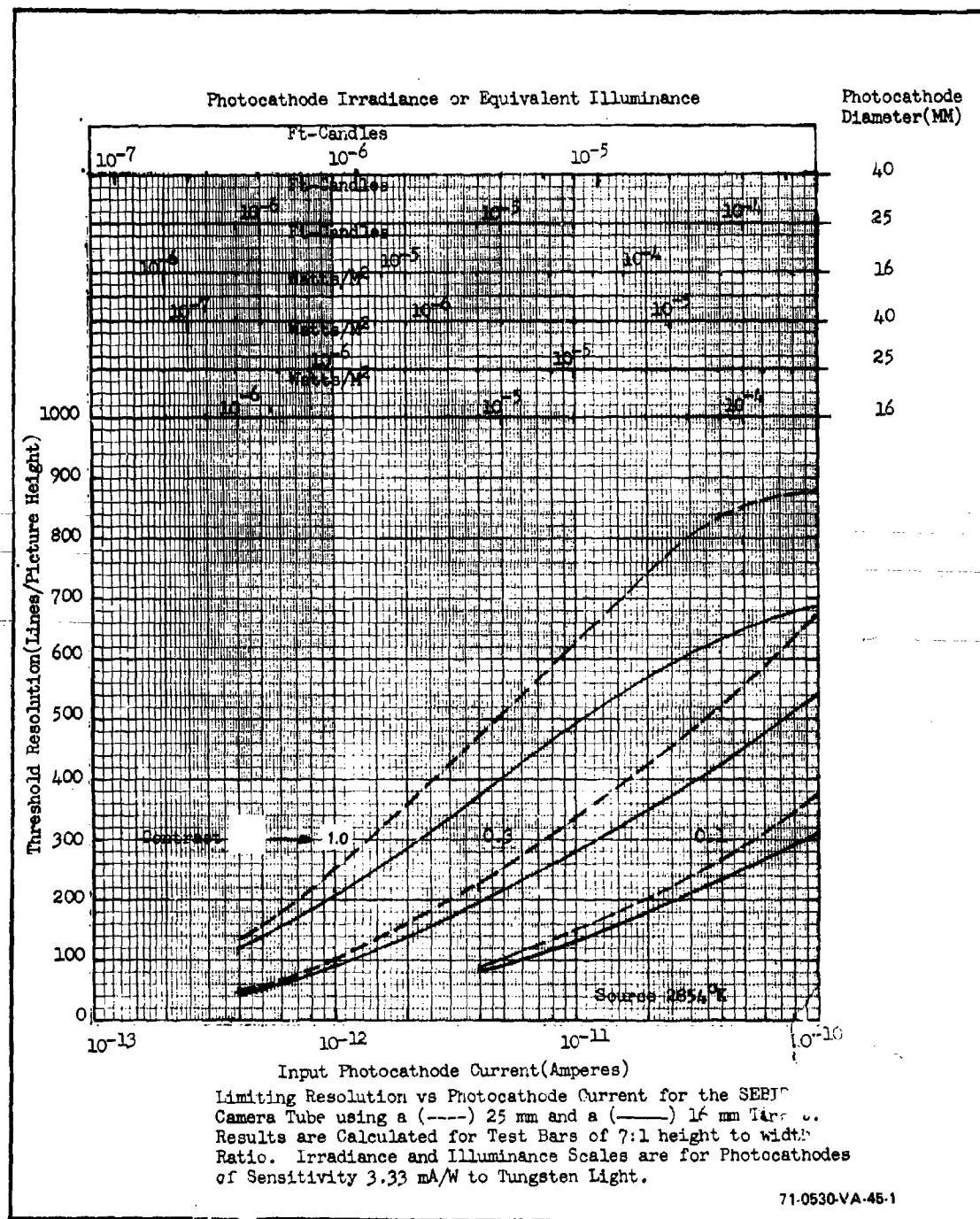


Figure 2. Limiting Resolution Versus Photocathode Current for the SEBIR Camera Tube

$$\text{SNR}_{D/A} = \left[\frac{n_v t}{a} \right]^{1/2} \frac{|R_o(N_h)|^{1/2}}{N_h} \left[\frac{i_{\max}}{e_v \cdot e_h \cdot e} \right]^{1/2} \quad (221)$$

We can now solve the above equation for i_{\max} and determine threshold resolution directly by setting $\text{SNR}_{D/A}$ equal to 5.3 and by using the modulation transfer curves of figure 84.

The MTF curves require some explanation. In the current state of the art, the photocathodes are of very high resolution compared to that of the intensifier's phosphor. Hence, as the photocathode of the SEBIR camera tube is reduced in diameter, the intensifier phosphor diameter must be reduced to match. This results in a reduction in overall sensor modulation transfer as shown. The designation 80/40, 80/25, etc, refers to the ratio of intensifier photocathode diameter to intensifier phosphor diameter.

Finally, the threshold resolution versus input photocathode current curves are calculated using equation 221 and plotted in figures 85 and 86. Note that

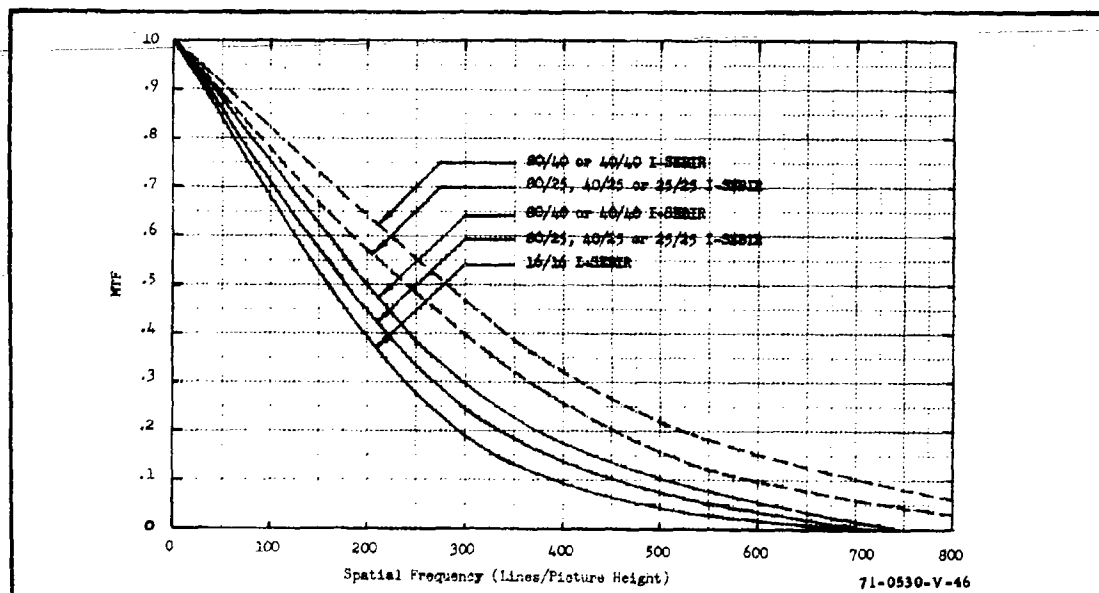
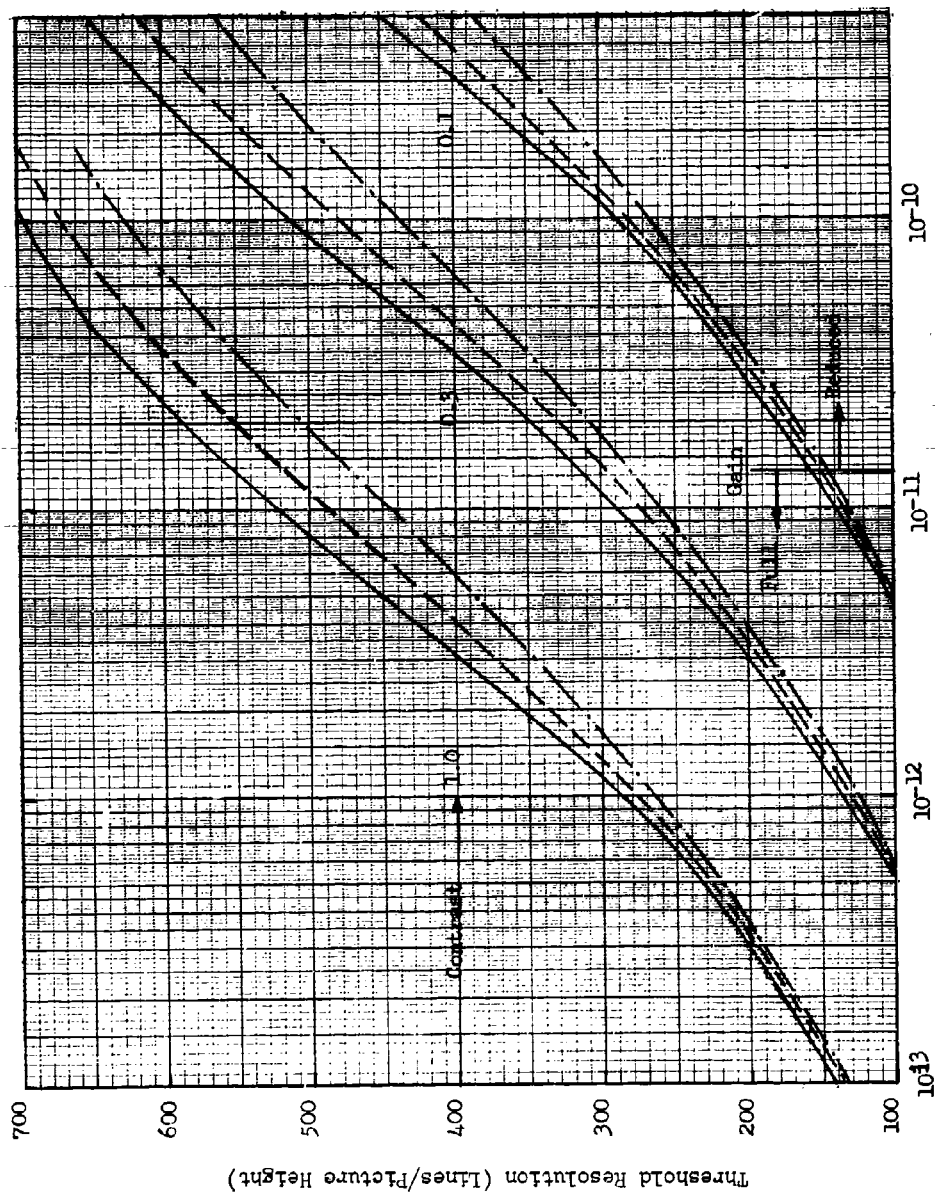


Figure 84. Modulation Transfer Function for Various Intensifier-SEBIR Tubes

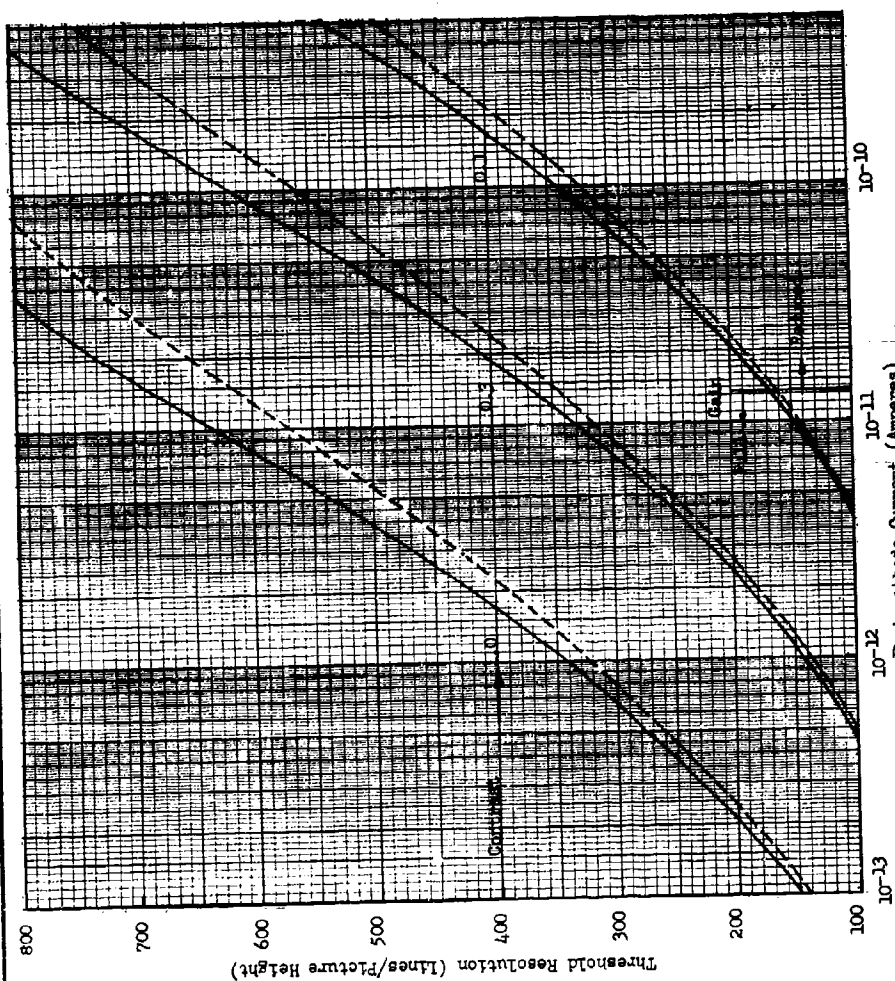


Photocathode Current (Amperes)

Threshold Resolution vs Input Photocathode Current for Intensifier-SEBIR Camera
 Tube with 16mm Target and (—) 40/40 or 80/40, (- - -) 25/25 or 40/25 or 80/25,
 or (---) 16/16mm Intensifiers, Calculations are for Test Bars of 7:1
 Height to Width Ratio.

71-0530-V-47

Figure 85. Threshold Resolution Versus Input Photocathode Current for Intensifier -
 SEBIR Camera Tube With 16-mm Target



Threshold Resolution vs Input Photocathode Current for Intensifier-SEBIR Camera Tubes with 25 mm Target and (---) 80/40 or 40/40, or (---) 80/25, 40/25 or 25/25 mm Intensifiers. Calculations are for Test Bars of 7:1 Height to Width Ratio. 71-0530-V-48

Figure 86. Threshold Resolution Versus Input Photocathode Current for Intensifier - SEBIR Camera Tubes With 25-mm Target

for input photocathode currents above 1.32×10^{-11} ampere, the sensor gain will be excessive and must be reduced in order to stay within the dynamic range of the sensor (assumed to be limited to about 1 microampere in output signal current). The threshold resolution versus photocathode irradiance curves are shown for a variety of I-SEBIR camera tubes in figure 87. The curves are shown for an input contrast of 100 percent. A factor of about 10 times irradiance is needed for input contrast of 30 percent and 100 times more for input contrasts of 10 percent.

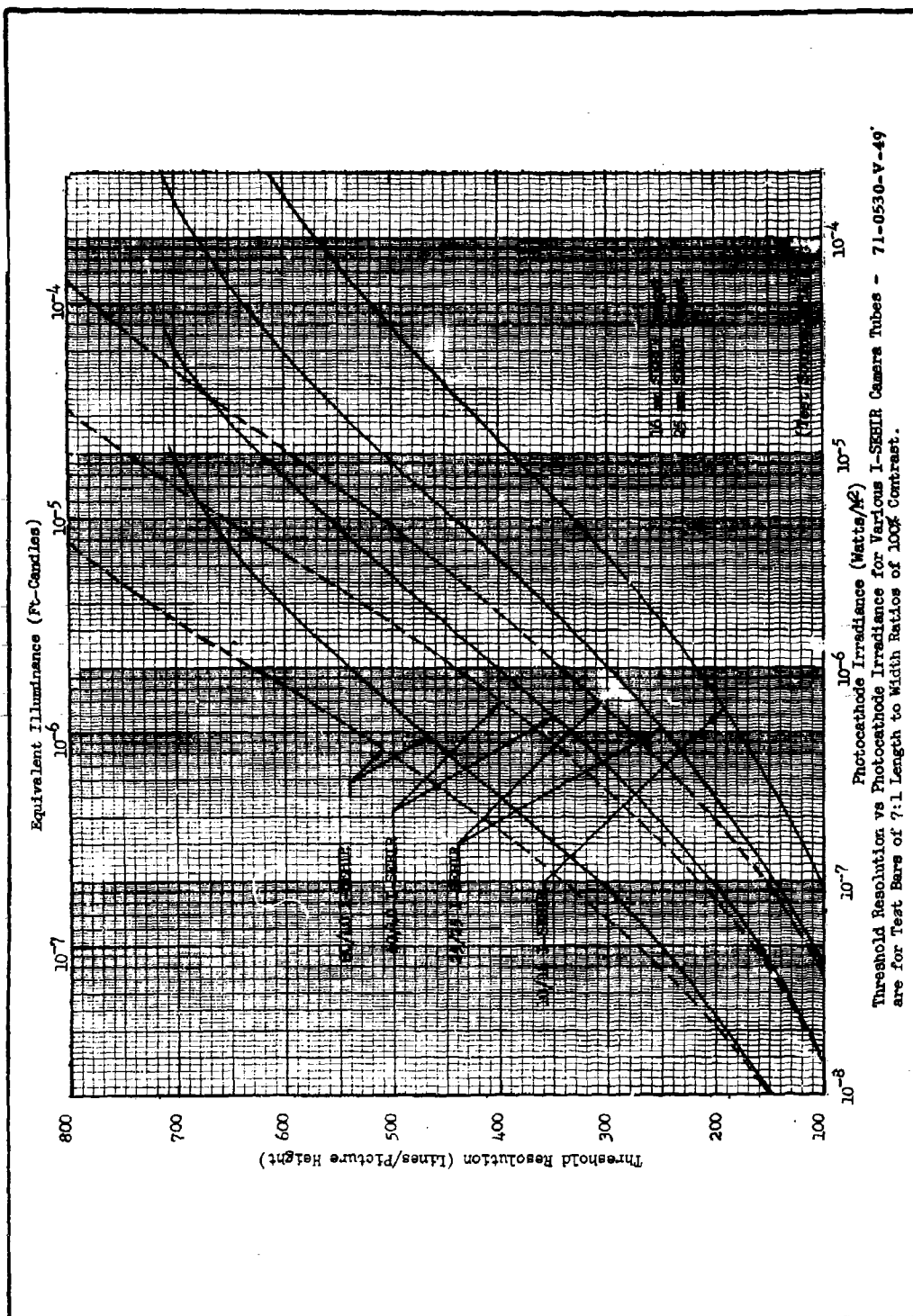


Figure 87. Threshold Resolution Versus Photocathode Irradiance for Various I-SEBIR Camera Tubes - Calculations are for Test Bars of 7:1 Length to Width Ratios of 100 Percent Contrast

SECTION XII

VIDICON CAMERA TUBES

The term vidicon is used generally to describe those television camera tubes that employ a photoconductive photosurface, but it is also used to describe many other types of tubes in which the photosurface acts both as a photon-to-electron transducer and also as the signal storage medium. In this section, the term vidicon, when unmodified by other descriptors, will be restricted to tubes in which the surface is an Antimony-Trisulfide photoconductor. A second type of vidicon employs the silicon target used in the SEBIR camer tube, except that the target is mounted just behind the tube's glass faceplate, and the scene photon image is focused directly on it, rather than a photoelectron image generated by a separate photoemitter as in the case of the SEBIR. This tube is designated as the Silicon Vidicon and abbreviated SiV. A third type of vidicon is one using a lead oxide layer as its photosurface and it will be designated as the lead oxide vidicon or PbOV. One version of the SiV is known as the TIVICON*, and one version of the PbOV is known as the Plumbicon**.

12.1 PRINCIPLES OF OPERATION

All of the vidicons, including the SiV and PbOV operate in a similar manner, except for the details of the primary photoprocess. The schematic of a typical vidicon type of camera tube is shown in figure 88. A transparent signal electrode is deposited on the first surface of the photoconductor or "target". The faceplate can be either glass or a fiber-optic plate.

* Trademark of Texas Instruments, Inc.

** Trademark of Amperex Electronics Corp.

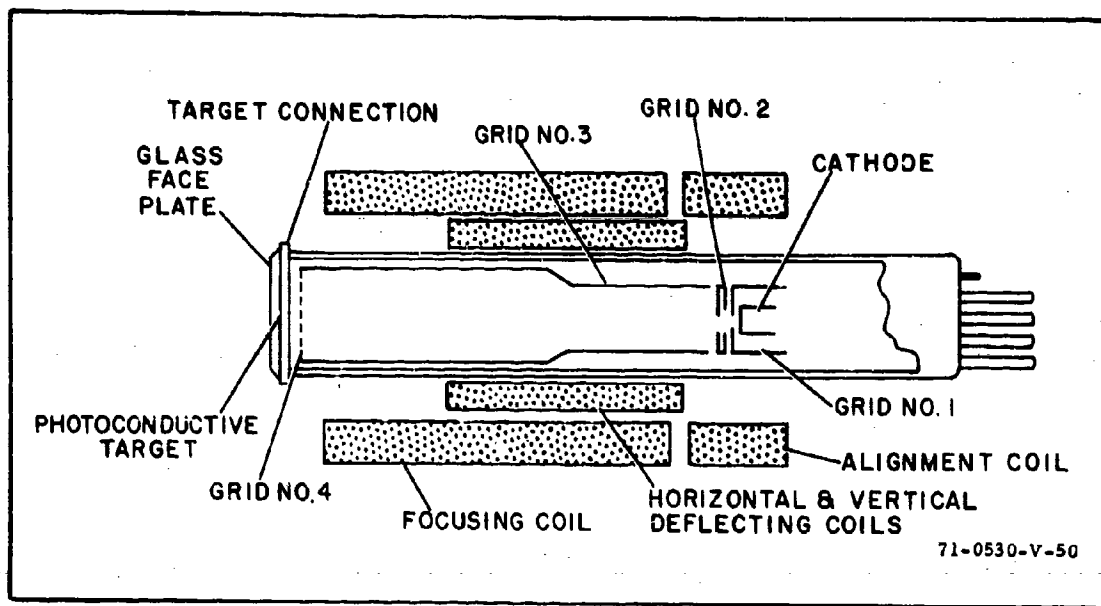


Figure 88. Schematic of Vidicon and Associated Focus, Deflection and Alignment Coils

Ordinarily, the signal electrode is biased 15 to 40 volts positive with respect to the electron gun. The side of the photosurface facing the electron gun is periodically charged to the electron gun potential by the action of the scanning electron-beam. If light is incident on a resolution element of the photosurface during the interval between successive scans, electrons are generated within the photosurface and move in an appropriate direction so as to discharge the charge stored on it. However, current cannot flow in the external target lead resistor until the beam once again passes the illuminated point. The function of the beam is to recharge the photosurface point-by-point back to gun-cathode potential, and the resulting charging current flowing through the target lead constitutes the video signal. Signal storage results from the fact that scene light impinging on a point on the photosurface continually discharges it between successive passes of the beam. The charge replaced by

the beam is the total integrated amount of discharge during the period between scans. This period is called the frame time. In commercial practice the frame time is 1/30 second.

There are usually three important time constants in the operation of the tube. First, there is a signal storage time constant, consisting of the product of photosurface capacitance and resistivity. This time constant should be long compared to the frame time. A second time constant is associated with the photoprocess itself and has to do with the mobility of charge carriers. The third time constant is a product of the beam resistance times the photosurface capacitance. Both the second and third time constants, which collectively limit the speed and efficiency of signal readout, should be short.

As is well known, photoconductors and other photosensitive semiconductors can provide photon conversion efficiencies larger than unity, but when the additional requirements of signal storage and a reasonable time constant are imposed, this possibility is precluded for practical purposes. Because of this lack of gain in the photosurface, the limiting noise becomes that of the camera's video preamplifier in real-time imaging applications. While considerable care should be exercised in the design of the preamplifier, the extraordinary measure of incorporating a low-noise internal secondary emission preamplifier, such as a return beam electron multiplier or isocon readout, is seldom warranted, except in very special applications. This is due to the fact that the lag characteristics of these tubes are light level dependent, and at the light levels where the reduced noise of the electron multiplier is effective, the lag far exceeds that tolerable for real-time imaging of scenes in motion. These lag effects are more serious for the vidicon than for the SiV or PbOV vidicons, but are of concern in either case.

12.2 THE SILICON VIDICON

As previously noted, the silicon photoconductor used in the SiV is identical to the SEBIR target described in Section XI and illustrated in figure 77. In the SEBIR mode, a photoelectron image impinges on the silicon target, and it

is the function of the target to both amplify and store the image for subsequent readout by the electron scanning beam. In the vidicon case, the target converts the scene photons to electrons directly and stores the image for readout but provides no signal amplification. Although vidicons of any kind are relatively insensitive, the SiV is considerably more sensitive than either the ordinary vidicon or the PbOV. It is also less laggy at the lower light levels. Large irradiance overexposures can be tolerated without harm.

The spectral response of the SiV is shown in figure 89 and it is seen to be relatively uniform from 0.45 to 0.9 microns. Its quantum efficiency exceeds 50 percent over much of this spectral band. To 2854°K tungsten radiation, sensitivities of the order of 45 mA/W are typically recorded. The signal current, I , versus photosurface irradiance, H , characteristic is given by the formula

$$I = \sigma A H / e_v \cdot e_h \quad (222)$$

and plotted in figure 90 assuming a tungsten source and a photocathode of

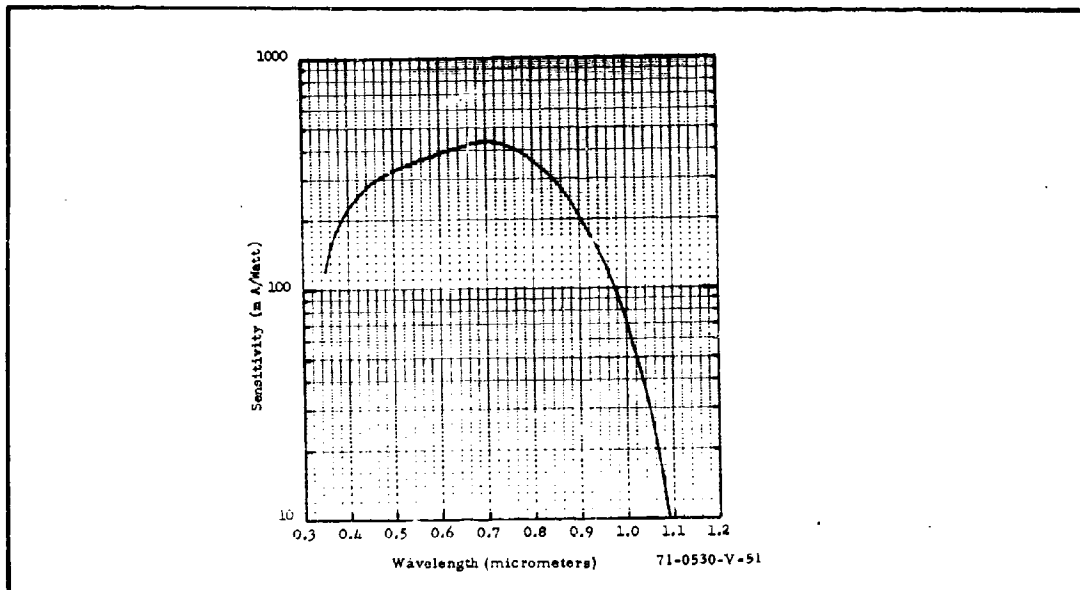


Figure 89. Spectral Response of the Silicon Vidicon

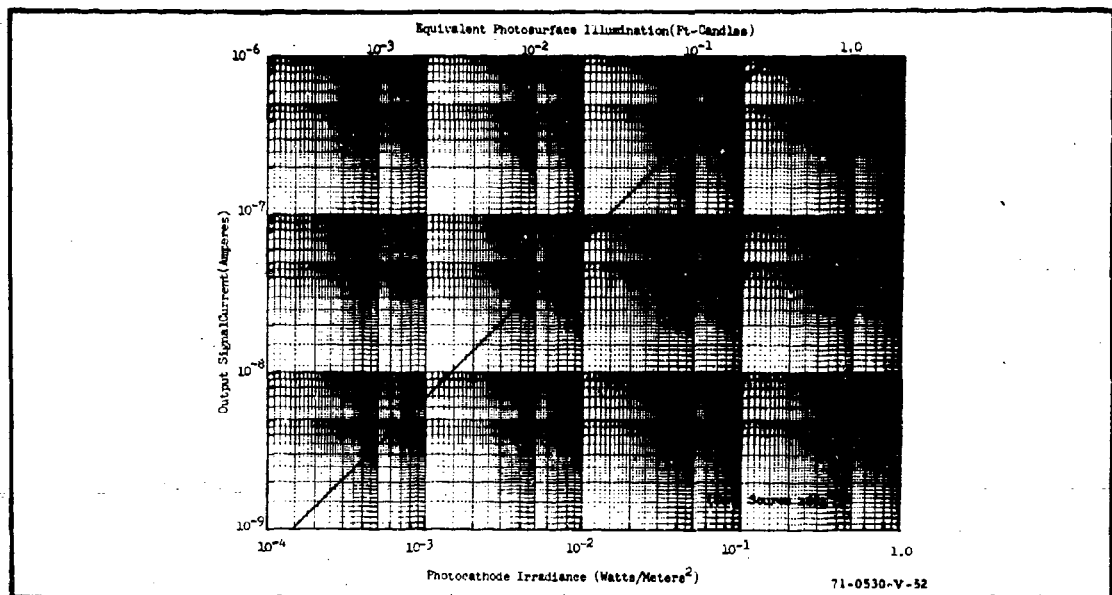


Figure 90. Output Signal Current Versus Photosurface Irradiance Transfer Characteristic for the Silicon Vidicon with 16-mm Photosurface Diameter

diameter 16 mm, a 4 x 3 picture aspect ratio, a sensitivity of 45 mA/W and a scan efficiency of 0.79.

The MTF of the SiV is plotted in figure 91 as a function of spatial frequency. Since the SiV is preamp noise-limited over its range of operation, the display S/N ratio for a bar test pattern of constant bar height to width ratio, n_v , becomes simply

$$\text{SNR}_{D/A} = \left[t n_v \Delta f_v / \alpha \right]^{-1/2} \cdot \frac{|R_o(N_h)|}{N_h} \cdot \frac{C I_{\max}}{I_P} \quad (223)$$

where I_P is the rms preamplifier noise as before. The above equation is solved for the irradiance, H , using equation 222, and threshold resolution is calculated using $n_v = 7$, $\Delta f_v = 10^7$, $\alpha = 4/3$, and an rms preamp noise of 3×10^{-9} amperes. The result is plotted for various contrasts in figure 92.

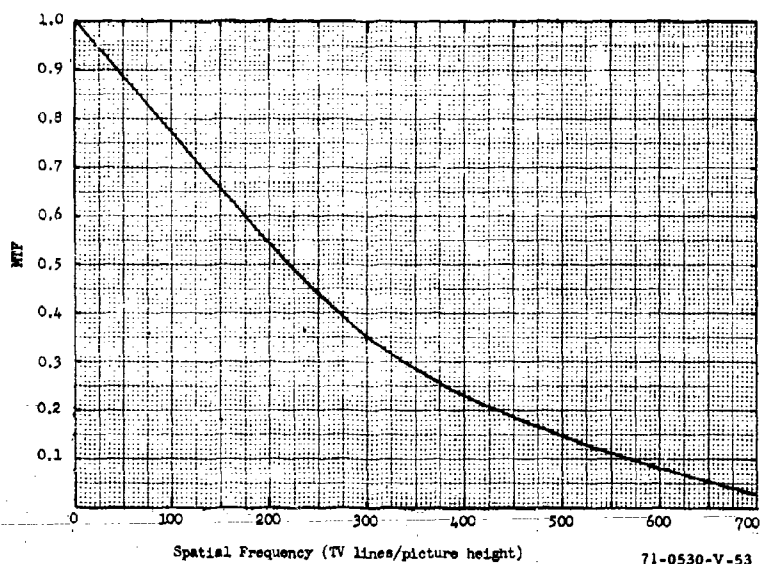


Figure 91. Modulation Transfer Curve for the Silicon Vidicon With Photosurface of 16-mm Diameter

In principle, one could fiber-optically couple an intensifier to a SiV; but in practice, this may not be readily accomplished, because the target would have to be in intimate contact with the fiber optic plate. So far as is known, this has not yet been achieved.

12.3 THE LEAD-OXIDE VIDICON

The lead-oxide vidicon or PbOV was developed after the vidicon but prior to the SiV. The photosurface of the PbOV consists of a layer of reversed biased PIN photodiodes. In operation, this surface is similar to that in a vidicon, except that the discharge of the layer capacitance by light takes place by hole-electron pairs photogenerated in the i-layer. Nearly all of the target potential is impressed across this layer, and the resulting electric field rapidly sweeps the holes generated to the electron gun or p-side and the electrons to the input window or n-side. The p and n contacts act as blocking electrodes, preventing the injection of carriers so that only

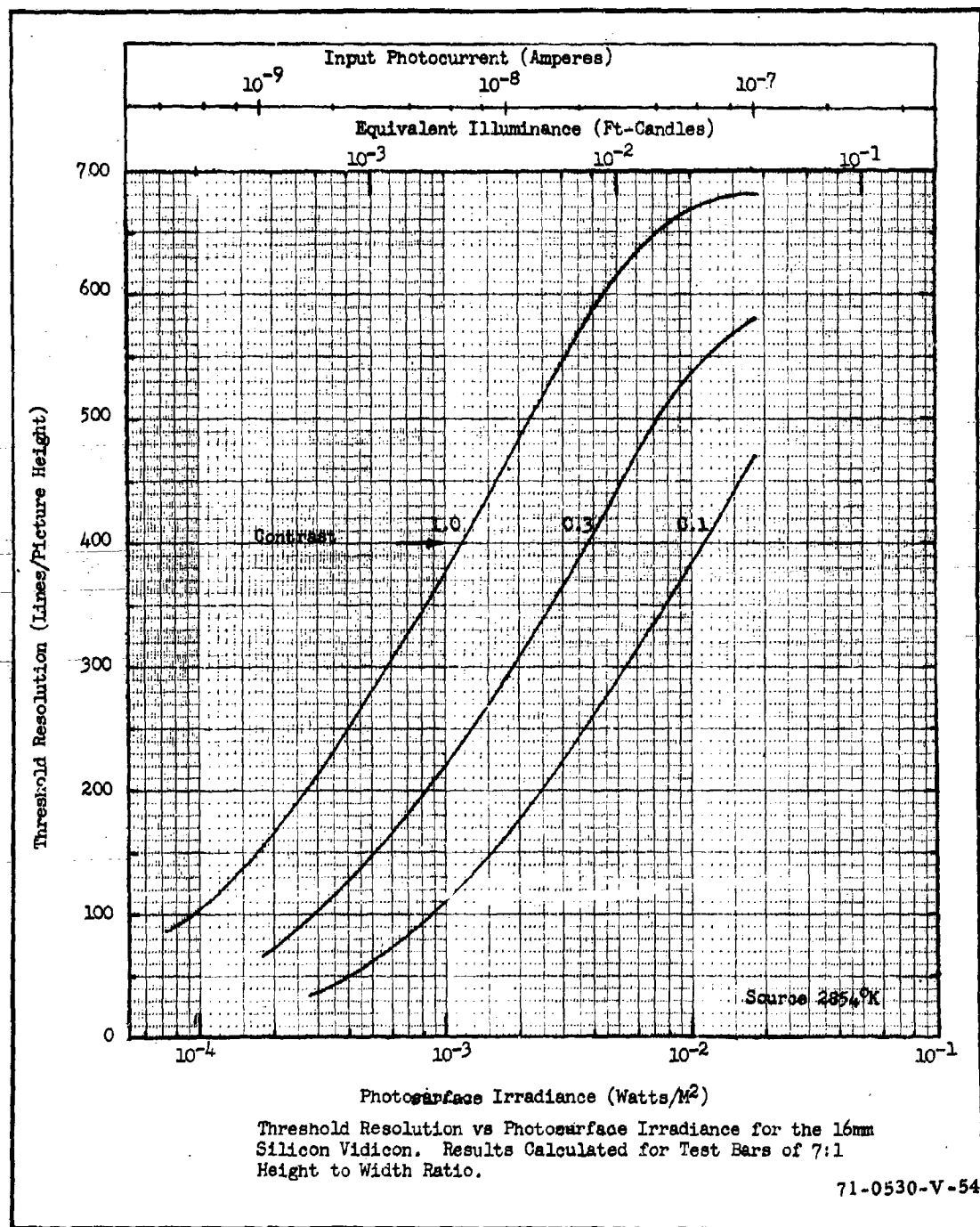


Figure 92. Threshold Resolution Versus Photosurface Irradiance for the 16-mm Silicon Vidicon

thermally-generated hole-electron pairs can contribute to the dark current. These are generated at a very low rate due to the 1.9 ev bandgap of PbO.

The advantages claimed for the PbOV are that its dark current is intrinsically very low, that the dark current reaches a saturation at a low level as target potential is increased, that the signal and dark currents are independent of temperature over a quite wide range about room temperature, and that the lag is quite small compared to that of a vidicon. The gamma of the PbOV, like the SiV is near unity as opposed to the value of 0.65 typical of vidicons. This is claimed to be an advantage in color TV and in ratio-metric applications. The PbOV is understood to be relatively immune to damage by bright lights as is the SiV.

The spectral response of the usual PbOV is shown in figure 93. The left ordinate applies to tubes with a glass faceplate, while the right ordinate applies to tubes with a fiber optic faceplate. PbOV surfaces are also available with greater red response at some sacrifice in MTF. The sensitivity to tungsten light with a glass faceplate is reported to be 7-9 mA/W and with a fiber-optic faceplate, 4-5 mA/W.

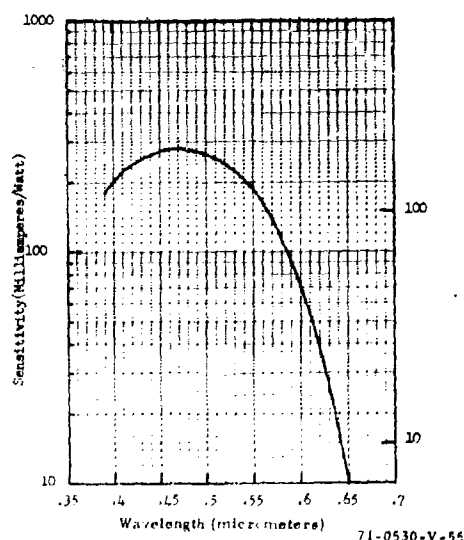


Figure 93. Spectral Response of the Standard Lead Oxide Vidicon Left Ordinate Applies to Tubes with Glass Faceplate - Right Ordinate, Fiber-Optic Faceplates

The signal current versus photosurface irradiance characteristics are plotted in figure 94, for an individual PbOV and for the PbOV in combination with a single and a double intensifier. The latter combinations are abbreviated I-PbOV and I^2 -PbOV. The photosurface of current PbOV tubes is 21.6 mm in diameter. While the sensitivity of the PbOV surface to tungsten light is comparable to that of a good S-25 surface, its sensitivity in the green is considerably higher. Thus, it is a better spectral match to the green P-20 phosphor. It is estimated that the electron gain at a P-20/PbOV phosphor-photocathode interface will be 100. A second intensifier will increase the overall gain to 4000.

The MTF's of the various PbOV and intensifier PbOV combinations are shown in figure 95. With these curves, we have sufficient data to calculate the display signal-to-noise ratio using equation 219 (Section XI) and the threshold resolution versus photocurrent characteristics in turn. These characteristics are shown for the PbOV (with glass faceplate) in figure 96 and for the I-PbOV and I^2 -PbOV in figure 97.

12.4 THE VIDICON

As previously discussed, the term vidicon, when unmodified by other descriptors, is restricted herein to those tubes in which the photosurface is an Antimony-Trisulfide photoconductor. Except for the detailed photon-to-electron conversion mechanism in the primary photoprocess, the principles of operation of the vidicon is identical to that of the SiV and PbOV. The main differences due to the photosurface are that the gamma or slope of the vidicon's signal current versus irradiance characteristic is less than unity, the lag due to the photoprocess is appreciable, and the dark current can be quite large even at room temperature. The vidicon's low gamma is sometimes an advantage, because it increases dynamic light latitude range and compensates somewhat for the larger than unity gammas of a cathode ray tube display.

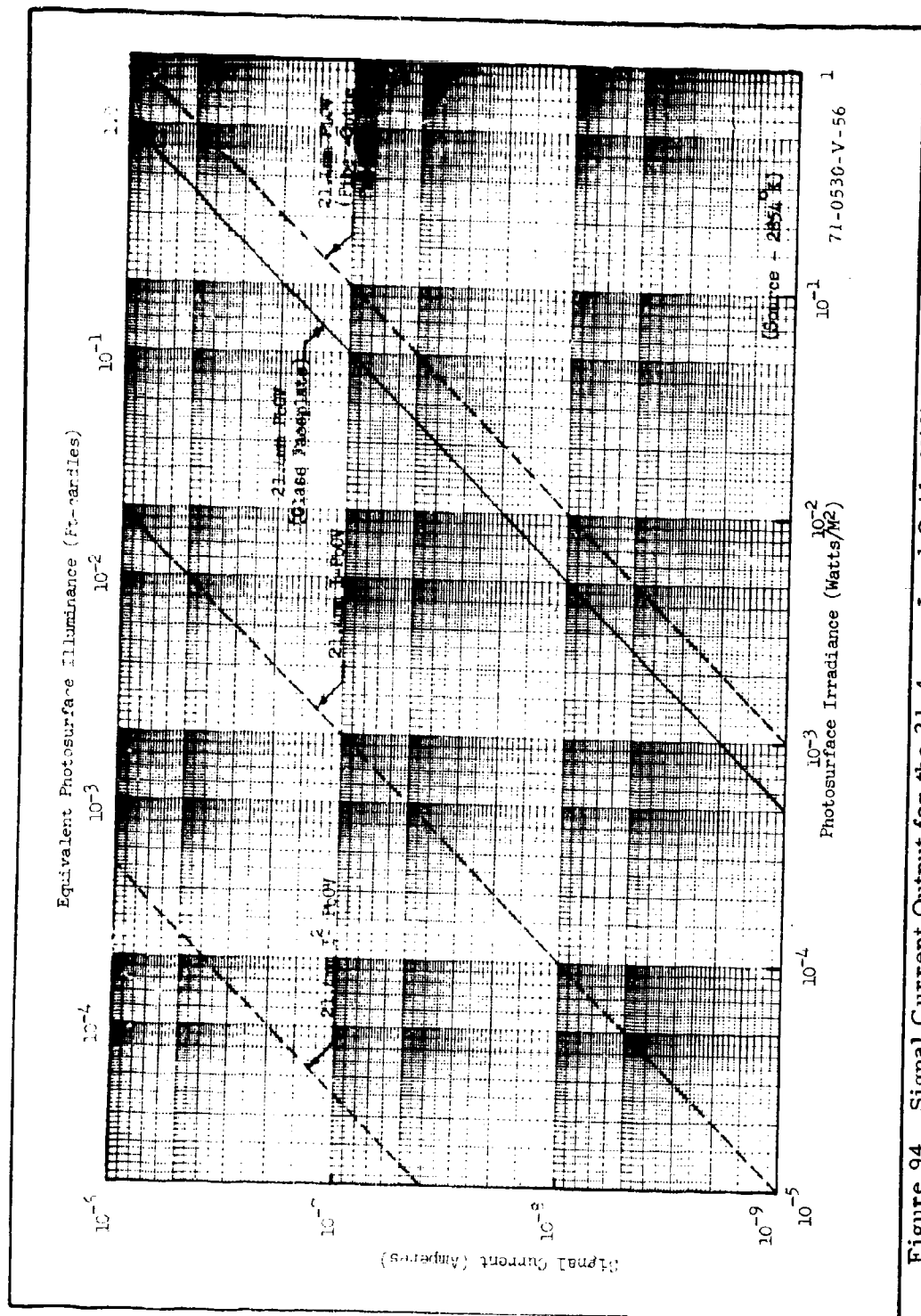


Figure 94. Signal Current Output for the 21.4-mm Lead Oxide Vidicon, Intensifier Lead Oxide Vidicon, and Double Intensifier Lead Oxide Vidicon as a Function of Photosurface Highlight Irradiance

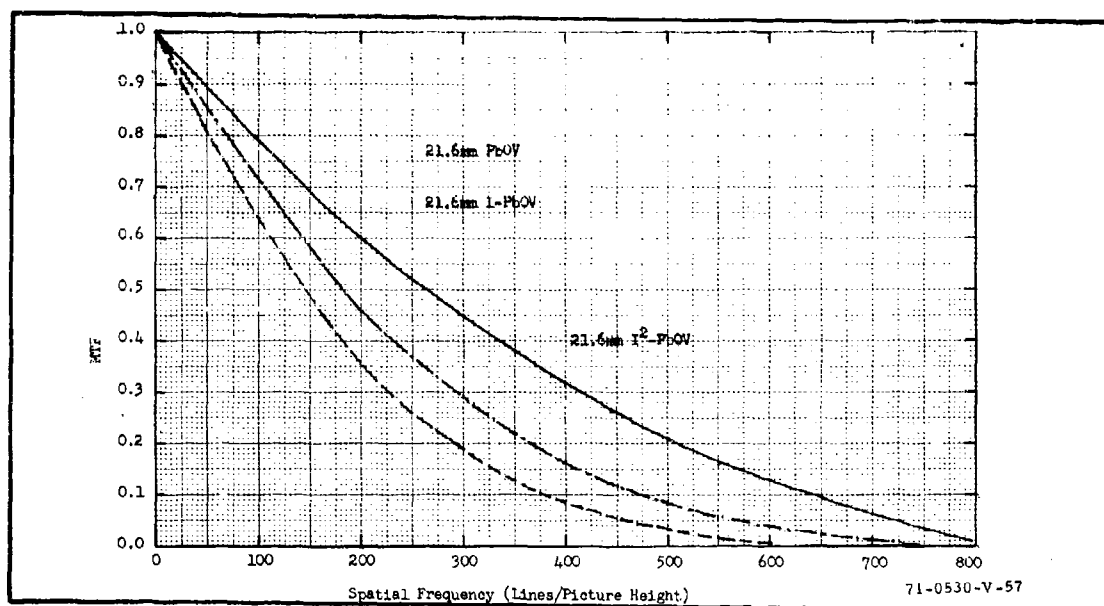


Figure 95. Modulation Transfer Function for the 21.6-mm Lead Oxide Vidicon, Intensifier Lead Oxide Vidicon, and Double Intensifier Lead Oxide Vidicon

The lag of a vidicon can be reduced by making its photoconductor fluffy and thus, thicker. However, this decreases sensitivity as well. In some applications, the lag is intentionally made long, because this increases the signal storage capability of the surface and permits slow scan operation. Aside from control of the photosurface's physical dimensions, lag can also be decreased by increasing the voltage across it. Actually, lag at a given photocurrent may increase somewhat as photosurface voltage is increased, but the increase in photosurface sensitivity obtained thereby usually results in a lower lag for a given value of input irradiance. Along with increased sensitivity, a larger photosurface potential results in an increase in dark current, which modulates surface non-uniformities and decreases picture quality.

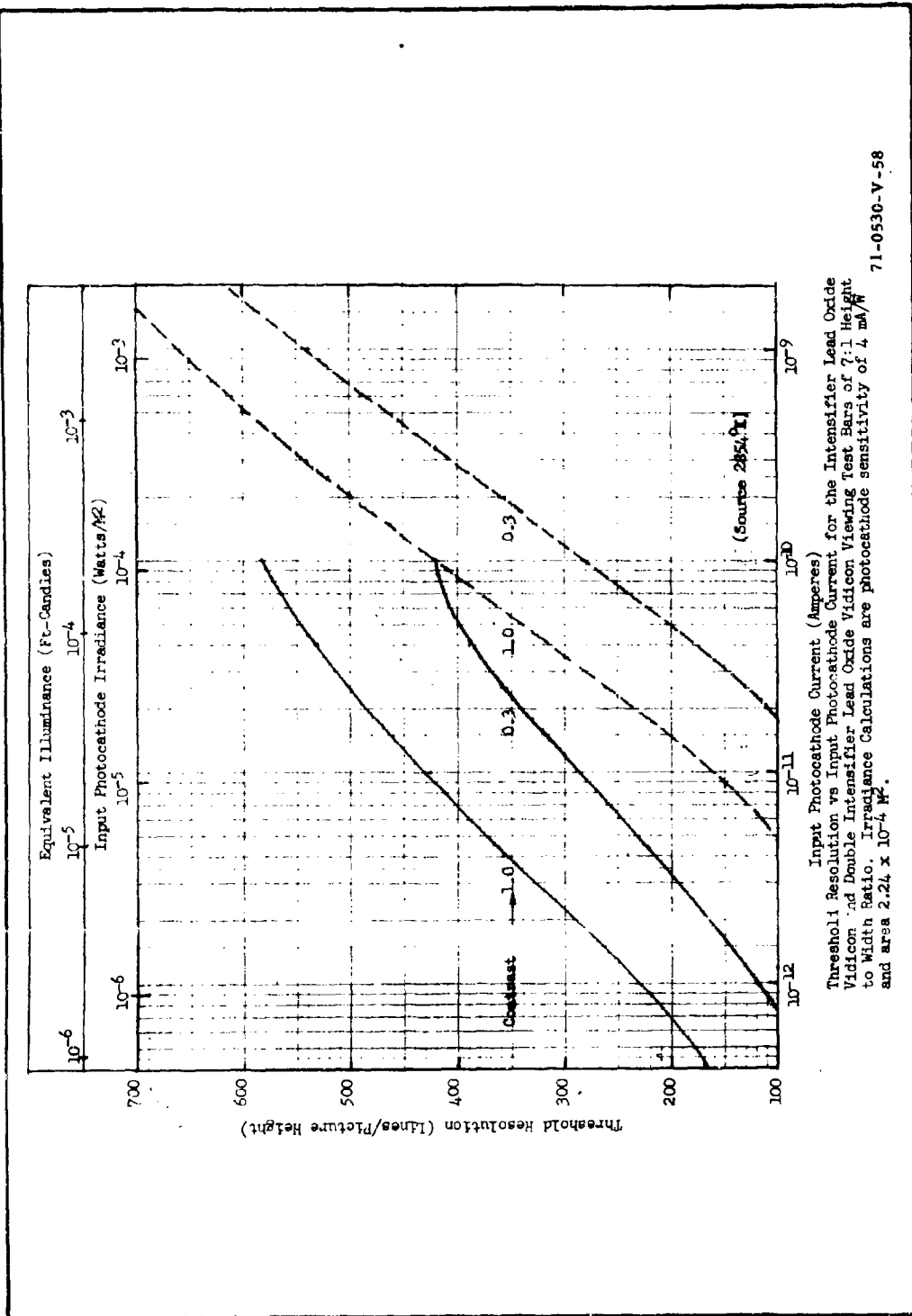


Figure 96. Threshold Resolution Versus Input Photocathode Current

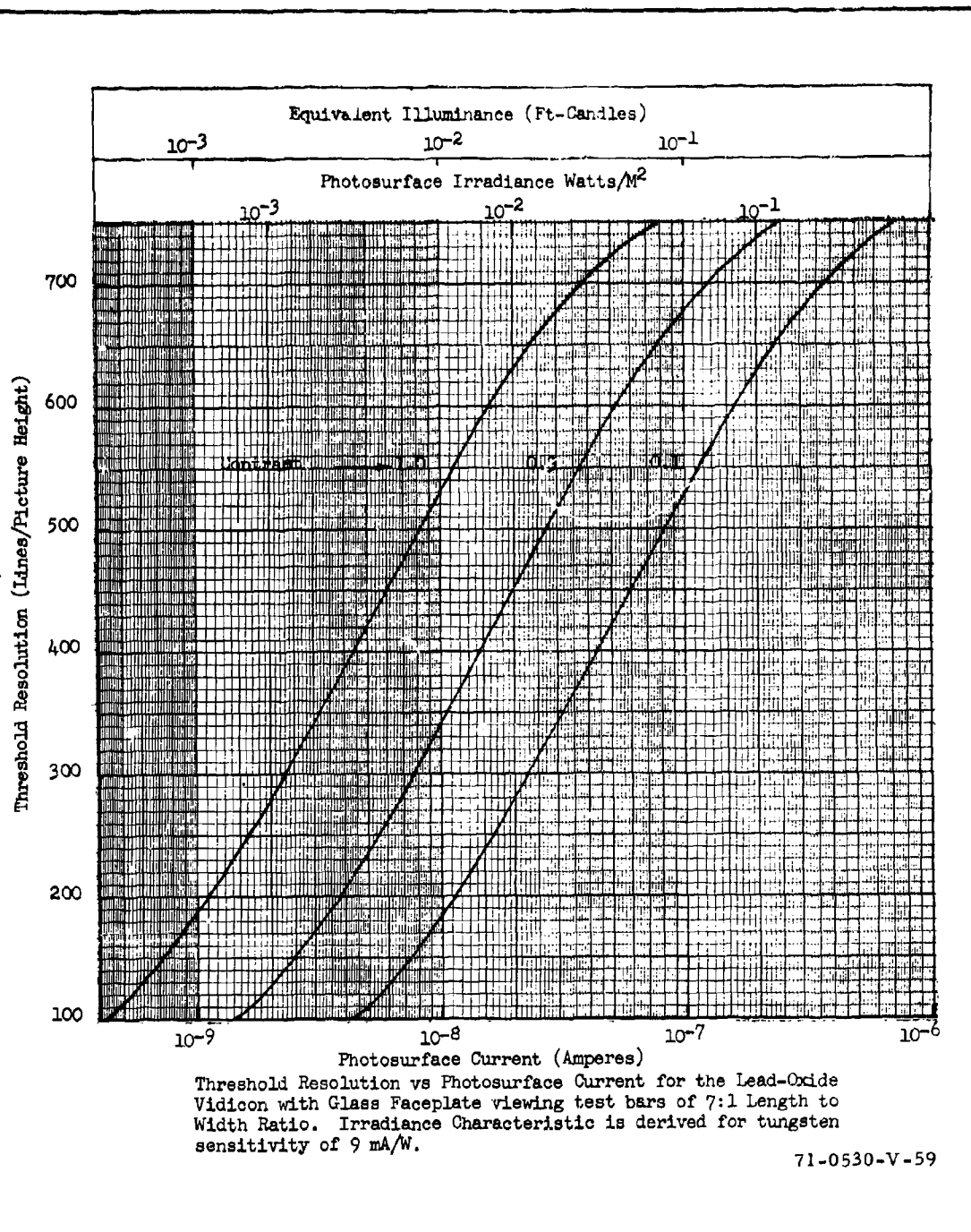


Figure 97. Threshold Resolution Versus Photosurface Current

The gamma of the Antimony-Trisulfide photosurface is very nearly equal to 0.65 but is somewhat variable. One problem with a gamma different than unity is that its absolute spectral responsivity is not unique, but rather, it depends upon the level of the photon flux incident upon it. Ordinarily, a curve is supplied by the manufacturer that is designated here as the specific spectral responsivity. This curve is a plot of sensitivity in amperes/watt of incident monochromatic radiation as is usually the case, but it is specific in that it holds only for the conditions under which it was measured. The method of measurement is to adjust the monochromatic irradiance of the photocathode at each wavelength to provide a given constant value of output current. With other values of input radiation or output current, different values for the specific responsivity would result, which makes the calculation of photocurrent to an arbitrary radiation source somewhat difficult. However, using a modification of an analysis by Selke²⁸ the specific responsivity can be generalized as follows.

A typical specific spectral responsivity curve which applies to the majority of antimony-trisulfide vidicons is shown in figure 98. At any wavelength λ , the photocurrent may be written as

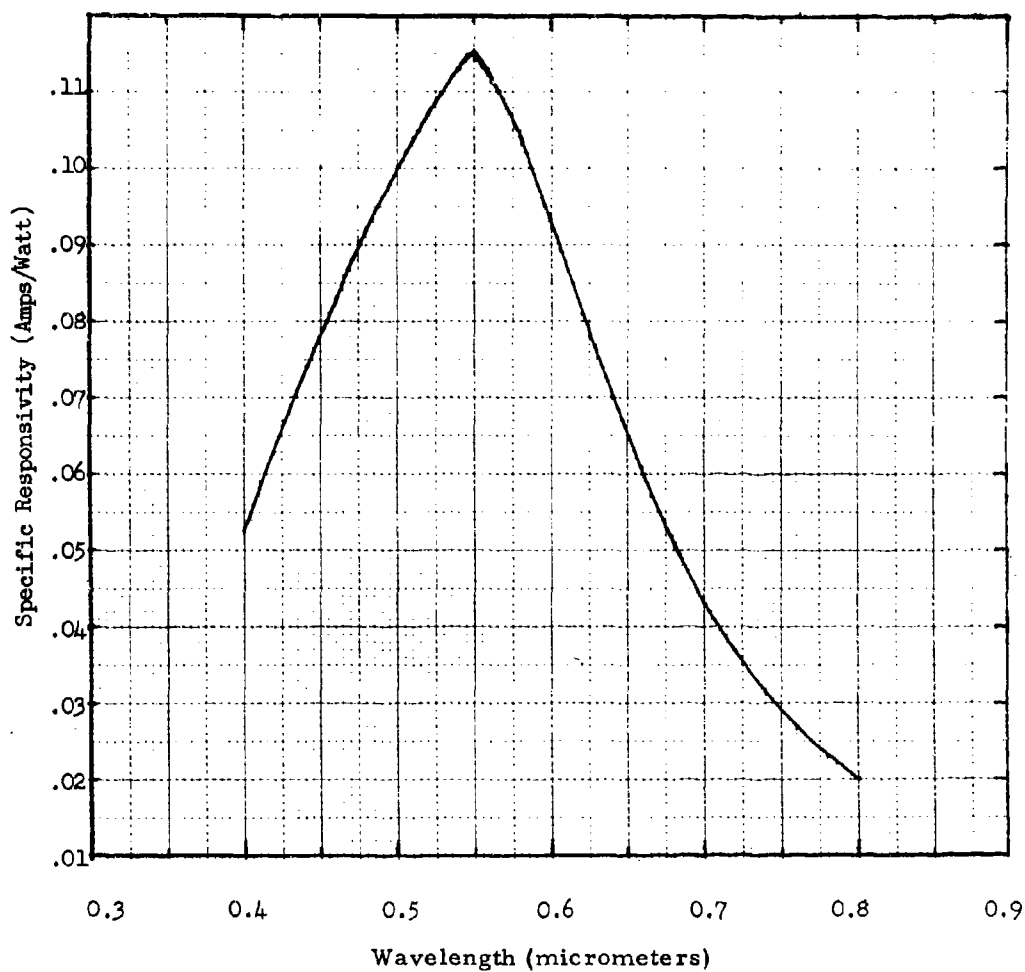
$$i_{\lambda} = \left[A k_{\lambda} H_{\lambda} \right]^{\gamma} / e_v \cdot e_h \quad (224)$$

where A is the scanned area, k_{λ} is a constant that will be called the spectral response factor, and $e_v e_h$ are the vertical and horizontal scan efficiencies respectively. Solving the above for k_{λ} we have that

$$k_{\lambda} = \frac{1}{A H_{\lambda}} \left[i \cdot e_v e_h \right]^{1/\gamma} \quad (225)$$

Numerical values for k_{λ} are found by use of the specific spectral responsivity curves of figure 98 and the equation,

$$H_{\lambda 1} = \frac{e_v e_h i_{\lambda 1}}{R_{\lambda 1} \cdot A} \quad (226)$$



Specific Spectral Responsivity for a Typical Porous Antimony-Trisulfide Photosurface for Equal Values of Signal Current at all Wavelengths (for Output Signal Current of $2 \cdot 10^{-8}$ A, Dark Current of $2 \cdot 10^{-8}$ A and Scanned Area of $\frac{1}{2}$ " x $\frac{3}{8}$ ".)

71-0530-V-60

Figure 98. Specific Spectral Responsivity for a Typical Porous Antimony-Trisulfide Photosurface

where $H_{\lambda 1}$ is the photocathode irradiance at wavelength λ_1 corresponding to the photocurrent $i_{\lambda 1}$ due to the specific sensitivity $R_{\lambda 1}$ from the curve.

Combining the above two equations we find that

$$k_{\lambda 1} = R_{\lambda 1} \left[i_{\lambda 1} e_v e_h \right]^{\frac{1-\gamma}{\gamma}} \quad (227)$$

The current $i_{\lambda 1}$ is $2 \cdot 10^{-8}$ amperes for the curve and $e_v e_h$ is typically 0.79. Thus,

$$\begin{aligned} k_{\lambda 1} &= R_{\lambda 1} \cdot \left[1.58 \cdot 10^{-8} \right]^{.538} \\ &= 6.36 \cdot 10^{-5} R_{\lambda 1} \end{aligned} \quad (228)$$

Thus, $k_{\lambda 1}$ is related to $R_{\lambda 1}$ by a constant. The constant $k_{\lambda 1}$ is independent of the output current provided that photosurface voltage is a constant.

(Sensitivity can be increased by increasing photosurface voltage at the expense of an increase in dark current.) We can now find the output signal current due to any arbitrary source of radiant energy from the formula

$$I = \left[A \int_0^{\infty} k_{\lambda} H_{\lambda} d_{\lambda} \right]^{\gamma} / e_v \cdot e_h \quad (229)$$

The vidicon is available in a wide variety of sizes, but only two will be treated here. The most common tubes available are those with a 16 or a 25 mm input photocathode diameter. The experimentally derived signal transfer curves are shown in figure 99 for two dark currents, two types of faceplates and two types of photocathode irradiance. A fiber-optic faceplate version is available for use in conjunction with cascaded intensifiers. The transmission of the fiber-optic faceplate is lower than that of the usual glass faceplate and is variable, depending on the type of light incident. When the fiber-optic vidicon is used in conjunction with lenses of long focal length, the incident radiation approximates collimated light. When the input is the output of an intensifier phosphor, the incident radiation is diffuse. For a vidicon unaided by intensifiers, the glass faceplate version is appropriate and will be used here.

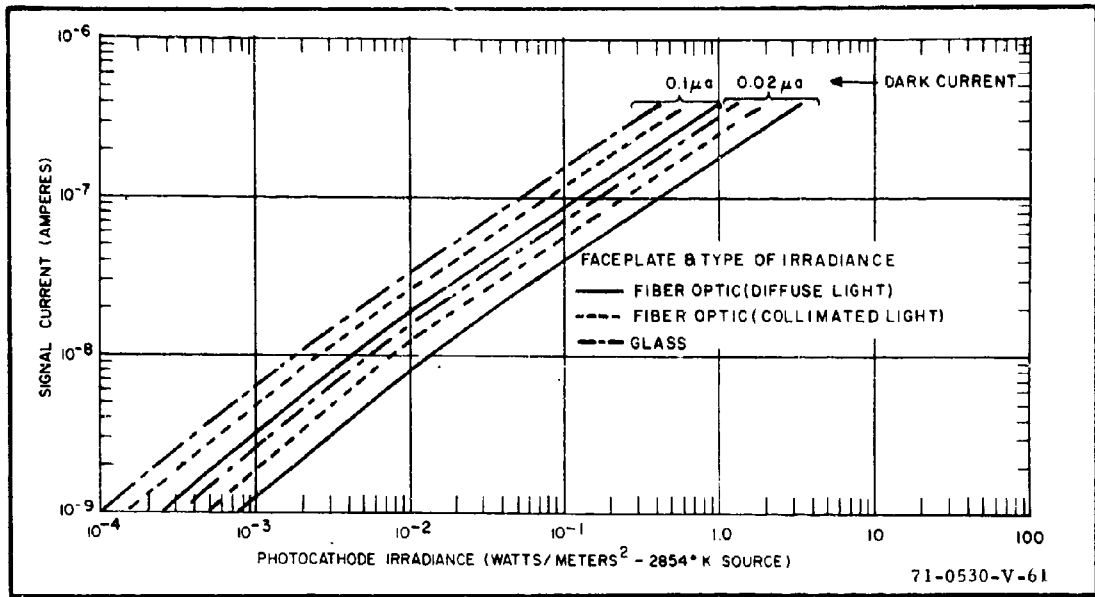


Figure 99. Signal Current Versus Photocathode Irradiance Characteristic for the 16- or 25-mm Vidicon

As can be seen, the gamma or slope of the signal transfer curve is less than unity and variable with irradiance, but it ordinarily falls in the 0.6 to 0.7 range. The curves of figure 99 apply equally to 16 mm or 25 mm vidicons, whereas ordinarily, we would expect the larger tube to produce a larger current at a given irradiance level. Apparently, the tube designers have elected to decrease sensitivity as photoconductor size is increased to keep lag within bounds. For a specific type of test source, such as the tungsten source operated at 2854°K, we may write the incremental signal due to an incremental irradiance ΔH_T as,

$$\begin{aligned} \Delta I &= (A k_T \Delta H_T)^Y / e_v e_h \\ &= \left[1 - (1-C)^Y \right] \left[A k_T H_T \max \right]^Y / e_v e_h \end{aligned} \quad (230)$$

where A is the effective photocathode area, k_T is the proportionality constant related to the photoconductor's sensitivity, and C is the input image contrast.

For the vidicon unaided by intensifiers, the display S/N ratio becomes

$$\text{SNR}_{D/A} = \left[\frac{n_v t \Delta f_V}{a} \right]^{1/2} \cdot \frac{|R_o(N_h)|}{N_h} \cdot \frac{[1-(1-C)^Y][A k_t H_T \max]^Y}{I_P e_v e_h} \quad (231)$$

The MTF's for the 16 mm and 25 mm photocathodes are shown in figure 100. These MTF's hold for high quality magnetically focused and deflected tubes operated for maximum resolution. Using these MTF's and the $\text{SNR}_{D/A}$ of equation 231, the threshold resolution versus photosurface current is plotted in figure 101 and versus photosurface irradiance in figure 102. The value of k_T used was 5.65×10^{-7} for the 16 mm vidicon and 2.32×10^{-7} for the 25 mm vidicon.

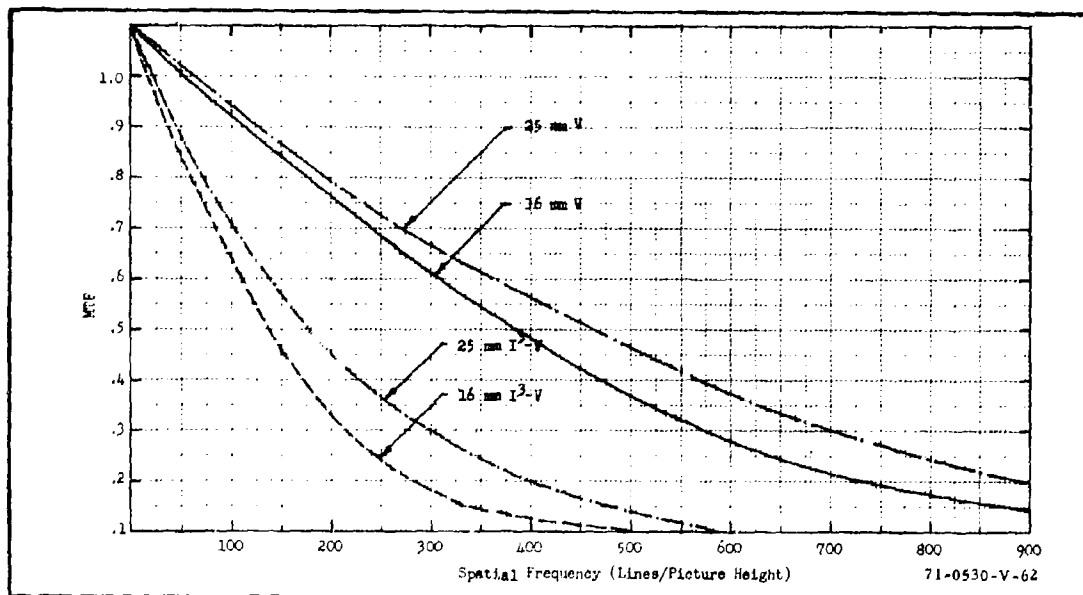


Figure 100. MTF for the 16- and 25-mm Vidicon and the 16- and 25-mm Triple Intensifier Vidicon

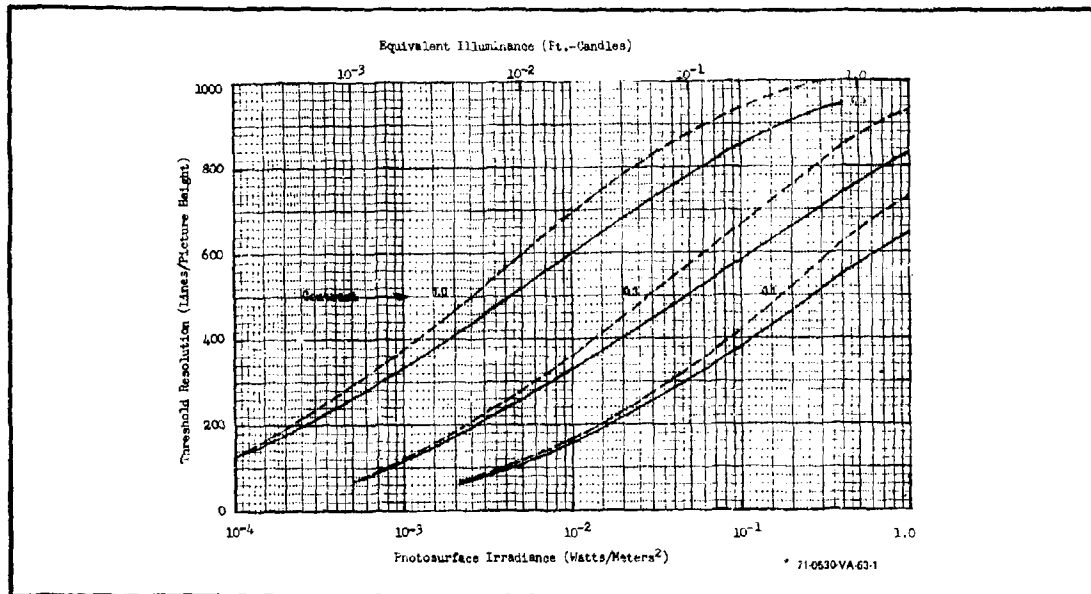


Figure 101. Threshold Resolution Versus Photosurface Irradiance for the (—) 16-mm and the (---) 25-mm Vidicon. Results Calculated for Test Bars of 7:1 Height to Width Ratio

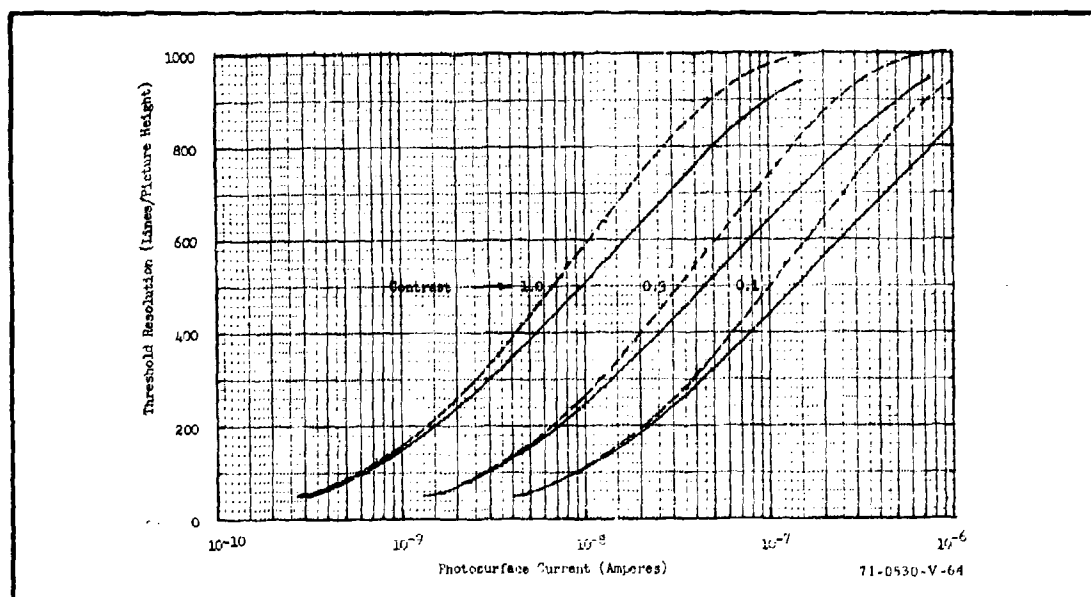


Figure 102. Threshold Resolution Versus Photosurface Current for the (—) 16-mm and the (---) 25-mm Vidicon. Test Bars are of 7:1 Height to Width Ratio

It should be noted that it is not customary to report the threshold resolution versus irradiance characteristic for vidicons because of photosurface lag. Like threshold resolution, lag is light level dependent. By the time that the image irradiance is increased sufficiently to make lag acceptable for the imaging of scenes in motion (above about 5×10^{-2} watts/meter²), the full resolving power of the vidicon is very nearly realized. Thus, this resolution versus irradiance characteristic is academic for all but very special applications.

By coupling a sufficient number of intensifiers to a vidicon with a fiber-optic faceplate, low-light-level capability can be achieved. In general, it will be found that the number of intensifiers needed to achieve an adequate lag characteristic will be greater than the number needed to merely gain sufficient sensitivity. Ordinarily, at least three intensifiers will be needed to image moving night scenes irradiated only by natural sources. However in special applications, combinations with only one or two intensifiers may be of interest. When an intensifier is used, the primary photoprocess becomes linear rather than sublinear, as is the case for the vidicon alone. The vidicon surface still imparts a gamma to the signal transfer characteristic, but its effect is that of a nonlinear amplifier.

The signal transfer characteristic assumed for the various intensifier vidicon combinations are shown in figure 103. The apparent light gain assumed for 1 stage of intensifier is 45, for 2 stages the gain is 1800, and for 3 stages, 45,000. The input photocathode radiant sensitivity is taken to be 4×10^{-3} amperes/watt. Without intensifiers, the vidicon signal current is equal to

$$I_Z = (k_z A_z H_z)^Y / e_v e_h \quad (232)$$

With intensifiers, the output current becomes

$$I_{IZ} = (G_{EI} k_{ZP} \sigma_I A_I H_I)^Y / e_v e_h \quad (233)$$

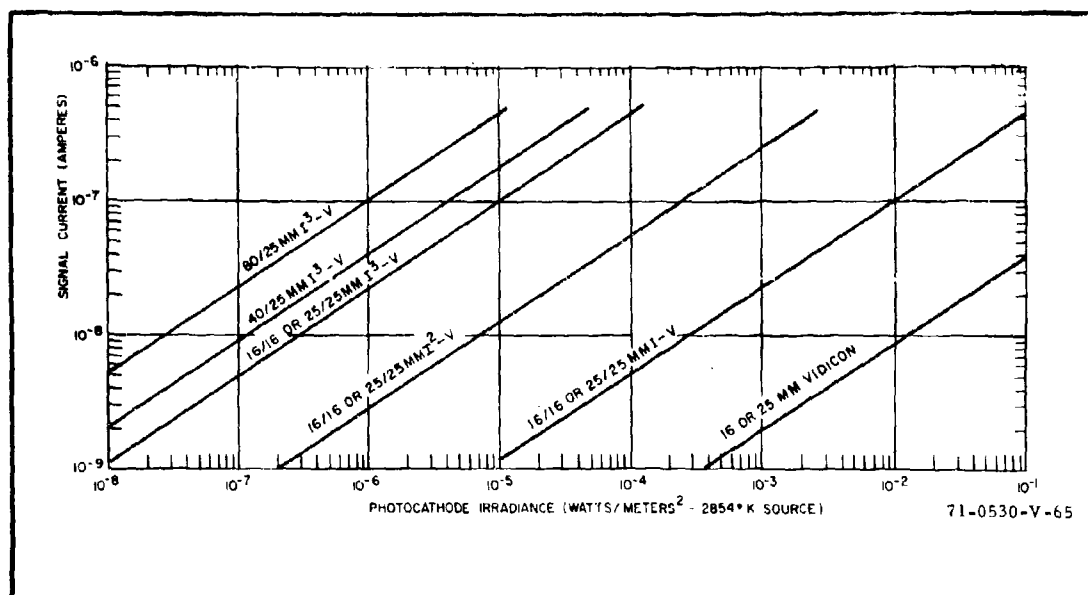


Figure 103. Signal Current Versus Photocathode Irradiance Characteristics for the 16- and 25-mm Vidicons With Their Intensifier Variants

where G_{EI} is the combined electron gains of the various intensifier phosphor/intensifier photocathode interfaces preceding the vidicon, and K_{Zp} is a "gain factor" for the final intensifier phosphor/vidicon photosurface interface, when $H_I = H_Z/G_L$ where G_L is the experimentally determined or assumed apparent light gain, $I_Z = I_{IZ}$ and,

$$K_{Zp} = \frac{k_Z A_Z}{\sigma_I A_I} \frac{G_L}{G_{EI}} \quad (234)$$

For a single intensifier, $G_{EI} = 1.0$, G_L was assumed equal to 45 with an area ratio of $A_Z/A_I = 1$, σ_I is taken to be 4×10^{-3} amperes/watt, and k_Z was previously noted to be 5.65×10^{-7} for the 16 mm vidicon, and 2.32×10^{-7} for the 25 mm vidicon. Thus, K_{Zp} is 6.38×10^{-3} and 2.61×10^{-3} for the 16 and 25 mm vidicons, respectively. The intensifier-vidicon current may also be written as

$$\begin{aligned}
 I_{IZ} &= G_{IZ} \sigma_I A_I H_I / e_v e_h \\
 &= G_{IZ} i / e_v e_h
 \end{aligned}
 \tag{235}$$

where G_{IZ} is the gain following the input photocathode. By comparison with equation 233,

$$G_{IZ} = \left(G_{EI} k_{ZP} \right)^Y (i)^{Y-1}
 \tag{236}$$

This gain is plotted in figure 104 for the two sizes of vidicons, assuming each is equipped with a triple intensifier of the same effective phototransducer area as the vidicon photosurface. The gains are seen to be sufficient to ensure that the overall sensors are photoelectron noise limited. Indeed, the gain is more than sufficient, but it must be to keep lag within bound.

The MTF's of the triple intensifier vidicons are shown in figure 100. With these MTF's and the SNR_D equation,

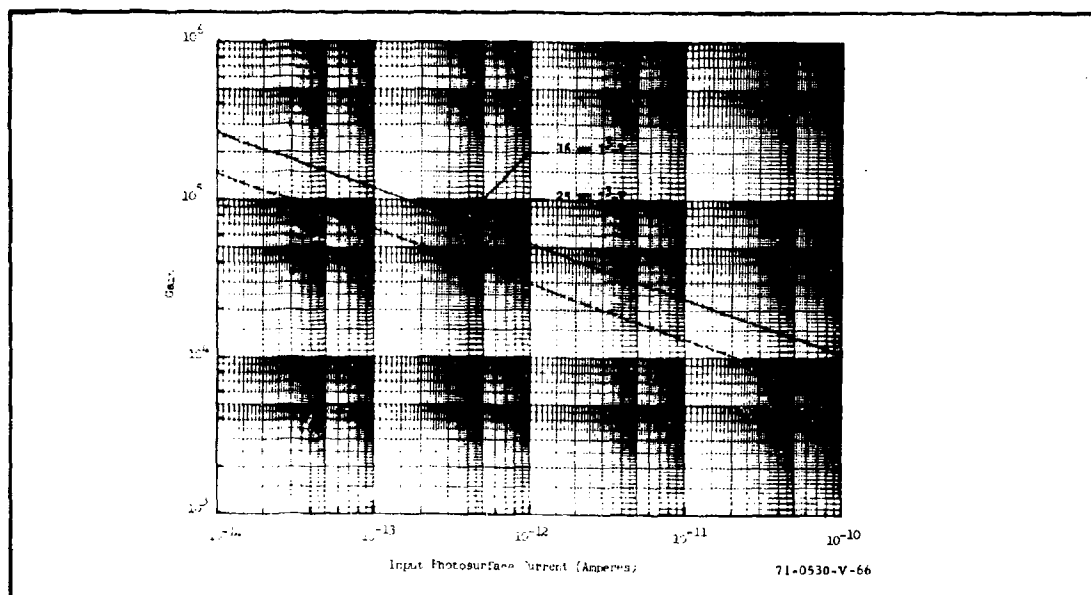


Figure 104. Prestorage Gain of the Triple Intensifier Vidicon for Intensifier and Vidicons of Equal Effective Phototransducer Area

$$\text{SNR}_D = \left[\frac{n_v t \Delta f_V}{a} \right]^{1/2} \frac{|R_o(N_h)|^{1/2}}{N_h} C \left[\frac{i/e_v e_h}{e \Delta f_V} \right]^{1/2} \quad (237)$$

the threshold resolution can be calculated. The results are plotted versus input photocurrent in figure 105 and versus input photocathode irradiance in figure 106.

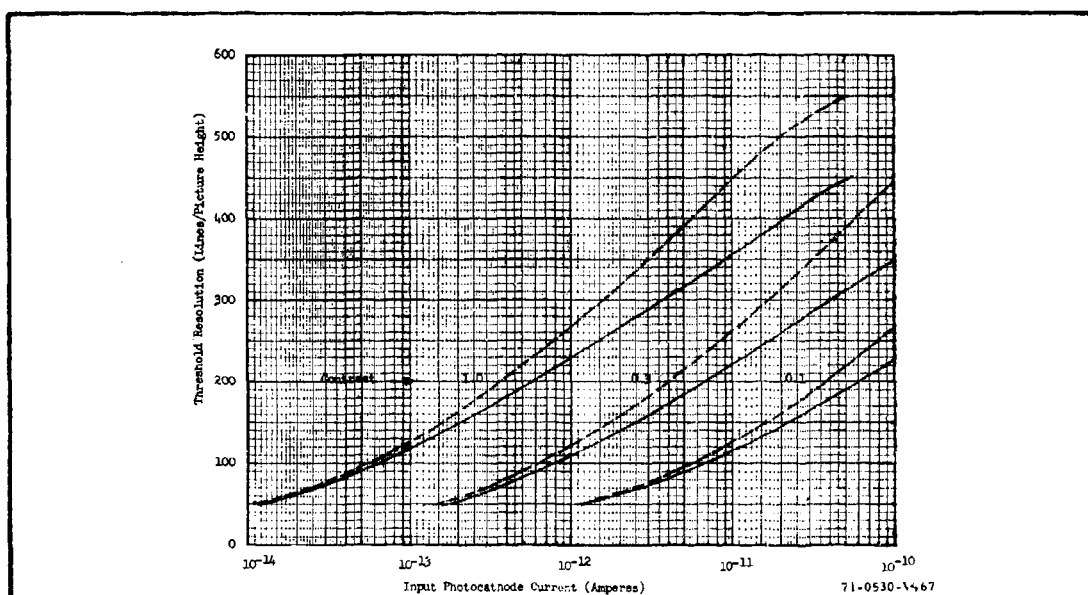


Figure 105. Threshold Resolution Versus Input Photocathode Current for the (----) 25-mm and the (—) 16-mm Triple Intensifier. Results Calculated for a Test Bar of 7:1 Height to Width Ratio

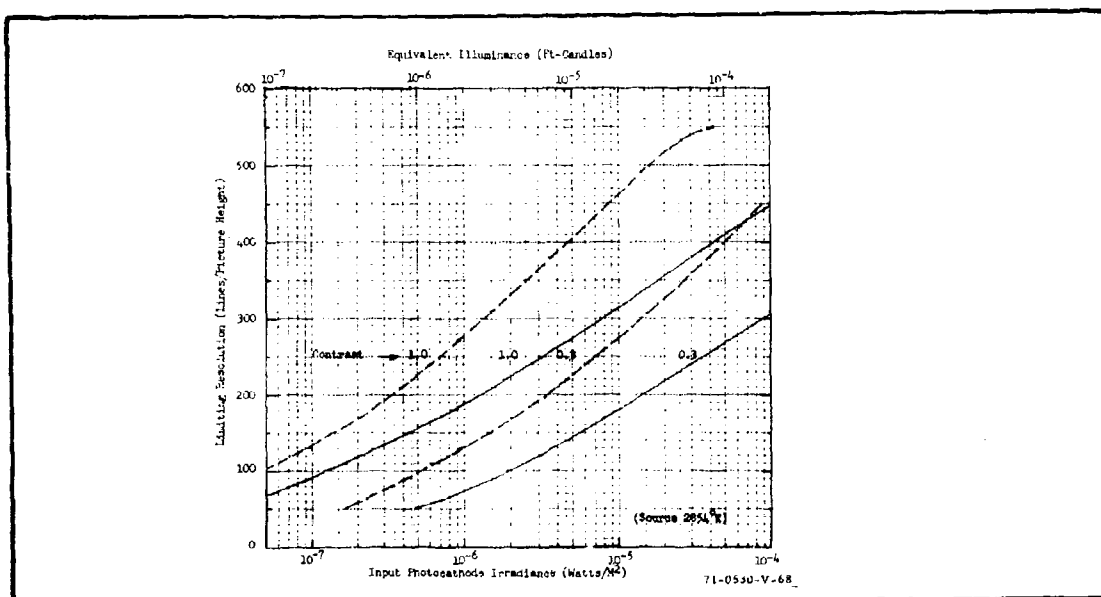


Figure 106. Threshold Resolution Versus Input Photocathode Irradiance for the (----) 25-mm and (—) 16-mm Triple Intensifier Vidicon. Calculations for a Test Bar of 7:1 Height to Width Ratio

SECTION XIII

THE SECONDARY ELECTRON CONDUCTION CAMERA TUBE

The Secondary Electron Conduction, or SEC, camera tube is virtually identical to the SEBIR camera tube described in Section XI, except for the target and, the addition of a suppressor mesh that is interposed between the target and the electron scanning beam gun as is shown in figure 107. This camera tube was developed in the early 1960's and in its intensifier version, it was the principal camera tube used in low-light-level cameras from 1965 to 1970. It is now being replaced by the SEBIR in most applications.

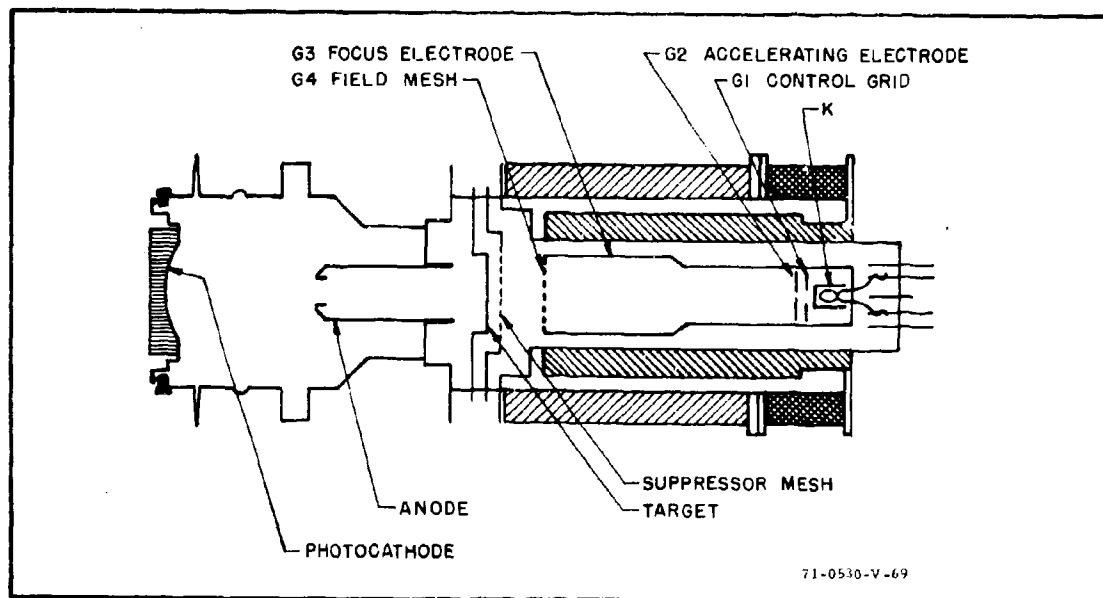


Figure 107. Cross Section of an SEC Camera Tube

The intensifier-SEC or I-SEC camera approaches the sensitivity of the intensifier-image orthicon described in Section XIV, is of lower lag and is much simpler to operate, because it needs no adjustment over the full range of its light transfer characteristic. The prominent feature of the SEC camera tube is its SEC target, which has high gain, high signal storage capability, and a low lag, which permits imaging of both stationary and moving scenes. Information losses in the neighborhood of bright scene highlights due to halation or "blooming", though still a problem, are minimized in this target. Because of the long signal storage capability of the target, the SEC camera can be used to integrate low-light-level images for extended periods or used in slow scan applications.

The SEC target consists of a fine mesh supporting a thin film of aluminum and a highly porous layer of potassium chloride. This KCl layer is stabilized at the electron-gun cathode potential by the electron scanning beam and an electric field is established across the layer by biasing the signal electrode positively.

Photoelectrons arriving at the target with energies of approximately 7 KeV penetrate the Al_2O_3 and Al layers and dissipate most of their energy within the layer by creating free secondary electrons. These electrons are released into the vacuum interstices between the KCl particles where they migrate in vacuum toward the signal plate. The electron conduction takes place in the vacuum rather than the conduction band of the KCl, which avoids the persistence effects caused by the trapping and subsequent release of charge carriers by shallow trapping centers. Also, because of the high resistivity of the low density target, the charge pattern can be stored for long periods of time.

The early SEC camera tubes were subject to damage by large over-exposures. This characteristic has been largely eliminated through use of the new mesh supported target described above but with a small loss in

target gain. The mesh greatly increases thermal capacity leading to a 30 fold improvement in burn resistance and prevents catastrophic damage. However, extreme over-exposures can still result in localized damage.

The function of the SEC target is to amplify and to store the electron image during the period between successive scans by the electron beam. The electron gain within the target is approximately 50 - 100 and the storage time is very long compared to the usual frame rates. The video signal is developed directly across the target load resistor as the electron beam replaces charge on the target point-by-point.

The low velocity electron beam that scans the target is produced by an electron gun consisting of an indirectly heated thermionic cathode, a control grid (G1) and an accelerating grid (G2) as shown in figure 107. The beam is focused at the target by the combined action of the uniform magnetic field of the external coil and the electrostatic field of (G3). A field mesh (G4) provides a uniform decelerating field. A second mesh electrode (G5), designated a suppressor mesh, is positioned close to the target surface to control the SEC target potential to just below the KCl crossover potential of about 15 volts. In the absence of this mesh, the target exhibits a runaway characteristic by charging up to the (G4) potential of 400 volts. The maximum resolving power of the SEC target is primarily limited by the interaction of the beam with the suppressor mesh rather than the SEC target. The signal output current is plotted vs photocathode irradiance for several SEC cameras in figure 108. The gamma of the curves is shown to be nearly unity, although in practice, it is variable from nearly 1 (at low light levels) to about 0.6 (at the higher light levels). This gamma is due to a variation in target gain. At the highest irradiance levels, the target saturates at a surface potential equal to that of the suppressor mesh (G5). In the curves shown, a hard knee in the signal transfer characteristic is shown, although in fact, the characteristic is more rounded. The hard knee assumption does not appreciably affect the calculations. A soft knee

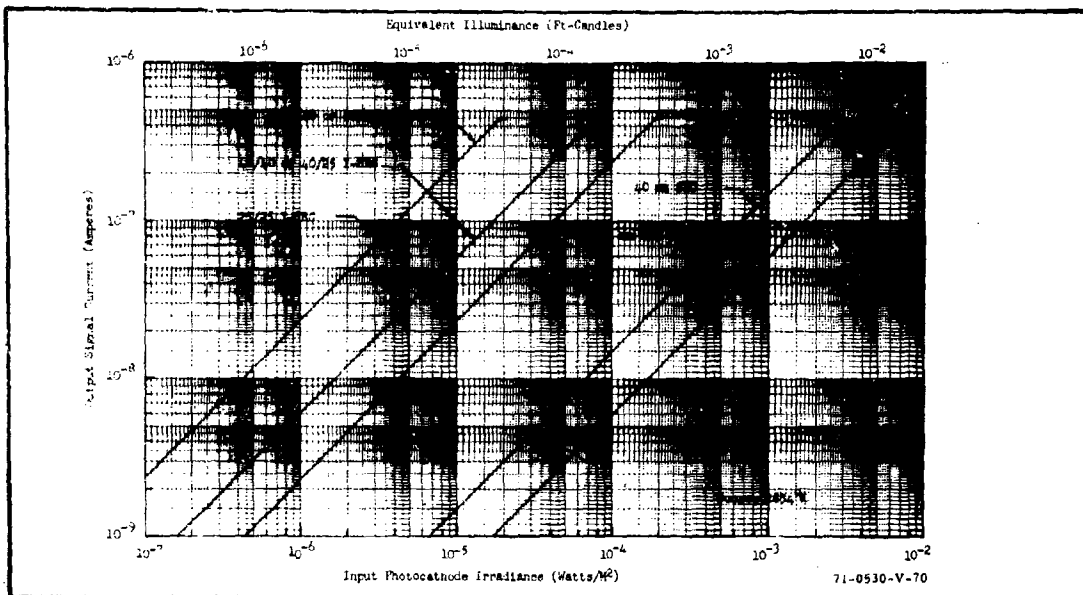


Figure 108. Output Signal Current Versus Input Photocathode Irradiance for Various SEC and Intensifier SEC Camera Tubes

is considered desirable in a real-time system, because it extends dynamic range, while at the same time limiting signal excursion. With the SEC image section operated at maximum potential, prolonged exposure at irradiance levels above the knee should be avoided due to the possibility of image burn-in. However, larger irradiances can be tolerated by reducing the photocathode voltage. This can be made automatic by peak-detecting the video signal and using the resulting signal to reduce image section voltage. Dark current in the SEC tube is practically nonexistent.

The SEC target gain is proportional to the photocathode voltage and can also be increased by increasing target voltage, but practical limits to maximum voltage are imposed by the onset of target gain and lag. At lower voltages, some degree of control can be exercised, but only at the expense of maximum signal storage capability and overall dynamic range. However, effective gain control can be obtained with photocathode voltage control. Over a range of 3.5 to 7.5 kV, a 15 to 1 gain control range can be obtained without

loss in resolution, but with an image rotation of about 1 degree at the lower voltage. At even lower voltages image rotation increases as well as target gain. Typically, the gain of the mesh supported target is approximately 50-75, we shall use the lower value in the calculations that follow.

A wide variety of SEC camera tubes is available. The principal differences between these tubes is the size of the photocathode and the size of the SEC target as varied by electronic zoom. Tubes with large photocathodes are more sensitive than those with smaller photocathodes, but only if they are used with optics of equivalent focal ratio and these larger optics will be considerably heavier. The maximum signal current capability for the various SEC cameras is mainly a function of the SEC target diameter, to which target capacitance is directly proportional. A large target is desirable from two viewpoints; first, the signal storage capability is increased and secondly, the amplitude response is improved, because the target-mesh assembly is the primary resolution limiting parameter. However, the larger target has a greater inter-electrode capacitance, which leads to an increase in preamp noise and a larger capacitance leading to an increase in readout time constant.

The following analysis will apply to a particular type of SEC camera tube, the WX31381, which incorporates electronic zoom so that the input photocathode can be switched from 25 to 40 mm while still using all of the 33 mm SEC target. The MTF of this target is shown in the solid curve of figure 109 and it applies to both input photocathode diameters. The $SNR_{D/A}$ for the SEC camera tube is written as

$$SNR_{D/A} = \left[\frac{n_v t \Delta f_v}{\alpha} \right]^{1/2} \frac{|R_o(N_h)|}{N_h} \frac{CG_{i \max} / e_v e_h}{I_p} \quad (238)$$

where the terms are as before except that G is the gain of the SEC target. Using this equation, the threshold resolution is calculated as a function of input photocathode current and plotted in figure 110 using $n_v = 7$, $\Delta f_v = 10^7$

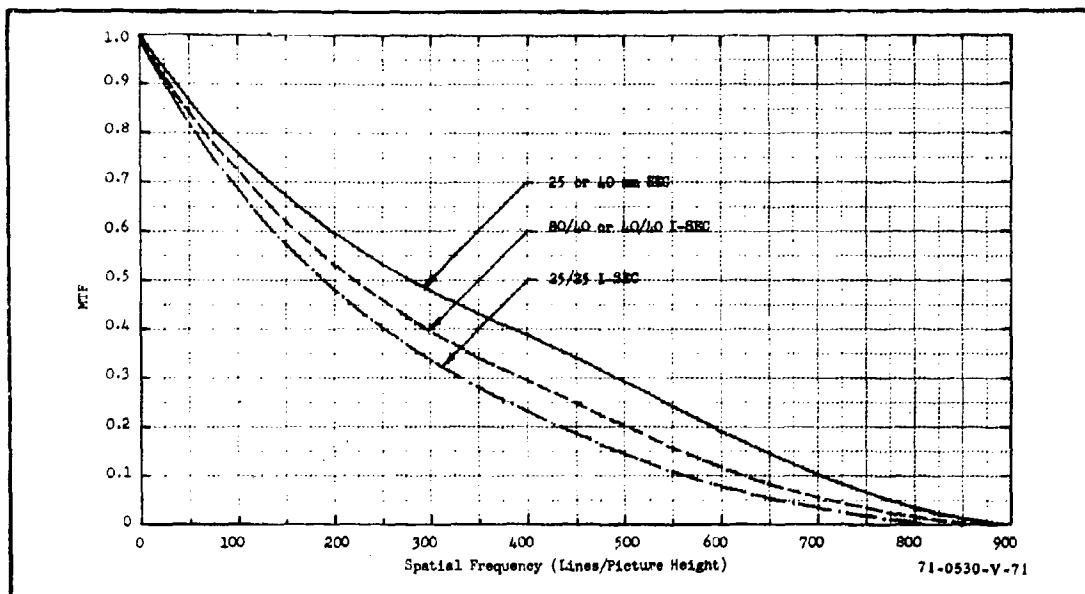


Figure 109. MTF of the WX31381 SEC Camera Tube Individually and in Combination With Intensifiers

Hz, and $G = 50$. Also, scales are included for photocathode irradiance and equivalent illuminance assuming the photocathode to be of radiant sensitivity 3.2×10^{-3} A/W.

When an intensifier is added, the MTF becomes as shown in figure 109. Note that the same MTF curve applies to intensifiers with 80 and 40 mm input photocathodes since both are limited by their 40 mm phosphors. With electronic zoom to a 25 mm input, the phosphor diameter is also 25 mm and MTF is lost as is shown by the lowest curve in the figure. The signal transfer characteristics are as shown in figure 108 and the $SNR_{D/A}$ equation is that used for the SEBIR camera tube (equation 219 (Section XI) with $N_v = n_v N_h$). With this understanding, the threshold resolution is plotted for the 80/40 and 40/40 I-SEC in figure 111 and for the 25/25 mm I-SEC in figure 112 using an overall intensifier-SEC target gain of 2000. Scales are also shown for irradiances and equivalent illuminances using a radiant sensitivity of 4×10^{-3} A/W for the input photocathode.

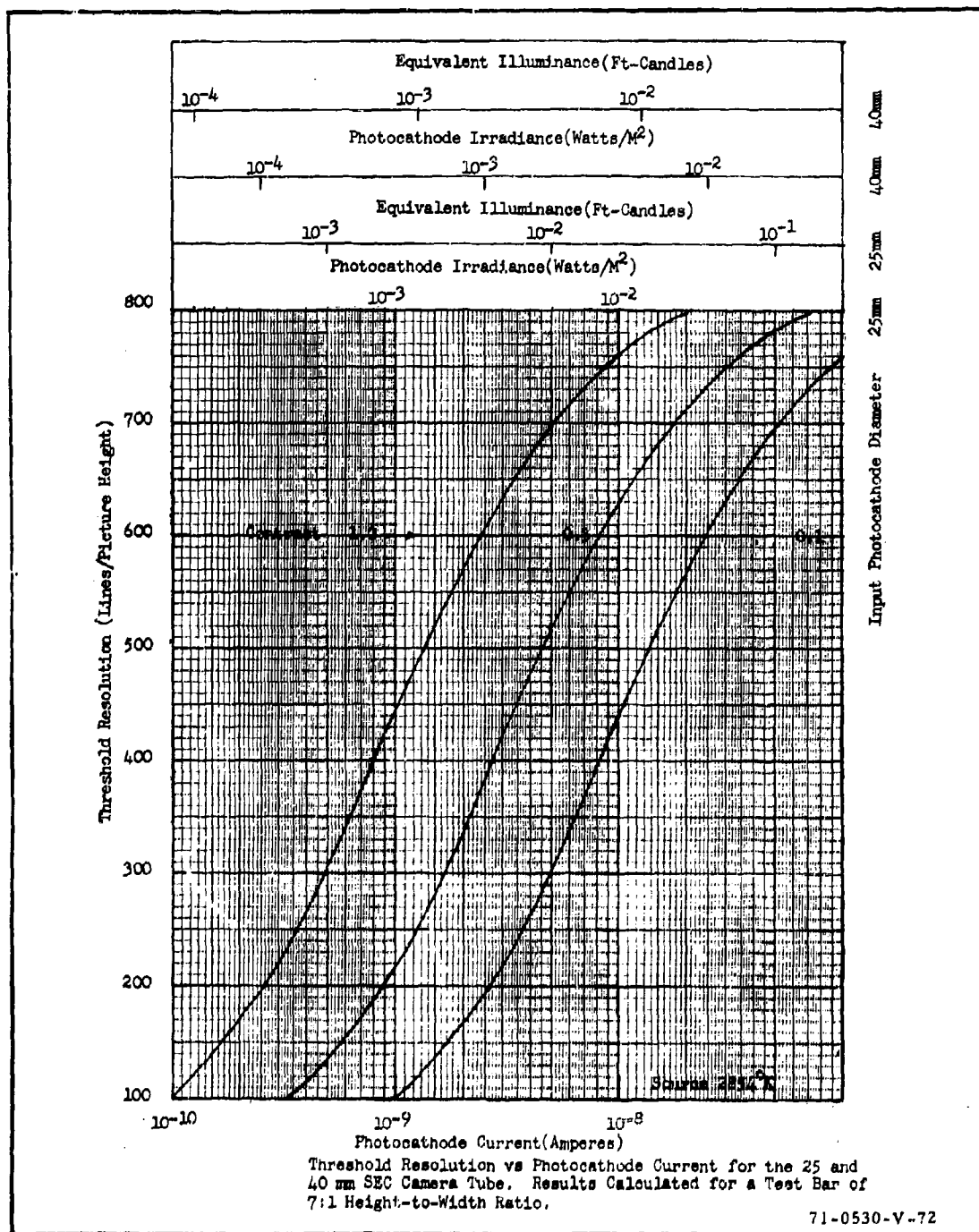


Figure 110. Threshold Resolution Versus Photocathode Current for the 25- and 40-mm SEC Camera Tube

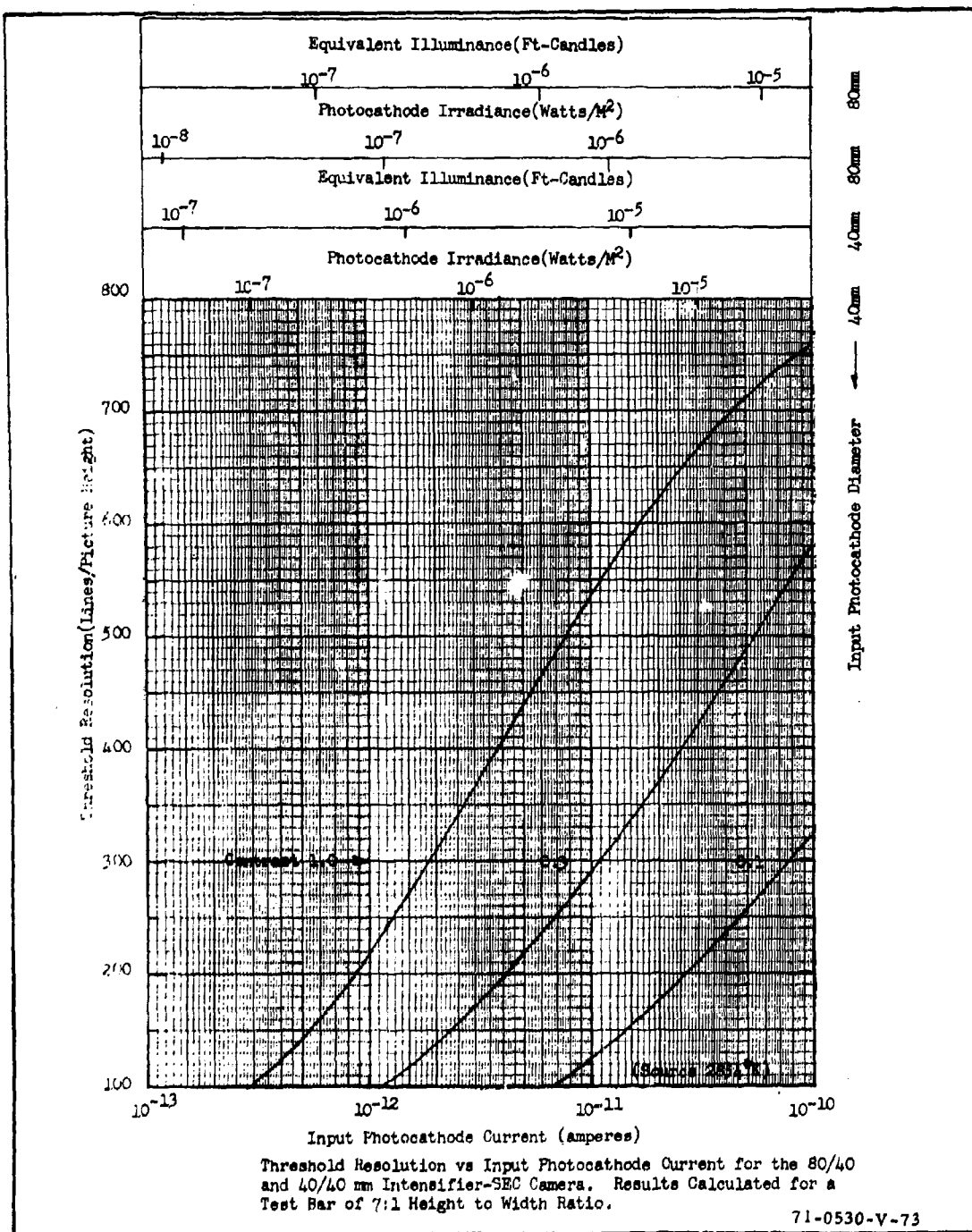


Figure 111. Threshold Resolution Versus Input Photocathode Current for the 80/40 and 40/40 mm Intensifier SEC Camera

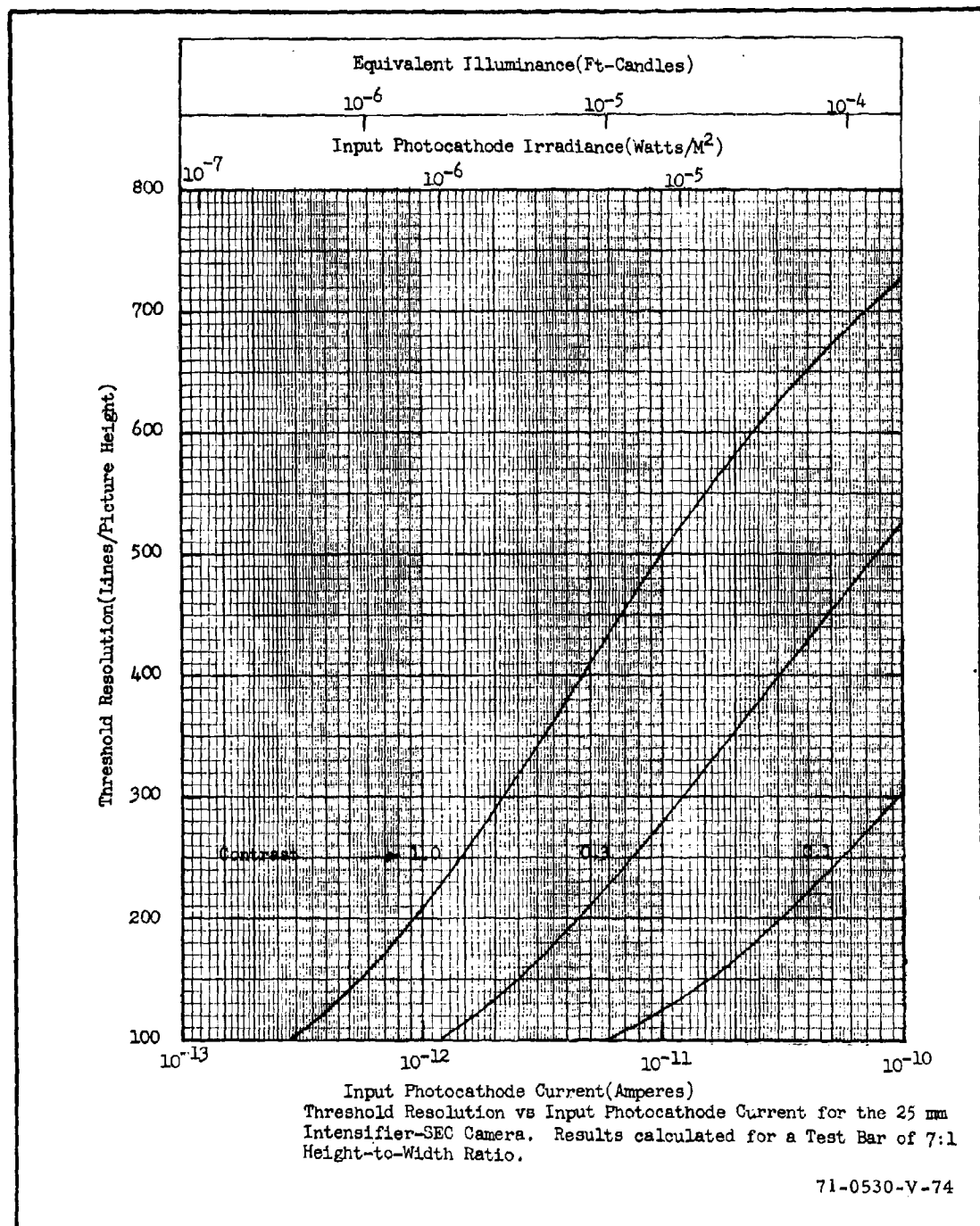


Figure 112. Threshold Resolution Versus Input Photocathode Current for the 25-mm Intensifier - SEC Camera

BLANK PAGE

SECTION XIV

IMAGE ORTHICONS AND IMAGE ISOCONS

The Image Orthicon, IO, was developed during World War II, and for a period of 20 years thereafter, it was the principal camera tube used in all commercial studio broadcasts. It was also the only tube capable of low-light-level operation during most of this period, and it is still a very capable performer. The Image Isocon, II, is similar to the IO in format and construction with the primary difference being in the read-out section. Both tubes use low-velocity, electron-beam scanning to extract the video signals and a low-noise, return-beam electron multiplier to amplify the signal within the tube. The primary difference is that the II derives its signal only from scattered scanning-beam electrons, while the IO accepts all of the returned beam for amplification. As a result, the noise in the picture low lights is very small for the II and is a maximum in the case of the IO. While the II provides superior S/N ratios at moderate photocathode light levels, it has an amplitude response that is light-level dependent. Thus, its low-light-level performance is generally inferior to that of an IO designed for this purpose. However, in practice, it is found that an image intensifier is needed for both the IO and II to reduce image lag to acceptably low levels and with the added intensifier, the light-level dependency of the II's amplitude-response becomes generally acceptable.

The thin-film metal-oxide targeted image orthicon is subject to permanent damage by extreme over-exposure although it can be electronically protected in most application. The II is reported to be immune from such effects.

14.1 THE IMAGE ORTHICON

The image orthicon is usually constructed in three sizes, described by the diameter of the image section. The three standard sizes are 2, 3 and 4 1/2 inches. The 2-in. size, developed mainly for applications requiring a minimum in size, weight, and power, has been abandoned mainly because of an overly restricted dynamic range and excessive lag. The 4 1/2-in. version is of main interest to commercial broadcast use. Its features are a very large signal storage capability and reduced bright light halving effects.

The 3-in. IO, which is still of current interest for low-light-level use, has a 40 mm photocathode in the version that is fitted with a fiber-optic faceplate. Ordinarily, the image section consists of an S-20 photoemissive-photocathode followed by a target. When struck by accelerated photoelectrons, this target emits secondary electrons in number greater than those incident. These electrons are emitted back toward the photocathode, but are collected by a mesh interposed between the photocathode and target. The image section is usually magnetically focused. The readout section consists of a magnetically focused and deflected scanning electron beam. Unlike the vidicon or SEC camera tube, the video signal is not read out at the target, but rather, the electron beam is returned to an electron multiplier. The signal, which is the difference between the original beam current and that which lands on the target, is greatly amplified by the internal electron multiplier.

The target, whose function is to both amplify and store the signal during the interval between scans has been fabricated of a number of materials. Originally, the target material was a soda-lime glass whose conductivity was ionic. The net gain of this target was about 3. The main problem with soda-lime glass is that the conducting ions always drift in the same direction causing the glass to become more resistive as the ions become depleted. This causes an increased tendency for images to burn-in after

a few hundred hours of operation. To extend tube life it was customary to slowly rotate or orbit the image incident on the target.

In the mid-1950's, the thin-film metal-oxide target was developed. The material used was principally magnesium-oxide, although other materials were used. The thin-film target is electron conducting, which solves the image burn-in problem. Also, secondary emission gain increased to as much as 10-15, resulting in a sensitivity increase. An even further advantage is that the target is but 1/10th the thickness of a glass target, and its conductivity, being anisotropic, is higher through the target than along its surface. Thus, these films displayed a higher resolving power than glass and a longer image storage capability, which is useful in slow scan and in astronomical applications. Being so very thin, the MgO target lacks strength necessitating a wider than normal target-to-mesh spacing. This reduces signal storage capability to the point where these tubes become marginal for studio broadcast use. However, image lag is reduced because of the reduction in capacitance, which makes these tubes suitable for low-light-level imaging.

Another target material developed is an electron conducting glass called "brown glass". These glasses usually contain transition metal-oxides in both bivalent and trivalent states. The mixture of doubly and triply ionized sites throughout the material permits electron conduction by hopping. These glasses eliminate the burn-in problem and low resolving capability of soda-lime glass, but their gain is no higher (about 3).

The IO is schematically diagrammed in figure 113. The photoelectron image is magnetically focused and accelerated to the target through a potential of about 600 volts. In tubes with magnetically focused image sections, this potential must be precisely maintained, ruling out electronic image-section gain control. Prior to impinging on the target, the photoelectrons must pass through the mesh, which has a photoelectron transmittance of between 0.6 to 0.7.

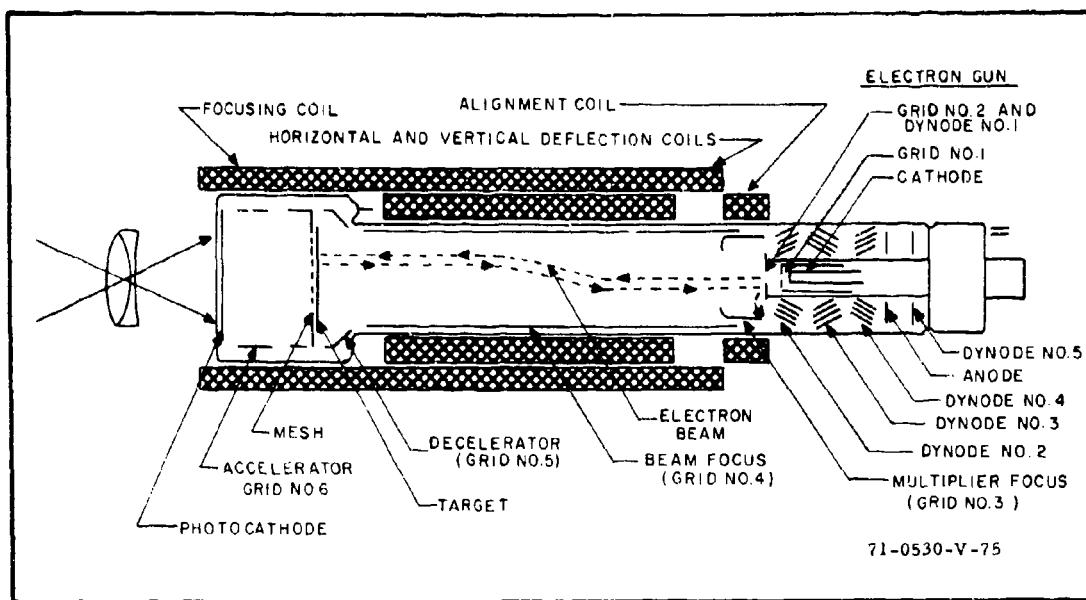


Figure 113. Schematic of Image Orthicon

Upon colliding with the target the photoelectrons cause secondary electrons to be emitted as shown in figure 114. These secondaries are collected by the mesh, which is biased 2 volts above the target. The capacitance, or signal storage capability, of the target-mesh assembly is determined by the mesh-to-target spacing, which can be as little as 0.7 mills (for glass targeted tubes) to up to 10 mills or more (for MgO targeted tubes).

The electron beam formed by the electron gun and the control and accelerating grids 1, 2 and 3, is further accelerated and focused by grid 4 and the focus coil, and then, the beam is magnetically deflected into a raster scanning pattern. Next, it is decelerated by grid 5. A portion of the beam lands on the photocathode according to the charge deficiency thereon, and the balance of the beam returns directly to grid 2, dynode 1. Were the focus perfect, the beam would pass back through the original

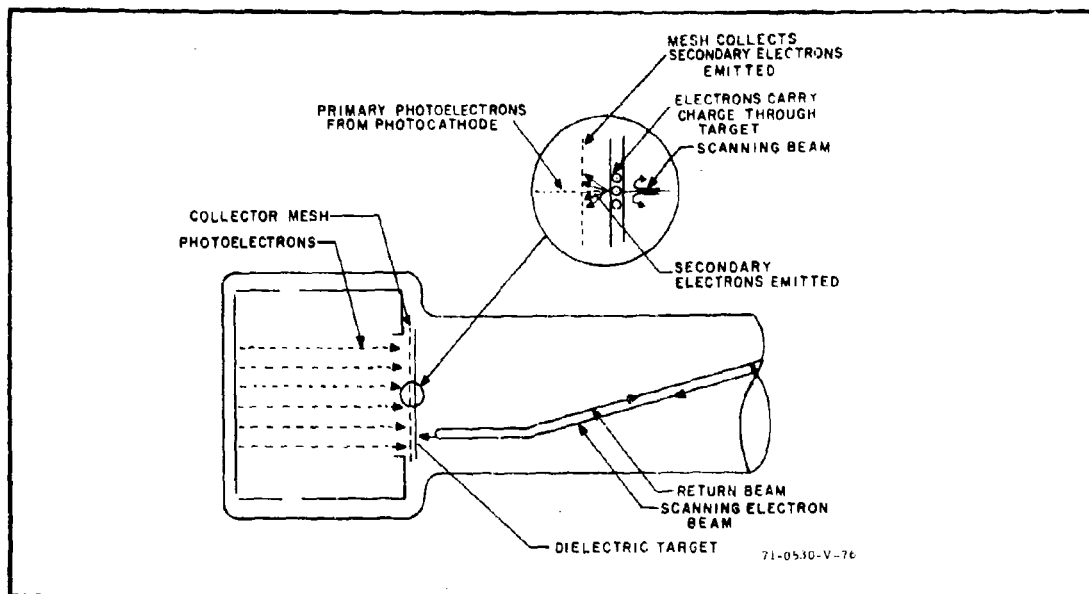


Figure 114. Cross Section Showing Action of Image Orthicon's Storage Target

aperture in this structure, but as a practical matter, they collide with dynode 1, which amplifies the returned portion by a factor of approximately 4. The amplified return beam signal is subsequently amplified further by dynodes 2 through 5. Including the gain of the first dynode, an overall signal amplification of about 500 to 1500 can be achieved. The electron multiplier serves the function of signal preamplifier. While it does not improve S/N ratio, it is comparatively noiseless compared to external preamplifiers. However, one of the principal noises in the IO is the shot noise of the beam.

The signal transfer characteristic for a thin-film MgO targeted IO is shown in figure 115. The gamma of this tube at low irradiance levels is near unity, while at the higher irradiance levels, the gamma drops off. In tubes with close-spaced meshes, the transition from unity gamma to zero gamma is quite abrupt. The limitation in this case is mainly target

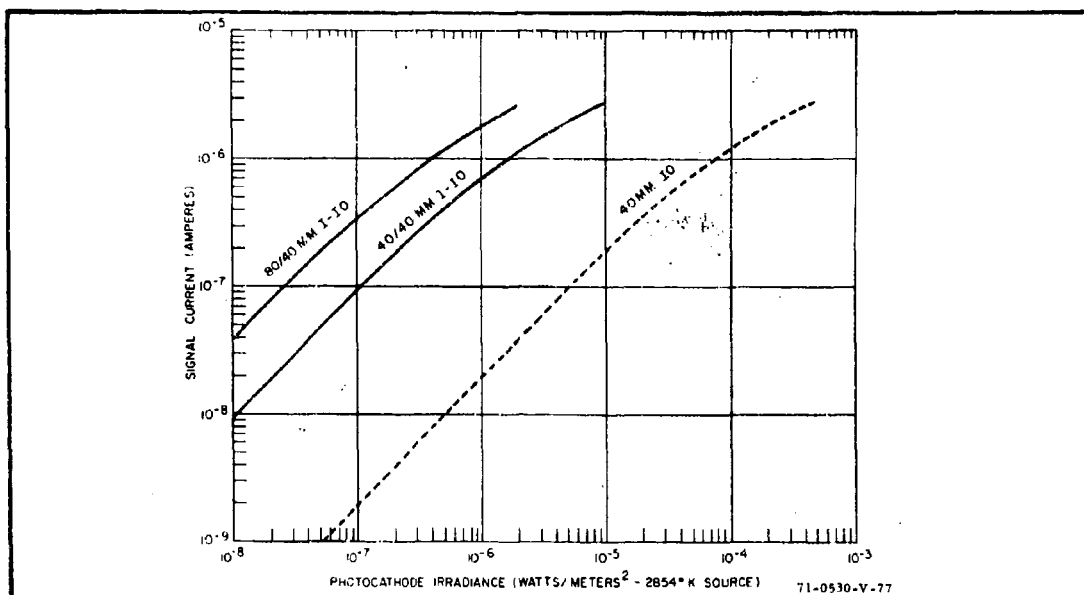


Figure 115. Signal Current Versus Photocathode Irradiance Characteristic for the 3-in. Thin-Film, Metal-Oxide Targeted Image Orthicon With and Without an Intensifier

capacitance. In thin-film targeted tubes with wide-spaced meshes, the transition is more gradual, being a combination of target gain reduction as photoelectron density increases, and target capacitance.

The signal current output of the IO is given by the relation

$$I = CG_M (G_T - 1) T_M i/e_v e_h \quad (239)$$

where the terms are as previously defined, except that G_M is the electron multiplier gain, T_M is the mesh transmittance, and G_T is the IO target gain. For calculation purposes, it is usual to assume a constant value for the multiplier gain and the net target gain ($G_T - 1$) is calculated from the equation

$$(G_T - 1) = \frac{e_v e_h I}{G_M T_M \sigma_T A H_T} \quad (240)$$

In the linear region of the signal transfer curve, $(G_T - 1)$ is approximately 10. The effective gain is specified as $(G_T - 1)$ for the IO, because the original photoelectron incident on the target must be discounted. This is only significant near the knee of the signal transfer curve, where the gain becomes quite small. It should be noted that it is quite difficult to measure IO parameters such as beam current, beam modulation, target gain, electron multiplier gain, etc., for not all terminals are brought out of the tube to a measuring point, and also because the currents involved are extremely small.

In the calculations that follow, electron multiplier gain is assumed to be 1000, the photocathode's radiant sensitivity is 3.2×10^{-3} amperes/watt for a 2854° tungsten source and T_M , the mesh transmittance, is taken to be 0.66.

In the previous sections, the modulation transfer functions for the various sensors have been reported. In making camera tube measurements, it is more usual to measure the square wave response using a bar pattern as the input image.

The uncompensated horizontal square wave response of the IO is not unique as can be seen in figure 116, where a super response and a more conventional response are shown. The super response, results from a charge redistribution effect that occurs when the target-mesh assembly becomes fully charged at a point. Secondary electrons from the target are then repelled by the mesh and fall back to the target in areas adjacent to the areas from which they were emitted. In the case of black and white bar patterns, the blacks are driven from a normal zero potential to a negative value. This effect is known as black halving and occurs for bright images of signal level above the knee of the signal transfer curve. Below the knee, the more normal appearing response, designated the regular response, is obtained. The MTF of the IO based on the regular response is plotted in figure 117.

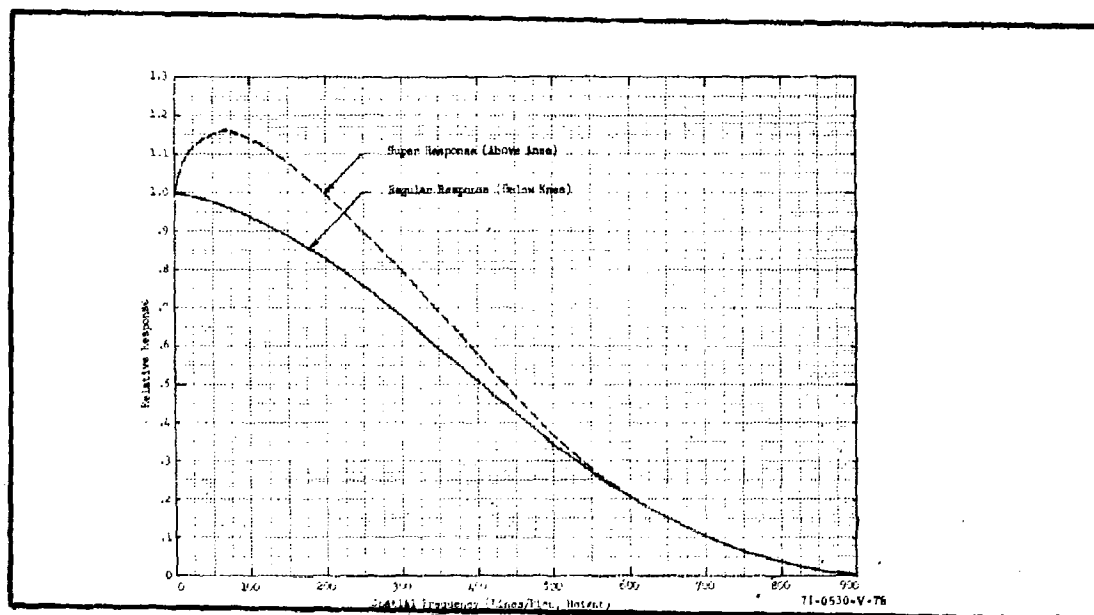


Figure 116. Uncompensated Horizontal Square Wave Amplitude Response for the 3-in. Thin-Film Targeted Image Orthicon

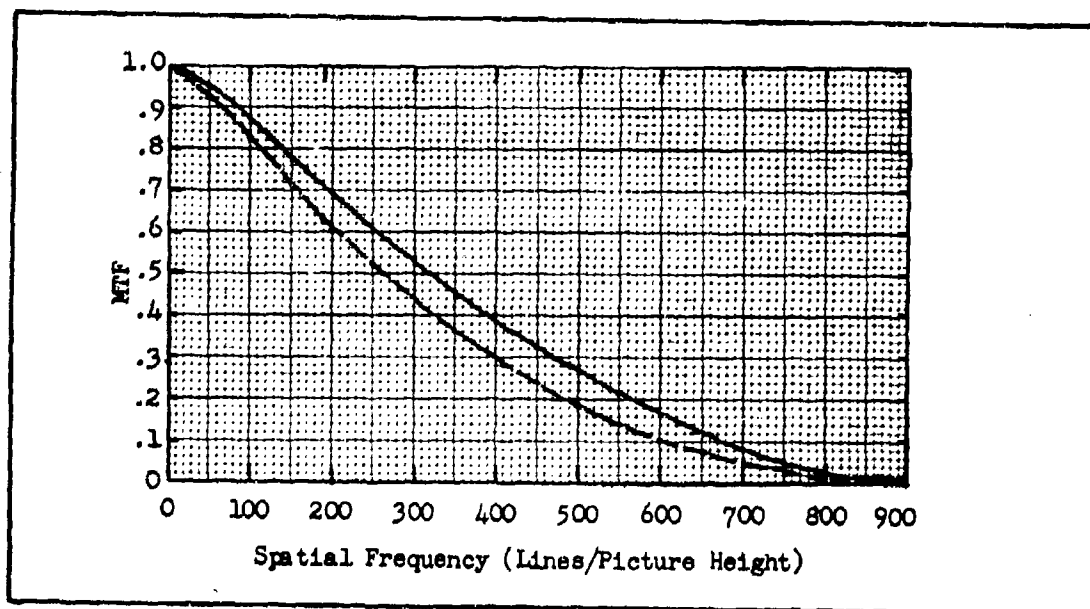


Figure 117. Modulation Transfer Function

There are several sources of noise in the image orthicon depending on the mode of operation. Analytically, the video, S/N ratio is written as,

$$\text{SNR}_{\text{VO}, 1} = \frac{G_M (G_T - 1) T_M i_{\text{max}} / e_v e_h}{(\bar{I}_e^2 + \bar{I}_B^2 + \bar{I}_T^2 + \bar{I}_D^2 + \bar{I}_P^2)^{1/2}} \quad (241)$$

where the numerator terms are as described above and the noises are equal to:

- a. The mean square photoelectron noise

$$I_e^2 = G_M^2 (G_T - 1)^2 T_M e \Delta f i_{\text{max}} / e_v e_h. \quad (242)$$

- b. The mean square beam noise

$$I_B^2 = G_M^2 (G_T - 1) T_M e \Delta f i_{\text{max}} / e_v e_h. \quad (243)$$

- c. The mean square target noise

$$I_T^2 = G_T G_M^2 T_M e \Delta f i_{\text{max}} / e_v e_h. \quad (244)$$

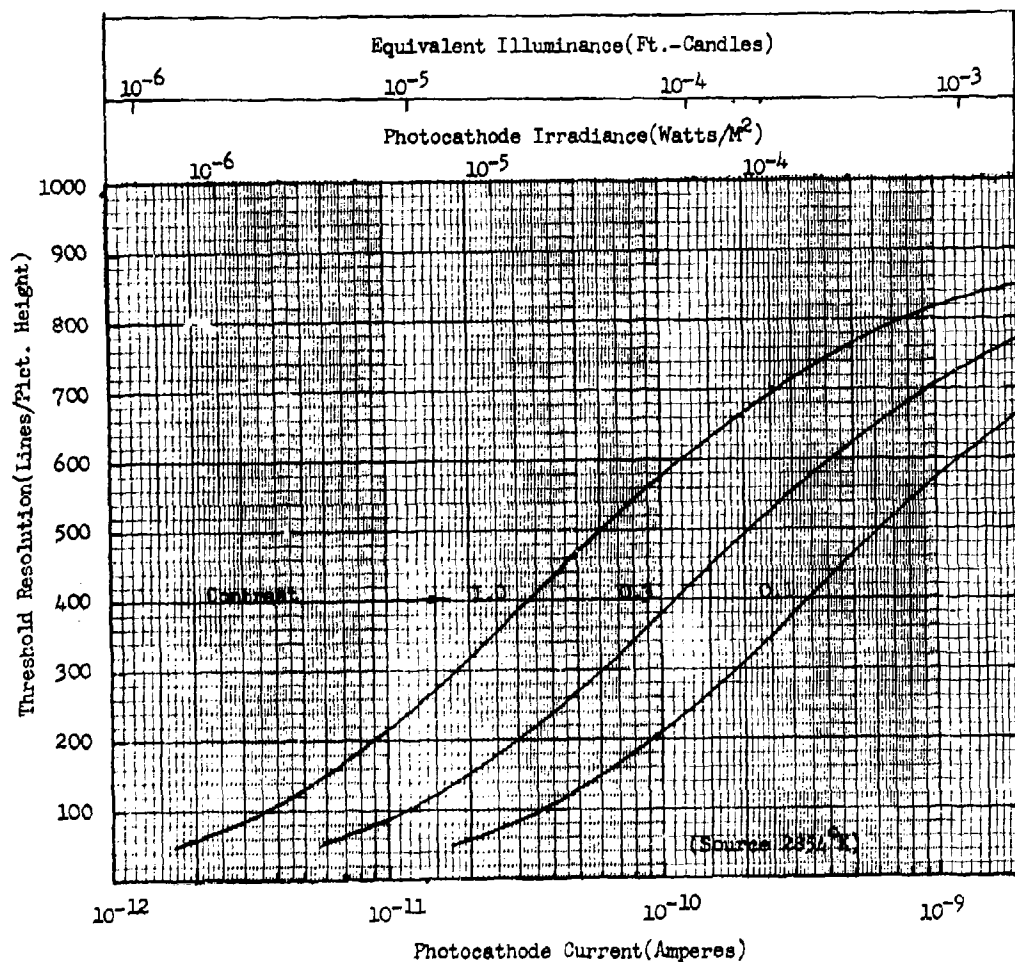
- d. The mean square first dynode noise

$$I_D^2 = G_{M1} G_{M4}^2 \left[\frac{1-m}{m} \right] (G_T - 1) T_M e \Delta f i_{\text{max}} / e_v e_h. \quad (245)$$

- e. The mean square preamp noise, computed from its measured rms value of I_P .

$$(246)$$

In equation 245, G_{M1} is the gain of the first dynode stage (about 4) and G_{M4} is the gain of the stages following it (about 250). In both equations 243 and 246, m is the beam modulation factor. It represents the fact that the beam can never be fully modulated and that, therefore, its value must be set at some value $1/m$ times higher than the highlight signal current i_{max} .



Threshold Resolution vs Photocathode Current for the Three-Inch Thin-Film-Targeted, Image Orthicon operated with Beam Current Fixed to Discharge Highlights near the Signal Current Knee. Test Bar of 7:1 Height-to-Width Ratio.

71-0530-V-80

Figure 118. Threshold Resolution Versus Photocathode Current

The sensor apertures filter the photoelectron noise and the target noise, but they have little effect on the beam noise and the dynode noise, and they have no effect on the preamp noise. The beam noise is ordinarily the largest noise, although it can be minimized by setting the beam current to a minimum value just sufficient to discharge the highlights in the scene. In making threshold resolution vs photocathode irradiance measurements in the laboratory, it is customary to reduce beam current as the test pattern radiance is decreased point-by-point. This condition is seldom achieved in viewing real scenes, although by continual manipulation of the beam control, some scenes can be made more discernible at the lower light levels if intrascene dynamic irradiance range is small.

In this report, it will be assumed that the beam current is fixed so that scene highlights at the knee are just discharged. For calculation purposes, the highlight irradiance will be taken to be 2×10^{-4} watts/M², and the beam modulation is taken to be 0.5. Actually, the beam modulation is variable with light level, but its magnitude and variability are not well documented. For a fixed beam current, the IO may be considered to be beam noise limited to a good first approximation. Thus, the $SNR_{D/A}$ may be written as

$$SNR_{D/A} = \left[\frac{n_v t}{\alpha} \right]^{1/2} \cdot \frac{R_o(N_h)}{N_h} \cdot \left[\frac{(G_T - 1)(T_M)/(e_v e_n)}{i_{so} e} \right]^{1/2} C i_{max} \quad (247)$$

where i_{so} is the fixed value of beam current (referenced to the input photocathode) and is taken to be 5.25×10^{-10} Amperes. The $SNR_{D/A}$ was calculated and the threshold resolution was determined and plotted vs input photocurrent in figure 118. For the calculations, $G_T = 10$, $T_M = 0.6$, $e_v e_h = 0.79$ and $n_v = 7$. A unity gamma was assumed. For the irradiance scales, a photocathode sensitivity of 3.2×10^{-3} A/W was used.

The lag of the IO is not generally acceptable for applications where the scene has any appreciable motion. Also, when the IO is set up with a

moderately high fixed beam current, its sensitivity becomes too low. An additional image intensifier stage substantially solves these problems. The sensitivity of the I-IO is not much greater than that of an IO operated with optimum beam current, but it does permit the operation of the I-IO without continual beam adjustment and its lag is greatly reduced. The added intensifier is assumed to have an S-25 photocathode of radiant sensitivity 4×10^{-3} amperes/watt and diameter of either 80 mm or 40 mm. The electron gain at the phosphor photocathode interface was assumed to be 40 as can be seen in the signal current vs irradiance curves of figure 115. The MTF of the I-IO is shown in figure 117. The $SNR_{D/A}$ is calculated from

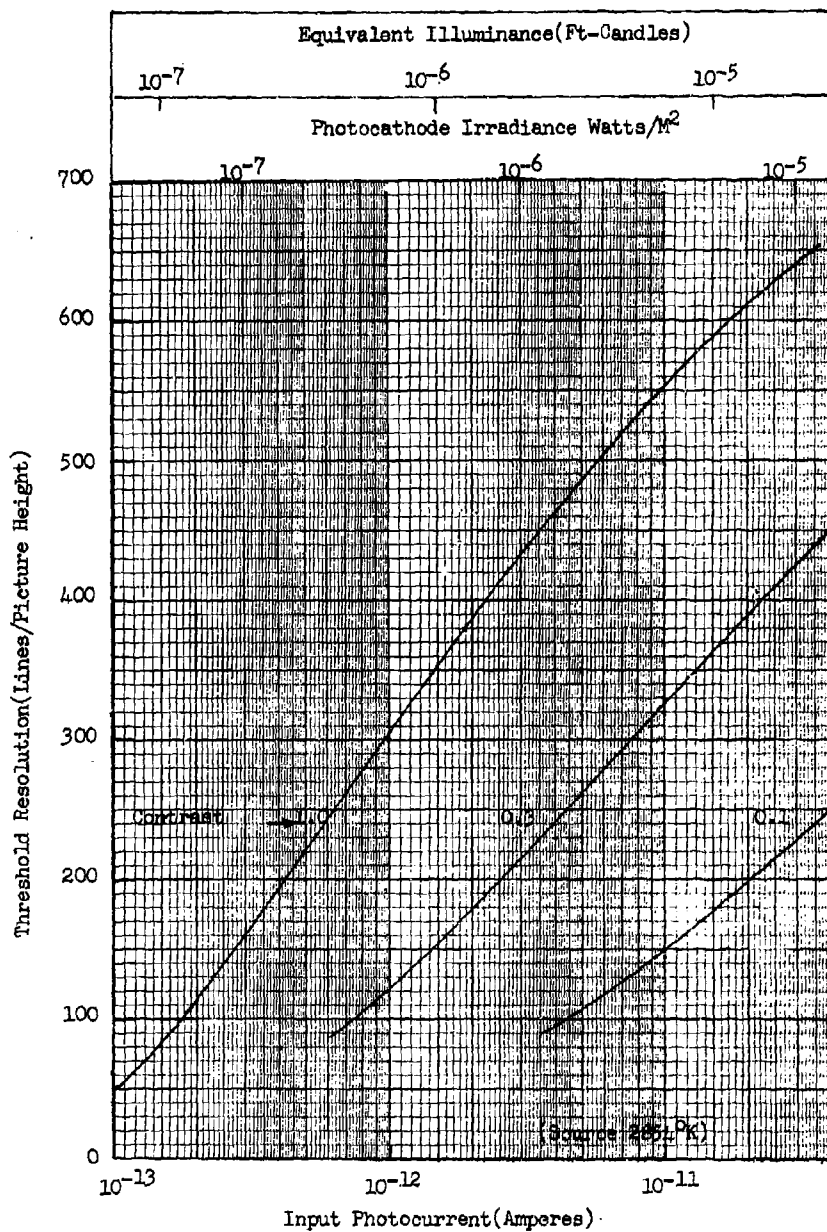
$$SNR_{D/A} = \left[\frac{n_v t}{\alpha} \right]^{1/2} \cdot \frac{|R_o(N_h)|}{N_h} \cdot \frac{[G G_I (G_T - 1) T_M i_{\max}/e_v e_h]}{\left[G_I^2 (G_T - 1)^2 T_M^2 e i_{\max}/e_v e_h \right] + A}^{1/2}$$

$$\text{where } A = + \frac{G_I (G_T - 1) T_M i_{so}}{m e_v e_h} \quad (248)$$

where G_T is the intensifier gain and in evaluation, i_{so} is equal to 1.31×10^{-11} Amperes. From this equation and the MTF curves, the threshold resolution vs photocurrent curves are generated and plotted in figure 119. The irradiance curves pertain to an input photocathode of sensitivity 4×10^{-3} A/W and area $7.68 \times 10^{-4} \text{ M}^2$.

14.2 THE IMAGE ISOCON

We turn next to a description of the image isocon or II. The essential features were described in 1949, but early tubes had set-up problems and incomplete beam separation problems which prevented the production of practical tubes. In the last few years, these problems have been solved to a satisfactory degree and tubes of high quality are now available. The main merits of the image isocon are an ability to provide very high S/N ratios and very high resolving powers with adequately illuminated scenes. Relative to an image orthicon, it is less sensitive, but it provides a



Threshold Resolution vs Input Photocurrent for the
Intensifier-Image Orthicon with Thin Film Target.
Test Bar Height to Width Ratio is 7:1

71-0530-V-81

Figure 119. Threshold Resolution Versus Input Photocurrent

picture that is noise-free in the blacks of the scene and a wider dynamic range. With an additional stage of image intensification, the II becomes capable of low-light-level imaging with a particular merit of being relatively immune from damage by bright lights.

The II is shown schematically in figure 120. The image section is essentially identical to that of the image orthicon as is the electron gun. The principal difference is in the return beam readout. In the II, the beam current i_b , approaching the target deposits enough electrons to discharge the target. The portion of the electron beam, i_{scat} , is scattered by interaction with the target and a third portion, i_{refl} , does not possess sufficient energy to reach the target and is specularly reflected. Thus, the total beam current can be written as

$$i_b = (G_T - 1) i + i_{scat} + i_{refl} \quad (249)$$

In the image orthicon, both the scattered and reflected beam components are returned to the electron multiplier, with the result that the output

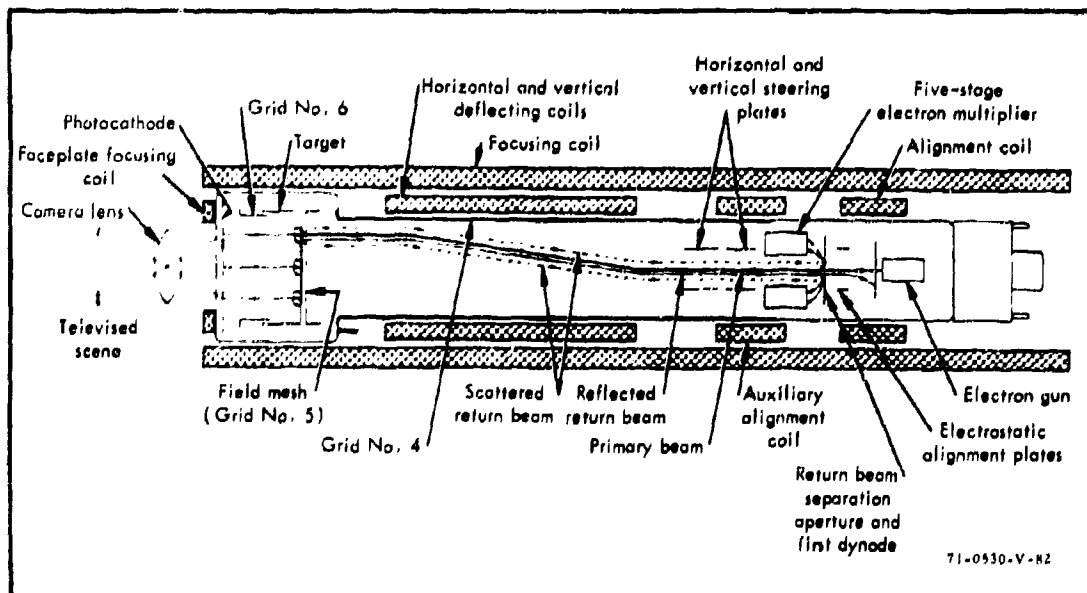


Figure 120. Schematic Arrangement of the New Image Isocon

current, I , is equal to

$$\begin{aligned} I &= G_M (i_b - (G_T - 1)i) \\ &= G_M (i_{\text{scat}} + i_{\text{refl}}) \end{aligned} \quad (250)$$

It is seen that I is a maximum when the image signal, i , is zero and thus, maximum beam noise occurs in the picture blacks.

The isocon readout makes use of the fact that the scattered portion of the electron beam i_{scat} is proportional to the target current $(G_T - 1)i$.

Thus,

$$i_{\text{scat}} = a (G_T - 1)i \quad (251)$$

where a is a scatter gain that depends upon the particular target material employed. To make use of this proportionality, it is necessary to separate the scattered electrons from the reflected electron beam. The method of separation is as shown in figure 121. The primary beam is seen spiraling

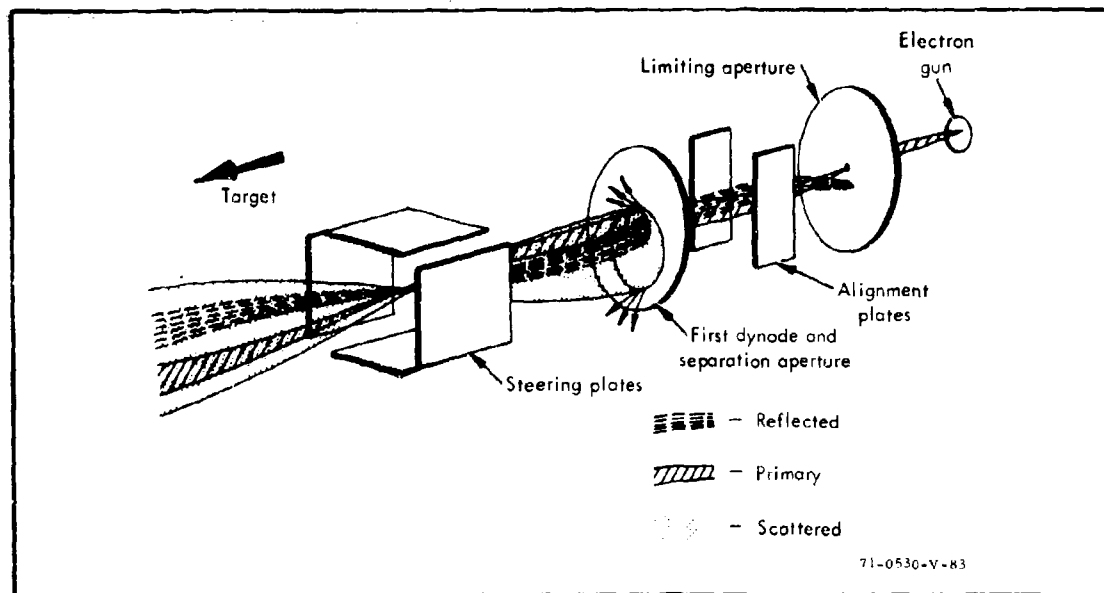


Figure 121. Image Isocon Beam Separation System

out from the gun through the limiting aperture, past the alignment plates, through the separation aperture of the first dynode, past the steering plates, and finally to the target.

At the target, the scattered electron beam and the reflected electron beam, which comprise the total return beam, are formed. The energy spread of the scattered electron is always greater than that of either the primary beam electrons or the reflected beam electrons. Therefore, the scattered electron beam always includes both the primary and reflected beams. The scattered electrons receive maximum energy increments from high signal (white) areas of the target and minimum energy from low signal (dark) areas and thus the maximum scattered beam diameter is therefore dependent upon the signal at the target as shown in figure 122. Since the reflected beam is included in the scattered beam, its position in the beam must be such that its removal will least disturb the collection of the desired portions of the scattered beam by the multiplier.

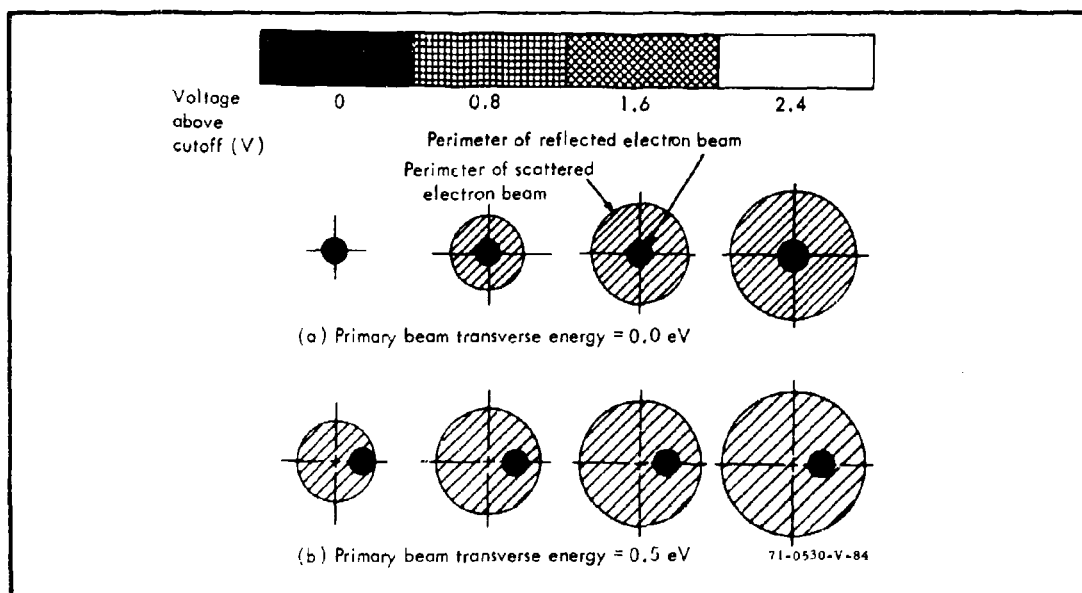


Figure 122. Return Beam Cross Section at an Antinode

If the outgoing (primary) beam is aligned with the magnetic focus field and approaches the target perpendicularly, the reflected beam leaves the target similarly aligned. The transverse energy of scattered electrons from low signal areas of the target will not be very different from that of the reflected beam, so that both will disappear into the separation aperture, and the result is a black clipped picture.

To collect scattered electrons with a full range of energies (representing all light levels on the target), it is necessary to apply transverse energy to the primary beam as shown in figure 122. This may be accomplished by placing a voltage across the alignment plates and/or by increasing the current in the auxiliary alignment coils. Through this action, the primary and reflected beams are removed from the center of the scatter beam.

The target material in the usual II is an electronically conducting glass. Because of the superior noise characteristics of the isocon readout, the II is reported to be more sensitive than an IO equipped with a similar target. However an IO with an MgO target will be more sensitive than an II with a glass target. For low-light-level use, the II will employ a wide spaced target-to-mesh assembly to increase sensitivity and reduce lag.

The output signal current, I , of the II, is related to the input photocathode current by the relation

$$I = G_M (G_T - 1) a K T_M i / e_v e_h, \quad (252)$$

where the terms are as described above, except that a is the scatter gain of the isocon readout and K is a signal reduction factor that has been variously attributed to field mesh transmittance or incomplete separation of reflected and scattered electrons. The scatter gain is reported to be about 2, and a value of 0.6 will be used for K .

The signal transfer curve reported for the II is shown in figure 123. For calculation purposes, G_M is taken to be 535, T_M is 0.66, σ_T is 3.2×10^{-3} amperes/watt, and A is $7.68 \times 10^{-4} M^2$. The target gain is calculated from the signal transfer curve, equation 252, and the relation $i = \sigma_T A H_T$.

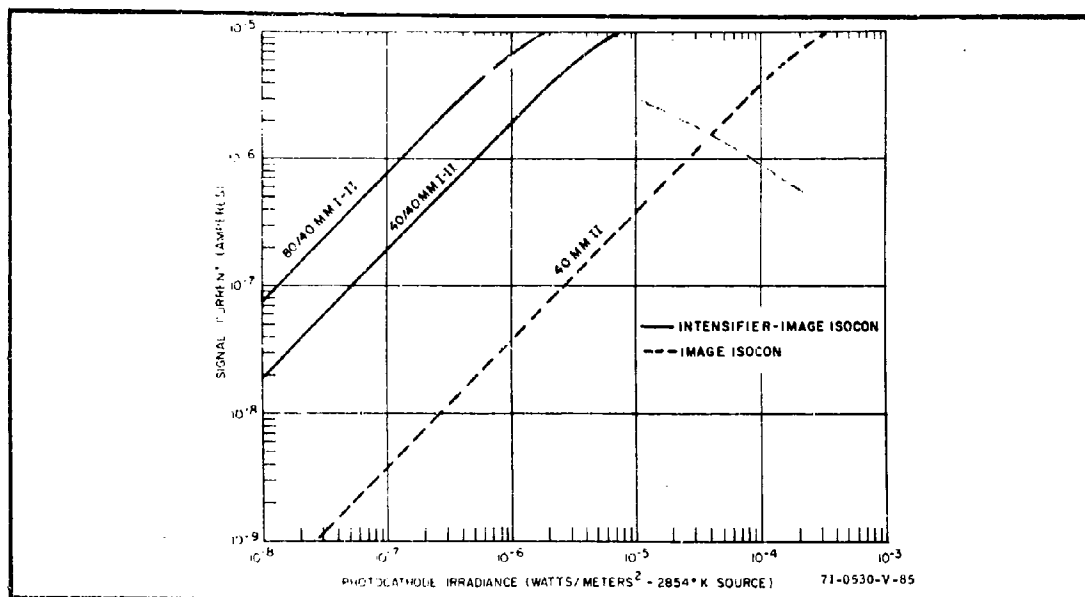


Figure 123. Signal Current Versus Photocathode Irradiance
Characteristic for the RCA C21095 Image Isocon
and Intensifier - Image Isocon

The amplitude response of the II is light level dependent. Some data in the form of an uncompensated square wave response is shown in figure 124 as reported by RCA in their data sheet of March 1968. Since that time, the light level dependency has gone largely unnoted in data sheets, although it is still acknowledged. More recent data implies a lesser degree of dependency. However, predictions made with the new data tend to be quite optimistic, and performance predictions will not be made pending further investigations. However, the signal and noise equation will be listed below.

The video S/N ratio is written in the following form for the image isocon.

$$\text{SNR}_{\text{VO}, 1} = \frac{I}{(\bar{I}_e^2 + \bar{I}_T^2 + \bar{I}_{BD}^2 + \bar{I}_{BH}^2 + \bar{I}_P^2)^{1/2}} \quad (253)$$

where I is the output signal current given by equation 252 and,

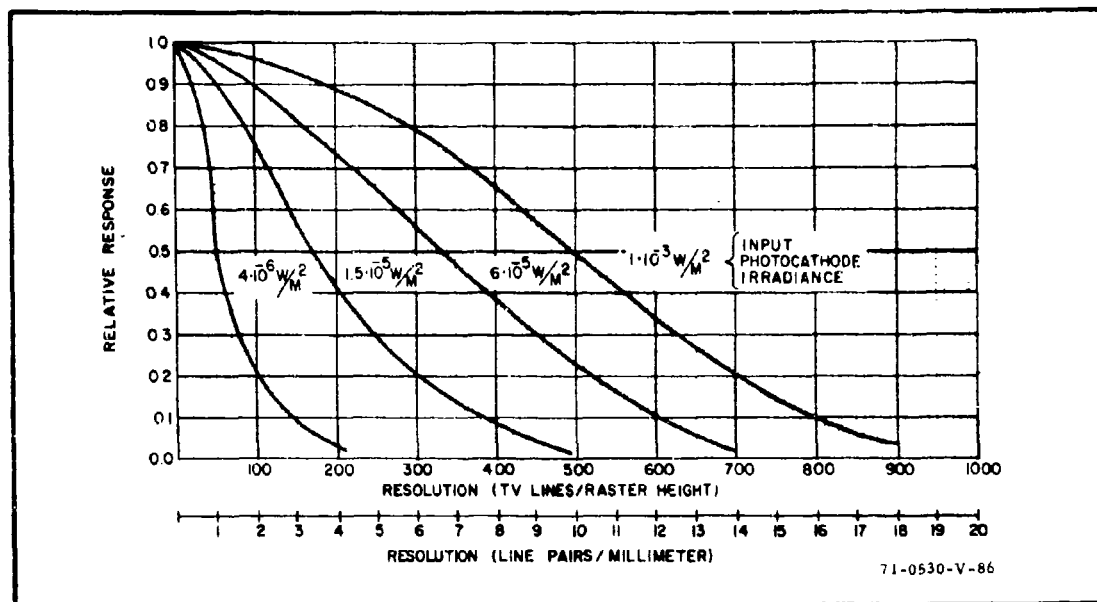


Figure 124. Uncompensated Horizontal Square Response for the RCA C21095 Image Isocon at Various Input Photocathode Irradiance Levels

a. \bar{I}_e^2 is the mean square photoelectron noise given by

$$\bar{I}_e^2 = G_M^2 (G_T - 1)^2 a^2 K^2 T_M e \Delta f i_{\max} / e_v e_h \quad (254)$$

b. \bar{I}_T^2 is the mean square target noise which is

$$\bar{I}_T^2 = G_M^2 G_T a^2 K^2 T_M e \Delta f i_{\max} / e_v e_h \quad (255)$$

c. \bar{I}_{BD}^2 is the mean square beam noise due to dark current,

$$\bar{I}_{BD}^2 = G_M^2 (G_T - 1) K e \Delta f T_M K_D i_{\max} / e_v e_h \quad (256)$$

d. \bar{I}_{BH}^2 is the mean square beam noise proportional to signal level

$$\bar{I}_{BH}^2 = G_M^2 (G_T - 1) a K e \Delta f T_M i_{\max} / e_v e_h \quad (257)$$

and \bar{I}_P^2 is the mean square preamplifier noise.

$$I_{RMS} = I_P \quad (258)$$

In the above expressions, the photoelectron, target, and preamplifier noises are quite conventional, but the beam current noise expressions assumed require some explanation.

The dark current represents that portion of the reflected electrons which are not separated from those scattered. In optimum operation, this is reported to be approximately 5 percent of the highlight signal current $(G_T - 1) T_M i_{max}/e_v e_h$. A second component of beam noise will be that due to the signal itself as represented by equation 257. Both the beam dark current and beam signal noises are difficult to measure and probably variable depending on camera setup, but their impact on performance will not be great in any event.

SECTION XV

RANGE ANALYSIS

Of fundamental concern to the electro-optical system designer is the determination of the range at which a given target can be detected, recognized, and identified. It is possible to estimate these ranges using the previously derived signal-to-noise ratio expressions, and the techniques for doing this will be discussed here.

First, the analytic model appropriate for range analysis for photoelectron-limited sensors will be discussed and then the model will be extended to include preamplifier-limited and photoelectron-limited sensors. An integral part of the range analysis is the influence of atmospherics on apparent contrast, and this is discussed next. In the latter parts of Section XV, the question of natural and active irradiance are considered. Then the level of target discrimination is discussed and finally examples are given of the calculation of detection and recognition ranges.

15.1 ANALYTICAL MODEL - PHOTOELECTRON-LIMITED SENSORS

As a beginning point in the derivation of the equations used for range analysis, we will use equation 7 which gives the display signal-to-noise ratio for a photoelectron-limited sensor of unity MTF. Equation 7, for convenience is repeated here as equation 259. In the equation, a factor of $(2-C)$ in the denominator has been dropped to give a better fit to measured data, see Section XI.

$$SNR_D = \frac{C \bar{n}_{xy} \max a t}{\left[\bar{n}_{xy} \max a t \right]^{1/2}} \quad (259)$$

C is the contrast of the image background calculated after the generation of the photoelectrons. C is defined as the difference between the scene

high-light and the scene low-light photoelectron rates divided by the scene high-light photoelectron rate. To a very good approximation, the contrast after the photoelectron generation is equal to the contrast of the target background at the input of the photocathode before the photoelectron generation. Of course, the contrast of the target background at the sensor is, in general, smaller than that at the target due to the influence of atmospheric effects as discussed below in the discussion on atmospheric effects. In equation 259, a is the area of the target image on the photocathode, t is the integration time of the eye, and \bar{n}_{xy} is the average highlight photoelectron rate which, in terms of the photoelectron current, i , electronic charge, e , and active area of the photocathode A , is given by equation 8, which is also repeated here as equation 260.

$$\bar{n}_{xy} \text{ max} = \frac{i}{eA} \quad (260)$$

Using equation 10 of Section II, equation 260 becomes

$$\bar{n}_{xy} \text{ max} = \frac{\sigma AH}{eA} = \frac{\sigma H}{e} \quad (261)$$

where σ is the photocathode responsivity in amperes per watt and H is the irradiance incident on the photocathode in watts per square meter.

The effect of the apertures of the sensor and lens is to smear the target image, and if $g(x, y)$ is the target envelope after the filtering, then, using the energy model which was discussed in Section III, we have that the area of the image after being filtered by the system aperture response (MTF's), is given by

$$a = \int_{-\infty}^{\infty} \int_{-\infty}^{\infty} g(x, y)^2 dx dy \quad (262)$$

Furthermore, if it is assumed that the impulse response of the sensor is separable into the product of a horizontal and a vertical response and, for convenience, that the two responses are equal, then for a square image we have that a is given by

$$a = \left[\int_{-\infty}^{\infty} g_x(x)^2 dx \right]^2 = \left[\int_{-\infty}^{\infty} g_y(y)^2 dy \right]^2 = (R_K x_o)^2 \quad (263)$$

where x_o is the width of the square at the input of the photocathode and R_K is the proportionality constant used in Section IV. Using equations 261 and 263 in equation 259 we have

$$SNR_D = \frac{C \frac{\sigma H t}{e} \left[\int_{-\infty}^{\infty} g_x(x)^2 dx \right]^2}{\left[\frac{\sigma H t}{e} \left[\int_{-\infty}^{\infty} g_x(x)^2 dx \right]^2 \right]^{1/2}} \quad (264a)$$

$$= C \left(\frac{\sigma H t}{e} \right)^{1/2} \int_{-\infty}^{\infty} g_x(x)^2 dx \quad (264b)$$

$$= C \left(\frac{\sigma H t}{e} \right)^{1/2} R_K x_o \quad (264c)$$

15.2 ANALYTICAL MODEL-PREAMPLIFIER-LIMITED AND/OR PHOTOELECTRON LIMITED

If the sensor is not photoelectron limited, the sensor gain G and the noise in the preamplifier must be included in the SNR_D expression. The effect of the gain is to increase the photoelectron current by G , and the noise due to the preamplifier can be added in quadrature to the photoelectron noise.

Including these two aspects, we have

$$SNR_D = \frac{C \frac{\sigma H t G}{e e_v e_h} \left[\int_{-\infty}^{\infty} g_x(x)^2 dx \right]^2}{\left[\frac{\sigma H t G^2}{e e_v e_h} \left[\int_{-\infty}^{\infty} g_x(x)^2 dx \right]^2 + \frac{I_{pa}^2 t_a}{\Delta f e^2 A} \right]^{1/2}} \quad (265)$$

where $e_v e_h$ is the scan efficiency and accounts for a larger current being generated due to the increased speed of the readout that is required to

accomplish a given frame time with a specified amount of dead time (flyback time); that is, $\frac{dq}{dt}$ is larger with dead time than what it would be if there were no dead time. In equation 265, G is the overall gain of the sensor and any intensifiers, and $g_x(x)$ is the target envelope after the input envelope is filtered by all of the apertures of the system. Δf is the video bandwidths over which I_{pa} is measured.

A simplification of the calculation occurs if an exponential fit to the system MTF (sine wave response) is made; that is, it is assumed that the system MTF is given by

$$R_o(N_{LP}) = \exp \left[- \frac{(2\pi N_{LP})^2 a^2}{2} \right] \quad (266)$$

and a is determined by fitting the system MTF to equation 266 at a particular frequency value, N_{LP} . For a square target x_o wide at the input of the system and with a particular value of a , the area of the output image, a , can be calculated and R_K determined using equation 263. In figure 31, R_K is plotted as a function of normalized target dimension x_o/a and the exponential MTF. Therefore, knowing a , one can obtain R_K as a function of x_o . In terms of R_K and x_o , equation 265 can be written as

$$SNR_D = \frac{C \frac{\sigma H t G}{e e_v e_h} \left[R_K x_o \right]^2}{\left[\frac{\sigma H t G^2}{e e_v e_h} \left[R_K x_o \right]^2 + \frac{I_{pa}^2 t (R_K x_o)^2}{\Delta f e^2 A} \right]^{1/2}} \quad (267)$$

The procedure for performing the range analysis is as follows. First, the required level of target discrimination is determined such as detection, recognition, identification. Corresponding to this discrimination level, a minimum target dimension must be resolved, ΔX , (see Section VI), and there is a required SNR_D calculated on the basis of a square of size ΔX^2 . For example, for a 50 percent probability of detecting a square target, ΔX , is the target dimension X_t , and SNR_D for the square is 2.8. For a given irradiance level, equation 267, or the photoelectron limited version equation

264, can be solved for the contrast at the sensor, C , as a function of input image size x_0 . Of course, x_0 is a function of range so we have the contrast, C , required by the SNR_D expression as a function of range and a plot can be made of the sensor's required contrast versus range. If one then calculates the actual contrast of the target background as a function of range and atmospheric conditions and then plots the result on the same graph as the required contrast, the intersection of the two curves gives the range which corresponds to the given target level of discrimination and atmospheric condition. In order to perform these calculations, we must consider the influence of atmospheric conditions on the apparent contrast of the target background. This will be considered next.

15.3 ATMOSPHERICS INTRODUCTION

The primary influence of atmospheric conditions on an electro-optical system is to reduce the contrast of the target background as viewed from a distance R . For a passive television sensor, the contrast is reduced by two phenomena: (1) light from the target background is absorbed and scattered out of the field of view, and (2) some of the ambient light from outside the field of view is scattered into the field of view. If H_T is the irradiance from the target and H_B that from the background, then assuming that $H_T > H_B$, at zero range the contrast is given by

$$C(0) = \frac{H_T - H_B}{H_T} \quad (268)$$

If δ is the amount by which H_T and H_B are reduced over a range R ($0 \leq \delta \leq 1$)* and H_{BC} is the total irradiance which is added into the field of view; then the contrast at range R is

* For convenience it was assumed that the reduction in H_T and H_B is the same.

$$\begin{aligned}
 C(R) &= \frac{(H_T \delta + H_{BC}) - (H_B \delta + H_{BC})}{H_T \delta + H_{BC}} \\
 &= \frac{H_T - H_B}{H_T + H_{BC}/\delta}
 \end{aligned}
 \tag{269}$$

and it is clear from equation 269 that both the loss of light from the target and background, and the addition of extra light degrades (reduces) the intrinsic target-background contrast.

For an active television system, the contrast is reduced by 1) light from the radiating source is absorbed and scattered out of the field of view in a manner similar to 1) above and, 2) some of the radiation from the radiator is backscattered by the atmosphere into the field of view which contributes a term analogous to 2) above. The net effect is a reduction in contrast with an increase in range.

A detailed consideration of the atmosphere must consider numerous factors such as altitude, slant range, amount of H_2O and CO_2 , different types of scattering particles and wavelength. In general, the calculation can get so detailed as to be virtually impossible to work with in practice. In the following, a simplified model will be discussed which, although far from complete, at least adequately represents a workable approximation to the real world situation for both the passive and the active viewing conditions.

15.3.1 Passive Irradiance

It is assumed that the transmission of the atmosphere is given by an exponential relationship between the atmospheric attenuation coefficient, σ , and range, R , as

$$T = \exp(-\sigma R) \tag{270}$$

The atmospheric attenuation coefficient is a function of many factors such as wavelength, slant range, altitude, and visibility. It is common to ignore the absorption due to water vapor and carbon dioxide which occurs at specific

wavelengths and to work with average curves over wavelength intervals. At sea level in the visible wavelength region, Middleton gives,

$$\sigma_o = \left(\frac{3.912}{R_v} \right) \quad (\text{visible spectrum}) \quad (271)$$

where R_v is the visibility range, that is the range at which the contrast transmission of the atmosphere over a horizontal path is reduced to 2 percent of the zero range value. The wavelength interval is taken to be from 380 to 720 nm. Values of visibility correspond to meteorological conditions such as fog, haze, clear and are used to include the influences of the various meteorological conditions on viewing. At altitudes above sea level, σ_o must be modified and two different correction factors are used as shown in figure 125. For horizontal paths at altitude h , the sea level value of the attenuation coefficient is multiplied by the correction factor for horizontal paths at altitude h from figure 125. For slant paths, the slant path value from figure 125 is used to multiply the sea level attenuation coefficient.²⁹

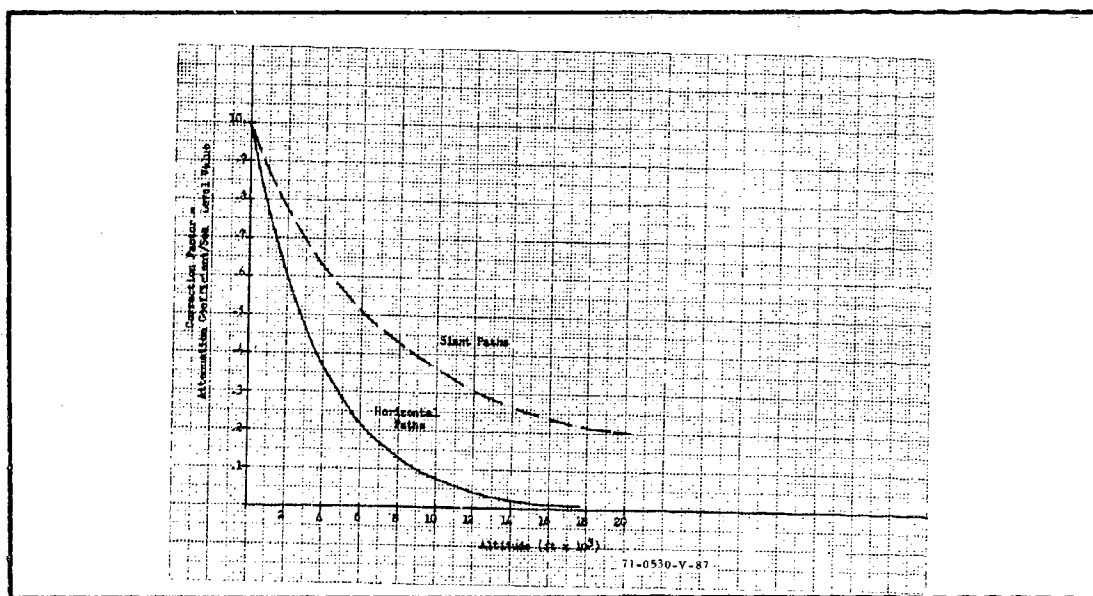


Figure 125. Correction Factor to Atmosphere Attenuation Coefficient

Middleton³⁰ has shown that for a vertical target viewed against a horizontal background the contrast at range R is given by

$$C(R) = C(o) \left[1 - K \left(1 - e^{-\sigma_o R} \right) \right]^{-1} \quad (272)$$

where $C(o)$ is the contrast of the target background at zero range (the intrinsic contrast) and K is the sky-ground ratio which can be as small as 0.2 for clear sky-fresh snow conditions and as large as 25 for overcast sky-forest conditions. Middleton suggests that for daylight irradiance levels that K is typically equal to $1/\rho_B$ for overcast sky conditions, where ρ_B is the average reflectivity of the background. For clear sky conditions he gives that $K = 0.2/\rho_B$. As a first approximation, it seems reasonable that for night viewing the clear sky condition can be used when the sky is clear and a fair amount of moon is out. The overcast condition applies to either overcast with moon or to starlight with or without overcast due to the diffuse nature of starlight. Representative values of K are listed in table XIV.

TABLE XIV
REPRESENTATIVE VALUES OF SKY-GROUND RATIO (K)

<u>Sky Conditions</u>	<u>Background</u>	<u>K</u>
Clear	Fresh Snow	0.2
Clear	Desert	1.4
Clear	Forest	5
Overcast	Fresh Snow	1
Overcast	Desert	7
Overcast	Forest	25

For a value of $K = 1$, the background and sky look the same. Using $K = 1$, equation 272 becomes

$$C(R) = C(o) \exp (-\sigma_o R) \quad (273)$$

which is Middleton's result for viewing a vertical target against the horizon sky. In figure 126, equation 272 has been plotted using normalized apparent

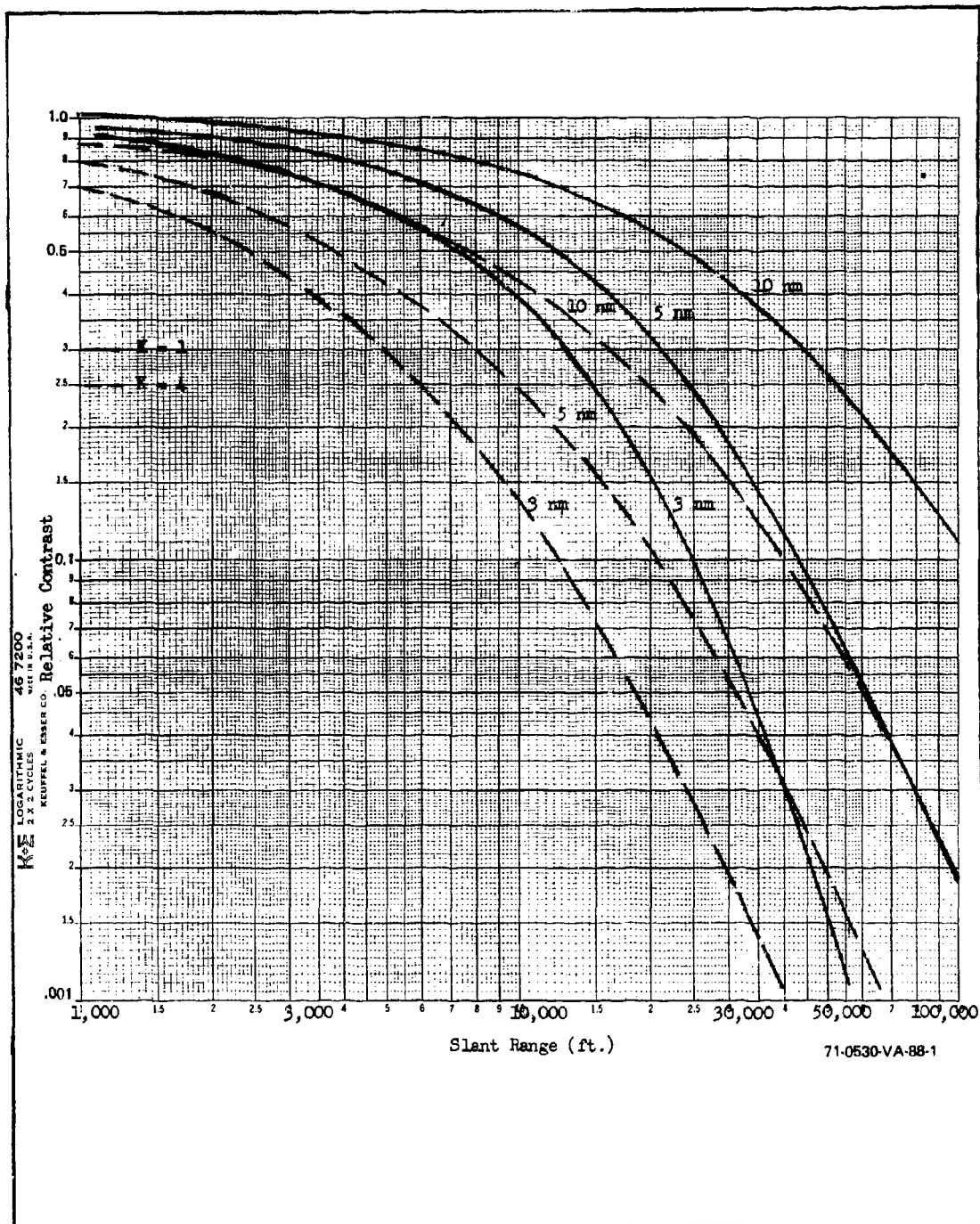


Figure 126. Relative Contrast Versus Slant Range for Aircraft
Altitude of 8,000 ft

contrast, $C(R)/C(o)$, versus range for two different values of sky-ground ratio and three values of visibility. For this plot, it has been assumed that the aircraft is at an altitude of 8,000 feet and that the target background is at sea level. The correction factor from figure 125 at 8,000-ft altitude for slant paths was used to modify the atmospheric attenuation coefficient.

15.3.2 Active Irradiance

For active night vision systems, it is common to use a covert irradiance. Presently, a GaAs laser operating at 850 nm offers a good tradeoff between covertness, adequate laser power and photocathode response. In the following we will be only concerned with GaAs sources. In this wavelength region, the atmospheric attenuation coefficient is somewhat smaller than that in the visible, typically smaller by about 30 percent. Steingold and Strauch³¹ maintain that the atmospheric attenuation coefficient is given by

$$\sigma_o = \frac{3.91 \times 10^{-3}}{V} \left(\frac{550}{\lambda} \right)^{0.585 V^{1/3}} \quad (274)$$

where V is the visibility in kilometers, λ is the wavelength in nanometers, and σ_o is the attenuation per kilometer for sea level altitudes. At other altitudes, the correction factors from figure 125 can be used as a first approximation. However, care must be taken to use the appropriate correction factor as we shall see.

A fraction of the radiated power is scattered by the atmosphere back into the field of view of the sensor, and the relative contribution of this backscatter can be so large as to swamp out the return from the target and background. For this reason, for systems designed for long-range operation, it is necessary to turn the sensor on only when target signals are being received in order to minimize the influence of atmospheric backscatter. There is normally a separation between the sensor and the radiator. This separation, together with the field of views of the sensor and radiator, allows backscatter to be received only from ranges greater than R_o , where R_o is the distance from the sensor to the first crossing of the fields of view of the sensor and irradiator. Let R_j be the slant range from the sensor to the target and R_1

the slant range from the sensor to the closest intercepted ground distance determined by the field of view. The contrast at range R_T is given, to a good approximation, by

$$C(R_T) = C(o) \left[1 + \frac{F_B}{F_S} \right]^{-1} \quad (275)$$

where

$$\frac{F_B}{F_S} = \frac{\sigma R_T^2}{8\rho e^{-2\sigma R_T}} \left\{ T \int_{R_o}^{R_1} \frac{e^{-2\sigma R}}{R^2} dR + \int_{R_1}^{R_T} \frac{e^{-2\sigma R}}{R^2} dR \right\} \quad (276)$$

where σ , R_o , R_1 , and R_T are defined as above; ρ is the reflectivity of either the target or the background, whichever is the larger; and T is the ratio of the transmission of the sensor when off to that when on. When equation 276 is large, the apparent contrast is small. To minimize the influence of the atmospherics on contrast, one makes T as small as possible. Of course, for the ideal case $T = 0$ (32, 33, 34). A detailed calculation involving various values of visibility, T and R_o , showed that the ideal case is approximated very closely if the ratio of $(T/R_o) = 10^{-8}$ for R_o expressed in feet. At aircraft altitudes other than sea level, σ_o must be modified using the appropriate horizontal correction factor from figure 125 for each incremental contribution of the backscatter since σ is now a function of altitude. This calculation can be most conveniently done by fitting an exponential curve to the horizontal correction factor curve of figure 125 so that the fit is exact at the altitude of the aircraft, H_A ; that is, if K_1 is the correction factor obtained from figure 125 for altitude H_A , then A is determined by

$$K_1 = e^{-AH_A} \quad (277)$$

For any other altitude H , which is determined by the slant range field of view and where along the slant path the backscatter is originating, σ is given by σ_H where

$$\sigma_H = \sigma_o \left(e^{-AH} \right) \quad (278)$$

This is the value which should be used in the exponential terms inside the brackets of equation 276. The target or background return must be corrected for the slant path as was done for the passive case, and this value of σ , called σ_S is used in the numerator and the exponential term of the denominator of the terms which multiply the bracketed terms of equation 276. Equation 276 then becomes

$$\frac{F_B}{F_S} = \frac{\sigma_S R_T^2}{8\rho e^{-2\sigma_S R_T}} \left\{ T \int_{R_o}^{R_1} \frac{e^{-2\sigma_H R}}{R^2} dR + \int_{R_1}^{R_T} \frac{e^{-2\sigma_H R}}{R^2} dR \right\} \quad (279)$$

This is the expression which should be used with equation 275 for aircraft altitudes different from sea level.

15.4 NATURAL ILLUMINATION

Before going further into range analysis, it is important to consider some aspects of natural irradiation which have been confused in the past. Specifically, it will be necessary to consider scene irradiance and scene illuminance.

To faithfully reproduce luminance contrasts, television camera tubes manufactured for use in the TV entertainment industry are purposely designed or otherwise altered to provide a spectral response like that of the human eye. Under these conditions, it is reasonably appropriate to measure tube performance in terms of psychometric quantities (luminance), and special calibrated test sources were developed for this purpose. However, for industrial or military use, luminance contrast is secondary to the detection or observation of specific objects, and the spectral responsivity of tubes optimized for these purposes can and do differ markedly from that of the human eye.

Since the test sources used for measuring entertainment tubes are quite suitable for measuring these specialized industrial and military tubes, tube manufacturers can hardly be faulted for using them. However, the calibration of these sources in psychometric units is totally unrealistic from a scientific viewpoint. But, as a practical matter, the specification in terms of psychometrics proved convenient for first order analysis of certain sensors which respond primarily in the visible because of the considerable quantity of psychometric measurements of scene light level conditions which have been made. These data are readily available and of widespread circulation. The measurement of the performance of electro-optical sensors was not precise and the error involved in using the psychometric units was often less than that of other measurement errors. However, as the measurement and specification procedure have improved, these errors have become limiting. Whatever the rationale in the past, the use of psychometric units for physical sensors other than photometers is fundamentally unsound and should therefore be intolerable to the scientific and engineering community. On the other hand, the conversion process to radiometric terms will not be an easy one for the use of psychometrics has become ingrained in the art.

In the following, two specific sensors which have spectral responses quite different from the eye will be considered. These sensors, which have response types classified as S-25 and S-20-XR (extended red), are assumed to be used for the viewing of neutrally reflective scenes irradiated by a combination of moonlight and airglow through several air masses. By happenstance, it is found that the performance using psychometric units does not differ by a large amount from that predicted using radiometric units but this is only a coincidence. The very same sensors could be used with the visible completely filtered out in which case totally different answers would be obtained.

15.4.1 Current Methods of Analysis Using Psychometric Units

In converting from psychometrics to radiometrics, it is first worthwhile to review the current methods of analysis using psychometric units. The specific examples used will be an S-25 photosurface and an S-20-XR (extended red) photosurface. The spectral responses of these two surfaces are shown in figure 127.

The luminous sensitivity of these surfaces is measured by using a 2854°K source. A known amount of light measured in footcandles is projected on the photocathode, and the current drawn from the surface is measured. The ratio in amperes/lumen, or more commonly microamperes/lumen, is known as the luminous sensitivity; the luminous sensitivity S can be calculated from the relation

$$S = \frac{\sigma_o \int_{\lambda} R(\lambda) W_{2854^{\circ}K}(\lambda) d\lambda}{680 \int_{\lambda} y(\lambda) W_{2854^{\circ}K}(\lambda) d\lambda} \quad \frac{\text{amperes}}{\text{lumen}} \quad (280)$$

where

- σ_o is the spectral responsivity of the photosurface at the peak in amperes/watt
- $R(\lambda)$ is the relative spectral response of the photosurface
- $W_{2854^{\circ}K}$ is the relative spectral emittance of a 2854°K source
- 680 is the peak response of the human eye in lumens/watt
- $y(\lambda)$ is the relative spectral response of the eye.

The result of performing the calculation using the S-25 surface is 198 microamperes/lumen which corresponds closely to that quoted by the manufacturer of 200 $\mu\text{A/lumen}$. With the S-20-XR surface, the calculation yields 131 $\mu\text{A/lumen}$ which does not correspond to the measured value of 196 $\mu\text{A/lumen}$. However, both numbers are probably correct, for the 196 figure is an average over the entire photocathode while the 131 corresponds to a particular 1/2-inch-diameter spot at which the spectral responsivity was measured (monochrometers usually have insufficient power to irradiate the entire photocathode).

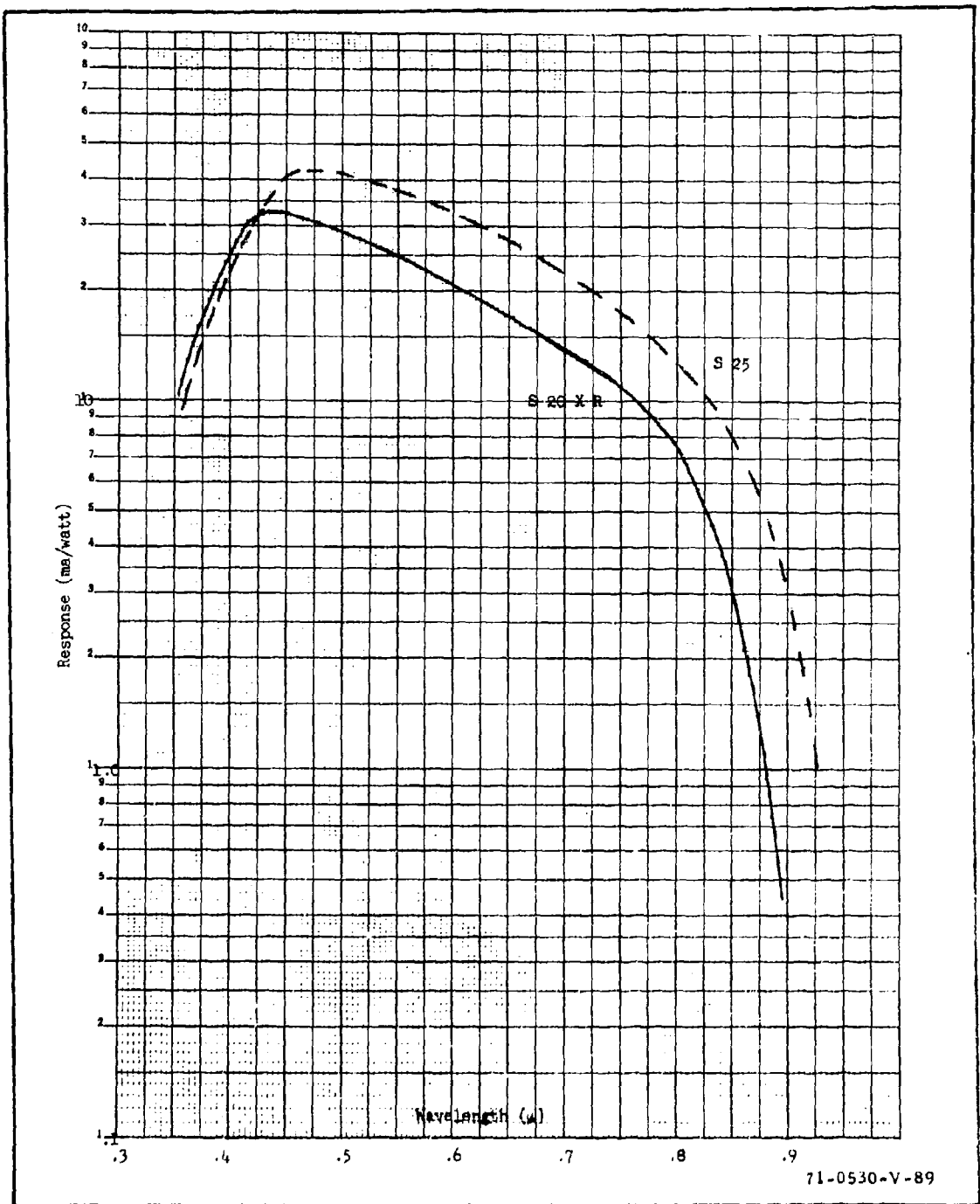


Figure 127. The Spectral Responsivity of Two Photocathodes

The illuminance of the earth or of a particular target on it is either measured with a photometer or calculated if the spectral irradiance of the source is known as follows:

$$E_S = 680 \int_{\lambda} y(\lambda) H(\lambda) d\lambda = \frac{\text{lumens}}{\text{ft}^2} = fC \quad (281)$$

where the terms are as before except for $H(\lambda)$ which is the source irradiance in watts/ft². The result of this calculation for four cases, of full moon, of 0.3 full moon, for 0.03 full moon, and .03 full moon all plus airglow and a function of the number of air masses between the moon and the irradiated area are compiled in tables XV through XX at the end of this section. The number of air masses between the illuminated area and the moon is shown in figure 128, and in figure 129, the spectral distribution for 0.1 full moon plus airglow is shown for various values of air masses.

In making system calculations, it is customary in current practice to use the illuminance calculated by equation 281 together with the photocathode

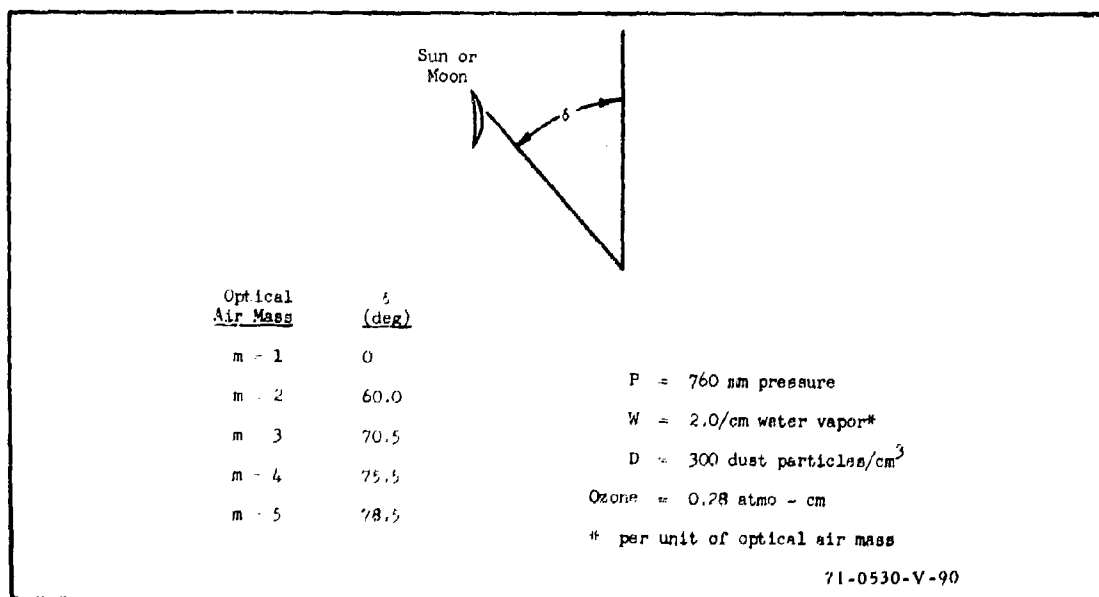


Figure 128. Air Mass Versus Source Declination

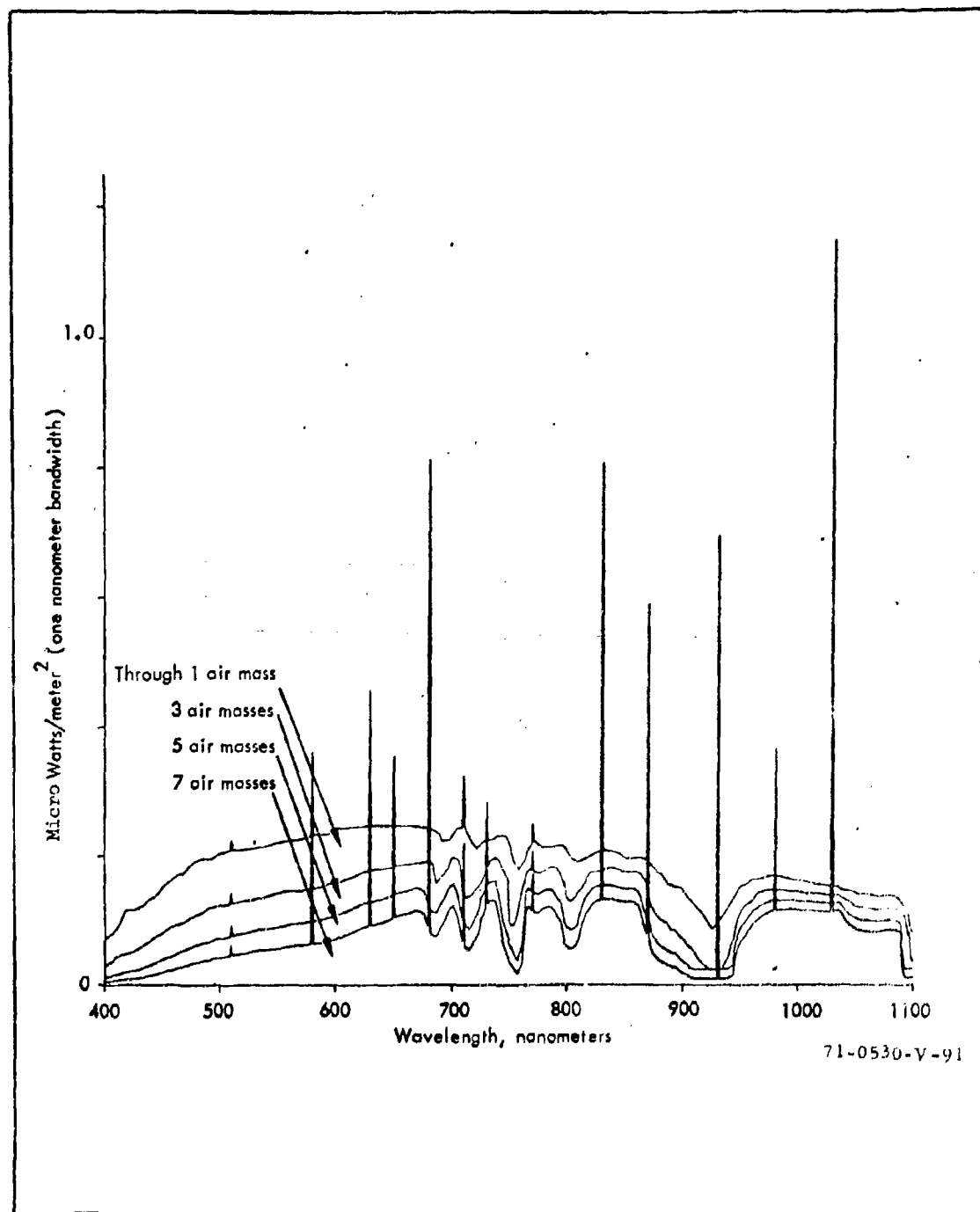


Figure 129. Irradiance from 0.1 x Full Moon Plus Airglow

luminous sensitivity as calculated in equation 280 to obtain the photocathode signal current from the relation

$$i_{pc} = \frac{\rho}{4T_{\#}^2} SAE_S \quad (282)$$

where ρ is the area reflectivity (assumed to be independent of wavelength), $T_{\#}$ is the T-stop of the objective lens, and A is the photocathode area.

15.4.2 Conversion to Radiometric Analysis

The luminous sensitivity of the photosurface, as defined by equation 281, has some utility as an indicator of photosurface quality. A quick conversion from $\mu\text{A}/\text{lumen}$ to $\mu\text{A}/\text{watt}$ can be obtained by noting that the luminous efficiency of tungsten at 2854°K is about 20 lumens/watt. Thus, a surface of luminous sensitivity 200 μA per lumen becomes 4,000 $\mu\text{A}/\text{watt}$ in radiometric terms (or perhaps 4 mA/watt would be more suitable). Alternatively, one can compute the radiant sensitivity P_R from the relation

$$P_R = \frac{\sigma_o \int_{\lambda} R(\lambda) W_{2854^\circ\text{K}}(\lambda) d\lambda}{\int_{\lambda} W_{2854^\circ\text{K}}(\lambda) d\lambda} \quad \frac{\text{amperes}}{\text{watt}} \quad (283)$$

The illuminance of the earth by natural radiant sources is quite commonly known and it would be desirable to develop radiometric equivalents such as

$$H_T = \int_{\lambda} H(\lambda) d\lambda \quad (284)$$

Tables are available for a number of sources in reference 35.

The integral of equation 284 was integrated over a spectral band of 0.35 to 0.94 micrometer for the four cases mentioned above (1.0, 0.3, 0.1 and 0.03 times full moon). As a rough rule of thumb, the natural irradiance from the three sources above in watts/ft^2 is about 1/14 of the value given in footcandles.

For sensor analysis purposes, two approaches can be taken. The most direct is to compute the sensor signal current from the equation

$$i_S = \frac{A\sigma}{4T^2} \int \rho(\lambda) R(\lambda) H(\lambda) d\lambda \quad (285)$$

The value of this integral in the form of $4T^2 i_S/A$ is provided for the two sensors in tables XV through XXII.

An alternate method corresponding to that used in current psychometric calculations is to define a specific radiant sensitivity similar to the radiant sensitivity term of equation 283 as

$$\sigma = \frac{\sigma_o \int R(\lambda) H(\lambda) d\lambda}{\int H(\lambda) d\lambda} \quad (286)$$

This term is also compiled in tables XV through XXII. This quantity has some use when viewing objects of neutral reflectivity; i.e., reflectivity which is constant with wavelength. In this event, one can calculate the signal current from the simple equation

$$i_S = \frac{\rho}{4T^2} \left[\sigma \cdot A \cdot H_T \right] = \sigma A H_{pc} \quad (287)$$

which compares directly with equation 282.

Now it is of interest to compare the results obtained using equation 282 with that obtained using equation 287 in the form

$$\frac{i_S \text{ (illuminance basis)}}{i_S \text{ (irradiance basis)}} = \frac{SAE_S}{\sigma A H_T} \quad (288)$$

as shown in tables XV through XXII. This ratio for the specific photosurfaces involved, and assuming neutral reflectivity, is very nearly a constant equal to about 1.25 for all three sources assumed. This result as mentioned above is pure happenstance although it is perhaps comforting to know that most of the rough first order calculations made using psychometric terms are very nearly correct (optimistic by about 25 percent). A short summary of the comparison for the S-25 photosurface is shown in table XXIII.

15.5 LEVEL OF DISCRIMINATION

J. Johnson's classification of discrimination as detection, orientation, recognition, identification, and his required resolution through the minimum target dimension of 2, 2.8, 8, and 12.8 TV lines respectively for the discrimination levels were discussed in Section VI. For recognition, it was shown that our experiments were consistent with Johnson's criteria.

For target detection, we will use X_t equal to the minimum target dimension, and for a 50 percent probability of detection, the corresponding value of SNR_D is 2.8. For target recognition, 8 TV lines must pass through the minimum target dimension. Using the correspondence between bar patterns of finite extent and real targets which was discussed in Section VI, we have, for a 50 percent probability of recognition of an 8-bar pattern of area equal to the target, that the SNR_D per bar required for a 50 percent probability of recognition is 5.3. Typically, real targets are approximately 2:1 in aspect so the bar pattern would be 16 bar widths long. Thus, SNR_D for a resolution element; that is, for a square of size $X_t/8$ by $X_t/8$, with a 50 percent probability is 1.25 and this is the value that should be used in solving the SNR_D equation. This procedure is rather crude in that it assumes that recognition of the target corresponds to the detection of squares of size $X_t/8$, but the preliminary experiments which were discussed in Section VI indicate that such a simplification can be made.

At first glance, it might seem that a lower SNR_D value was used for recognition than for detection. This is not so; however, since for detection SNR_D was calculated on the basis of the total area of the image whereas for recognition SNR_D was calculated on the basis of $1/(128)$ of the total area ($8 \times 8 \times 2$), and we have that SNR_D for recognition, based on the whole area is actually about 5 times larger than that needed for detection.

In any event, if X_t is the minimum target dimension and n is the required number of TV lines which must be passed through X_t , then, if the image

size on the photocathode, corresponding to X_t/n is x_o , the two can be related by the focal length f_L and the slant range to the target as

$$R = \frac{X_t f_L}{n x_o} \quad (289)$$

15.6 RANGE - PASSIVE SYSTEM, THREE-STAGE INTENSIFIER

As an example of the procedure used for performing a range analysis, we will assume that $\alpha = 2.31 \times 10^{-3}$ mm which makes equation 266 correspond closely to the MTF of a three-stage intensifier (see figure 22 in Section IV) for a plot of equation 266, for $\alpha = 2.3 \times 10^{-3}$ mm, and for a plot of a measured MTF for a three-stage intensifier. The three-stage intensifier is photoelectron limited and equation 264 will be used for the range analysis. Assume that we wish to detect a square target that is 10 ft on a side and that the focal length of the lens is 10 inches (250 mm). The required $(SNR)_D = 2.8$ for a 50 percent probability of detection. The number of resolution elements through the target is 1, and from equation 289, we have that slant range to the target, R , and image size at the input of the photocathode are related by

$$R = \frac{2,500}{x_o} \quad (290)$$

where x_o is in units of mm and R is in ft. If we further assume that the high-light reflectivity is 0.1 and the $T_{\#} = 1.58$ then the photocathode irradiance is given by

$$H_{pc} = \frac{\rho H_S}{4T_{\#}^2} = 10^{-2} H_S \quad (291)$$

Let $H_S = 10^{-3} \text{ W/m}^2$ which corresponds roughly to quarter-moon irradiance conditions, then we have that $H_{pc} = 10^{-5}$. For this value of H_{pc} , assuming that $\sigma = 4 \times 10^{-3} \text{ A/W}$ we have that equation 264 becomes

$$\frac{1.25 \times 10^{-5}}{R_K x_o} = C \quad (292)$$

Using the values of x_o and R_K from figure 31 and equation 290, C from equation 292 can be determined as a function of range and the various values of C and R are listed in table XXIV. At each range, the value of C is that required to satisfy the SNR_D equation for a 50 percent probability of detection. In figure 130, the required C is plotted as a function of range for three different scene irradiance values, 10^{-4} , 10^{-3} , and 10^{-2} W/m² which correspond roughly to clear night sky, quarter-moon and full-moon irradiance levels respectively. Also, plotted in figure 130 is the target background contrast as a function of range assuming an intrinsic contrast of $C_o = 0.3$ and a sky-ground ratio of 4, for three different visibilities. The sensor curves in figure 130 give the required C versus R relationship whereas the atmospheric curves give the available C versus R relationship and the intersection of the two sets of curves give R , for a 50 percent probability of detection under the assumed irradiance and visibility conditions. For instance, from figure 130 with full-moon irradiance conditions and 10-nmi visibility, the target can be detected with a 50 percent probability at 22,000 ft.

15.7 RANGE - PASSIVE SYSTEM ISEC

As an other example of range analysis, we will calculate the detection and recognition range for two different targets using an ISEC camera. The intensifier is an 80/40 intensifier which is assumed to be in the 40-mm mode, and the SEC is a Westinghouse WX 31223. The parameters used in the calculations are typical of those used for the 698DF ISEC camera.

The first target considered is a truck against a sand-grass background, and it is desired to calculate the range for a 50 percent probability of detecting the truck as a function of scene irradiance. For the calculation, it is assumed the intrinsic contrast of the target background is 0.6 and that the highlight reflectivity is 0.25. The focal length is 10 inches and the $T_{\#} = 1.7$. The minimum target dimension is 12 ft, and the required SNR_D

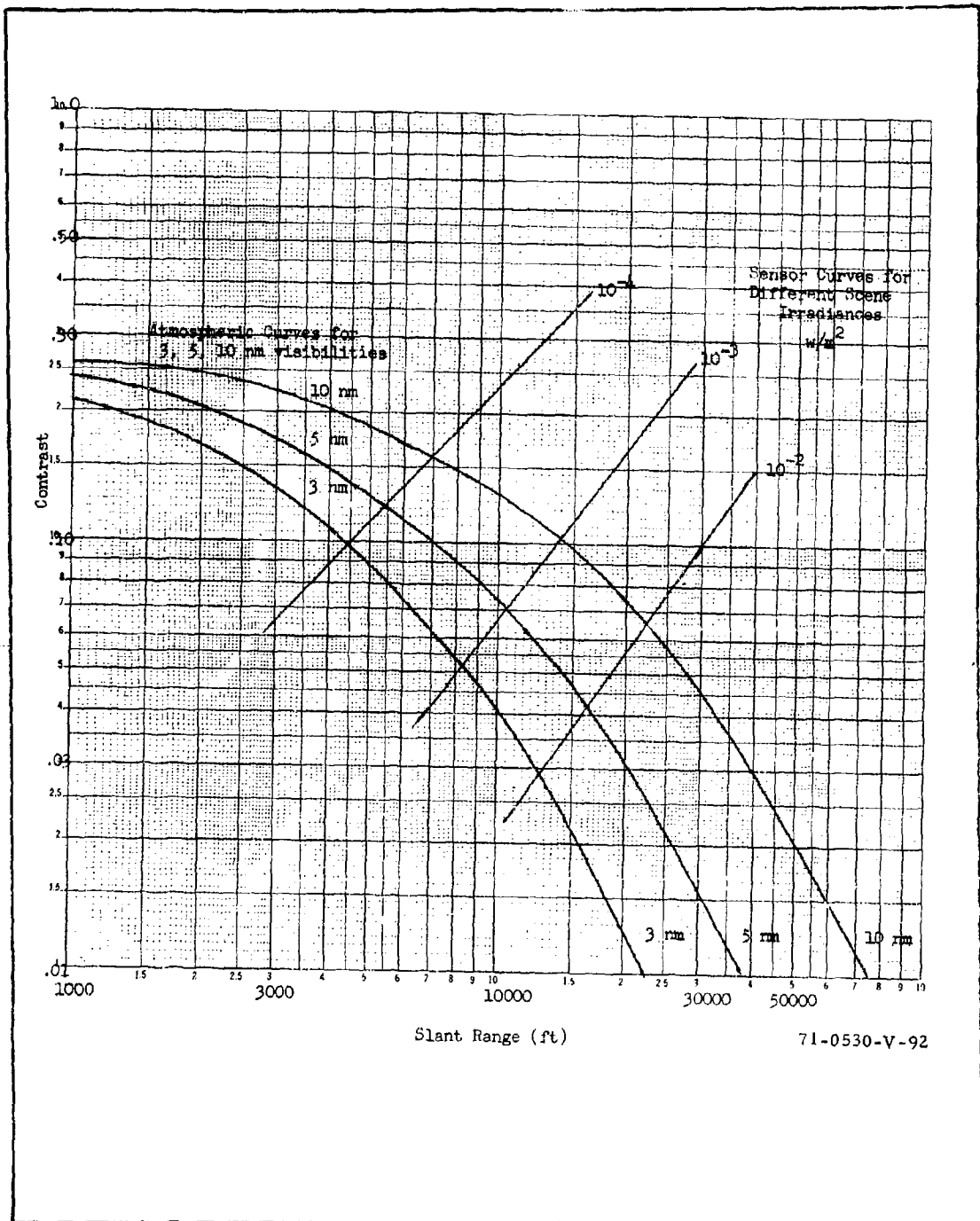


Figure 130. Required Contrast at Sensor for 50 Percent Probability of Detection and Contrast at Sensor as a Function of Range

for a 50 percent probability of detection of the truck is 2.8. The results of the calculation are shown in figure 131. Two different sky ground ratios, 1 and 4, and two visibilities 10 and 5 nmi were used. It was assumed for the calculation that the aircraft was at sea level.

As a final example, the range for a 50 percent probability of recognition of a bar panel will be calculated. The panel consisted of five bars, three black and two white. The bar width was 3 ft, and the panel was 12 x 15 feet. The ISEC characteristics used above are used here. For the calculation, the intrinsic contrast was 0.94, the highlight reflectivity 0.96, and the SNR_D for recognition of an incremental area of the panel was 1.2. As in the previous example, two sky-ground ratios, 1 and 4, and two visibilities, 5 and 10 nmi, were used. The results of the calculations are shown in figure 132.

15.8 RANGE - ACTIVE SYSTEM

For the active system, a pulsed GaAs irradiator and a gated receiver are assumed. The receiver is turned on once each scan line for a fraction of the flyback time. Rampolla has shown that the pulsed irradiator-gated receiver minimizes the contrast degrading effect of the atmosphere.³⁶ Indeed, at sea level under the relatively poor visibility condition of 3 nmi, the contrast at range R, with R of the order of 30,000 ft, is only about 1/2 the intrinsic value. If the aircraft is above sea level, the reduction in contrast is even less. For instance, if the aircraft is at 8,000 ft, then for R of the order of 40,000 ft, the contrast is only reduced by about 10 percent from the intrinsic value. For the active system, when target signals are being received, the photocathode current is given by

$$i_S = \frac{\Gamma \beta \rho P_t D_r^2 e^{-2\sigma_o R}}{4R^2} \quad (293)$$

where Γ is the transmission of the receiver optics, β the photocathode responsivity at 850 nm, ρ the scene reflectivity, P_t the average transmitted

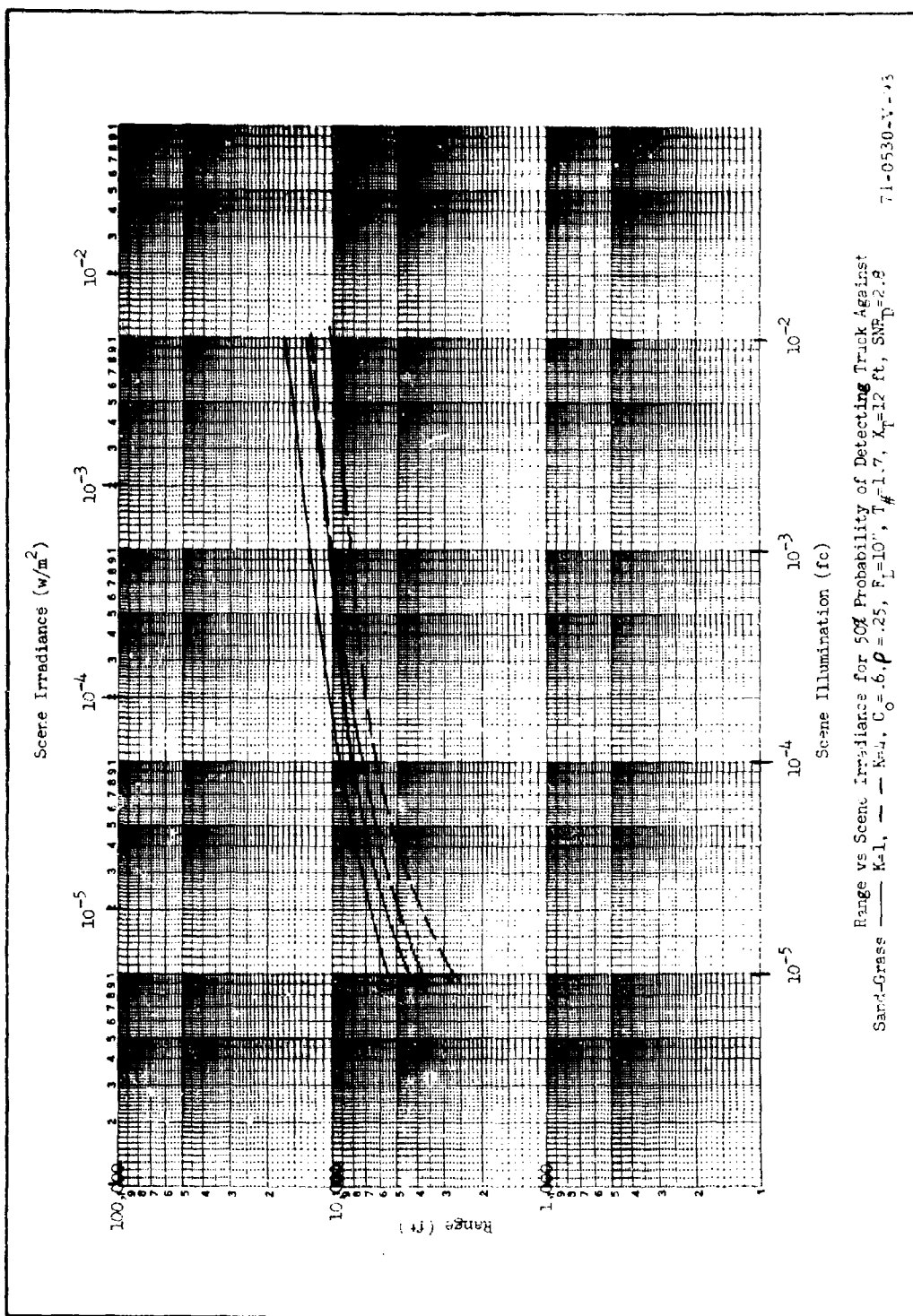


Figure 131. Range Versus Scene Irradiance for 50 Percent Probability of Detecting Truck Against Sand-Grass

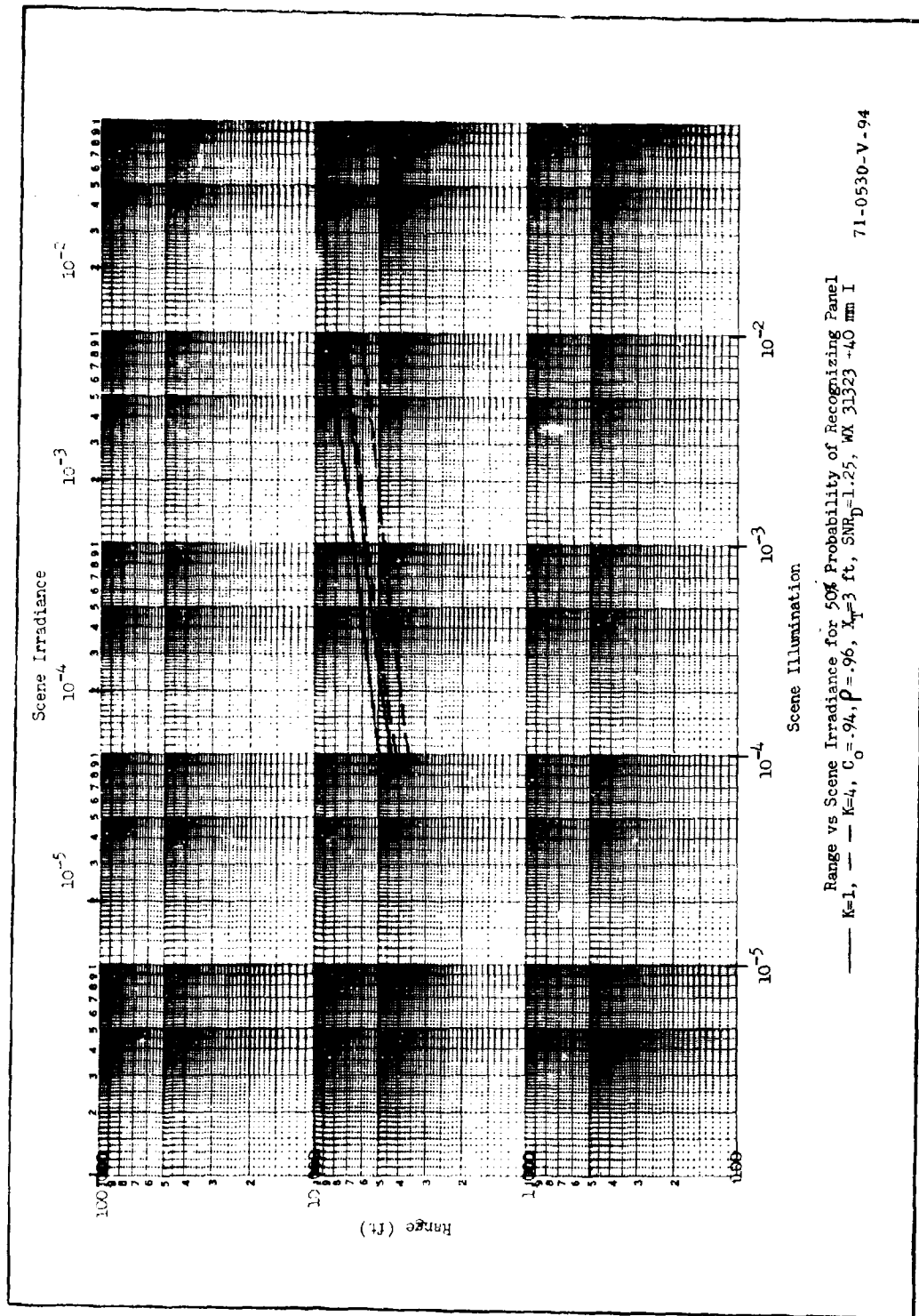


Figure 132. Range Versus Scene Irradiance for 50 Percent Probability of Recognizing Panel

laser power, D_r the receiver aperture diameter, and R the range. The atmospheric attenuation coefficient is given by equation 274. Using equation 293 in the place of equation 260, the SNR_D equation can be solved as before for the required contrast at the sensor for the given set of conditions. With equations 275 and 276, the contrast for the active system as a function of range and atmospheric conditions can be solved. In figure 133, the results of a range analysis for the active system are shown.

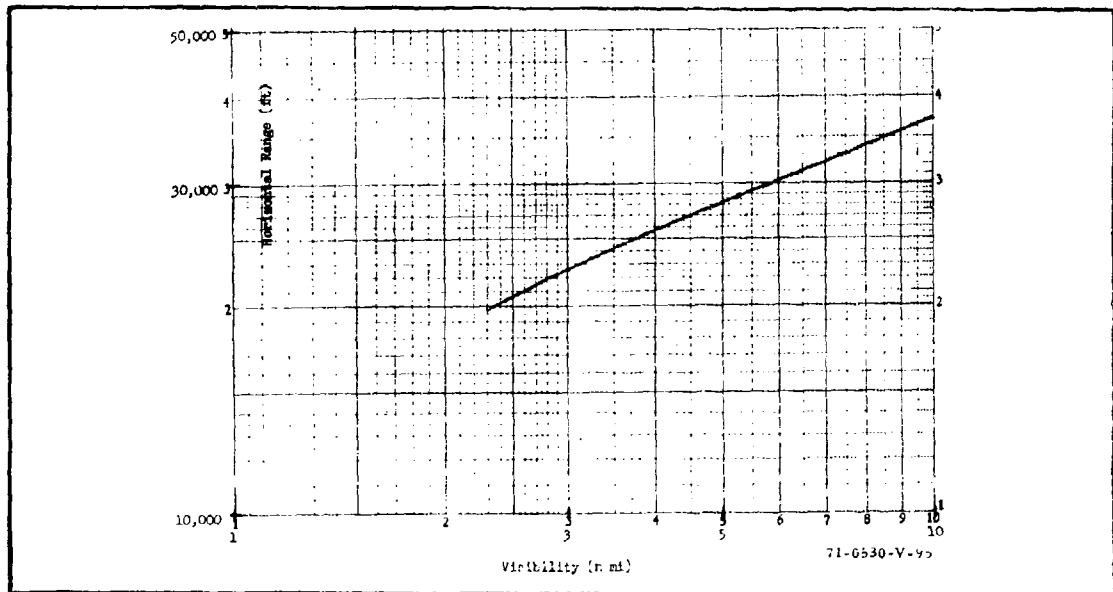


Figure 133. Detection Range Versus Visibility for Active System

15.9 SUMMARY

In Section XV, methods of predicting the range capability of sensors were devised. Using the elementary statistical model from Section II and the effect of aperture from Section IV, the range equation was significantly improved and refined. It is applicable for the photoelectron-limited system

(equation 264a, b, c) and for the preamplifier-limited system (equation 265). For the passive system, the signal current is given by equations 287 and 291; whereas for the active system, the signal current is given by equation 293.

Included in the range equation are the target size (X_t) and range (R), the sensor and target spatial characteristics ($g(X)$), the responsivity (σ) and area (A) of the photocathode, the irradiance incident onto the photocathode (H), the overall gain (G), the noise equivalent bandwidth (Δf), and noise current (I_{pc}) of the preamplifier, the target-background contrast (C) as seen at the sensor, the integration time of the eye (t), and the required value of $SNR_{D/A}$ for the given level of target discriminating (see Section VI, levels of discrimination and equation 289). Atmospheric attenuation coefficient and visibility (equation 271) and sky-ground ratio, C , table XII, are used to calculate the target-background contrast as a function of the degrading effect of the atmosphere for the passive case (equation 272). The sensor on-off ratio, atmospheric attenuation coefficient (equation 274) and sensor-radiation geometry are used to calculate the contrast (C) as a function of range for the active case (equations 275, 276). In both cases, the sea level values of the attenuation coefficient are modified using figure 125 for slant paths or horizontal paths above sea level. Using the above methods, the predicted range performance of both active and passive low-light-level television cameras are calculated.

TABLE XV
RELATIONSHIP BETWEEN RADIOMETRIC AND PSYCHOMETRIC
QUANTITIES, FULL MOON PLUS AIRGLOW WITH S-25 PHOTOCATHODE

	1 air mass	2 air masses	3 air masses	4 air masses	5 air masses	6 air masses
Natural Illuminance I_c	1.532×10^{-2}	1.228×10^{-2}	1.004×10^{-2}	8.2×10^{-3}	6.67×10^{-3}	5.42×10^{-3}
Natural Irradiance W/ft^2	1.066×10^{-3}	8.718×10^{-4}	7.309×10^{-4}	6.06×10^{-4}	5.052×10^{-4}	4.246×10^{-4}
Radiant Sensitivity A/ft^2	2.537×10^{-5}	2.042×10^{-5}	1.676×10^{-5}	1.368×10^{-5}	1.113×10^{-5}	9.157×10^{-6}
Radiometric Responsivity A/W	2.379×10^2	2.343×10^2	2.294×10^2	2.258×10^2	2.203×10^2	2.157×10^2
Luminous Sensitivity A/lm	1.983×10^{-4}	1.983×10^{-4}	1.983×10^{-4}	1.983×10^{-4}	1.983×10^{-4}	1.983×10^{-4}
Correction Factor $\frac{i_{pc}}{i_{pc}}$ illuminaance bases irradiance bases	1.287	1.281	1.277	1.277	1.277	1.261

71-0530-T-96

TABLE XVI
RELATIONSHIP BETWEEN RADIOMETRIC AND PSYCHOMETRIC
QUANTITIES, 0.3 FULL MOON PLUS AIRGLOW WITH S-25 PHOTOCATHODE

	1 air mass	2 air masses	3 air masses	4 air masses	5 air masses	6 air masses
Natural Illuminance I_c	4.602×10^{-3}	3.696×10^{-3}	3.013×10^{-3}	2.46×10^{-3}	2.007×10^{-3}	1.601×10^{-3}
Natural Irradiance W/ft^2	3.237×10^{-4}	2.624×10^{-4}	2.199×10^{-4}	1.818×10^{-4}	1.525×10^{-4}	1.277×10^{-4}
Radiant Sensitivity A/ft^2	7.663×10^{-6}	6.146×10^{-6}	5.04×10^{-6}	4.106×10^{-6}	3.365×10^{-6}	2.745×10^{-6}
Radiometric Responsivity A/W	2.367×10^2	2.342×10^2	2.291×10^2	2.259×10^2	2.207×10^2	2.15×10^2
Luminous Sensitivity A/lm	1.983×10^{-4}	1.983×10^{-4}	1.983×10^{-4}	1.983×10^{-4}	1.983×10^{-4}	1.983×10^{-4}
Correction Factor $\frac{i_{pc}}{i_{pc}}$ illuminaance bases irradiance bases	1.279	1.281	1.274	1.277	1.271	1.264

71-0530-T-97

TABLE XVII
RELATIONSHIP BETWEEN RADIOMETRIC AND PSYCHOMETRIC
QUANTITIES, 0.1 FULL MOON PLUS AIRGLOW WITH S-25 PHOTOCATHODE

	1 air mass	2 air masses	3 air masses	4 air masses	5 air masses	6 air masses
Natural Illuminance f_c	1.539×10^{-3}	1.27×10^{-3}	1.011×10^{-3}	8.25×10^{-4}	6.742×10^{-4}	5.402×10^{-4}
Natural Irradiance W/ft^2	1.087×10^{-4}	8.82×10^{-5}	7.408×10^{-5}	6.151×10^{-5}	5.151×10^{-5}	4.345×10^{-5}
Radiant Sensitivity A/ft^2	2.567×10^{-6}	2.061×10^{-6}	1.693×10^{-6}	1.382×10^{-6}	1.129×10^{-6}	9.327×10^{-7}
Radiometric Responsivity A/W	2.363×10^{-2}	2.336×10^{-2}	2.285×10^{-2}	2.246×10^{-2}	2.192×10^{-2}	2.147×10^{-2}
Luminous Sensitivity A/lm	1.983×10^{-4}	1.983×10^{-4}	1.983×10^{-4}	1.983×10^{-3}	1.983×10^{-3}	1.983×10^{-3}
Correction Factor $\frac{l_{pc}}{l_{pc}}$ illuminance basis $\frac{l_{pc}}{l_{pc}}$ irradiance basis	1.278	1.261	1.273	1.274	1.272	1.234

71-0530-T-98

TABLE XVIII
RELATIONSHIP BETWEEN RADIOMETRIC AND PSYCHOMETRIC
QUANTITIES, 0.03 FULL MOON PLUS AIRGLOW WITH S-25 PHOTOCATHODE

	1 air mass	2 air masses	3 air masses	4 air masses	5 air masses	6 air masses
Natural Illuminance f_c	4.672×10^{-4}	3.766×10^{-4}	3.089×10^{-4}	2.536×10^{-4}	2.078×10^{-4}	1.7×10^{-4}
Natural Irradiance W/ft^2	3.336×10^{-5}	2.724×10^{-5}	2.3×10^{-5}	1.926×10^{-5}	1.623×10^{-5}	1.381×10^{-5}
Radiant Sensitivity A/ft^2	7.832×10^{-7}	6.317×10^{-7}	5.211×10^{-7}	4.289×10^{-7}	3.521×10^{-7}	2.928×10^{-7}
Radiometric Responsivity A/W	2.347×10^{-2}	2.319×10^{-2}	2.266×10^{-2}	2.227×10^{-2}	2.169×10^{-2}	2.12×10^{-2}
Luminous Sensitivity A/lm	1.983×10^{-4}	1.983×10^{-4}	1.983×10^{-4}	1.983×10^{-4}	1.983×10^{-4}	1.983×10^{-4}
Correction Factor $\frac{l_{pc}}{l_{pc}}$ illuminance basis $\frac{l_{pc}}{l_{pc}}$ irradiance basis	1.2716	1.2713	1.2635	1.2604	1.2479	1.2382

71-0530-T-99

TABLE XIX
RELATIONSHIP BETWEEN RADIOMETRIC AND PSYCHOMETRIC
QUANTITIES, FULL MOON PLUS AIRGLOW WITH S-20-XR PHOTOCATHODE

	1 air mass	2 air masses	3 air masses	4 air masses	5 air masses	6 air masses
Natural Illuminance I_c	1.532×10^{-2}	1.228×10^{-2}	1.005×10^{-2}	8.2×10^{-3}	6.671×10^{-3}	5.416×10^{-3}
Natural Irradiance W/ft^2	1.066×10^{-3}	8.718×10^{-4}	7.309×10^{-4}	6.06×10^{-4}	5.052×10^{-4}	4.246×10^{-4}
Radiant Sensitivity A/ft^2	1.742×10^{-5}	1.396×10^{-5}	1.139×10^{-5}	9.255×10^{-6}	7.482×10^{-6}	6.135×10^{-6}
Radiometric Responsivity A/W	1.634×10^{-2}	1.601×10^{-2}	1.559×10^{-2}	1.527×10^{-2}	1.481×10^{-2}	1.445×10^{-2}
Luminous Sensitivity A/lm	1.308×10^{-4}	1.308×10^{-4}	1.308×10^{-4}	1.308×10^{-4}	1.308×10^{-4}	1.308×10^{-4}
Correction Factor $\frac{I_{pc} \text{ illuminance basis}}{I_{pc} \text{ irradiance basis}}$	1.236	1.237	1.234	1.245	1.253	1.241

71-0530 T-100

TABLE XX
RELATIONSHIP BETWEEN RADIOMETRIC AND PSYCHOMETRIC
QUANTITIES, 0.3 FULL MOON PLUS AIRGLOW WITH S-20-XR PHOTOCATHODE

	1 air mass	2 air masses	3 air masses	4 air masses	5 air masses	6 air masses
Natural Illuminance I_c	4.602×10^{-3}	3.696×10^{-3}	3.013×10^{-3}	2.46×10^{-3}	2.007×10^{-3}	1.601×10^{-3}
Natural Irradiance W/ft^2	3.237×10^{-4}	2.621×10^{-4}	2.199×10^{-4}	1.816×10^{-4}	1.525×10^{-4}	1.277×10^{-4}
Radiant Sensitivity A/ft^2	5.261×10^{-6}	4.199×10^{-6}	3.424×10^{-6}	2.777×10^{-6}	2.007×10^{-6}	1.838×10^{-6}
Radiometric Responsivity A/W	1.625×10^{-2}	1.6×10^{-2}	1.557×10^{-2}	1.528×10^{-2}	1.483×10^{-2}	1.44×10^{-2}
Luminous Sensitivity A/lm	1.308×10^{-4}	1.308×10^{-4}	1.308×10^{-4}	1.308×10^{-4}	1.308×10^{-4}	1.308×10^{-4}
Correction Factor $\frac{I_{pc} \text{ illuminance basis}}{I_{pc} \text{ irradiance basis}}$	1.229	1.237	1.236	1.245	1.247	1.245

71-0530 T-101

TABLE XXI
RELATIONSHIP BETWEEN RADIOMETRIC AND PSYCHOMETRIC
QUANTITIES, 0.1 FULL MOON PLUS AIRGLOW WITH S-20-XR PHOTOCATHODE

	1 air mass	2 air masses	3 air masses	4 air masses	5 air masses	6 air masses
Natural Illuminance I_c	1.539×10^{-3}	1.22×10^{-3}	1.011×10^{-3}	8.26×10^{-4}	6.742×10^{-4}	5.402×10^{-4}
Natural Irradiance W/t^2	1.087×10^{-4}	8.82×10^{-5}	7.408×10^{-5}	6.151×10^{-5}	5.15×10^{-5}	4.345×10^{-5}
Radiant Sensitivity A/t^2	1.76×10^{-6}	1.407×10^{-6}	1.149×10^{-6}	9.33×10^{-7}	7.579×10^{-7}	6.243×10^{-7}
Radiometric Responsivity A/W	1.62×10^{-2}	1.592×10^{-2}	1.55×10^{-2}	1.517×10^{-2}	1.471×10^{-2}	1.437×10^{-2}
Luminous Sensitivity A/lm	1.306×10^{-4}	1.306×10^{-4}	1.306×10^{-4}	1.306×10^{-4}	1.306×10^{-4}	1.306×10^{-4}
Correction Factor $\frac{1pc \text{ illuminance basis}}{1pc \text{ irradiance basis}}$	1.228	1.217	1.237	1.243	1.249	1.215

71-0530-T-102

TABLE XXII
RELATIONSHIP BETWEEN RADIOMETRIC AND PSYCHOMETRIC
QUANTITIES, 0.03 FULL MOON PLUS AIRGLOW WITH S-20-XR PHOTOCATHODE

	1 air mass	2 air masses	3 air masses	4 air masses	5 air masses	6 air masses
Natural Illuminance I_c	4.672×10^{-4}	3.767×10^{-4}	3.089×10^{-4}	2.536×10^{-4}	2.077×10^{-4}	1.7×10^{-4}
Natural Irradiance W/t^2	3.336×10^{-5}	2.724×10^{-5}	2.299×10^{-5}	1.926×10^{-5}	1.623×10^{-5}	1.381×10^{-5}
Radiant Sensitivity A/t^2	5.368×10^{-7}	4.308×10^{-7}	3.534×10^{-7}	2.895×10^{-7}	2.363×10^{-7}	1.957×10^{-7}
Radiometric Responsivity A/W	1.609×10^{-2}	1.581×10^{-2}	1.537×10^{-2}	1.504×10^{-2}	1.456×10^{-2}	1.417×10^{-2}
Luminous Sensitivity A/lm	1.308×10^{-4}	1.308×10^{-4}	1.308×10^{-4}	1.308×10^{-4}	1.308×10^{-4}	1.308×10^{-4}
Correction Factor $\frac{1pc \text{ illuminance basis}}{1pc \text{ irradiance basis}}$	1.223	1.229	1.228	1.231	1.236	1.221

71-0530-T-103

TABLE XXIII
SCENE AND SENSOR PARAMETERS

PSYCHOMETRIC				RADIOMETRIC			RATIO OF PSYCHOMETRIC RADIOMETRIC
SYMBOL	QUANTITY	UNITS	APPROX OR TYPICAL VALUE	SYMBOL	QUANTITY	UNITS	
E	Illuminance *	fc	1	H_T	Irradiance * (over spectral band 0.35 - 0.94 micrometers)	$\frac{\text{watts}}{\text{ft}^2}$	
	1.0 Full Moon + Airglow	fc	1.23×10^{-2}				8.72×10^{-4} 14.1
	0.3 Full Moon + Airglow	fc	3.7×10^{-3}				2.62×10^{-4} 14.1
	0.1 Full Moon + Airglow	fc	1.22×10^{-3}				8.82×10^{-5} 13.8
	0.03 Full Moon + Airglow	fc	3.77×10^{-4}				2.724×10^{-5} 13.8
S	Luminous Sensi- tivity of S-25 Photocathode	$\frac{\mu A}{fc}$	200	P_R	Radiant Sensi- tivity of S-25 Photocathode	$\frac{mA}{\text{watt}}$	4 50
				P_S	Specific Radiant Sensitivity of S-25 Photocathode	$\frac{mA}{\text{watt}}$	
					1.0 Full Moon + Airglow		23.4
					0.3 Full Moon + Airglow		23.4
					0.1 Full Moon + Airglow		23.3
					0.03 Full Moon + Airglow		23.2

* For two air masses.

71-0530 T-104

TABLE XXIV

CALCULATION OF CONTRAST REQUIRED AT SENSOR TO SATISFY
 EQUATION 291 FOR $H_S = 10^{-3} \text{ W/m}^2$ SQUARE TARGET, 10 FT
 WIDE, MTF OF 3-STAGE INTENSIFIER

$\frac{x_o}{a}$	$\frac{x_o}{m \times 10^{-5}}$	R_K	R (ft)	C
1.0	2.31	0.282	110,200	1.92
2.0	4.61	0.491	54,800	0.55
3.0	6.93	0.636	36,600	0.28
4.0	9.24	0.726	27,400	0.19
6.0	13.86	0.816	18,300	0.11
8.0	18.48	0.863	13,800	0.08

* Impossible condition since by definition of C , $C \leq 1$.

SECTION XVI

SYSTEM SYNTHESIS

Systems synthesis is mainly involved with the selection of system components which provide a certain level of performance at a minimum in equipment complexity. In synthesizing electro-optical sensory systems, the first step must be to select the sensor and size the optical system. The objective lens, in particular, usually has major impact on system size, weight, power, and cost since it strongly influences other system elements such as the mirrors and servomechanisms used to point and stabilize the line of sight and the viewing windows which contribute so heavily to aerodynamic drag. The need to accurately determine system elements leads directly to a need for analytical sensory system performance prediction methods if we are to avoid the costly cut and try methods used so extensively in the past.

In addition to reducing the time and cost in developing prototype equipment, analytical prediction models lead to improved understanding of sensor principles of operation and to better methods of describing sensor parameters. In turn, improved methods of specification evolve. Also, the analysis should suggest the direction that future sensor developments should take. In this section, some of these uses of the prediction models will be described.

Before proceeding, it is desired to note one of the major successes of the analytical models developed. Prior to their development, the only method of comparing different types of sensors was a competitive laboratory evaluation. Ideally, these comparisons would be made by some independent and unbiased laboratory on the same day using the identical test procedure on each of the candidate systems. These conditions can hardly ever be achieved and, even if possible, are very costly and time consuming.

To assemble a typical developmental sensor package can require months of time and hundreds of thousands of dollars and the test results will apply only to the single sample tested. With the analytical techniques, we can predict most of the performance parameters of almost any sensor or combinations of sensors such as intensifiers and television camera tubes at the cost of only a few man-hours of computational labor. Also, these calculations compare tubes on an equal basis which would seldom be the case in laboratory evaluation, particularly when different laboratories and test procedures are involved. However, lab evaluation cannot be entirely escaped since certain sensor parameters such as lag, dynamic range, and stationary pattern noises are not yet well enough understood. Efforts are continuing in this area and progress will be made.

The methods of predicting the threshold resolution versus irradiance characteristic for sensors have been described in considerable detail in the preceding sections. In the course of the work, the models have been considerably refined. In the new method of analysis, it was found that the length of the bars used in the repetitive bar patterns used to measure threshold resolution can have considerable effect on the measured results. In current industry and military practice, it is not usual to specify either the type or dimensions of the test pattern, yet, without this knowledge, comparisons are not valid. Therefore, it is strongly urged that any threshold resolution specification include a test pattern specification. However, although a standardized pattern is a convenience in comparing sensors, it is not necessarily desirable to specify a single pattern type as a standard because certain patterns may be more desirable than others depending on the sensor used, the test conditions, and the other uses to which the pattern may be put such as a simultaneous measurement of aperture response and threshold resolution. However, the quantitative relationships between the pattern actually used and some standard should be determined and the data converted to the standard. It is felt that this is both possible and practical to do.

One feature of the new models developed in this program is that the spatial filtering of signal related noise by the sensor apertures is taken into account. This is of no moment when the sensor is primarily system noise limited as for example by its preamplifier noise but matters a great deal when the sensor is photoelectron limited as will be shown. In particular, it will be found that a video signal-to-noise ratio specification can lose much of its meaning unless proper account is taken of the spatial filtering effect. It is observed that it is not usual to specify video signal-to-noise ratio in television practice except in isolated instances, but it is quite usual in FLIR equipments. The starting point of this analysis is the basic SNR_D equation for bar patterns which is written as

$$SNR_D = \left[\frac{n_v t \Delta f_V}{a} \right]^{1/2} \cdot \frac{SNR_{V,N,C}}{N_h} \quad (294)$$

where n_v is the bar pattern height-to-width ratio; t is the sampling time; a is the picture aspect ratio; Δf_V is the video bandwidth (to be defined below); $SNR_{V,N,C}$ is the video signal-to-noise ratio measured for a bar pattern of contrast, C , and spatial frequency N_h . Suppose first that the MTF in the horizontal and vertical is unity and that the system is band-limited by the video amplifier. Let the noise be photoelectron and uniform density in the frequency domain. The video bandwidth Δf_V is determined by the equation

$$\Delta f_V = \frac{a N_v \cdot N_h}{2 t_f} \quad (295)$$

where N_v is equal to the number of scan lines in the vertical, t_f is the frame time, and N_h is the highest bar pattern spatial frequency of interest. Both N_v and N_h are measured in lines per picture height. Suppose $a = 4/3$, $N_v = N_h = 1,000$, and that $t_f = 1/30$ sec. The $\Delta f_V = 20 \times 10^6$ Hz.

Suppose the video signal-to-noise ratio is measured using an input pulse of unit contrast and amplitude. This will be proportional to

$$\text{SNR}_{V,N} \approx \frac{1}{[e \Delta f_V]^{1/2}} \quad (296)$$

where e is the charge of an electron. Next, we assume that the sensor has an MTF of $R_o(N_h)$. If a bar pattern of very low spatial frequency N_{ho} is used, the signal amplitude is virtually unchanged. However, the sensor's MTF may now become the limiting bandwidth rather than that of the video amplifier. In terms of a noise equivalent bandwidth Δf_n ,

$$\Delta f_n = \frac{N_y}{2 t_f} \int_0^{N_{hc}} |R_o(N_h)|^2 dN_h \quad (297)$$

where N_{hc} is the spatial frequency at which $R_o(N_h)$ becomes essentially zero. Suppose the MTF has the form

$$R_o(N_h) = \left[1 - N_h/N_{hc} \right] \quad (298)$$

and that $N_{hc} = 1,000$. Then Δf_n through equation 86 (Section V) becomes

$$\Delta f_n = \frac{\alpha N_v}{2 t_f} \frac{N_{hc}}{3} \quad (299)$$

When evaluated using the same numbers as for equation 295, $\Delta f_n = 6.67 \times 10^6$ Hz. The video signal-to-noise ratio which would be measured using a test pattern of low spatial frequency would be

$$\text{SNR}_{V,O} \approx \frac{1}{[e \Delta f_n]^{1/2}} \quad (300)$$

The result is that a higher video signal-to-noise ratio is measured for a system with a degrading aperture included than for a system with a unity MTF. Thus, in this case, the sensor quality is inversely proportional to video signal-to-noise ratio is approximately the same for either case so long as the pattern is of low spatial frequency since Δf_n must be substituted for

Δf_V in equation 294 when the MTF is the limiting bandwidth. The main point is that a minimum video signal-to-noise ratio specification can lead to an inferior system which would be quite opposite to the intent of the specification.

We turn next to the subject of resolution which is specified in several different ways. In television practice, it is most common to use lines per picture height; i. e.,

$$N_{TV} = \frac{Y}{\Delta y} \frac{\text{lines}}{\text{picture height}} \quad (301)$$

where Y is the picture height and Δy is the width of a half cycle of a periodic test pattern. The dimensionless character of N_{TV} is most convenient when a number of imaging and reimaging steps are involved and in which the image area may change one or more times. No account need be taken of the image dimension changes when specifying resolution in dimensionless form which makes the process of multiplying MTF's together to get an overall MTF particularly easy. However, N_{TV} alone is not sufficient to specify sensor resolution — the sensor's picture height is also needed.

In specifying the resolution of lenses, photographic film and direct view light amplifiers, it is most usual to employ the measure line pairs (or cycles) per millimeter defined as

$$N_{LP} = \frac{1}{2\Delta y} = \frac{N_{TV}}{2Y} \frac{\text{line pairs}}{\text{mm}} \quad (302)$$

where Δy or Y are in units of millimeters. N_{LP} is a unique measure of sensor resolving power when referenced to the input photosurface. However, it is not a unique measure of sensory system resolution for which the lens focal length must also be known. On the other hand, it is the most useful measure of a sensor because in most cases, the designer has considerable latitude in selecting a lens. A FLIR represents an important exception in that the sensitivity of its detection is intimately associated with the lens because of cold shielding requirements. As a result, it is more usual in FLIR analysis to give overall sensory system resolution in angular units of cycles (or line pairs) per milliradian. In this case,

$$N_{\theta} = \frac{F_L \cdot N_{LP}}{1,000} \quad (\text{cycles/mr}) \quad (303)$$

The function N_{θ} is a unique measure of a sensory systems resolution. Another less commonly used measure is the ground resolution x_g which is equal to

$$x_g = \frac{R}{1,000 N_{\theta}} \quad \frac{\text{feet}}{\text{line pairs}} \quad (304)$$

From a sensory system analysis viewpoint, N_{θ} is preferred since resolution given in angular units is unique while x_g is range dependent. However, when the detectability of a specific target is considered, it becomes ultimately necessary to consider ground resolution.

All of these various measures of resolution were used in this report. In general, we used that measure which has been most common for the sensor in question in the past. However, in the future, it is recommended that the primary unit of resolution for sensors be N_{LP} (even in the case of FLIR) and that the primary measure for systems be N_{θ} .

A sensor's response to a sine wave test pattern is a product of the broad area signal response multiplied by the sensor's MTF. In many systems, aperture correction is applied to offset the signal falloff with increasing spatial frequency. The value of aperture correction has been controversial for photoelectron-limited sensors since the signal and noise occupy the same spatial frequency spectrum, and aperture correction amplifies signal and noise alike. Thus, the image signal-to-noise ratio remains unchanged as correction is applied. However, a second possibility must be considered. As the incremental signal at the display decreases due to the sensor's MTF, the signal may drop below the fluctuation noise due to the display's average brightness as was suggested in Section VII. This possibility will be examined in more detail in the next effort. Experimentally, it has been noted that aperture correction appears to be of positive benefit even with photoelectron-limited sensors.

We have observed that the sensor's apertures filter photoelectron noise. In this study, some progress in estimating the degree of filtering has been made although further efforts are indicated. As the accuracy improves, it will become possible to estimate the amount of useful sensor gain needed and to provide methods of optimizing sensor performance by programming this gain with high-light irradiance.

In the above, we have discussed some of the benefits to be derived from the models developed. In the continuation program, more emphasis will be placed on applications of the theory although further fundamental investigations will be conducted to extend the models to more complicated (and more realistic) scenes.

REFERENCES

1. Sendall, R. L.; Proc. IRIS, 1970.
2. Rose, A., JOSA, 38, Feb. 1948.
3. deVries, H., Physica, 1943, pp 553-564.
4. Coltman, J., and Anderson, A., Proc. IRE, May, 1960.
5. Blackwell, H., JOSA, 36, 11, Nov. 1946.
6. Moroney, M., Facts From Figures, Pelican Books, 1960.
7. Brownly, Industrial Experimentation, Chemical Publishing Co., Inc., 1947.
8. Legault, R., Photoelectron Imagery Devices, Vol I, Plenum Press, NY (1971)
9. Davenport and Boot, Random Signals and Noise, McGraw Hill, 1958.
10. CRC Standard Mathematical Tables - Chemical Rubber Publishing Co.
11. Schade, O., Sr., JOSA, 46, 9 Sept. 1956.
12. Linfoot, E., JOSA, 45, 10, Oct. 1955.
13. Goodman, J., Introduction to Fourier Optics, McGraw Hill, 1968.
14. Bracewell, R., The Fourier Transform and Its Application, McGraw Hill, 1965.
15. Schwartz, M., Information Transmission, Modulation and Noise, McGraw Hill, 1959.
16. Cuccia, C., Harmonics, Sidebands and Transients in Communication Engineering, McGraw Hill, 1959.
17. Coltman, J., JOSA, 44, 6, June 1954.
18. O'Neill, E., IRE, Trans. On Information Theory, June 1956.
19. Limansky, I., The Electronic Engineer, June 1968.
20. Rosell, F., JOSA, May 1969.
21. Parton and Moody, Imaging Tube Symposium, Oct. 1961, U.S. Government Printing Office Report NASA-SP-2.

22. Schade, O., Sr., SMPTE, 64, Nov. 1955.
23. Johnson, J., Image Intensifier Symposium, Ft. Belvoir, Va., Oct. 6-7, 1958.
24. Schade, O., Sr., SMPTE, 56, Feb. 1951.
25. Campbell, F.W., Proc. IEEE, 56, 6 Jan. 1968.
26. Schade, O., Sr., SMPTE, 61, Aug. 1953.
27. Schober; Hilz, JOSA, 55, Sept. 1965.
28. Selke, L., IEEE Trans. Electron Devices, ED-16, No 7, July 1969.
29. Electro Optics Handbook, RCA Defense Electronic Products Aerospace Systems Division, Burlington, Mass.
30. Middleton, WEK; Vision Through the Atmosphere, University of Toronto Press, 1958.
31. Steingold, H.; Strauch, R.; Applied Optics, Jan. 1969.
32. Wilson, R.H.; Rampolla, R.W.; Smith, G.V.; "Detection and Recognition Ranges For a TV System Under Ambient and Covert Action Illumination Conditions" (W) Aerospace and Electronic Systems Division, TM #50512, Jan. 7, 1970.
33. Willson, R.H.; Smith, G.V.; "The Effect Of Incomplete Intensifier Turn Off On Detection Range For a Covert Active System" (W) Aerospace and Electronics Division, TM #E0513, Jan. 23, 1970.
34. Willson, R.H., "The Influence of Gate Transition Time on System Performance For An Active Illuminator - Gated Sensor LLLTV" (W) Aerospace and Electronics Systems Division, Sept. 4, 1970.
35. Biberman, L.; Dunkelman, L.; Fickett, M.; Funke, R.; IDA Research Paper 232, Jan. 1966.
36. Rampolla, R.W., "Backscatter Effects in Active Illumination Systems" Paper presented at summer program, Photo Electronic Imaging Devices, University of Rhode Island, August 8, 1969.